

# The American Monsoon System: variability and teleconnections

Jorge Luis García Franco

Wadham College  
University of Oxford

*A thesis submitted for the degree of  
Doctor of Philosophy*

Michaelmas 2021

## Abstract

This thesis investigates the representation of the variability and teleconnections of the American Monsoon System in the Met Office Hadley Centre general circulation models. The models exhibit a number of important biases including an overestimation of the strength of the East Pacific Inter-tropical Convergence Zone (ITCZ) and the position of the Atlantic ITCZ is simulated southward of the observed position. The representation of the seasonality and magnitude of monsoon precipitation in the North American and Central American monsoons has improved compared to previous generations of the models, however, the spatial distribution of precipitation in the South American Monsoon is still poorly represented due to biases in the equatorial Atlantic sea-surface temperatures. These models stand-out for their representation of the seasonal cycle of precipitation in southern Mexico and Central America, where a bimodal signal known as the Mid-summer drought (MSD) has been observed for centuries. A wavelet transform method is developed to diagnose the timings of the bimodal seasonal cycle and results illustrate that the method can be used to diagnose monsoon timings in any monsoon region for any precipitation time-series, including climate model output. Using this method, a number of theories that explain the existence and timing of the MSD signal in southern Mexico and Central America are evaluated using reanalysis and CMIP6 simulations. These results suggest that the most consistent theory with the models and reanalysis explains the MSD through the effect of seasonally varying moisture transport driven by the seasonal cycle of the moisture transport in the Caribbean Sea. The simulations show that the teleconnections of El Niño-Southern Oscillation to the American Monsoon System associated with the perturbation to the Walker circulation are linked with the stratospheric quasi-biennial oscillation (QBO). An analysis of the CMIP6 pre-industrial experiments of HadGEM3 and UKESM1 shows that the tropical route of QBO teleconnections in the simulations involves ocean-atmosphere phenomena such as the ITCZs, the Indian Ocean Dipole and the Walker circulation. Atmosphere-only and coupled ocean-atmosphere experiments are performed where the zonal winds in the equatorial stratosphere are specified to improve the representation of the QBO and evaluate directly the impact of the QBO on tropical climate. The experiments with the relaxation of the winds result in a weaker or null response to the QBO winds, in contrast to the free-running models. The results of these experiments highlight the importance of SST feedbacks and the interaction of tropical waves with the zonal flow in the stratosphere for the interaction of the QBO on tropical convection.

# The American Monsoon System: variability and teleconnections



Jorge Luis García Franco

Wadham College

University of Oxford

A thesis submitted for the degree of

*Doctor of Philosophy*

Michaelmas 2021

# Abstract

This thesis investigates the representation of the variability and teleconnections of the American Monsoon System in the Met Office Hadley Centre general circulation models. The models exhibit a number of important biases including an overestimation of the strength of the East Pacific Inter-tropical Convergence Zone (ITCZ) and the position of the Atlantic ITCZ is simulated southward of the observed position. The representation of the seasonality and magnitude of monsoon precipitation in the North American and Central American monsoons has improved compared to previous generations of the models, however, the spatial distribution of precipitation in the South American Monsoon is still poorly represented due to biases in the equatorial Atlantic sea-surface temperatures.

These models stand-out for their representation of the seasonal cycle of precipitation in southern Mexico and Central America, where a bimodal signal known as the Mid-summer drought (MSD) has been observed for centuries. A wavelet transform method is developed to diagnose the timings of the bimodal seasonal cycle and results illustrate that the method can be used to diagnose monsoon timings in any monsoon region for any precipitation time-series, including climate model output. Using this method, a number of theories that explain the existence and timing of the MSD signal in southern Mexico and Central America are evaluated using reanalysis and CMIP6 simulations. These results suggest that the most consistent theory with the models and reanalysis explains the MSD through the effect of seasonally varying moisture transport driven by the seasonal cycle of the moisture transport in the Caribbean Sea. The simulations show that the teleconnections of El Niño-Southern Oscillation to the American Monsoon System associated with the perturbation to the Walker circulation are linked with the stratospheric quasi-biennial oscillation (QBO). An analysis of the CMIP6 pre-industrial experiments of HadGEM3 and UKESM1 shows that the tropical route of QBO teleconnections in the simulations involves ocean-atmosphere phenomena such as the ITCZs, the Indian Ocean Dipole and the Walker circulation.

Atmosphere-only and coupled ocean-atmosphere experiments are performed where the zonal winds in the equatorial stratosphere are specified to improve the representation of the QBO and evaluate directly the impact of the QBO on tropical climate. The experiments with the relaxation of the winds result in a weaker or null response to the QBO winds, in contrast to the free-running models. The results of these experiments highlight the importance of SST feedbacks and the interaction of tropical waves with the zonal flow in the stratosphere for the interaction of the QBO on tropical convection.

# Contents

<b>List of Abbreviations</b>	<b>vi</b>
<b>1 Introduction</b>	<b>1</b>
1.1 Motivation . . . . .	1
1.2 Thesis aims and outline . . . . .	4
<b>2 Background</b>	<b>8</b>
2.1 The tropical circulation and the global monsoon . . . . .	8
2.2 The American Monsoon System . . . . .	15
2.3 A review of the physical mechanisms for the Midsummer drought . . . . .	18
2.4 El Niño Southern Oscillation: impacts to the American monsoon system . .	22
2.5 Stratosphere-Troposphere Coupling in the Tropics . . . . .	25
2.5.1 The Quasi-biennial oscillation (QBO) . . . . .	26
2.5.2 Tropical teleconnections of the QBO . . . . .	27
<b>3 Data and methods</b>	<b>32</b>
3.1 Observations and reanalysis data . . . . .	32
3.1.1 Gridded precipitation datasets . . . . .	32
3.1.2 ERA-5 . . . . .	35
3.2 The Unified Model of the Met Office Hadley Centre . . . . .	36
3.2.1 The Global Coupled Configurations of HadGEM3 . . . . .	36
3.2.2 The CMIP6 experiments . . . . .	37
3.3 The Moist Static Energy Budget . . . . .	40
<b>4 The American monsoon system in UKESM1 and HadGEM3</b>	<b>43</b>
4.1 Introduction . . . . .	43
4.2 Methods and data . . . . .	45
4.3 Surface temperature and low-level wind . . . . .	47
4.4 The Atlantic and Pacific ITCZs and the SACZ . . . . .	52
4.5 Precipitation and convection in the AMS . . . . .	57
4.5.1 Mean seasonal precipitation . . . . .	57
4.5.2 The annual cycle of rainfall . . . . .	61

4.5.3	Characteristics of convective activity . . . . .	63
4.6	ENSO Teleconnections . . . . .	66
4.6.1	Canonical teleconnections . . . . .	66
4.6.2	The role of ENSO flavours . . . . .	71
4.6.3	A possible influence of the QBO on tropical ENSO teleconnections .	74
4.7	Summary and discussion . . . . .	78
<b>5</b>	<b>A wavelet transform method to determine monsoon onset and retreat</b>	<b>83</b>
5.1	Introduction . . . . .	83
5.2	Data . . . . .	86
5.2.1	Precipitation datasets and reanalysis data . . . . .	86
5.2.2	Model data . . . . .	87
5.3	The wavelet transform method . . . . .	87
5.3.1	Identification of Monsoon Onset and Retreat . . . . .	89
5.3.2	Extension for Application to the MSD signal . . . . .	93
5.3.3	Comparative Methodologies . . . . .	94
5.4	Results . . . . .	96
5.4.1	The North American Monsoon . . . . .	97
5.4.2	The Indian Monsoon . . . . .	101
5.4.3	The midsummer drought . . . . .	104
5.5	Summary and discussion . . . . .	112
<b>6</b>	<b>The Midsummer drought in the MOHC CMIP6 experiments</b>	<b>116</b>
6.1	Introduction . . . . .	116
6.2	Data and methods . . . . .	120
6.2.1	Observations and reanalysis data . . . . .	120
6.2.2	CMIP6 data . . . . .	121
6.2.3	Determination of the timings of the MSD . . . . .	121
6.3	Climatological features . . . . .	122
6.4	The role of East Pacific SSTs . . . . .	130
6.5	The role of cloud-radiative effects . . . . .	137
6.6	The role of the Caribbean Low-Level Jet . . . . .	145
6.7	A short look at the MSD through the lense of the moist static energy budget	151
6.8	Summary and discussion . . . . .	160

<b>7</b>	<b>The tropical route of QBO teleconnections in UKESM1 and HadGEM3</b>	<b>165</b>
7.1	Introduction . . . . .	165
7.2	Methods and data . . . . .	167
7.2.1	CMIP6 data . . . . .	167
7.2.2	Indices . . . . .	168
7.2.3	Analysis techniques . . . . .	168
7.3	Teleconnections in the pre-industrial control experiments . . . . .	169
7.3.1	Seasonal variability . . . . .	170
7.3.2	Impacts over the ITCZ and the monsoons . . . . .	174
7.3.3	ENSO, the IOD and the Walker circulation . . . . .	179
7.4	Summary and discussion . . . . .	187
<b>8</b>	<b>Tropical Teleconnections of the QBO in the UM with a nudged stratosphere</b>	<b>190</b>
8.1	Introduction . . . . .	190
8.2	The nudging protocol . . . . .	192
8.2.1	The importance of biases in the UTLS for stratosphere-tropospheric coupling . . . . .	193
8.2.2	The nudging protocol . . . . .	194
8.3	Results from nudging experiments . . . . .	199
8.3.1	Tropical UTLS variability . . . . .	200
8.3.2	Atmosphere-only experiments . . . . .	202
8.3.3	Coupled experiments . . . . .	208
8.4	Summary and discussion . . . . .	219
<b>9</b>	<b>Conclusions</b>	<b>222</b>
9.1	Summary . . . . .	222
9.2	Limitations and future work . . . . .	226
<b>Bibliography</b>		<b>230</b>

## List of Abbreviations

<b>AMS</b>	American Monsoon System.
<b>CLLJ</b>	Caribbean Low-Level Jet.
<b>CMIP</b>	Coupled Model Intercomparison Project.
<b>CRE</b>	Cloud-radiative Effect.
<b>ENSO</b>	El Niño-Southern Oscillation.
<b>GCM</b>	General Circulation Model.
<b>IOD</b>	Indian Ocean Dipole.
<b>ITCZ</b>	Inter-tropical Convergence Zone.
<b>MOHC</b>	Met Office Hadley Centre.
<b>MSD</b>	Mid-summer Drought.
<b>MSE</b>	Moist Static Energy.
<b>OLR</b>	Outgoing Longwave Radiation.
<b>QBO</b>	Quasi-biennial Oscillation.
<b>SACZ</b>	South Atlantic Convergence Zone.
<b>SAMS</b>	South American Monsoon System.
<b>SST</b>	Sea-surface Temperature.
<b>TWC</b>	Total water content.
<b>WT</b>	Wavelet Transform.

# 1

## Introduction

The American Monsoon System (AMS) is the main source of rainfall for the most part of Latin America and the southwestern United States, which are regions where agricultural activity is economically crucial and where a vast wealth of ecosystems and biodiversity are present. Changes to the amount, timings and location of rainfall over different temporal scales has direct consequences for the livelihood of the people and for ecosystems in the regions. Improving our physical understanding of the mechanisms that cause temporal changes to the AMS rainfall is crucial to improve our medium-range forecasts and our climate predictions which could ultimately render key information for risk assessments, climate adaptation and agricultural strategies. In this context, this thesis aims to tackle outstanding questions in the American Monsoons in a global climate model with particular interest in better understanding the physical mechanisms associated with variability and teleconnections of this monsoon.

### 1.1 Motivation

Temporal and spatial variability of rainfall is important for society throughout the planet for various reasons, but the relevance of the timing and strength of rainfall is emphasized in agriculturally active and biodiversity hotspot tropical regions (Sultan et al., 2005; Jain et al., 2015). In the AMS, changes to rainfall on inter-annual scales can produce long-lived droughts that are associated with crop loss and forest fire intensification (Chen et al.,

2009; Harvey et al., 2018). A large body of monsoon research is consequently focused on understanding the physical mechanisms responsible for precipitation variability across temporal and spatial scales (Wang et al., 2017; Gadgil, 2018).

The AMS was recognized as a monsoon only after the 1990s, which is relatively recent, as the definition for a monsoon has evolved from an initial dynamical definition based on a reversal of the prevailing winds to an agronomical definition that recognizes the seasonality of precipitation as the dominant feature of a monsoon (Wang et al., 2017; Gadgil, 2018). This fact, however, means that our understanding of the AMS is more limited compared to other monsoons given the lower number of studies on the AMS from a monsoon perspective when compared to other monsoons such as the Indian monsoons, where monsoon forecasts exist since the 19th century (Blanford, 1886). For this reason, several primary questions about general aspects of the AMS remain open including unknown mechanisms for interannual variability and teleconnections.

Recently, theories for general or global monsoon dynamics (Bordoni and Schneider, 2008; Biasutti et al., 2018; Hill, 2019; Geen et al., 2020) have arisen in an effort to coherently explain the monsoons through a general physical mechanism. Most of these theories aim to explain a global inter-hemispheric band of convection that is driven by the seasonal cycle of solar insolation. Several characteristics of the North and South American monsoons, however, challenge the basic physical inferences or predictions of most of these theories, which means that these newly developed frameworks cannot easily be applied to the AMS to further understand their variability.

The lack of understanding of the basic physical mechanisms that drive the seasonal cycle of rainfall in the southern Mexico and Central America is one example of the gaps in the literature of the AMS. The so-called Midsummer drought is a robust bimodal feature of the seasonal cycle of precipitation during the wet season that has had implications for agricultural practices in the region since the Mayan Empire (AD 800-900) (Jobbová et al., 2018). In spite of the importance for region-wide agricultural practices, the physical mechanisms that can explain this seasonal variation of rainfall remain disputed over recent years (Karnauskas et al., 2013; Herrera et al., 2015; Zermeño-Díaz, 2019).

Climate research in South America has recently focused to investigate the non-linear responses of precipitation of the AMS to teleconnections from the El Niño-Southern Oscillation (ENSO), which occurs just on the western coast of the continent. ENSO phenomena has been well-known by Peruvian fishermen for centuries and has shaped agricultural practices and caused mass migrations (Caramanica et al., 2020). Nevertheless, the understanding of the effect of ENSO over South America and the AMS in general is still somewhat limited. For example, two ENSO events that are very similar in the central Pacific can cause teleconnections with different locations and strengths and the reasons behind these varying effects are not well understood.

One key tool to understand the causes for regional changes to monsoon rainfall are general circulation models (GCMs). These models are useful to evaluate the roles of climate features such as orography, vegetation-atmosphere and ocean-atmosphere feedbacks, ENSO and their impacts over many aspects of Earth's climate including monsoons (Zhou et al., 2016). However, the use of GCMs to address key questions of the AMS has been scarce. In fact, detailed accounts of the biases –differences between the simulated climate of a model and the real world – are rarely done with explicit emphasis on the AMS. In other words, GCMs are rarely evaluated in the AMS, so our understanding is deficient both in the knowledge of the relevant biases in current GCMs for the AMS but also because of a relative scarce use of GCMs to address scientific questions related to the AMS.

This thesis focuses on the AMS and the outstanding questions regarding the climate variability and teleconnections affecting this monsoon. This thesis begins (Chapter 4) by evaluating a state-of-the-art climate model, the UK Met Office Unified Model (UM) in the AMS region and comparing the model with several observational datasets, with assessing the roles of biases in the large-scale circulation that affect regional monsoon rainfall biases. This assessment highlights that UM model is fit for the purpose of investigating two outstanding research questions in the AMS and monsoon literature: the physical mechanisms that control the seasonal cycle of rainfall in southern Mexico and Central America, and the role of the tropical stratosphere for tropical convection and monsoons.

For the first research question, Chapter 5 describes a new method to determine monsoon timings, including the timings of bimodal regimes of precipitation in observations and climate

model output. This method is then used in Chapter 6 to investigate the physical mechanisms of the seasonal cycle of precipitation in southern Mexico and Central America.

## 1.2 Thesis aims and outline

The main aim of this thesis is to investigate the physical causes of variability and the mechanisms associated with teleconnections to the AMS. The specific key aims of this thesis are:

1. To characterize the large-scale biases in a state-of-the-art GCM that are relevant for the representation of rainfall in the AMS.
  - (a) To characterize the main biases in the thermodynamical and dynamical features over the large scale tropical domain and the regional AMS sub-domains.
  - (b) To evaluate the roles of large-scale biases, horizontal resolution and the use of Earth system processes for regional monsoon representation.
  - (c) To assess the representation of the teleconnection associated with the main driver of interannual variability, i.e., ENSO in a GCM with specific emphasis on the causes for non-linearity and non-asymmetry in the teleconnections.
2. Evaluate the seasonal variability of the monsoon onset, withdrawal and intra-seasonal changes in the GCM and compare to observational datasets.
3. Describe and investigate the physical mechanisms associated with the seasonal cycle of rainfall in Central America and southern Mexico by testing previous hypothesis of physical mechanisms within the model.
4. To investigate the role of stratospheric-tropospheric coupling in the tropics and the role of the tropopause for convection in the AMS and for ENSO teleconnections.

The remainder of this thesis is structured as follows:

- Chapter 2 provides a review of the literature on key aspects of the American monsoons. The chapter begins by introducing the concepts of monsoons, their different physical

interpretations as a global phenomena and the place of regional monsoons in the global scale. Then, the North and South American monsoons are introduced and detail is given on the applicability of large-scale monsoon theories to these regional monsoons. This section is followed by a literature review of the proposed physical mechanisms that drive the seasonal cycle of rainfall in Central America, southern Mexico and the Caribbean. El Niño-Southern Oscillation impacts over North and South America and, finally, the chapter summarises the literature on stratospheric-tropospheric coupling in the tropics, discussing possible mechanisms by which the stratospheric quasi-biennial oscillation may be influential for tropical convection.

- Chapter 3 describes the observational datasets used in this thesis, composed of four gridded precipitation datasets and one reanalysis dataset: ERA5. The chapter also described the UK Met Office Hadley Centre Unified Model (UM) and the configurations of the UM used in this thesis and in the Coupled Model Intercomparison Project phase 6 (CMIP6).
- Chapter 4 evaluates the representation of the AMS in three configurations of the UM model submitted to CMIP6. The chapter describes large-scale biases over the tropics and regional scale biases in the precipitation amount and seasonality in key regions of the AMS. ENSO teleconnections are also evaluated over the AMS examining the non-linearity of simulated and observed teleconnections and the role of ENSO flavours. This chapter highlights relevant questions that are of interest to the wider AMS community. In particular, two aspects are emphasized that are tackled in the remaining chapters: first, the skill of the models in reproducing a bimodal signal in the seasonal cycle of rainfall in Central America and southern Mexico and second, a possible modulation of ENSO teleconnections by the stratospheric quasi-biennial oscillation. The majority of the work in this chapter has been published in *Weather and Climate Dynamics* as García-Franco et al. (2020).
- Chapter 5 details a wavelet covariant transform method used to diagnose changes to the timings of the monsoon by determining the onset and retreat dates from precipitation

time-series. The method is extended to be used to determine the timings of bimodal regimes, and even whether or not a bimodal regime exists or not in a given region. The method is illustrated in the North American and Indian monsoons, and for the Mid-summer Drought signals of the Caribbean and southern Mexico. This chapter has been published in the *The International Journal of Climatology* as García-Franco et al. (2021).

- Chapter 6 uses the method of the previous to investigate the physical mechanisms that cause the bimodal regime of precipitation in southern Mexico in the UM CMIP6 models. The chapter tests elements of three leading hypothesis for the Mid-summer drought, specifically the chapter examines the roles of the East Pacific sea-surface temperatures, the cloud-radiative effects and shortwave radiation and the Caribbean Low-Level Jet. Furthermore, the chapter uses a moist static energy budget, which provides useful insight as to the causes for the changes to precipitation within the rainy season in these regions.
- Chapter 7 investigates the tropical route of QBO teleconnections in the pre-industrial control experiments of HadGEM3 and UKESM1. The observational evidence that links the QBO with the ITCZ, ENSO and the Walker circulation is examined within these simulations to evaluate whether similar relationships to the observations are found within a state-of-the-art GCM. The results from these CMIP6 simulations are very similar to observations suggesting robust relationships between the QBO phase, the ITCZs and the Walker circulation.
- Chapter 8 follows up on the topic of QBO teleconnections in the tropics by describing the realization of several experiments using a GCM with a nudged stratosphere. These experiments aim to alleviate biases with the representation of the QBO as well as to test the causal pathway through which the tropical troposphere and stratosphere interact with each other. The results of this chapter show that when the relaxation was applied most of the teleconnections observed in the control experiments disappear, indicating either that the mechanisms that modulate stratospheric-tropospheric coupling were

obscured by the experimental design or that the QBO variability is not driving these teleconnections.

# 2

## Background

This chapter provides the necessary background for the topics of the thesis; first by summarising the main aspects of the tropical circulation and of the global monsoon and discussing the existing theories to explain the monsoon phenomena. Then, the American Monsoon System is introduced and detail is given on the Midsummer drought of southern Mexico and Central America and El Niño Southern Oscillation teleconnections to this monsoon. Finally, a summary of the literature on the role of stratospheric-tropospheric coupling in the tropics for monsoon variability is given, first by describing the stratospheric quasi-biennial oscillation (QBO) and existing evidence linking the QBOWith deep convective systems, such as monsoons.

### 2.1 The tropical circulation and the global monsoon

Tropical climate is a result of the strong solar insolation received year-round that generally provides a stronger heating of the surface compared to extra-tropical latitudes. These latitudinal differences in insolation generate a meridional heat transport by the coupled atmosphere-ocean system. This means that the tropics have a positive annual net energy and the extra-tropics show an annual negative net energy.

The dynamics in the tropics is also distinct from extra-tropical latitudes due to other physical features such as the relative extent and location of the continents, the way in

which gravity waves propagate throughout the atmosphere and a different impact of Earth's rotation upon the dynamics of parcels. Generally, tropical dynamics is considered to be less well understood than mid-latitude dynamics, because most of the assumptions of mid-latitude dynamical frameworks break down in the tropics, but also because reliable data in the tropics was scarce until satellites began providing continuous reliable observations of the tropics in the 1980s (Emanuel, 2007; Webster, 2020).

Moist convection is arguably one of the characteristic traits of tropical climate as the dynamics and thermodynamic effects of deep moist convection provide important feedbacks to the regional and large-scale circulation (Emanuel et al., 1994; Webster, 2020). Anomalous convection and the associated feedbacks are a key factor in tropical teleconnections through their role in the generation of large-scale propagating waves and resulting anomalous circulation (Hartmann, 2015; Li and Hsu, 2018). Moist convective systems span different spatial and temporal scales, from short-lived cumulonimbus showers to tropical cyclones that can survive more than a week on the open ocean. Over sufficiently long scales, the mean deep moist convective activity also plays a significant role in determining the large-scale tropical circulation typically divided into meridional and zonal overturning circulations, the Hadley and Walker circulations.

The Hadley cell is the meridional overturning circulation that arises from the differential heating between the tropics and the midlatitudes. This overturning cell is characterized by ascending motions in the tropics and descending motions in the subtropics, and acts to transport heat poleward from the equator (Lorenz, 1967). The ascending section of the Hadley circulation migrates meridionally with the seasonal cycle, the winter and summer cells interact with each other but also with the midlatitudes through eddy momentum fluxes (Bordoni and Schneider, 2008). The Hadley cell is not zonally symmetric; the boreal summer Hadley cell, for instance, is primarily a result of ascent in the Indian Ocean and the west Pacific regions with a minor contribution from ascending motions in Central and North America (Hoskins et al., 2020).

The annual mean of solar radiation at the top of the atmosphere is roughly zonally distributed, however, the energy balance at the surface and the tropical circulation are not zonally symmetric. A prominent example of zonal asymmetry in the tropics is the Walker

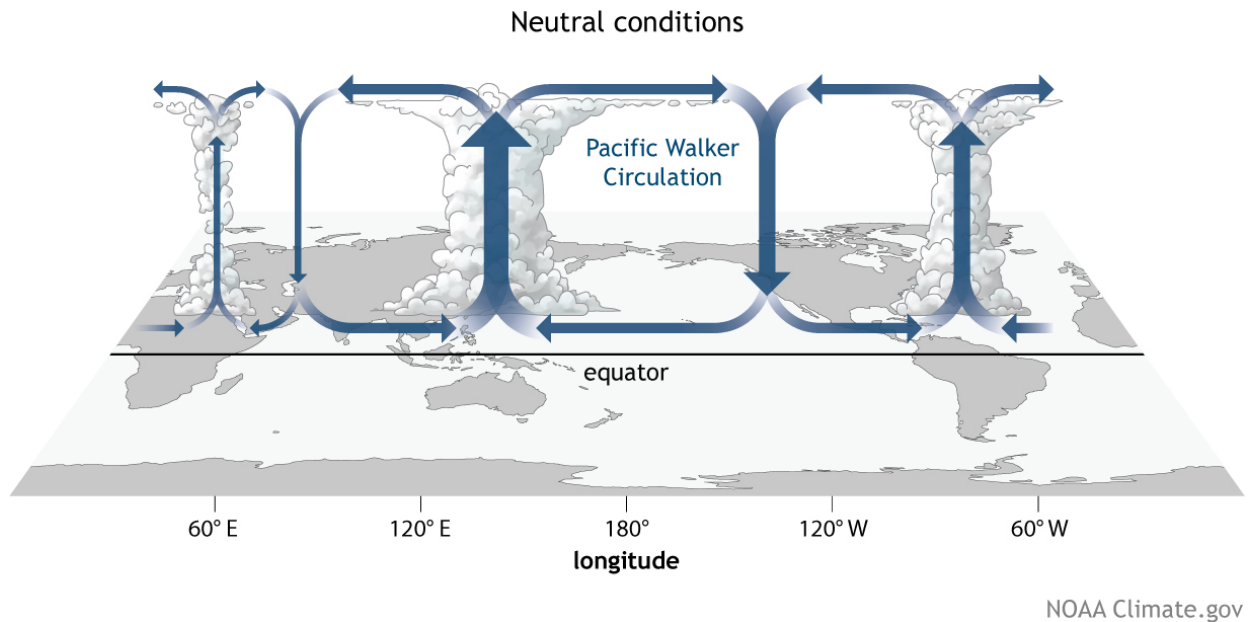


**Figure 2.1:** A schematic of the Walker circulation, depicting the mean zonal and vertical circulations, under neutral conditions of El Niño-Southern Oscillation. Schematic originally from: [www.climate.gov/](http://www.climate.gov/).

circulation. The Walker circulation is the zonal overturning circulation that is found in the equatorial Pacific Ocean, illustrated in Figure 2.1 and characterized by ascending motion over the West Pacific and descending motions over the East Pacific (Walker, 1924; Bjerknes, 1969; Gill, 1980). The dynamic and thermodynamic effects of the location and strength of convection associated with the Walker circulation have strong impacts across all the tropics and also the extratropics, known as teleconnections (Cai et al., 2019).

The Inter-tropical Convergence Zone (ITCZ) is a tropical band of convective clouds and precipitation that migrates meridionally with the seasons (Schneider et al., 2014). The ITCZ is arguably one of the most relevant features of tropical climate due to the strong influence on the low- and upper-level circulation associated with ITCZ, the high tropospheric heating due to deep moist convection in the ITCZ and the largest precipitation rates in the tropics are found in the ITCZ. The ITCZ is characterized by a strong convergent flow in the low levels and a strong divergent flow at upper levels. The meridional migration of the ITCZ, as well as the mean latitude of the ITCZ, results from the energy and momentum balances so that the ITCZ is predominantly north of the equator because of the inter-hemispheric temperature contrast (Donohoe et al., 2013; Bischoff and Schneider, 2016).

One of the phenomena of tropical climate that first generated interest in climate research is the monsoon (Halley, 1687). The word *monsoon* stems from the Arabic word for *season* and is closely associated with the very first conceptions of a monsoon. The first widely accepted view of a monsoon was that the monsoon was the result of a large-scale land-sea breeze associated with the differential warming of the land and the ocean that force a seasonal reversal of the low-level winds that is also associated with the seasonal cycle of rainfall (Halley, 1687).

The traditional definition of the monsoon as a land-sea breeze is now known to present several shortcomings. Firstly, several mid-latitude regions would fit a monsoon definition based solely on a seasonal reversal of the wind (Gadgil, 2018), and secondly, regions that are now recognized as a region with a monsoon climate, e.g. in South America, do not show a seasonal reversal of the winds, and the wind flow may just exhibit seasonal changes in direction and strength (Vera et al., 2006). For these reasons, the land-sea breeze view of monsoons has recently been replaced by three alternative conceptions, an ITCZ-monsoon framework, a convective quasi-equilibrium interpretation and a moist static energy (MSE) zonal-mean energetic interpretation (Biasutti et al., 2018; Hill, 2019; Geen et al., 2020).

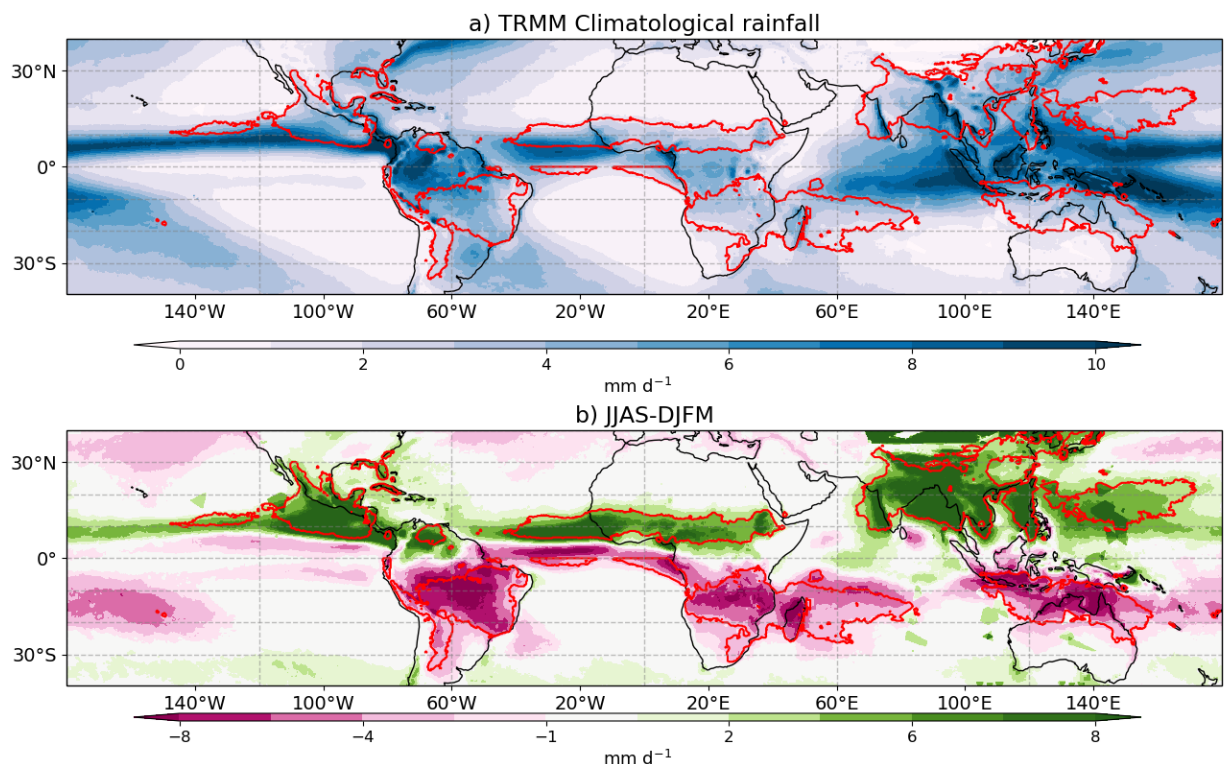
The first framework explains monsoons as a poleward extension of the ITCZ into land generalizing all monsoons as an expression of global tropical convergence resulting from the energy balance (Chao and Chen, 2001; Gadgil, 2018). This interpretation has led to the concept of *the global monsoon*, a term that encompasses all the regions in the tropics that exhibit a strong seasonality in precipitation (Zhou et al., 2016; Gadgil, 2018). In practice, the global monsoon refers to those regions of the planet where more than 70% of the total annual rainfall is observed during the local summer season, therefore, the concept of a global monsoon recognises the seasonality of precipitation as the key feature to diagnose a monsoon (Zhou et al., 2016; Wang et al., 2017).

Figure 2.2 shows the global monsoon as depicted by the TRMM dataset. By this definition, the majority of the regions over land between 5 and 10 degrees away from the equator are part of the global monsoon. A regional monsoon, such as the Indian Monsoon, is then a subset of the global monsoon with unique regional characteristics that shape this monsoon differently to other regional monsoons in terms of the seasonality, the strength

and the dynamics. The American Monsoon System is then the regional monsoon that is located in the subtropics of North and South America.

Bordoni and Schneider (2008) provide an alternative conceptual view of monsoons, describing the characteristic rapid onset of a monsoon as a regime transition of the Hadley cell from an eddy-momentum driven circulation, which resembles a canonical ITCZ regime, to a thermally direct circulation which resembles a monsoon-like circulation. The zonal mean MSE meridional gradient drives the ITCZ location and determines the strength of the overturning circulation by modulating the ventilation from midlatitude cooler and drier air in a feedback mechanism (Geen et al., 2020). Even though this framework is posited as an axisymmetric framework, their predictions were broadly consistent with the Asian monsoon circulation.

Convective quasi-equilibrium (CQE) is a theory for moist convection where convection sets the vertical temperature and moisture profiles to a convectively neutral state, thereby



**Figure 2.2:** a) Climatological mean annual rainfall rates in the tropics using data from the Tropical Rainfall Measurement Mission (TRMM) dataset (1999-2018). b) The mean rainfall rate difference between boreal summer (JJAS) and austral summer (DJFM). The red contours highlight the regions where the mean summer rainfall amount accounts for more than 55% of the mean total annual rainfall accumulation.

setting the free tropospheric temperature (Neelin, 2007). For a monsoonal circulation, this theory emphasizes the coupling of convection and dynamics predicting that the subcloud layer equivalent potential temperature maxima must be collocated with the free tropospheric saturation equivalent potential temperature (Nie et al., 2010; Geen et al., 2020). The rapid onset of the Asian monsoon has been shown to be associated with the boundary layer moist entropy distribution, in agreement with predictions of CQE (Nie et al., 2010; Boos, 2015; Ma et al., 2019).

Several studies examine the monsoon as a large-scale phenomena through an axisymmetric framework that assumes zonal symmetry investigated through global energetic diagnostics (e.g. Faulk et al., 2017; Geen et al., 2019; Byrne and Zanna, 2020). The zonal-mean framework is common to the Hadley cell interpretation of monsoons (Bordoni and Schneider, 2008), as well as the ITCZ-monsoon theory. However, regional monsoons are shaped by the asymmetries imposed by the orography, the characteristics of the surrounding ocean basins, land-sea contrasts and also the role of vegetation-hydrology coupling (Wang et al., 2017; Pascale et al., 2019). The importance of zonal asymmetries has raised multiple issues with large-scale so-called monsoon dynamics theories, as several predictions of these theories are not consistent with observations of regional monsoons (e.g. Nie et al., 2010; Smyth et al., 2018; Biasutti et al., 2018; Pascale et al., 2019).

The MSE budget and methodology is detailed in section 3.3 but a broad description of the method and summary of results arising from the MSE budget applied to the monsoon phenomena is given below. The MSE budget framework suffers both from theoretical and practical shortcomings. One practical shortcoming is that the calculation of the budget terms post hoc in reanalysis or models results in very large residuals (Hill, 2019), so these frameworks work best when the calculations of the budget terms are integrated online at each time-step (e.g. Ma et al., 2019). The theoretical shortcoming is that the surface fluxes over land, e.g., in the Sonoran and Saharan deserts and the deep Amazon make the estimations of the roles of hydrology-vegetation feedbacks and their potential contributions to the MSE budget in observations very difficult to assess (Boos and Korty, 2016; Pascale et al., 2019). The use of simpler moisture budgets has proven useful in a regional monsoon context to investigate the sources of moisture for a monsoon in current (Ordoñez et al., 2019; Martinez

et al., 2019) and future climates (Smyth and Ming, 2020), but this budget is mostly a tool and not a coherent theory for process-level understanding of monsoons.

Recent reviews acknowledge that all these frameworks have significant shortcomings when applied to regional local monsoons (Biasutti et al., 2018; Hill, 2019; Geen et al., 2020). These reviews conclude that a framework that reconciles the global energetic perspective with the characteristics of regional monsoons would be crucially important and very useful, but as several authors point out (e.g. Biasutti et al., 2018; Hill, 2019), also very hard to formulate. For example, the North and South American Monsoons depart from CQE, as precipitation does not follow the maxima in subcloud equivalent potential temperature (Nie et al., 2010; Geen et al., 2020).

The Hadley cell interpretation of monsoons has significant shortcomings to depict some regional monsoons, particularly those that are not the Asian monsoon as the overturning circulation in the South Asian monsoon is strong enough to be represented by a clear thermally direct regime. However, this energetic framework assumes no zonal transport of energy, which minimizes the role of orography and land-sea interaction (Biasutti et al., 2018). One might reasonably infer from these results that the timing of transition in zonal mean overturning cells would be similar for monsoons at different longitudes but similar latitudes, which is not the case (Wang et al., 2017). Furthermore, a monsoon restricted to a small area, such as the North American and African monsoons may not show a clear zonally averaged overturning regime, and may be significantly affected by local shallow and deep circulations (Zhai and Boos, 2015). For instance, Smyth et al. (2018) shows that the simulated West African monsoon when forced with different solar forcings exhibits a decoupling between the zonal-mean ITCZ location, the strength of the local Hadley cell and the monsoon rainfall, in opposition to the predictions of this framework (Bordoni and Schneider, 2008).

In short, despite significant progress in our understanding of the monsoon phenomena at the planetary-scale through zonal mean energetic frameworks, there is an important gap between large-scale theories of monsoon dynamics and the observed regional monsoons. The next section presents a summary of the American Monsoon literature, which explains the characteristics of these monsoons through the effect of regional features and dynamics, seemingly detached from the literature in this section.

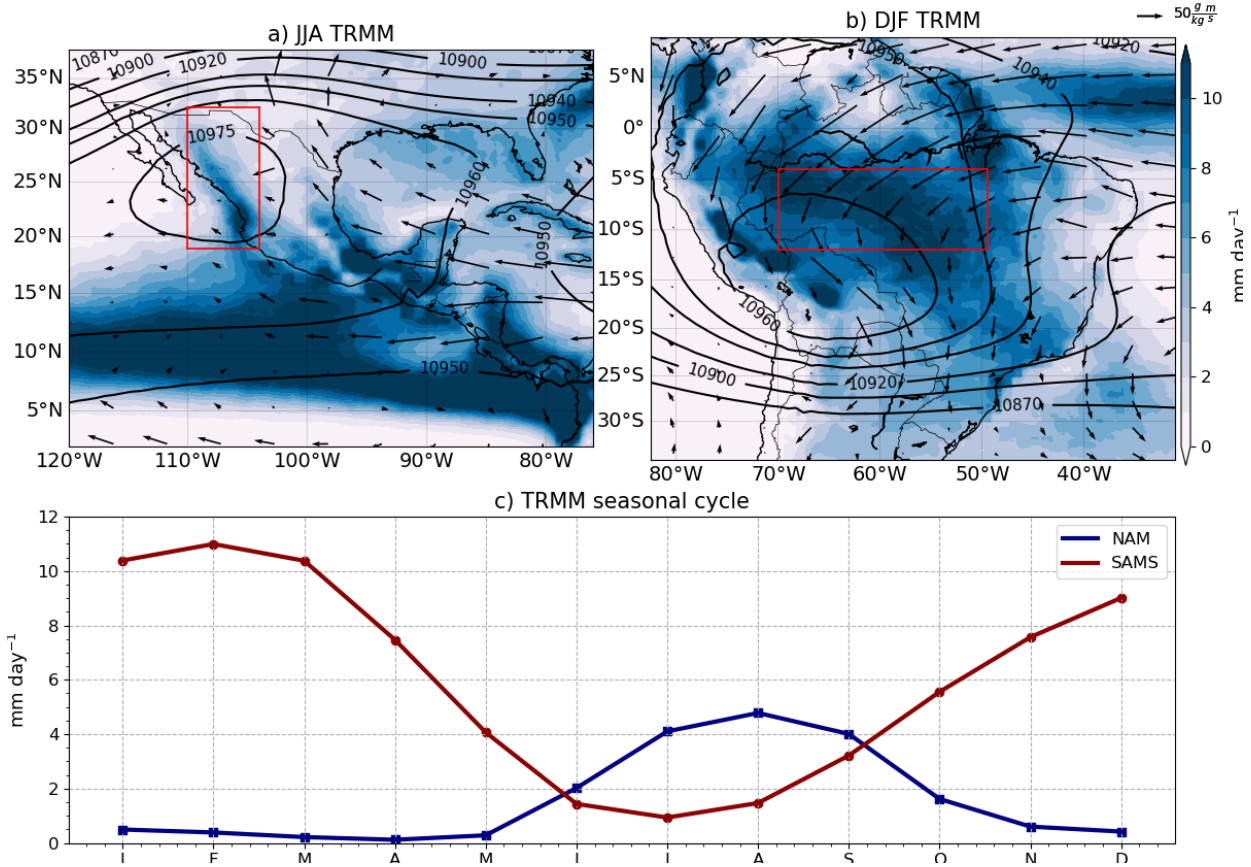


**Figure 2.3:** Climatological mean a) boreal and b) austral summer rainfall (shading), 850 hPa moisture flux (vectors) and geopotential height at 250 hPa (contours) in a) southern North America and b) South America. c) Monthly-mean seasonal march of precipitation in the TRMM dataset for two area-averaged time-series, the North American Monsoon (NAM) and the South American Monsoon System (SAMS) shown in the red rectangles in a-b).

## 2.2 The American Monsoon System

The American Monsoon System (AMS) is the main source of rainfall for tropical Latin America and is typically subdivided into the North and South American monsoon systems (Vera et al., 2006). Although the spatial definition of the AMS is quite varied amongst studies, a general consensus is that the North American Monsoon is found in south-western North America (Figure 2.3a) extending north from central-west Mexico into the southwestern United States and the South American Monsoon is centred in the deep Amazon south to the river mouth (Figure 2.3b) (Adams and Comrie, 1997; Stensrud et al., 1997; Vera et al., 2006).

The seasonal cycle of rainfall in the North American Monsoon is characterised by a wet July-August-September season and significantly drier conditions during the rest of the year

(Adams and Comrie, 1997) (Figure 2.3c). Three temporal stages describe the evolution of the North American Monsoon (Adams and Comrie, 1997; Geil et al., 2013). First, the onset stage (May-June) starts with a strong surface warming that leads to very high temperatures in the desert region. Simultaneously, the sub-tropical jet weakens and migrates north decreasing the frequency of mid-latitude disturbances in the monsoon region (Douglas et al., 1993; Turrent and Cavazos, 2009). These factors combine to develop a low-level thermal surface low pressure linked with an upper-level anticyclone and moisture influx from the nearby Gulf of California and easternmost Pacific Ocean (Douglas et al., 1993; Geil et al., 2013).

Maturity (July-August) is the peak period of monsoon rainfall characterised by sustained deep convection (Barlow et al., 1998) and significant increases in low and mid-level moisture flux convergence and mid-level latent heating (Adams and Comrie, 1997; Cook and Seager, 2013). This latent heating caused by deep convection can be diagnosed in the upper-level geopotential height (Figure 2.3a) in the form of an anticyclone centred on the monsoon region. The moisture flux convergence decreases in August, after which precipitation recycling (Dominguez et al., 2008) plays an important role in keeping deep convection active until September.

Decay (September-October) is the last stage of the monsoon, in many ways opposite to the onset stage, as is characterised by the equatorward migration of the sub-tropical jet (Higgins et al., 1997; Geil et al., 2013), evaporation in the nearby basins decreases and deep convection in the monsoon region gradually disappears (Douglas et al., 1993).

The origin of the high levels of moisture at low and midlevels in the monsoon region has been a matter of debate for a long time (Adams and Comrie, 1997; Barlow et al., 1998; Vera et al., 2006; Ordoñez et al., 2019). A large number of studies acknowledge that the main source of moisture for the North American Monsoon is the East Pacific Ocean and to a second order, mid-level moisture advected from the Gulf of California can mix in the column (e.g. Adams and Comrie, 1997; Stensrud et al., 1997; Vera et al., 2006; Turrent and Cavazos, 2009; Ordoñez et al., 2019).

The South American Monsoon System (SAMS) is a primary source of precipitation for South America, especially in the Amazon region (Gan et al., 2004; Vera et al., 2006; Jones and Carvalho, 2013). During austral summer (DJF), monsoon rainfall accounts for over 60%

of the total annual precipitation in the Amazon (Gan et al., 2004; Marengo et al., 2012), whereas austral winter rainfall accounts for less than 5% of the total annual rainfall (Vera et al., 2006). In the central Amazon, convective precipitation is observed from early October but the main rainy season extends from December to April (Machado et al., 2004; Adams et al., 2013), whereas convection in southeastern Brazil and Paraguay starts in November and peaks in January and February (Marengo et al., 2001; Nieto-Ferreira and Rickenbach, 2011).

A surface heat low appears in Bolivia in early austral summer, known as El Chaco Low, as a result of strong warming in austral spring (Marengo et al., 2012; Sulca et al., 2018). As this surface heat-low strengthens, low-level convergence drives the circulation into the low region. Simultaneously, an upper-level anti-cyclone (Fig. 2.3b), known as the Bolivian High, develops in the same region as a signature of strong deep convection and latent heating (Marengo et al., 2001; Vera et al., 2006).

This low-level wind circulation importing moisture from the Atlantic is one of the most important features of the SAMS (Marengo et al., 2012; Wang et al., 2017) as the flow modulates the moisture flux to the mainland and influences the occurrence of active and break phases of the SAMS (Jones and Carvalho, 2002), as well as changes in the temporal and spatial distribution of rainfall (e.g. Giannini et al., 2004; Bombardi and Carvalho, 2011).

As described in the previous sections, both the North and South American monsoon thermodynamics do not follow the CQE propositions, i.e., the maximum low-level moist static energy is not collocated with the maximum free tropospheric temperature. One possible reason for this is that the free-troposphere over southwestern North America is significantly drier than in other monsoon regions, decoupling the free troposphere from the boundary layer. One alternative hypothesis is that ventilation of low moist entropy air from the midlatitudes is responsible for this decoupling of the boundary layer and the free troposphere in the American monsoons (Boos, 2015).

## 2.3 A review of the physical mechanisms for the Mid-summer drought

The characteristics of the seasonal cycle of precipitation in northwestern Central America, the Caribbean and southern Mexico fit the definition of a monsoon climate (Wang et al., 2017) with a clear separation of the wet and dry seasons. However, this region shows a unique climatological precipitation feature. After monsoon onset, rainfall decreases considerably around the midsummer; this decrease is followed by a secondary increase in precipitation in the late summer (Mosiño and García, 1966), and for this reason this feature of the seasonal cycle is most commonly referred to in the literature as the Midsummer drought (MSD) (Magaña et al., 1999).

The intraseasonal variations of precipitation associated with the MSD have been known for centuries and have shaped agricultural practices in the region. For example, ancient mayan texts suggest that agricultural rituals associated with the plea for rain-bearing clouds to the gods were significantly more frequent during the drier MSD period (Jobbová et al., 2018). In current days, the MSD is well known by local farmers who refer to the drier midsummer period as ‘El Veranillo’ in Central America and ‘canícula’ in southern Mexico because the drier period coincides with the Canis Major constellation appearing in the sky (Dilley, 1996).

The two peak structure of the MSD has been diagnosed in the observed climatological precipitation of several regions of Mexico, El Salvador, Belize, Guatemala, Costa Rica and Cuba (e.g. Mosiño and García, 1966; Magaña et al., 1999; Durán-Quesada et al., 2017; Perdigón-Morales et al., 2018; Martinez et al., 2019). However, notable differences in the seasonal cycle of precipitation have been found between the mainland Central America and the Caribbean islands. The so-called first peak of precipitation occurs in June and the second peak in September in northern Central America whereas the two peaks are observed in May and October in the Caribbean.

In spite of extensive research to understand the physical mechanisms associated with the MSD (e.g. Magaña et al., 1999; Giannini et al., 2000; Gamble et al., 2008; Herrera et al., 2015; Maldonado et al., 2017; Straffon et al., 2019), debate remains over which is the leading-order mechanism that causes rainfall to decrease at midsummer and increase again at the end of

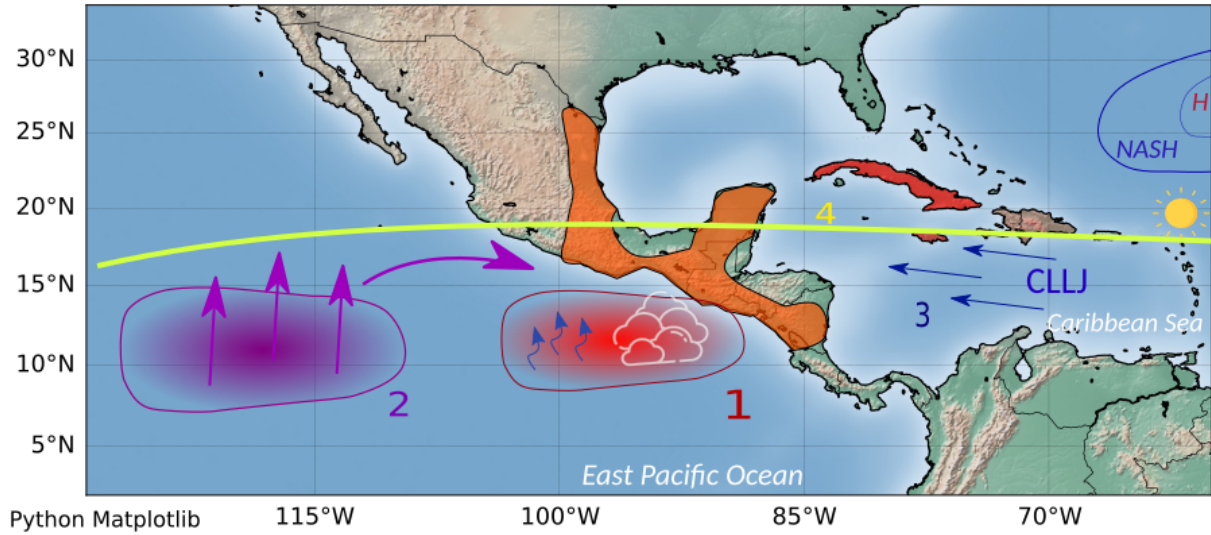


**Figure 2.4:** A schematic of the Intra-Americas Seas region, depicting the four main mechanisms associated with the Midsummer drought in Mesoamerica (orange) and the Caribbean region (red). (1) The radiative-convective feedback mechanism associated with a double peak in East Pacific SSTs proposed by Magaña et al. (1999). (2) The ascending region west of the continent produces an anomalous descending motion over the continent through a direct circulation, argues Herrera et al. (2015). (3) The Caribbean Low-Level Jet (CLLJ) modulates the moisture transport for all the region, with several studies supporting the hypothesis that seasonal cycle in the CLLJ is the main mechanism for seasonal fluctuations in rainfall (Durán-Quesada et al., 2017; Martinez et al., 2019). (4) The double-crossing of the solar declination angle, proposed by Karnauskas et al. (2013), suggests that each peak of precipitation is associated with peaks in the total shortwave radiation reaching the surface.

the summer. Fundamental questions remain unclear such as whether the MSD is caused by two precipitation enhancing mechanisms (Karnauskas et al., 2013) or a mechanism that inhibits rainfall at midsummer (Durán-Quesada et al., 2017). Furthermore, the association between the MSD in Central America and in the Caribbean is still disputed (Gamble et al., 2008), as most studies suggest that the two regimes are unrelated and therefore two different explanations are required to account for the two MSDs in these regions. Figure 2.4 summarises the four main mechanisms that will be addressed in this section and in this thesis.

One of the first hypotheses to account for the bi-modal distribution of rainfall was proposed by Hastenrath (1967) who argue that a double crossing of the ITCZ can explain the MSD so that the first peak of precipitation is associated with early summer northward crossing of the ITCZ and the second peak the return or southward displacement of the ITCZ during late summer. However, this theory fails to explain the MSD signal seen at latitudes

as high as 29°N (Perdigón-Morales et al., 2018; Zhao et al., 2020), a feature that will be shown in this thesis, which is further north than the northernmost extension of the ITCZ (Schneider et al., 2014), and certainly the ITCZ does not cross twice so far from the equator.

Magaña et al. (1999) and Magaña and Caetano (2005) proposed a mechanism driven by radiative-convective feedbacks between the East Pacific (EP) sea-surface temperatures (SSTs) and deep tropical convective clouds (mechanism 1 in Figure 2.4). The coupling between the height and strength of convection, the incoming shortwave radiation and the SSTs are the key features of their framework. The EP SSTs peak in May triggering large evaporative fluxes and deep convection in the EP ITCZ and the western coast of Central America. The high convective clouds produce a radiative cooling effect at the surface due to a decreased incoming shortwave radiation associated with the reflectance of shortwave radiation by clouds. This cooling decreases SSTs and deep convective activity and thus accounts for the decrease of rainfall during the midsummer. The second peak in September is driven by an opposite mechanism, i.e., the decreased frequency of deep convective clouds during the MSD period in July and August reduce the cooling effect of the anvil clouds and increase the incoming shortwave radiation at the surface, SSTs and surface fluxes, all of which leads to an increase in precipitation during late August and September (Magaña et al., 1999).

A large number of studies, in contrast, propose that the seasonal evolution of the North Atlantic Subtropical High (NASH) is the leading mechanism for the MSD (e.g. Mapes et al., 2005; Small et al., 2007; Gamble et al., 2008; Curtis and Gamble, 2008; Muñoz et al., 2008; Martinez et al., 2019; Corrales-Suastegui et al., 2020). The NASH is the subtropical anticyclone in the North Atlantic Ocean that migrates southwest during early boreal summer. The expansion and intensification of the NASH in boreal summer, according to these studies, strengthens the low-level trade winds, controlling the seasonal cycle of a low-level jet found in the core of the Caribbean Sea known as the Caribbean Low-Level Jet (CLLJ).

The CLLJ is a key regional feature of the climate of the Caribbean and the Intra-Americas Sea because the strength and direction of the flow in the Caribbean controls the underlying Caribbean SSTs and the regional moisture transport (Giannini et al., 2000; Mestas-Nuñez et al., 2007; Martinez et al., 2019; García-Martínez and Bollasina, 2020). However, studies disagree on the specific roles that the CLLJ and the NASH play for the

precipitation over the Mesoamerican region. For example, some studies (e.g. Giannini et al., 2000; Mestas-Nuñez et al., 2007; Gamble et al., 2008) suggest that the expansion of the western flank of the NASH strengthens the CLLJ which cools the SSTs, through the effect of wind stress and mixed-layer mixing. The cooling of SSTs diminishes evaporation and therefore low-level moisture which ultimately leads to less precipitation. In contrast, other studies propose that the seasonal cycle of the CLLJ (mechanism 3 in Figure 2.4) modulates seasonal variations of precipitation by modulating the regional moisture transport (Small et al., 2007; Muñoz et al., 2008; Herrera et al., 2015; Durán-Quesada et al., 2017; Martinez et al., 2019). In this second hypothesis, the changes to the intensity of CLLJ influenced by the NASH modify the convergence and divergence patterns in the Intra-Americas Sea. In other words, the midsummer strengthening of the CLLJ increases moisture divergence, drying the atmospheric column over the Caribbean.

Herrera et al. (2015) shows that during the drier months in Central America in the Midsummer, convective activity west of the central American continent gets stronger with heavier precipitation (mechanism 2 in Figure 2.4). Their evidence suggests that the gap flow that originated from the CLLJ in the Caribbean Sea controls the location of ascending and descending motions, and the MSD may be explained by the seasonal variations of the coupling of the low-level wind flow with the underlying EP SSTs. Herrera et al. (2015) further argued that the exit region of the CLLJ is located to the east of the region of strongest MSD signal, which suggests that the moisture divergence effect over the central American MSD is minimal.

A different mechanism, proposed by Karnauskas et al. (2013), argues that the biannual crossing of the solar declination angle can control precipitation and explains the bimodal characteristics of the seasonal cycle (mechanism 4 in Figure 2.4). In this mechanism, the MSD is driven by two precipitation enhancing periods that are separated by a relatively normal, and drier, period. This theory differs from those previously discussed which explained the MSD through mechanisms that inhibit convective activity in the midsummer whereas Karnauskas et al. (2013) argues that the solar declination angle that crosses twice through Central America, once during June and a second time during September, increases convective activity during each crossing.

The variations of incoming shortwave radiation associated with the declination angle modulate the SSTs, surface fluxes and therefore convective activity. In other words, the first crossing of the solar declination angle increases the incoming shortwave radiation which increases the SSTs, evaporation and leads to a peak of precipitation, i.e., the first peak. After the shortwave radiation is reduced the MSD period appears. The second crossing of the solar declination angle, similarly, explains the second peak as the second increase in incoming shortwave promotes more deep convection than during the MSD.

Other mechanisms have been proposed arguing that the MSD is a result of vertical wind shear affecting convective instability or the Saharan dust controlling the microphysics of clouds (Angeles et al., 2010). For instance, Perdigón-Morales et al. (2019) also finds a link between the frequency and spatial distribution of the first peak rainfall rates and the Madden-Julian Oscillation.

## 2.4 El Niño Southern Oscillation: impacts to the American monsoon system

El Niño-Southern Oscillation (ENSO) is a phenomena that primarily affects the local ocean and atmosphere of the equatorial Pacific Ocean, but these changes are profoundly important for the global climate system, which is why ENSO is commonly known as the leading mode of interannual variability. The term '*El Niño*' was initially coined by Spanish colonizers when they learnt from Peruvian fishermen that the ocean surface temperatures in the easternmonst Pacific Ocean increased notably in some years around December time. For religious reasons, the colonizers termed the SST increase as Christ Child – *El Niño*.

Later on, sir Gilbert Walker (1924) coined the term *Southern Oscillation* to describe the synchronous changes to the sea-level pressure of the Indo-Pacific region and South America. Walker (1924) and Walker (1932) are the first analyses of synchronous effects of the tropical circulation over local precipitation, temperature and pressure. Further research (e.g. Troup, 1965) would highlight that these remote changes in pressure were driven by the east-west pressure gradient in the equatorial Pacific.

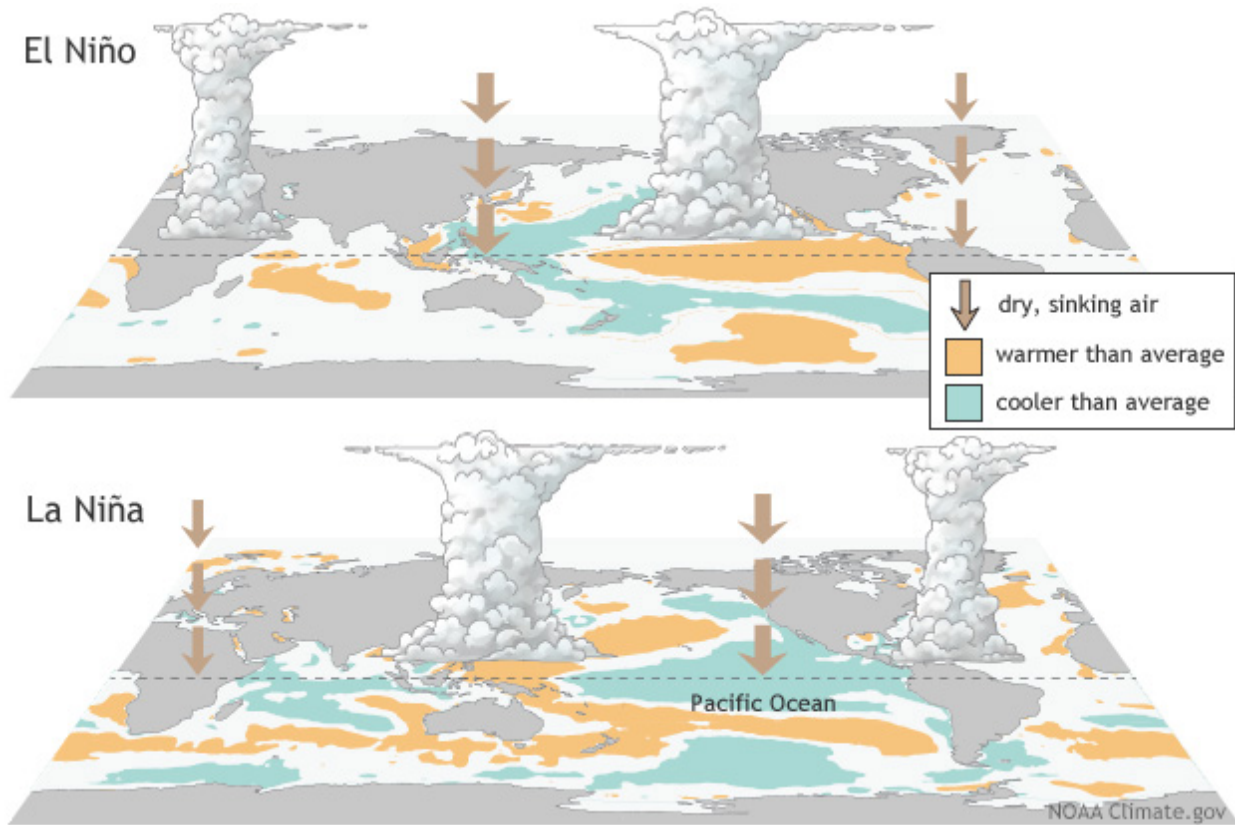


**Figure 2.5:** Schematic of the positive (upper) and negative (lower) phases of ENSO. Regions with tall clouds indicate more ascent and convection than normal whereas brown arrows indicate dry descending air. Obtained from the National Oceanic and Atmospheric Administration at <https://www.climate.gov/enso>.

The changes in the pressure field associated with the Southern Oscillation (SO) are now part of what is known as the Walker circulation, which intertwines the dynamics of the zonal circulation in the East Pacific with the SSTs over the underlying ocean. ENSO is then characterized as a coupled phenomena composed of an oceanic part, *El Niño*, and an atmospheric component associated with the zonal circulation but best characterized by changes to the surface pressure field, the Southern Oscillation.

ENSO has several unique features, such as no robust periodicity as events may occur every 2 to 7 years and a seasonal phase-locking that are associated with ENSO events peaking in boreal winter in observations (Wang and Picaut, 2004). Even though the underlying physics that cause ENSO and explain the variability in the periodicity of the phenomena is still debated (Wang and Picaut, 2004; Christensen et al., 2017), several aspects are now better understood. For example, the local effect that ENSO events have over on the

location and strength of deep convection in the equatorial Pacific have long been thoroughly described (Trenberth, 1997; Neelin et al., 1998).

During a neutral state of ENSO, the Walker circulation is found in the climatological state, with ascent and wet conditions in the West Pacific and descent and drier conditions in the East Pacific. During El Niño the Walker circulation and low-level trade winds weaken which is associated with an eastward shift of deep convection along the equatorial Pacific (Figure 2.5), with convective rainfall becoming more frequent in the central and even eastern Pacific than normal (Neelin et al., 1998; Wang and Picaut, 2004). During La Niña the opposite happens and the Walker circulation strengthens which leads to stronger convection in the West Pacific and stronger ascent on the East Pacific (Figure 2.5).

In other words, ENSO imposes a strong control on the location and strength of the Walker circulation (Figure 2.5). These changes to the strength and position of the convective regions in the Pacific Ocean can then propagate to other regions of the planet; these far-distant effects are commonly known as *teleconnections*. For example, ENSO has a direct effect over other tropical regions outside of the Pacific through the Walker circulation, see Figure 2.5, as upper-level wind anomalies induce anomalous vertical motions over the monsoons in West Africa (Ropelewski and Halpert, 1986, 1987) or South America (Sulca et al., 2018). Other mechanisms of ENSO teleconnections to higher latitudes include changes to the position and strength of sub-tropical jets (Fereday et al., 2020), changes to the Pacific and North American circulation patterns (Bayr et al., 2019) as well as impacts to the North Atlantic via the stratospheric polar vortex (Domeisen et al., 2019).

In South America, the effects of ENSO are felt throughout the continent and throughout economic sectors from Peruvian fishermen (Takahashi, 2004) to the Amazon rain-forest and the plainlands in South-eastern South America (Grimm, 2011; Marengo et al., 2012). One key aspect of current research on ENSO impacts to South America is the observed non-linearity and non-symmetry in the teleconnections, which has mainly been attributed to ENSO diversity (Tedeschi et al., 2015; Cai et al., 2020). A non-linear teleconnection refers to a non-linear scaling between the strength of an ENSO event, typically measured by an SST index, and the magnitude of the response, in most cases precipitation response.

Observations have shown that the maximum SST anomaly does not always appear in the same region of the Pacific Ocean (Ashok and Yamagata, 2009; Domménget et al., 2013). These differences in the SST patterns are referred to as ENSO *diversity* or *flavours* which can be broadly summarized as two flavours for each phase. The flavours or types of event are defined based on the location of the SST anomaly so the most common division is into Central and Eastern Pacific events. In observations, each type of event is usually also associated with the strength of the event (Domménget et al., 2013), with eastern Pacific events being usually stronger than Central Pacific events.

The strength and patterns of ENSO teleconnections to the SAMS have been shown to depend on the type of event (Rodrigues et al., 2011; Sulca et al., 2018). Cai et al. (2020) provides a recent review on the differences in the impacts that Central and Eastern Pacific (CP and EP) events have on South American precipitation and climate features. The observed record shows that the teleconnections affecting the Amazon and northeastern Brazil are most pronounced during EP El Niño events and CP La Niña events than the CP El Niño events and EP La Niña events. This recent review also highlights the need for further modelling work to test observation-driven hypothesis, as the observed record is too short to make confident statements about the mechanisms associated with ENSO teleconnections.

## 2.5 Stratosphere-Troposphere Coupling in the Tropics

The troposphere is the lowermost layer of the atmosphere ranging from the surface up to 10-15 km where the vertical temperature profile is characterized by a decrease of temperature with height so that convective instability plays an important role for vertical motions. The layer above the troposphere is called the *stratosphere* where the vertical temperature gradient is reversed and temperatures increase with height so that the atmosphere is stable to upward motions, this layer and spans from 10-20 km up to 50 km in altitude (Andrews et al., 1987). The transition layer in between the troposphere and the stratosphere is referred to as the tropopause, which is a transition region where the vertical temperature gradient reverses and the atmosphere is stable to upward motions.

Stratosphere-troposphere coupling refers to events or processes where the two layers are notably affected by each other so that the temperature or wind flow of the two layers vary together, or *couple*. One prominent example of this coupling is the effect of the stratospheric polar vortices over the zonal flow in the troposphere (Thompson et al., 2005; Domeisen et al., 2019). However, semi-periodic climatic variability in either layer can also have effects over the other layer. The dominant mode of interannual variability in the equatorial stratosphere is such an example and is introduced in the following section.

### 2.5.1 The Quasi-biennial oscillation (QBO)

The stratospheric quasi-biennial oscillation (QBO) was discovered 60 years ago through balloon observations that revealed that the zonal winds reverse direction in a semi-periodic way with accompanying temperature variations (Ebdon, 1960; Reed, 1964). The QBO has then been characterized by further observations as alternating easterly and westerly wind regimes associated with a descending zonal wind shear from up to 50 km down to 10 km, with a mean oscillatory period of 28 months (Baldwin et al., 2001). The downward propagation of the easterly and westerly wind regimes, amplitude and the mean period have been explained by the interaction of a broad spectrum of gravity and Kelvin waves of tropospheric origin with the equatorial stratospheric zonal mean flow (Baldwin et al., 2001).

The wind variation in the middle stratosphere associated with the QBO are greater than the seasonal cycle (Andrews et al., 1987) and this vertical wind shear imposes a temperature signal through the thermal wind relationship, which can be expressed as:

$$\frac{\partial u}{\partial z} = \frac{-R}{H\beta} \frac{\partial^2 T}{\partial y^2}, \quad (2.1)$$

where  $\partial u / \partial z$  is the vertical shear of the zonal wind,  $R$  is the ideal gas constant,  $y$  is the latitude,  $H$  is a scale height of the atmosphere (7-8 km) and  $\beta$  is the first derivative of the Coriolis term in the meridional coordinate  $y$ .

In order to maintain thermal wind a westerly (easterly) vertical shear requires a latitudinal temperature gradient with a warm (cold) temperature anomaly over the equator. These temperature anomalies are achieved through an induced mean meridional circulation, often

referred to as the secondary circulation of the QBO (Plumb and Bell, 1982; Li et al., 1995; Baldwin et al., 2001; Ribera et al., 2004). This anomalous circulation is characterized by reduced upwelling during westerly shear phases and increased upwelling during the easterly phase. These meridional circulation perturbations adiabatically warm (anomalous descent at the equator) and cool (anomalous ascent) for westerly and easterly shears, respectively, at the equator.

These induced meridional circulations also give rise to an ozone anomaly, with positive (negative) ozone anomalies associated with a descending wester (easterly) QBO phase, which further enhances the temperature anomalies. The temperature anomaly driven by the meridional circulations impact the height and temperature of the tropopause in the tropics (Baldwin et al., 2001; Tegtmeier et al., 2020a,b). The easterly phase of the QBO (QBOE) is associated with a higher and colder tropopause in the tropics whereas the westerly phase (QBOW) is observed with lower and warmer tropical tropopause (Tegtmeier et al., 2020a). These variations in the tropopause characteristics, amongst other effects associated with the QBO, have been hypothesized to affect, to different extents, a range of tropical phenomena, and in particular, deep convective systems.

The combination of dynamic and thermodynamic effects of the QBO in the equatorial stratosphere are associated with long-distance impacts across the stratosphere (Holton and Tan, 1980; Lu et al., 2020) and down to the surface (Garfinkel and Hartmann, 2010; Gray et al., 2018). The most well-known teleconnection of the QBO is with the polar stratosphere, in particular, how the direction of the zonal mean flow in the equatorial stratosphere modulates the propagation of extratropical waves and therefore also influences the wintertime stratospheric polar vortex (Lu et al., 2020), which can have profound impacts over the surface in polar and midlatitude regions.

### 2.5.2 Tropical teleconnections of the QBO

The influence of the QBO on the dynamic and thermodynamic characteristics of the tropical upper-troposphere-lower stratosphere (UTLS) region has raised interest in possible indirect effects of the QBO over tropical deep convection and clouds. Gray (1984) was amongst the first to suggest an influence of the QBO over tropical systems, in particular, that Atlantic

tropical cyclone activity was enhanced during QBOW compared to QBOE. Gray et al. (1992) further argued that the anomalous vertical wind shear in the UTLS associated with the QBO affects the strength of convection in monsoonal and convergence zones to the extent that the vertical wind shear can modify ENSO frequency. Their results suggest that El Niño events are favoured during QBOE and La Niña events are more frequent during QBOW.

The evidence by Gray et al. (1992) has motivated further observational and modelling research on QBO tropical teleconnections; some of this research has contested Gray's results (e.g. Chan, 1995; Camargo and Sobel, 2010; Hansen et al., 2016). For example, Giorgetta et al. (1999) was amongst the first to use a global climate model (ECHAM4) to investigate the effects of the QBO over tropical convection. Giorgetta et al. (1999) focused on the role that the QBO plays in modulating the strength of the East Asian and Indian monsoons. Their findings suggest that monsoon variability was partially modulated by the QBO, with strong effects over the properties of clouds at 100 hPa. Giorgetta et al. (1999) argues that these differences could be explained by the effect of the QBO on the UTLS static stability and a consequent effect over the vertical extent of deep tropical convection.

Further modelling work has been carried out, for instance by Garfinkel and Hartmann (2010) and Garfinkel and Hartmann (2011) that used the Whole Atmosphere Community Climate Model (WACCM) to understand the effect of the QBO over tropical precipitation, the subtropical jets and the wintertime polar vortex. Garfinkel and Hartmann (2010) shows that the canonical ENSO teleconnections to the North Pacific are stronger during QBOW in WACCM and reanalysis suggesting that the QBO modulates the wave propagation activity associated with ENSO events. Garfinkel and Hartmann (2011) uses perpetual winter conditions in the WACCM model to show that the QBO modifies the upper-tropospheric zonal wind at the equator and the strength and location of subtropical jets, particularly at their exit region, as the subtropical jet is weakened during QBOE conditions.

The response of convection to the UTLS temperature anomalies associated with the QBO was investigated in cloud-resolving model simulations by Nie and Sobel (2015). Their experimental design used the System for Atmospheric Modelling (SAM), varying SST boundary conditions with increments over a baseline SST level of 301 K, the use of the

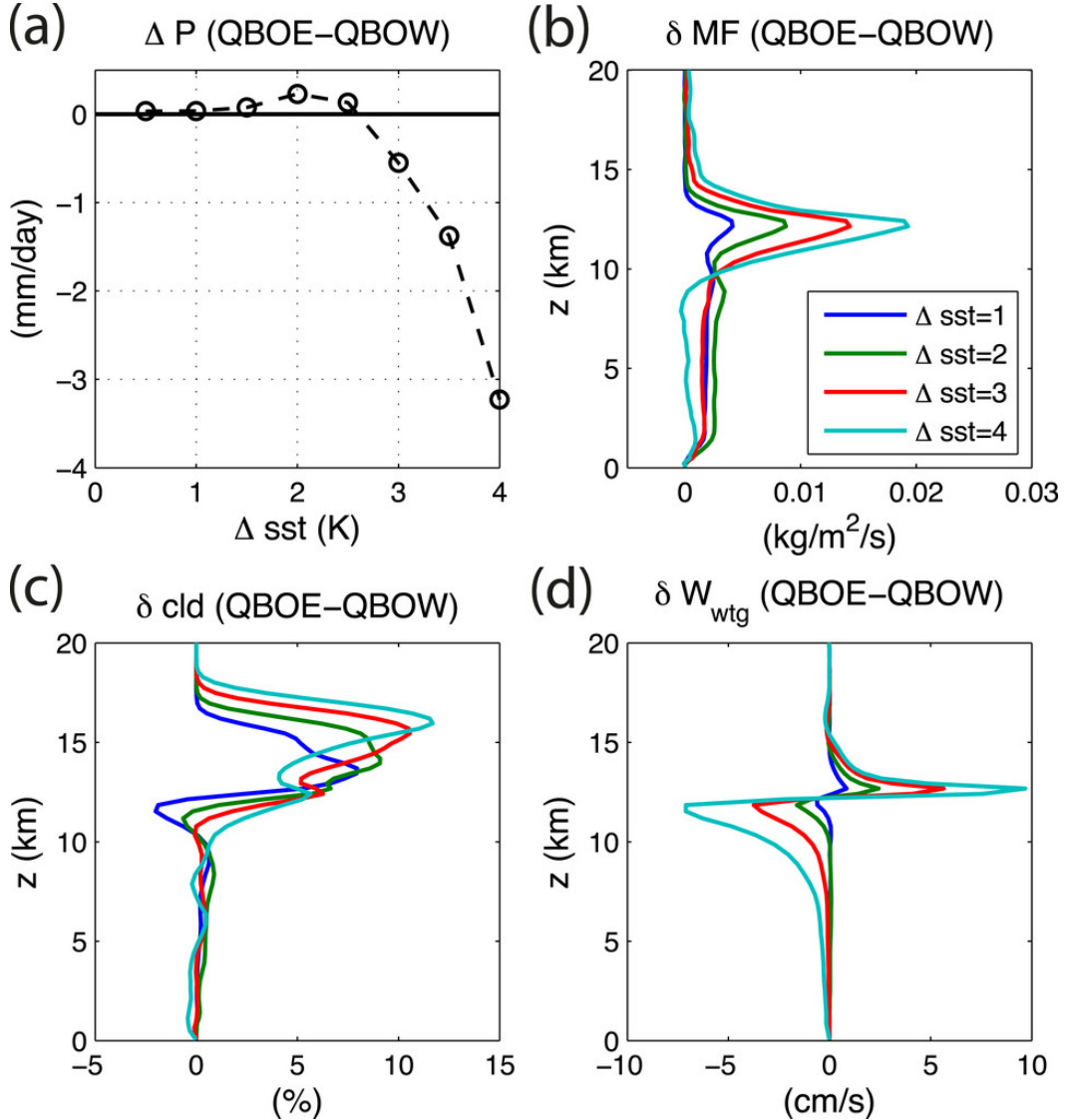


**Figure 2.6:** (a) QBO anomalous precipitation as a function of SST forcing. The  $\delta \text{sst}$  are increments over a baseline of 301 K throughout the whole model domain. (b)–(d) The differences of mass flux in cloud cores, cloud fraction, and the parametrized large-scale vertical velocity derived from the weak temperature gradient approximation, respectively, between experiments with the QBOE and QBOW temperature profiles. Figure 3 from Nie and Sobel (2015).

weak-temperature gradient (WTG)<sup>1</sup> approximation and an idealized vertical temperature profile to simulate the effect of the QBO temperature signal. Figure 2.6 shows that the precipitation differences between QBO phases depend on the SST forcing. The precipitation difference between QBO temperature anomalies is positive under relatively small SST

<sup>1</sup>The weak temperature gradient approximation makes use of the relatively small horizontal gradients of temperature and density in the tropics, which simplifies some of the primitive equations and has allowed several numerical analyses of tropical dynamics using simplified models (Sobel et al., 2001).

anomalies but in experiments with large SST anomalies this difference becomes negative and overall larger than under small SSTs. The difference in mass flux and cloud fraction is also sensitive to the underlying SSTs, as increased mass flux during QBOE is increased for larger SSTs. In other words, the QBO influence on precipitation is non monotonic and largely depends on the underlying SST field.

The results of Nie and Sobel (2015) suggest that the QBO influences convection in two ways that are non-linear and the authors argue are the result of competing mechanisms. Their argument is that since the mass flux in the upper troposphere is increased during QBOE but there is also an increase in gross moist static stability (GMS) the result is an increase in the efficiency of large-scale vertical motions during QBOE for large SSTs, which acts to reduce precipitation. Secondly, the QBO modifies the fraction of high-level clouds resulting from deep convection which modifies the radiative heating to the column which increases precipitation during QBOE. Figure 2.6a then shows how these competing effects change for different SSTs with the gross moist stability mechanism dominating for large SSTs.

Various attempts have been made to determine a relationship between the QBO and deep convection in observations. One influential study by Collimore et al. (2003) analysed satellite-derived out-going long-wave radiation (OLR) in the tropics composited by QBO phase. These composites suggest that OLR is significantly different between QBO phases in most monsoon regions, such as Central America and the West Pacific, with an overall indication that convective activity is reduced during QBOW compared to QBOE. This influence, however, was not found to be zonally symmetric and in fact the longitudinal variations of the QBO-related OLR differences were suggestive enough that Collimore et al. (2003) argue for a possible role for the QBO to modulate the Walker circulation, which would explain the lack of zonal symmetry in their results.

Another relevant study by Liess and Geller (2012) found that satellite-derived cloud thickness and frequency and upper-level velocity potential had a significant and longitudinally asymmetric response to the QBO. In particular, their results show increased convective activity during QBOE in the West Pacific but the opposite for the East Pacific. For this reason, Liess and Geller (2012) also argue that the strength of the tropical overturning

circulation may be modulated by the QBO, indicating the possible role of both the vertical wind shear and the upper-level static stability to modulate deep convection.

The topic of QBO tropical teleconnections has regained attention due to recent findings suggesting a link between the QBO and the Madden-Julian Oscillation (MJO) (Son et al., 2017) which motivated extensive research (see e.g. Lee and Klingaman, 2018; Wang et al., 2019; Martin et al., 2020) due to the worldwide impact of the MJO. The MJO in observations shows a stronger amplitude and more predictability during QBOE, but further inspection in cloud-permitting and forecast models have not provided conclusive answers to this puzzle (Martin et al., 2019, 2020).

Questions still arise as to whether this tropical link is real or due to chance, for instance Wang et al. (2019) argued that the increased predictability of the MJO under the QBOE phase is included in the initial conditions, and thus not a result of a mechanistic effect of the QBO on the MJO. More generally, whether the QBO has a considerable effect on deep convection in general is debated as several plausible mechanisms exist in the literature (see e.g. Nie and Sobel, 2015) such as the effect of wind shear, the tropopause height, the cold-point temperature, static stability and/or feedbacks with very high cirrus and cumulonimbus clouds.

# 3

## Data and methods

### 3.1 Observations and reanalysis data

Continuous and reliable observations of Earth's atmosphere and ocean have only been possible in recent decades, due to the advent of satellites. In particular, precipitation analyses have benefited greatly from satellite-derived estimates of precipitation in regions where station-data is non-existent such as over oceans. This thesis uses several data sources for precipitation from various gridded precipitation datasets. Several dynamic diagnostics are also used in this thesis, which are taken from the latest reanalysis from the European Centre from European Centre for Medium-Range Weather Forecasts (ECMWF), described below. Table 3.1 summarises relevant information of the observations and reanalysis datasets used in this study.

#### 3.1.1 Gridded precipitation datasets

The Tropical Rainfall Measurement Mission (TRMM) dataset is a multi-satellite multi-sensor infra-red precipitation product. Several versions are available that use with different algorithms and calibrations with surface rain-gauge data (Huffman et al., 2007). This thesis uses the daily product TRMM version 7 3B42 provided by the Goddard Earth Sciences Data and Information Services Center (Mission, 2011) at [https://disc.gsfc.nasa.gov/datasets/TRMM\\_3B42\\_7/](https://disc.gsfc.nasa.gov/datasets/TRMM_3B42_7/).

### 3. Data and methods

33

**Table 3.1:** Summary of the datasets used in this study. For each dataset, the acronym used hereafter, the period of coverage, the field used and the horizontal resolution are shown. Some datasets extend further back in time, but only the satellite-era period is used in most of the datasets. The variables used are: precipitation, surface-air temperature ( $2mT$ ), sea-level pressure (SLP), SSTs, the x and y components of the wind ( $u, v$ ), the lagrangian tendency of air pressure ( $\omega$ ), outgoing longwave radiation (OLR), geopotential height (GPH) and specific humidity ( $q$ ).

Dataset/ Version	Acronym	Variable	Period	Data type	Resolution	Reference
Global Precipitation Climatology Project v2.3	GPCP	Precipitation	(1979-2018)	Surface and satellite	2.5°x2.5°	(Adler et al., 2003)
Global Precipitation Climatology Centre Climate Prediction Center Merged Analysis of Precipitation	GPCC CMAP	Precipitation	(1940-2013) (1979-2016)	Surface station Satellite calibrated with surface rain-gauge	0.5°x0.5°	(Becker et al., 2011) (Xie and Arkin, 1997)
Climatic Research Unit TS v4. Climate Hazards Infrared Precipitation with Stations Tropical Rainfall Measurement Mission 3B42 V7 Hadley Centre SST3	CRU4 CHIRPS	Surface temperature Precipitation	(1979-2017) (1981-2018)	Surface station Surface rain-gauge and satellite	0.5°x0.5°	(Harris et al., 2014) (Funk et al., 2015)
European Centre for Medium-Range Forecasting ERA-5	TRMM HadSST ERA-5	Precipitation SST $2mT$ , SLP, $u$ , $v$ , $\omega$ , OLR, $q$ , SST, GPH, precipitation	(1999-2018) (1940-2018) (1979-2018)	Satellite calibrated with surface station Buoy and satellite Reanalysis	0.25°x0.25° 2.5°x2.5° 0.75x0.75°	(Huffman et al., 2010) (Kennedy et al., 2011) (C3S, 2017; Hersbach et al., 2020)

A set of microwave and infra-red sensors onboard low earth orbit (LEO) satellites, such as the Microwave Imager (TMI) and the Advanced Microwave Scanning Radiometer-Earth Observing System (AMSR-E), provide the main source of information about hydrometeors for TRMM. The microwave sensor data is used to calibrate the infrared data to produce a first estimate of precipitation. However, even using the products of several satellites there is a sparse sampling of time-space precipitation in passive microwave techniques. Therefore, this data is complimented by infrared measurements onboard geosynchronous earth orbit satellites. Other sources of information include a radar onboard TRMM and rain gauge analysis. Details of the research product can be found in Huffman et al. (2007) and Huffman et al. (2010).

The Climate Prediction Center Merged Analysis of Precipitation (CMAP) dataset is a global merged product of satellite and ground based observations but also constrained by a numerical model (Xie et al., 2007). This dataset was first produced at monthly-mean resolution (Xie and Arkin, 1997) but is now available as a collection of products at several temporal scales. The pentad-scale version of CMAP is used in this study.

The Climate Hazards Infrared Precipitation with Stations (CHIRPS) is a relatively more recent merged product of precipitation (Funk et al., 2015). This dataset uses high-resolution rain-gauge station data that is complimented by satellite cloud cold duration estimates for regions where station data is sparse. The products are calibrated with TRMM data (Funk et al., 2015), so they cannot be considered a fully independent source of information from TRMM.

All these datasets have shortcomings, advantages and uncertainties in their representation of precipitation. The algorithm of merged products such as TRMM to combine different satellite sensors and calibration techniques as well as surface station rain-gauge data results in products that may have shortcomings to accurately depict extreme events (Trejo et al., 2016). As the source data of most of these datasets is shared, the datasets cannot be considered to be fully independent sources of information.

The TRMM dataset has a high horizontal and temporal resolution and was used in several CMIP assessments (Geil et al., 2013; Jones and Carvalho, 2013) as a reliable source of precipitation (Carvalho et al., 2012). Therefore, TRMM is used in this thesis as the best estimate for the spatial and temporal characteristics of rainfall. However, the period

covered by TRMM (1998-2018) is too short to analyse statistically robust teleconnections or variability, so GPCP, GPCC and CHIRPS are used to evaluate longer term variability. Although a thorough validation and comparison of these datasets across the AMS domain is missing, several studies have analysed one or more of these datasets in regions of the AMS (e.g. Franchito et al., 2009; Dinku et al., 2010; Trejo et al., 2016).

### 3.1.2 ERA-5

A reanalysis is a numerical description of the state of the atmosphere on a global or regional scale with a full set of gridded diagnostics available at multiple vertical levels, in other words "maps without gaps" (Hersbach et al., 2020). A reanalysis takes a set of physically consistent blend of observations that are used to constrain a forecasting model by relaxing the model towards these observations (e.g. Fujiwara et al., 2021). Reanalysis are key tools for climate and weather research as they provide full pictures of the atmospheric state for long periods, a feature that could not be possible with our current purely observational tools. For this reason, reanalyses are typically used to validate GCM output.

The latest reanalysis from ECMWF, the fifth generation of their reanalysis, is called ERA5. ERA5 uses the Integrated Forecasting System (IFS) model and a 4D variational data assimilation system (4D-Var), a larger number of data sources for assimilation and also provides output on higher horizontal resolution (Hersbach et al., 2020). The output is available on hourly to monthly-mean frequencies, from 1000 hPa to 0.1 hPa in the vertical and with horizontal resolutions as high as 0.25°. In this thesis, the resolution of all ERA5 data, unless otherwise stated is of 0.75° and all data was downloaded from the Climate Store at <https://climate.copernicus.eu/climate-reanalysis>.

ERA5 presents a notable improvement in the representation of the water cycle, by increasing the mean correlation to precipitation datasets such as GPCP. ERA5, as all reanalysis, resolves precipitation rates in the driving physical model using the convective scheme and parametrisation. However, this reanalysis also assimilates radiances from several satellite instruments such as Global precipitation monitoring mission Microwave Imager, TMI and ASMR-2 Hersbach et al. (2020). This assimilation of satellite data has improved the representation of the water cycle in ERA5 compared to older reanalysis such

as ERA-interim (e.g. Hénin et al., 2018). These improvements are also due to changes to the parametrisations of the microphysics of clouds and rain (Forbes and Ahlgrimm, 2014) and the diurnal cycle of convection (Bechtold et al., 2014).

## 3.2 The Unified Model of the Met Office Hadley Centre

The UK Met Office Hadley Centre (MOHC) released the first version of the Hadley Centre Global Environmental Model (HadGEM1) in 2006 (Johns et al., 2006), and has since continuously updated the HadGEM model and submitted experiments from the model to the various phases of the Coupled Model Intercomparison Project (CMIP), which is the backbone of the Intergovernmental Panel on Climate Change (IPCC) reports. This section first describes the third generation of the HadGEM model and subsequently describes the experiments from these versions of the model submitted for CMIP6.

### 3.2.1 The Global Coupled Configurations of HadGEM3

The MOHC Unified Model (UM) is a weather and climate global model that is based on a seamless modelling approach, which means that the UM consists of a dynamical core and parametrization schemes that can be used across a wide range of temporal and spatial scales. The UM version that was used for CMIP6 experiments and is used throughout this thesis employs the Global Coupled (GC) configuration 3.1 (GC3.1) (Williams et al., 2018; Walters et al., 2019) which in turn is composed of the components: Global Atmosphere 7.0 (GA7.0), Global Land 7.0 (GL7.0), Global Ocean 6.0 (GO6.0), and Global Sea Ice 8.0 (GSI8.0). The GC3.1 configuration runs with 85 atmospheric levels, 4 soil levels and 75 ocean levels and can be run with atmospheric horizontal resolutions ranging from 10 - 135 km (at the midlatitudes) with varying resolutions for the ocean component as well. The model top of GC3.1 is 85 km above sea level (Walters et al., 2019).

The GA7.0 configuration, described in Walters et al. (2019), built on previous configurations principally by updating a number of parametrisation schemes including the rain and ice-cloud treatment as well as the convection scheme. Four critical errors were pinpointed and tackled by GA7.0 which include rainfall deficits in the Indian monsoon, temperature

and humidity biases in the tropopause layer, deficiencies in numerical conservation and surface flux biases over the Southern Ocean. The GO6.0 configuration (Storkey et al., 2018) is in turn based on the NEMO ocean model code (version 3.6) and is responsible for determining the sea-ice extent, the ocean mixed-layer depth and deep water formation, amongst other key ocean processes.

In most GCMs, precipitation is a result of two simulated processes. First, precipitation due to grid-scale processes referred to as large-scale precipitation, is estimated by the microphysics, or cloud scheme, that evaluates the cloud fraction and saturation within the grid-box column where precipitation occurs by processes such as warm rain (Walters et al., 2019). The second process that simulates precipitation is associated with convection of varying depths and is considered a sub-grid process calculated by the convection scheme.

In GC3.1 the convective scheme follows three stages, according to Walters et al. (2019), first a diagnosis of the boundary layer to establish whether convection should occur at a given time-step and separately diagnoses shallow or deep convection, second, the shallow or deep convection schemes are called and third, a call for mid-level convection. In other words, the convective scheme first decides whether the thermodynamic profile at each grid-point fits certain parameters that measure the buoyancy of the parcels and vertical velocity profile, which then separates areas of deep and shallow convection. After these routines, the model implements the mid-level convection scheme to remove instabilities from above the shallow convective regions or below the deep convective regions.

The closure of the deep convective scheme follows the convective available potential energy (CAPE) closure of Fritsch and Chappell (1980) which regulates the amount, strength and duration of convection based on availability of buoyant energy. In addition, the scheme couples the detrainment rates of plumes to the column relative humidity and buoyancy as described in Derbyshire et al. (2011). Further details of the GC3 configuration including model description and biases can be found in Williams et al. (2018) and Kuhlbrodt et al. (2018).

### 3.2.2 The CMIP6 experiments

The MOHC submitted output from several experiments to various projects part of CMIP6 using different variations of the GC3.1 configuration, i.e., varying horizontal resolution and

**Table 3.2:** Summary of the CMIP6 simulations in this study. The experiment, CMIP activity name, acronym model years, and number of ensemble members used in this study are presented for each simulation.

Model / Resolution	Experiment	Period	Activity	Acronym	Ens.	Reference
HadGEM3 N96	re-industrial control	1850-2350	CMIP/DECK	GC3 N96-pi	1	(Menary et al., 2018; Ridley et al., 2018)
HadGEM3 N216	pre-industrial control	1850-2000	CMIP/Deck	GC3 N216-pi	1	(Menary et al., 2018; Ridley et al., 2019c)
HadGEM3 N96	historical	1979-2014	CMIP/DECK	GC3-hist	4	(Andrews et al., 2020; Ridley et al., 2019b)
HadGEM3 N216	historical	1979-2014	CMIP/DECK	N216-hist	1	(Ridley et al., 2019c)
HadGEM3 N96	amip	1979-2014	CMIP/AMIP	GC3-amip	5	(Ridley et al., 2019a)
HadGEM3 N216	amip	1979-2014	CMIP/AMIP	N216-amip	1	(Ridley et al., 2019a)
HadGEM3 N96	1%CO <sub>2</sub>	1950-2000	CMIP	GC3 1%CO <sub>2</sub>	1	(Ridley et al., 2019a)
HadGEM3 N216	abrupt-4×CO <sub>2</sub>	1950-2000	CMIP	GC3 abrupt-4×CO <sub>2</sub>	1	(Ridley et al., 2019a)
HadGEM3 N96	amip-lwoff	1979-2014	CFMIP	GC3-amip lwoff	1	(Webb et al., 2017)
HadGEM3 N216	amip-m4K	1979-2014	CFMIP	GC3-amip m4K	1	(Webb et al., 2017)
HadGEM3 N96	amip-p4K	1979-2014	CFMIP	GC3-amip p4K	1	(Webb et al., 2017)
HadGEM3 N96	SSP1	2050-2100	ScenarioMIP	GC3 SSP1	1	(O'Neill et al., 2016)
HadGEM3 N96	SSP2	2050-2100	ScenarioMIP	GC3 SSP2	1	(O'Neill et al., 2016)
HadGEM3 N96	SSP5	2050-2100	ScenarioMIP	GC3 SSP5	1	(O'Neill et al., 2016)
HadGEM3 N216	SSP1	2050-2100	ScenarioMIP	N216 SSP1	1	(O'Neill et al., 2016)
HadGEM3 N216	SSP2	2050-2100	ScenarioMIP	N216 SSP2	1	(O'Neill et al., 2016)
HadGEM3 N216	SSP5	2050-2100	ScenarioMIP	N216 SSP5	1	(O'Neill et al., 2016)
UKESM1	pre-industrial control	2060-2600	CMIP	UKESM-pi	1	(Tang et al., 2019b)
UKESM1	historical	1979-2014	CMIP	UKESM-hist	5	(Tang et al., 2019a)
UKESM1	SSP1	2050-2100	ScenarioMIP	UKESM SSP1	1	(O'Neill et al., 2016)
UKESM1	SSP2	2050-2100	ScenarioMIP	UKESM SSP2	1	(O'Neill et al., 2016)
UKESM1	SSP5	2050-2100	ScenarioMIP	UKESM SSP5	1	(O'Neill et al., 2016)

varying representation of processes. The main model, HadGEM3 GC3.1 (hereafter GC3) is the latest version of the HadGEM model, and was run at two horizontal resolutions for CMIP6: a low resolution configuration, labelled as N96, with an atmospheric resolution of  $1.875^\circ \times 1.25^\circ$  and a  $1^\circ$  resolution in the ocean model and a medium resolution configuration, labelled N216, with atmospheric resolutions of  $0.83^\circ \times 0.56^\circ$  and a  $0.25^\circ$  oceanic resolution (Menary et al., 2018).

The dynamical core of the GC3.1 configuration used in the submissions of HadGEM3 to CMIP6 is used in a new Earth System model that aims to better represent ocean-biogeochemical, air-soil and air-chemistry interactions, the UK Earth System Model 1 (UKESM1). The UKESM1 was recently developed aiming to improve the UM climate model adding processes of the Earth System (Sellar et al., 2019). These additional components include ocean biogeochemistry with coupled chemical cycles, tropospheric-stratospheric interactive chemistry which aim to better characterise atmospheric chemistry, for example, aerosol-cloud and aerosol-radiation interactions (Mulcahy et al., 2018; Sellar et al., 2019). The physical atmosphere-land-ocean-sea-ice core of the HadGEM3 GC3.1 underpins the UKESM1, so that the UKESM1 and the HadGEM3 have the same dynamical core but the UKESM1 has the additional components mentioned above.

This study uses output from several CMIP6 experiments, which are outlined in Table 3.2. First, the pre-industrial control (piControl) simulations, which are run with constant climate forcing that represents the best estimate for pre-industrial (1850) forcing of aerosols and greenhouse gas levels. Second, historical experiments are 164-yr integrations for 1850-2014 that include historical forcings of aerosol, greenhouse gas, volcanic and solar signals since 1850 (Eyring et al., 2016; Andrews et al., 2019a). The historical experiments of HadGEM3 and UKESM1 are composed of 4 and 9 ensemble members, respectively, but the results will be presented as the ensemble mean for the 1979-2014 period in order to provide a direct comparison with the observed datasets in the same period. These experiments will be referred to as GC3-hist and UKESM1-hist hereafter. For further details, Andrews et al. (2020) extensively describes the historical simulations of HadGEM3-GC3.1.

In contrast to the pre-industrial control experiments, the historical experiments use time-varying aerosol and greenhouse gas emissions and land-use change (Eyring et al., 2016).

In Latin-America, land-use change for agricultural purposes has dramatically decreased tree cover in Central America and south-eastern Brazil since the 1950s (Lawrence et al., 2012), thereby affecting the surface energy balance. The regional emissions of carbonaceous aerosols, nitrogen oxides and volatile organic compound in Latin America are also considered in the historical experiments. These emissions are noteworthy, e.g., due to the impact of black carbon emissions by increased biomass burning in the Amazon and northern Central America (Chuvieco et al., 2008).

The Atmosphere Model Intercomparison Project (AMIP) is a CMIP project that uses atmosphere-only (AO) simulations of the climate to understand the role of SST biases, variability and forcing climate signals. The standard AMIP experiment covers the period 1979-2014 and uses the observed SST fields in this period to drive the models with the same forcing as the historical simulations. Other AMIP experiments may use model-driven SSTs of other experiments to disentangle other processes. This thesis uses the five ensemble members of the AMIP experiment from GC3.

### 3.3 The Moist Static Energy Budget

The moist static energy (MSE) measures the gravitational, sensible heat and latent heat energy within a column and is therefore conserved following air parcels under moist adiabatic processes (Neelin and Su, 2005; Back and Bretherton, 2006; Ma et al., 2019). The use of the MSE budget has proven useful to understand tropical convective phenomena such as ENSO biases (Annamalai, 2020) and teleconnections (Neelin and Su, 2005), tropical cyclones (e.g. Wing et al., 2019), the MJO (Inoue and Back, 2015), axi-symmetric monsoons (e.g. Bordoni and Schneider, 2008) and regional monsoons (e.g. Smyth et al., 2018; Ma et al., 2019), to name a few examples.

The MSE arises from the first law of thermodynamics which decomposes the internal energy of a system into two components: one associated with heat in or out of the system and the second component associated with work done by the system. The MSE, also denoted as  $h$  is given by:

$$h = Lq + C_p T + gz = Lq + s \quad (3.1)$$

where  $C_p$  is the heat capacity at constant pressure,  $T$  is the air temperature,  $L$  is the latent heat of vaporization,  $q$  is the specific humidity and  $s$  is the dry static energy. Equation 3.1 separates the total moist energy of a parcel into a dry component also referred as dry-air enthalpy or heat content (Emanuel, 2007), and the last term is the potential energy associated with the gravitational acceleration. The MSE is conserved under pseudo-adiabatic processes and thus is considered to be a key variable of a moist system, a state variable that is not created or destroyed by convection but rather re-distributed by the coupling of convection with the large-scale circulation (Chou and Neelin, 2004; Emanuel, 2007).

The MSE budget equation can be derived from adding the thermodynamic and moisture equations that arise from the primitive equation (Neelin and Su, 2005), first by writing the material derivative as:

$$\frac{Dh}{dt} = \frac{\partial h}{\partial t} + \nabla \cdot \vec{u} h_p + \frac{\partial p}{\partial t} \frac{\partial h}{\partial p} \quad (3.2)$$

where  $\vec{u}$  is the horizontal wind vector,  $p$  is the air pressure used as a vertical coordinate so that  $\partial p / \partial t = \omega$ . The vertically integrated budget equation arises by rearranging and integrating equation 3.2 in the pressure coordinate (Back and Bretherton, 2006; Inoue and Back, 2015; Annamalai, 2020), leading to:

$$\left\langle \frac{dh}{dt} \right\rangle = - \left\langle \vec{u} \cdot \nabla_p h \right\rangle - \left\langle \omega \frac{\partial h}{\partial p} \right\rangle + F, \quad (3.3)$$

where the angle brackets  $\langle \rangle$  denote vertical integrals from the surface pressure level up to the 100 hPa level, i.e.:

$$\left\langle \right\rangle = \int_{p_0}^{100} dp, \quad (3.4)$$

and the term  $F$  denotes the net forcing of MSE which is given by the surface fluxes and the radiative heating of the column:

$$F = LH + SH + \langle LW \rangle + \langle SW \rangle \quad (3.5)$$

where  $SH$  and  $LH$  are the surface turbulent sensible and latent heat fluxes, respectively, and  $LW$  and  $SW$  are the longwave and shortwave column-integrated heating rates, respectively.

The gross moist stability (GMS or  $\gamma$ ) was derived by Neelin and Held (1987) from the MSE budget in equation 3.3 aiming to quantify the strength of convection to the outflow of energy in the tropics. The GMS has been continuously used (Raymond et al., 2009; Inoue and Back, 2015; Nie and Sobel, 2015; Inoue et al., 2021) as a ratio of a lateral outflow of entropy or energy divided by a measure of the strength of convection per unit area. In this thesis, the vertical component of the GMS, referred to as  $M_v$  is used following (Inoue and Back, 2015):

$$\gamma_v = M_v = \frac{\left\langle \omega \frac{\partial h}{\partial p} \right\rangle}{\left\langle \omega \frac{\partial s}{\partial p} \right\rangle}. \quad (3.6)$$

The  $M_v$  in addition to the MSE budget is used in two chapters of these thesis to understand how the large or regional-scale circulation is related to convection.

# 4

## The American monsoon system in UKESM1 and HadGEM3

This chapter evaluates the representation of the AMS in the CMIP6 models: UKESM1 and HadGEM3. The pre-industrial control, historical and AMIP experiments are evaluated highlighting the role of large and regional-scale biases for the representation of the monsoon dynamics, as well the representation of ENSO teleconnections. The impacts of increased horizontal resolution and representing Earth System processes for the representation of the monsoon are described and discussed.

### 4.1 Introduction

The response of regional monsoons to greenhouse forcing remains an open question (Zhou et al., 2016; Pascale et al., 2019) because the observational record is too short to exhibit significant trends but also because biases in GCMs increase uncertainty in future model projections. Although the thermodynamical response to greenhouse forcing in the tropics seems to be relatively well constrained, the dynamical response is less clear (Shepherd, 2014). The American Monsoon System (AMS), as with most monsoon regions, is shaped by regional dynamical features which makes the dynamical biases particularly relevant when understanding the precipitation response to forcing in a monsoon region.

In spite of current recognition as a monsoon, the AMS has received less attention by the modelling community compared to the Asian or African monsoons. The assessment of climate models in monsoon regions is key to understanding current and future changes to the water cycle in tropics. However, in the AMS, model assessments are usually only done in a handful of studies per CMIP phase. These studies only provide a wide view of the biases of each generation of models while usually highlighting which biases have improved and which biases remain from previous model generations (see e.g. Geil et al., 2013; Ryu and Hayhoe, 2014). However, a deeper evaluation of individual models can be used to provide better insight into the processes associated with climatological biases in the large-scale circulation and ultimately better understand the causes for the model biases in AMS rainfall.

For example, in the South American Monsoon, CMIP5 models improved from the CMIP3 phase in their simulations of the distribution of precipitation during monsoon maturity and exhibited an improved seasonal cycle (Jones and Carvalho, 2013; Yin et al., 2013). However, some biases such as the underestimation of rainfall in the central Amazon have persisted from the first generation of GCMs up until CMIP5 (Li et al., 2006; Yin et al., 2013). The geographic distribution of rainfall during austral fall and several characteristics of the South Atlantic Convergence Zone are also poorly represented in CMIP5. However, these studies provided little evidence as for the reasons for the improvements or the remaining biases in the models. A clear motivation to evaluate models in the South American Monsoon is that the accurate simulation of the geographic distribution and seasonality of rainfall in the Amazon rainforest is a relevant issue due to the impact of the rainforest on climate and society (e.g. Li et al., 2006; Malhi et al., 2009; Yin et al., 2013).

Climate research in recent decades has aimed to reduce uncertainty in climate projections by improving GCMs, but different approaches taken by modelling centres are seemingly disconnected (Jakob, 2014). One approach is to reduce horizontal grid spacing down to km resolution to rely less on parametrizations and more on physical laws to represent clouds and convection (Palmer and Stevens, 2019). A second approach aims to include new explicit representation of Earth System processes to better characterise complex land-atmosphere-ocean biogeochemical cycles that may provide a better constraint on large-scale aspects of the climate such as climate sensitivity, a parameter that depends on the carbon cycle (Marotzke

et al., 2017; Sellar et al., 2019; Andrews et al., 2019a). Finally, recent modelling centres have chosen to include stochastic parametrisations of sub-grid processes since this approach has improved seasonal forecasts and may therefore improve climate projections (Palmer, 2019).

Model validation and assessment is important to analyse the effect of new parametrisations and to highlight missing processes but also evaluate which route provides the more substantial model improvement, stochastic parametrisations, increased resolution or Earth System processes. The focus of this chapter is then to evaluate the CMIP6 experiments from HadGEM3 GC3.1 (GC3) and UKESM1 in the AMS. In this chapter and remainder of the thesis, the AMS is considered to be composed of the North and South American monsoon systems, while also including the Midsummer drought region of southern Mexico and Central America as part of the AMS (as in e.g. Vera et al., 2006; Pascale et al., 2019).

The remainder of this chapter is organised as follows. The following section described the data and methods used in this chapter. Section 4.3 compares modelled and observed climatological temperature, sea-level pressure and low-level wind fields, whereas section 4.4 analyses the Pacific and Atlantic ITCZs. Section 4.5 analyses the spatial and temporal characteristics of rainfall and convection in the AMS while section 4.6 documents the simulated teleconnections of ENSO. A summary and discussion of the results is provided at the end of the chapter.

## 4.2 Methods and data

The model assessment of this chapter will use a range of experiments from the MOHC, described in section 3.2 using the HadGEM3 and the UKESM1 models. The experiments from HadGEM3 run at N96 (labelled GC3 N96) and at N216 (labelled GC3 N216) resolutions are used to evaluate the role of horizontal resolution whereas Earth System Model UKESM1, which is run at N96 resolution in all the experiments, is used to evaluate the effect of representing atmospheric chemistry and other processes for the representation of the monsoon. In this chapter, the term low resolution will refer to both UKESM1 and GC3 N96 experiments whereas medium resolution refers to GC3 N216 experiments.

The historical experiments are used to evaluate model skill in reproducing the observed period whereas the AMIP experiment from GC3 N96 is used to highlight the role of SST biases. The historical experiment data is used only in the 1979-2014 period to directly compare with the observed period whereas the whole pre-industrial and AMIP available data is used. All the observational datasets used in this chapter are thoroughly described in chapter 3 but in summary in this chapter, the surface or near-surface air temperature data is taken from the CRU4 dataset and ERA5, whereas precipitation is used from the different datasets described in the previous chapter. The dynamical features such as wind speed and vertical velocity are taken from ERA5.

The climate indices of ENSO and the QBO used in this chapter were obtained by the following process. For ENSO, the deseasonalized and detrended time-series of the area-averaged SSTs (EN3.4 region [190-240°W,5°S-5°N]) is used as an index to composite months into positive, negative and neutral phases. A month is determined to be in the positive, El Niño, phase when the index is higher than +0.65 K and a negative phase, La Niña, when the index is more negative than -0.65 K to select moderate to strong events. A neutral month is found where the magnitude of the index is smaller than 0.5 K and months with an index between 0.5 and 0.65 are discarded as they are borderline weak ENSO events or neutral cases. Other indices, including the use of a 5-month running mean (Trenberth et al., 1998), were tested without significantly changing the results. Previous studies (e.g. Menary et al., 2018; Kuhlbrodt et al., 2018) showed that the MOHC models reasonably simulate several characteristics of ENSO such as the period and SST patterns.

Similarly, for the QBO, the deseasonalized and detrended time-series of the equatorially averaged [10°S-10°N] zonal-mean zonal wind at the 70 hPa level is used as the QBO index for both reanalysis and model data. The westerly phase of the QBO (QBOw) is determined when the index is greater than  $2 \text{ m s}^{-1}$  and the easterly phase (QBOe) when the index is less than  $-2 \text{ m s}^{-1}$ .

### 4.3 Surface temperature and low-level wind

This section evaluates how these simulations represent the near-air surface temperature and low-level wind fields in the vicinity of the AMS region (Figures 4.1 and 4.2). The biases of the historical experiments, computed as the differences between the model and observed fields, are shown in Figures 4.1c, d) for GC3 N96-hist and e, f) for UKESM1-hist. Only statistically significant differences are shown, according to a Welch t-test (Wilks, 2011), which accounts for the difference in sample size and variance between model and observations/reanalysis data. The significance for simulations with multiple ensemble members is estimated first for each ensemble member and then combined into a single probability or p-value using Fisher's method (Fisher, 1992). Pattern correlations and root-mean square error (RMSE) are shown in Figures 4.1c-f and in Table 4.1.

During DJF, the simulations show a colder-than-observed sub-tropical North America and a warm bias over the Amazon ( $\approx +3.5$  K). The west coast of South America also shows a significant warm bias ( $> +4$  K) in the historical simulations. The simulated circulation in austral summer in South America has a significant bias in the easterly flow coming from the equatorial and subtropical Atlantic. The low-level wind biases suggest a weaker easterly flow from the Atlantic into southeastern Brazil but also a strong southward flow from northern to southern South America. The South America Low-Level Jet, i.e., the low-level northwesterly flow in Bolivia, observed in Figure 1a, is stronger in the simulations. This stronger than observed jet is suggestive of a stronger moisture transport to the La Plata Basin, which has been associated with a drying of the Amazon and positive precipitation anomalies at the exit region of the jet (Marengo et al., 2012; Jones and Carvalho, 2018).

In turn, in boreal summer (Figures 4.1d, f), positive temperature biases are observed in southwestern North America ( $> +3.5$  K), which are higher in UKESM1-hist than in GC3 N96-hist. The easterly flow west of Central America has a negative bias in UKESM1 suggesting a weaker flow that crosses from the Caribbean Sea into the East Pacific Ocean. Also in JJA, the simulated East Pacific surface temperatures are colder than observed for both historical experiments. The inclusion of Earth System processes appears to make no improvement on the low-level circulation biases.

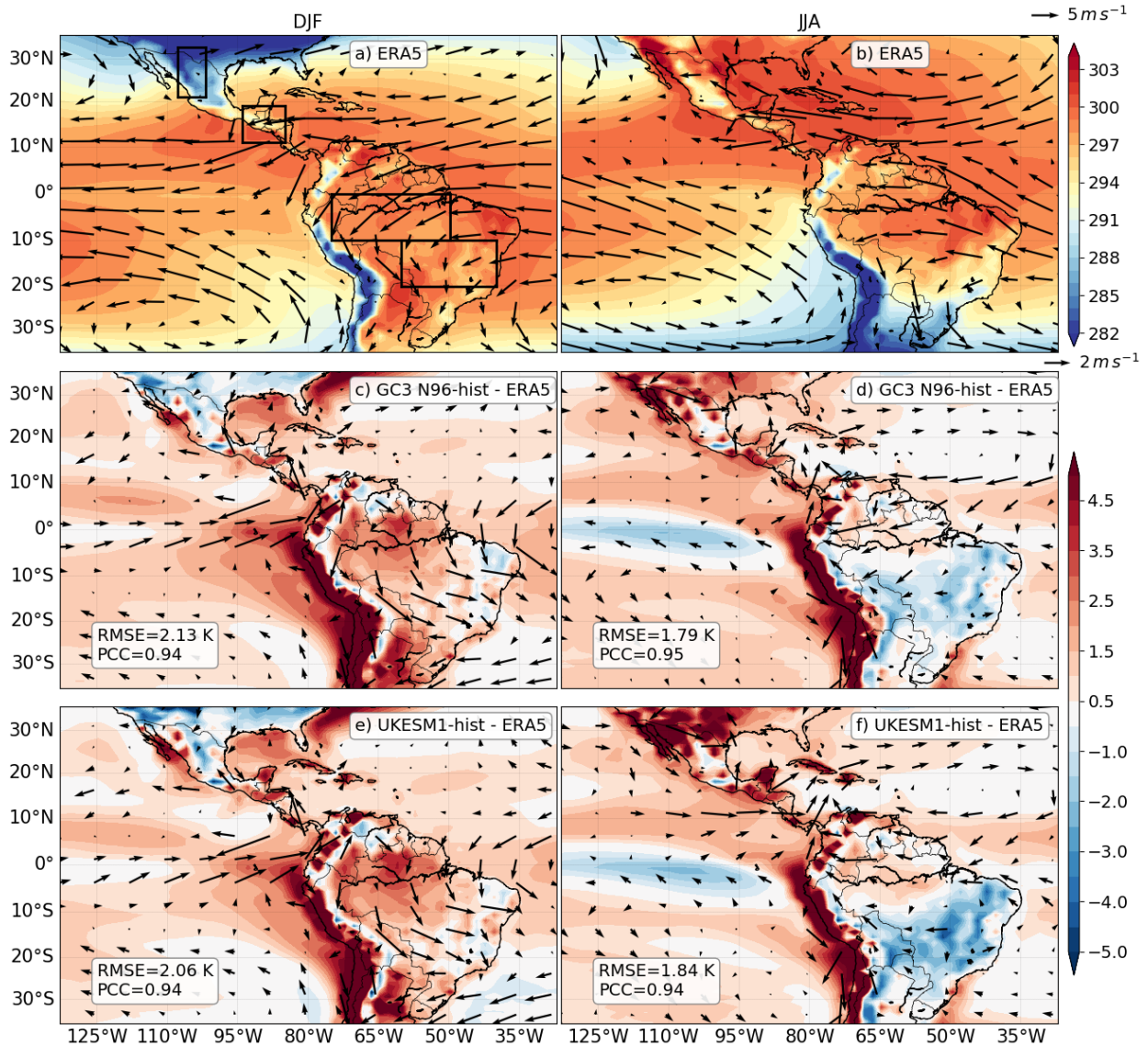


**Figure 4.1:** (a, b) Temperature (color-contours in K) and wind speed (vectors) at 850 hPa DJF and JJA climatologies in ERA5. The biases are shown as the differences between the ensemble mean from the historical experiment of (c, d) GC3 N96 and (e, f) UKESM1 and ERA5. The climatologies and biases are shown for (a, c, e) boreal winter (DJF) and (b, d, f) boreal summer (JJA). Only differences statistically significant to the 95% level are shown, according to a Welch t-test for each field. The key for the size of the wind vectors is shown in the top right corner of panels b) and d). The root-mean square error (RMSE) and pattern correlation coefficient (PCC) are shown on the bottom left of c-f.

The piControl simulations (Figures 4.2a-d) have some similar biases to the historical simulations. In DJF, the piControl simulations show a similar positive bias in the Amazon than the historical experiments, although smaller, as well as a similar bias in the circulation in South America, with the smallest biases in GC3 N216-pi. In JJA, the piControl simulations

**Table 4.1:** Root-mean square error (RMSE) and pattern correlation coefficients (PCC) for each season and each model experiment. Near surface air temperature ( $t2m$ ), wind components ( $u$  and  $v$ ) and mean-sea level pressure ( $mslp$ ) are assessed against ERA-5 and precipitation ( $pr$ ) against TRMM.

Variable	Experiment	DJF	DJF	MAM	MAM	JJA	JJA	SON	SON
		RMSE	PCC	RMSE	PCC	RMSE	PCC	RMSE	PCC
t2m	GC3 N96	1.28	0.98	1.3	0.96	1.38	0.96	1.31	0.96
t2m	GC3 N216	1.05	0.99	1.07	0.98	1.02	0.98	0.98	0.98
t2m	GC3 Hist	2.06	0.94	1.75	0.93	1.73	0.94	2.05	0.92
t2m	UKESM-hist	2.03	0.94	1.77	0.93	1.8	0.94	2.0	0.93
t2m	GC3 AMIP	1.17	0.98	1.12	0.97	1.2	0.97	1.2	0.97
u	GC3 N96	0.78	0.99	0.59	0.99	0.9	0.98	0.87	0.98
u	GC3 N216	0.78	0.99	0.59	0.99	0.9	0.98	0.87	0.98
u	GC3 Hist	1.02	0.98	1.04	0.97	0.92	0.98	0.84	0.98
u	UKESM-hist	1.04	0.98	1.01	0.97	0.91	0.98	0.82	0.98
u	GC3 AMIP	0.96	0.98	0.77	0.99	1.18	0.97	1.09	0.96
v	GC3 N96	0.75	0.93	0.66	0.93	0.65	0.95	0.59	0.94
v	GC3 N216	0.6	0.96	0.5	0.95	0.57	0.96	0.54	0.94
v	GC3 Hist	0.76	0.94	0.72	0.92	0.66	0.95	0.59	0.94
v	UKESM-hist	0.75	0.93	0.69	0.92	0.65	0.95	0.6	0.93
v	GC3 AMIP	0.67	0.95	0.52	0.95	0.68	0.94	0.61	0.93
mslp	GC3 N96	1.33	0.96	1.03	0.97	1.15	0.96	0.95	0.97
mslp	GC3 N216	1.11	0.97	0.9	0.97	1.1	0.96	0.89	0.97
mslp	GC3 Hist	1.31	0.97	1.12	0.96	1.08	0.96	0.94	0.97
mslp	UKESM-hist	1.4	0.97	1.15	0.96	1.14	0.95	0.99	0.97
mslp	GC3 AMIP	1.15	0.97	0.87	0.97	1.09	0.96	0.93	0.97
pr	GC3 N96	2.02	0.79	2.24	0.71	1.62	0.9	1.69	0.86
pr	GC3 N216	1.58	0.88	1.72	0.85	1.4	0.93	1.57	0.89
pr	GC3 Hist	2.05	0.78	2.49	0.64	1.69	0.88	1.69	0.86
pr	UKESM-hist	1.96	0.8	2.39	0.66	1.71	0.88	1.62	0.87
pr	GC3 AMIP	1.42	0.9	1.61	0.88	1.95	0.88	1.8	0.88

do not show the positive temperature bias in northwestern North America observed in the historical experiments. However, the bias in the zonal wind over the easternmost Pacific is present in both piControl and historical simulations.

Figures 4.2e, f show the difference between the historical and piControl experiment of GC3 N96, illustrating the response to historical forcing in GC3 N96. The temperature response in austral summer in South America is observed as 1.5 K whereas in JJA in North America temperatures were 4 K higher in the historical experiment than in the piControl. A very similar temperature pattern response to historical forcing was observed for UKESM1 (not shown) although of slightly different magnitude. The only significant difference in

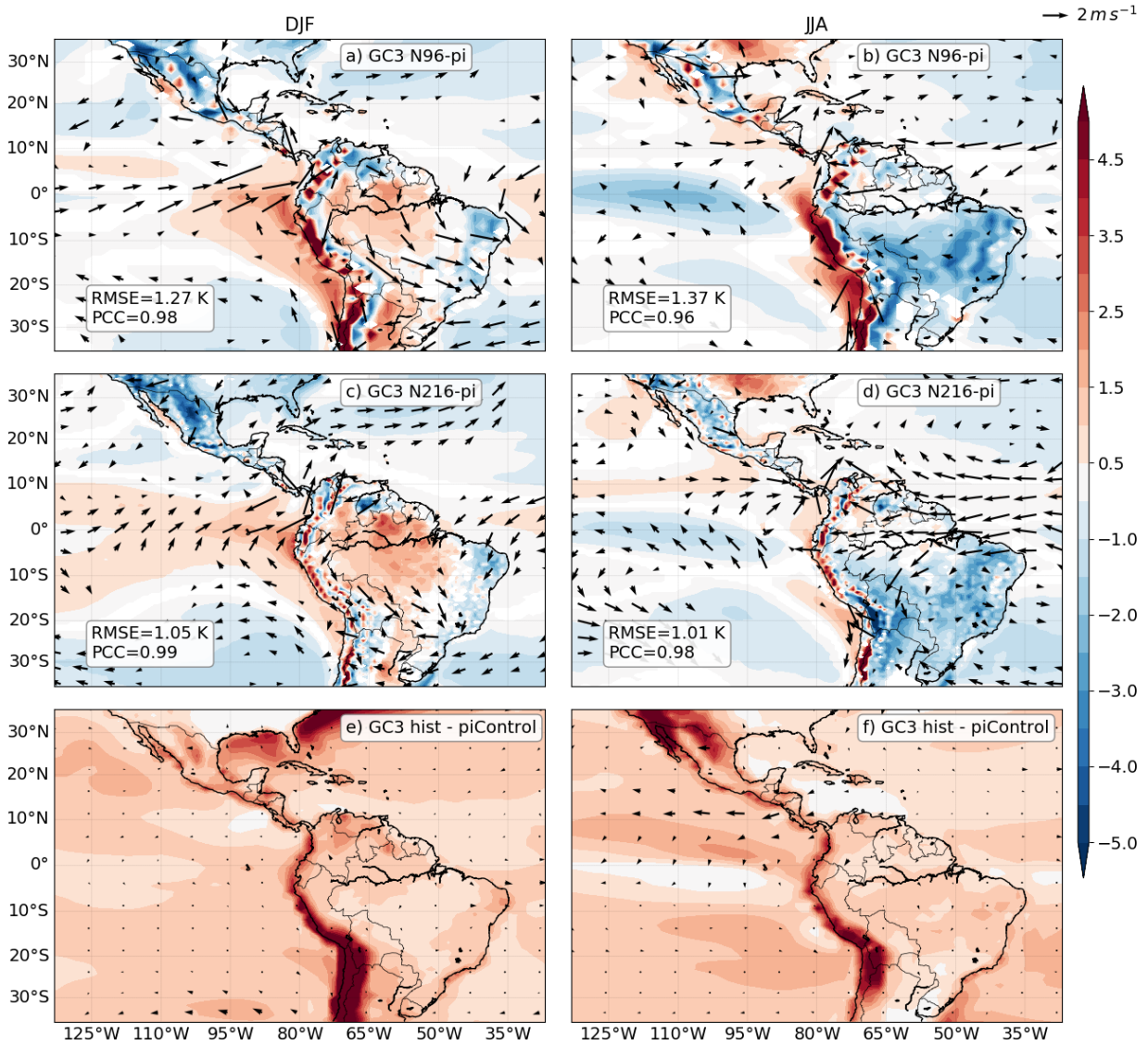


**Figure 4.2:** As in Figure 4.1, but showing the differences between the piControl simulations of (a, b) GC3 N96-pi and (c, d) GC3 N216-pi, and ERA5. (e, f) show the statistically significant differences between the historical (1979-2014) and piControl experiments of GC3. The RMSE and PCC are shown on the bottom left of a-d.

low-level winds, as a response to historical forcing, are the easterlies in the East Pacific Ocean during JJA, which are stronger in the historical simulation.

The seasonal cycle of temperature in key regions (depicted in Figure 4.1a) of the AMS is shown in Figure 4.3, comparing the simulations to ERA5 and the CRU4 dataset. The temperature in the North American Monsoon region ranges from the boreal winter mean temperature of 12°C to a maximum in June close to 27°C. Although the piControl simulated

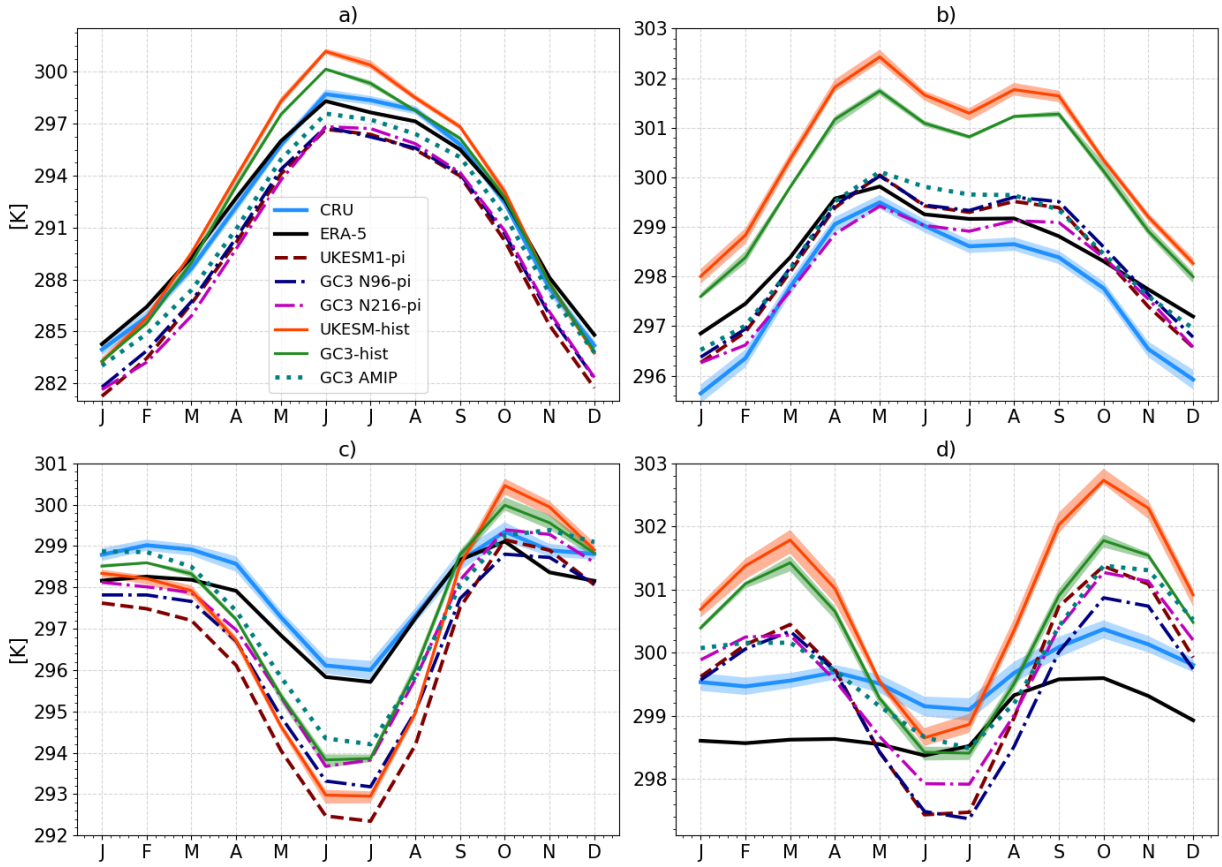


**Figure 4.3:** Monthly-mean temperature in the (a) North American Monsoon [ $19\text{--}35^{\circ}\text{N}, 110\text{--}103^{\circ}\text{W}$ ], (b) the Midsummer drought [ $11\text{--}19^{\circ}\text{N}, 95\text{--}85^{\circ}\text{W}$ ] (c) Eastern Brazil [ $20\text{--}10^{\circ}\text{S}, 60\text{--}40^{\circ}\text{W}$ ] and (d) the Amazon basin [ $-10\text{--}0^{\circ}\text{S}, 75\text{--}50^{\circ}\text{W}$ ] regions. The shadings for the CRU dataset represents the observational uncertainties and for the historical simulations the shading is the ensemble spread. The regions for this plot are shown in Figure 4.1a.

temperatures are colder than observed throughout the year, the models reasonably reproduce the seasonal cycle, which may be relevant for the simulated monsoon onset timing and strength (Turrent and Cavazos, 2009). The historical experiments notably show a colder than observed winter and a warmer than observed summer.

The piControl simulations show a colder-than-observed winter in southern Mexico and northern Central America. The historical experiments show a warming signal, when compared to the piControl simulations, of about 1.5 K in winter and 2 K in the summer in this region. In spite of these biases, all the experiments follow closely the seasonal cycle in North and Central America.

However, the seasonal cycle in South American regions (Figures 4.3 c, d) of southeastern

Brazil and the central Amazon shows notable temperature biases. The simulations show a stronger than observed seasonal cycle, especially the historical experiments. For example, the modelled temperature difference between late austral winter and spring was  $\approx 4$  K whereas the observed temperature varies by less than 1 K in the same period. The models show a warm bias in the Amazon region (Fig. 4.3 d) which peaks in austral spring (SON), during the development of the monsoon (Marengo et al., 2012). In southeastern Brazil, the seasonal cycle is reasonably well reproduced but with a significant cold bias throughout the year which maximizes during austral winter (JJA), as models (e.g. UKESM1) simulate a temperature 4 K lower than observed. In all panels of Figure 4.3, the historical experiments show a significant warming signal as a response to historical forcing, which is generally stronger in UKESM1 than in GC3 N96.

The near-surface air temperature and the low-level wind structure during monsoon season are intertwined with the processes that lead to monsoon rainfall which means that the biases presented in this section will likely be related to biases in precipitation, e.g., through cloud feedbacks. For example, a biased wind structure in eastern Brazil as well as the positive warm bias in the central Amazon during DJF may indicate biases in the moisture transport and cloud cover that lead to the dry Amazon bias (Jones and Carvalho, 2013). The next section provides an assessment of a large-scale feature that is intimately related with monsoon rainfall: the Intertropical Convergence Zones.

## 4.4 The Atlantic and Pacific ITCZs and the SACZ

The AMS is intertwined with the seasonal migration of the East Pacific and Atlantic ITCZ as the ITCZ largely determines regions of ascending and descending motions, moisture transport and the hemispheric energy balance (Oueslati and Bellon, 2013; Li and Xie, 2014; Zhou et al., 2016; Cai et al., 2019). In particular, the North American monsoon and MSD are mostly influenced by the East Pacific ITCZ whereas the South American monsoon is affected by the strength and position of the Atlantic ITCZ (Yoon and Zeng, 2010; Marengo et al., 2012).

Figure 4.4 shows the observed and modelled climatological rainfall and the ITCZ climatological positions. Three simulations are shown; two low-resolution (N96) runs,

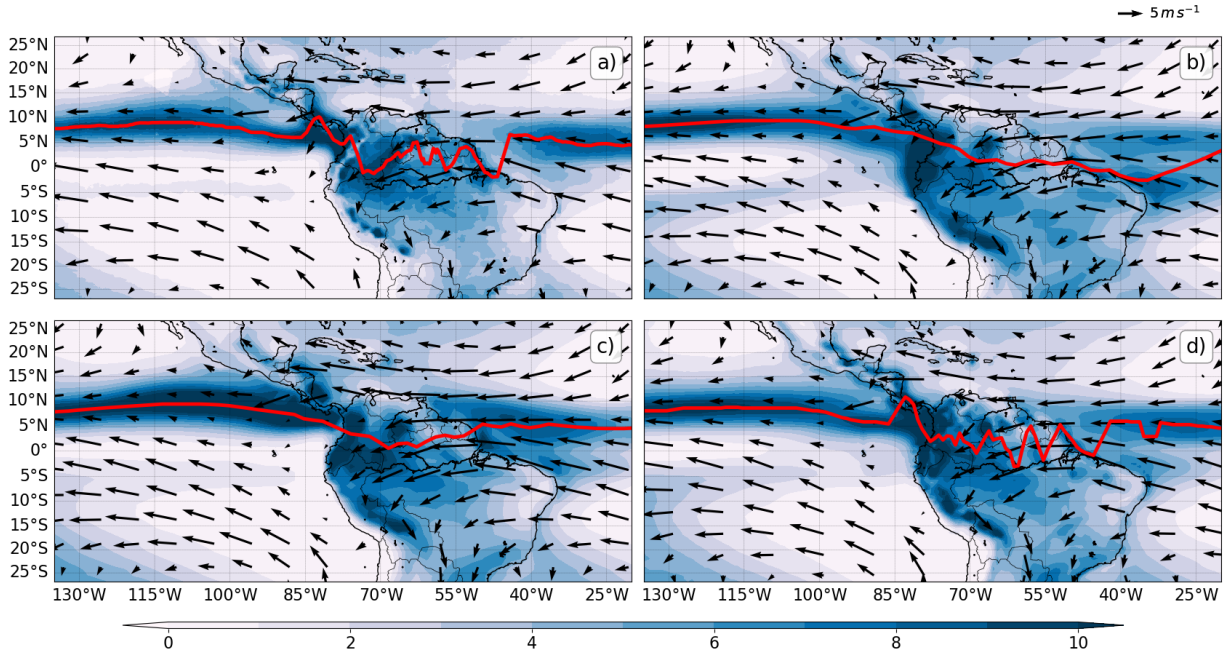


**Figure 4.4:** Climatological precipitation [ $\text{mm day}^{-1}$ ] and low-level wind speed (850-hPa) in (a) TRMM and ERA-5, (b) the ensemble-mean UKESM-historical, (c) GC3-amip and (d) GC3 N216-pi. The red line highlights the maximum rainfall for each longitude as a proxy for the position of the ITCZ.

the ensemble-mean UKESM1-historical, the ensemble mean GC3 AMIP and a medium resolution run, GC3 N216-pi. Other simulations are not shown as all the coupled low resolution (N96) simulations from UKESM1 and GC3 N96 showed very similar precipitation and ITCZ characteristics whereas the AMIP and medium-resolution experiments showed notable differences to the rest.

The climatological ITCZ in TRMM (Figure 4.4a) is found, on average, at  $8^\circ\text{N}$  in the East Pacific and at  $6^\circ\text{N}$  in the Atlantic. All the simulations reasonably represent the climatological position of the East Pacific (EP) ITCZ; however, the modelled Atlantic ITCZ near the coast of Brazil is found south of the equator at  $3^\circ\text{S}$  in the coupled model simulations. The location of the ITCZ in GC3 N216-pi and the spatial distribution of rainfall is more consistent with TRMM dataset than the rest of experiments. Rainfall near the Amazon river mouth is significantly larger in the low resolution simulations than in the TRMM dataset. However, the GC3 AMIP shows the best agreement with TRMM in ITCZ position and rainfall distribution.

The seasonal cycle of the ITCZ location, precipitation rates and low-level winds in both basins are shown in Figure 4.5, for TRMM, UKESM1-hist, GC3 AMIP, GC3 N96-pi and

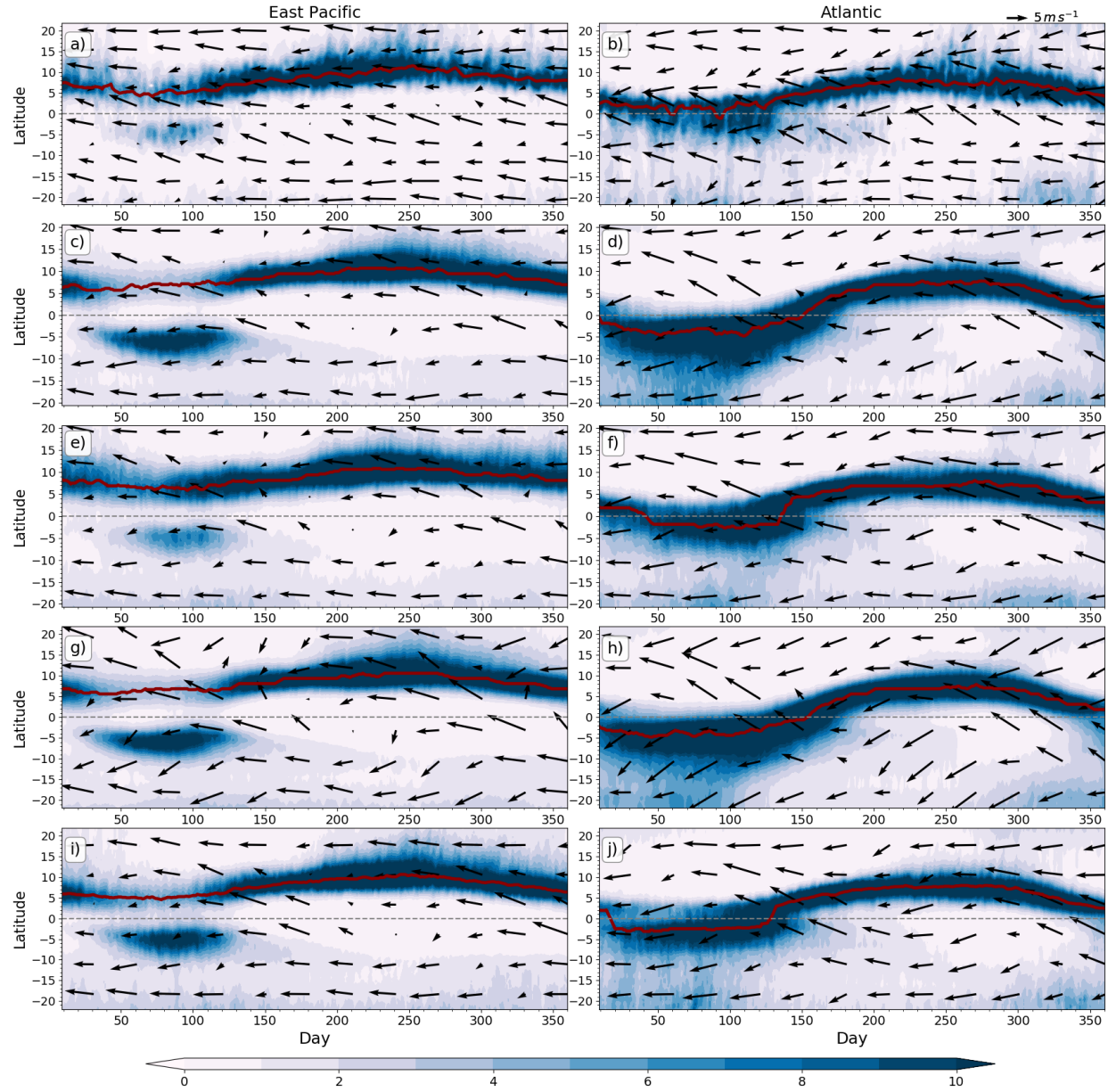


**Figure 4.5:** Time-Latitude plot of daily mean rainfall (colour contours) and low-level wind speed (850 hPa) longitudinally averaged over the (a, c, e, g) East Pacific [ $150^{\circ}\text{W}$ - $100^{\circ}\text{W}$ ] and (b, d, f, h) Atlantic [ $40^{\circ}\text{W}$ - $20^{\circ}\text{W}$ ] Oceans. (a, b) show rainfall from TRMM and winds from ERA-5, (c, d) the ensemble-mean UKESM-historical, (e, f) GC3 AMIP, (g, h) GC3 N96-pi and (i, j) GC3 N216-pi. The red solid line shows the ITCZ as the latitude of maximum precipitation.

GC3 N216-pi. The EP ITCZ in observations (Fig. 4.5a) migrates southwards during the first days of the year and is weakest and at its southernmost position at  $5^{\circ}\text{N}$  around day 100 (mid-April). During boreal spring, the EP ITCZ migrates northward reaching a peak latitude and maximum rainfall at  $10^{\circ}\text{N}$  by day 250, or early September. The EP ITCZ during boreal

winter is weaker than during the rest of the seasons. The low-level winds are predominantly easterly, which are stronger away from the ITCZ and weaker and convergent near the ITCZ position. The position and seasonal migration of the EP ITCZ is reasonably well represented in the four simulations (Figs. 4.5c, e, g, i), but a noticeable bias in precipitation is observed in boreal winter south of the equator in the coupled simulations. The modelled low-level winds in the coupled simulations show significant biases near the ITCZ. These wind biases are observed as stronger wind vectors converging toward the ITCZ during boreal summer and spring and stronger wind vectors diverging away from the equator during boreal winter.

The observed Atlantic ITCZ (Figure 4.5b) has a similar seasonal cycle to the EP ITCZ. The Atlantic ITCZ is close to 4°N at day 1 and migrates southwards at the start of the year reaching its southernmost position at 0° at the end of March. During boreal spring, the Atlantic ITCZ migrates north, reaching 8°N at the start of boreal summer. In contrast to the EP ITCZ, the maximum rainfall in the Atlantic ITCZ does not weaken during any season. The boreal winter position of the modelled ITCZ is displaced south with respect to the observations. The simulated ITCZ crosses south of the equator during boreal winter, with maximum precipitation rates of 12 mm day<sup>-1</sup> found in the 0-10°S region. After boreal spring, the modelled ITCZ crosses back north of the equator and matches the observed ITCZ reasonably well for boreal summer and fall. Low-level wind vectors near the Atlantic ITCZ (Figures 4.5f and h) suggest a simulated southerly bias north of the equator and a stronger northerly flow south of 10°S.

The biases in the Atlantic ITCZ can also be observed in the Walker circulation as significant negative  $\omega$  and  $q$  biases just north and south of equatorial South America indicative of weaker convective activity. The Atlantic Ocean in the simulations shows a biased negative  $\omega$  (more ascent) south of the equator and a positive  $\omega$  bias (less ascent) north of the equator in the low resolution simulations. The magnitude of the biases in the Atlantic ITCZ and overturning circulations described above were associated with the horizontal resolution of the simulations. These biases were of similar magnitude in all the coupled model simulations run at the lower resolution N96, regardless of the type of experiment. However, these biases were reduced in the medium resolution experiments of GC3 N216 and in the GC3 N96 AMIP experiment which corrects SST biases (Figures 4.5f, j).

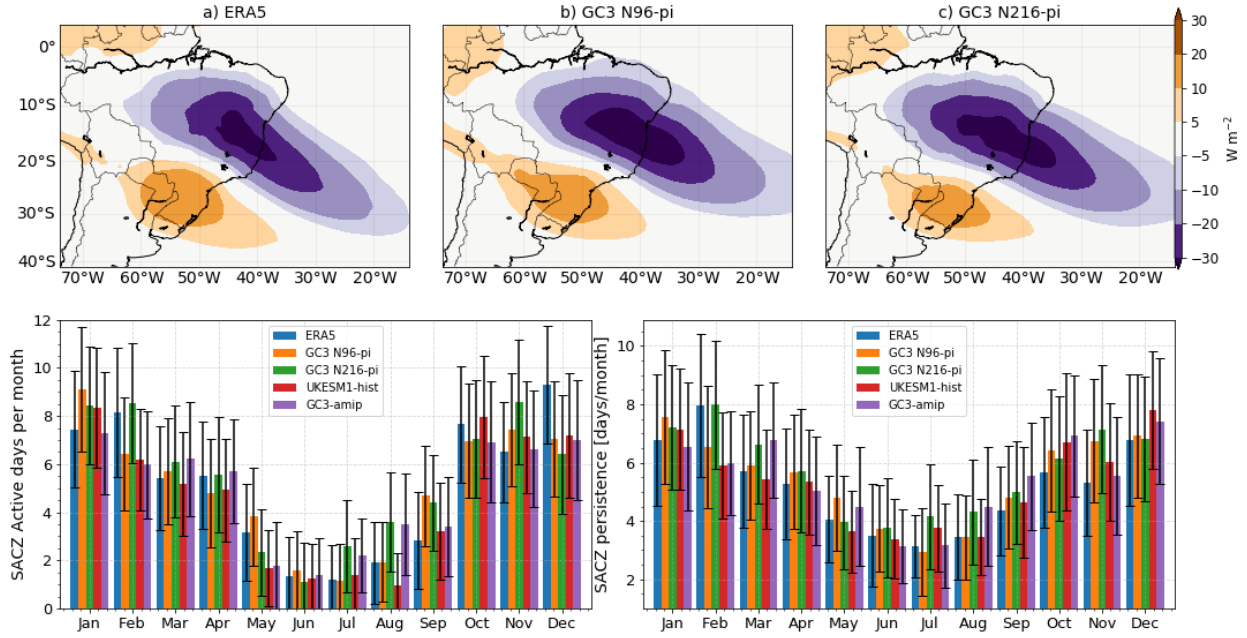


**Figure 4.6:** (a, b, c) OLR anomalies during active South Atlantic Convergence Zone (SACZ) events. (d, e) Frequency of active SACZ days and length of active SACZ events in reanalysis and model data, the standard deviation is shown as the error bar. The SACZ active days are constructed by first computing the first EOF of the monthly-mean deseasonalized OLR and then the daily OLR, previously filtered to remove periods higher than 99 days, is projected on the EOF pattern to produce a time-series of pseudo-principal components. Active SACZ days are found when this time-series of pseudo-PCs is greater than 1, and the persistence is measured as the number of continuous days where the time-series is greater than 1.

The South Atlantic Convergence Zone (SACZ) is a northwest-southeast oriented band of convection and is a prominent influence on the South American Monsoon mean and extreme rainfall (Carvalho et al., 2004; Marengo et al., 2012; Jorgetti et al., 2014). The SACZ is primarily characterized by convergence oriented northwest-to-southeast that promotes rainfall in southeastern Brazil. The position of the SACZ and strength are an important factor for variability of the South American monsoon on different temporal and spatial scales (Carvalho et al., 2004; Marengo et al., 2012; Jorgetti et al., 2014).

The SACZ in this simulations, defined by the outgoing long-wave radiation empirical orthogonal function analysis (Figure 4.6) closely resembles the pattern found in ERA5. The SACZ active days and the persistence of the SACZ are also compared and found to be in relatively good agreement between reanalysis and model datasets. The simulations from UKESM1, and GC3 N96 and N216 appear to reasonably simulate the spatial pattern of

active SACZ days characterized by the low OLR in southeastern Brazil and higher OLR in the La Plata Basin. Similarly, the seasonal cycle of the frequency and persistence of SACZ active days is very well represented by the models with peak activity found from November through January and very little activity during austral winter. The impact that an accurate representation of the SACZ activity in GCMs has for representing short-scale variability of the South American Monsoon System is an open question, as the SACZ is rarely assessed in CMIP analyses.

GCMs have showed little improvement in their representation of ITCZs (Oueslati and Bellon, 2015). This bias has persisted through CMIP phases largely because the position, strength and seasonal migration of the ITCZ is hard to represent accurately. These features are controlled by ocean-atmosphere feedbacks that intertwine the local and regional circulation with cloud-radiative feedbacks and the atmospheric and oceanic transport of energy (Schneider et al., 2014; Oueslati and Bellon, 2015; Byrne and Schneider, 2016; Byrne and Zanna, 2020). This section shows that the CMIP6 MOHC models reasonably simulate the location of the East Pacific ITCZ but poorly represent the location of the austral summer Atlantic ITCZ and overestimate precipitation over the East Pacific ITCZ. The location and seasonal variability of the SACZ is also fairly well simulated by all the models. The implication of the results in this section for AMS precipitation will be addressed in the last section this chapter.

## 4.5 Precipitation and convection in the AMS

### 4.5.1 Mean seasonal precipitation

The austral summer (DJF) rainfall distribution in South America of the TRMM dataset and the simulations for GC3 N216-pi, UKESM-hist and GC3-amip (Figure 4.7) shows several noteworthy biases in the coupled simulations. The maximum austral summer rainfall in TRMM (Figure 4.7a) is found as a northwest-southeast oriented band of precipitation from the core Amazon region into southeastern Brazil, which is related to the SACZ. The biases are illustrated (Figures 4.7e-h) as the precipitation difference between the simulations and TRMM.

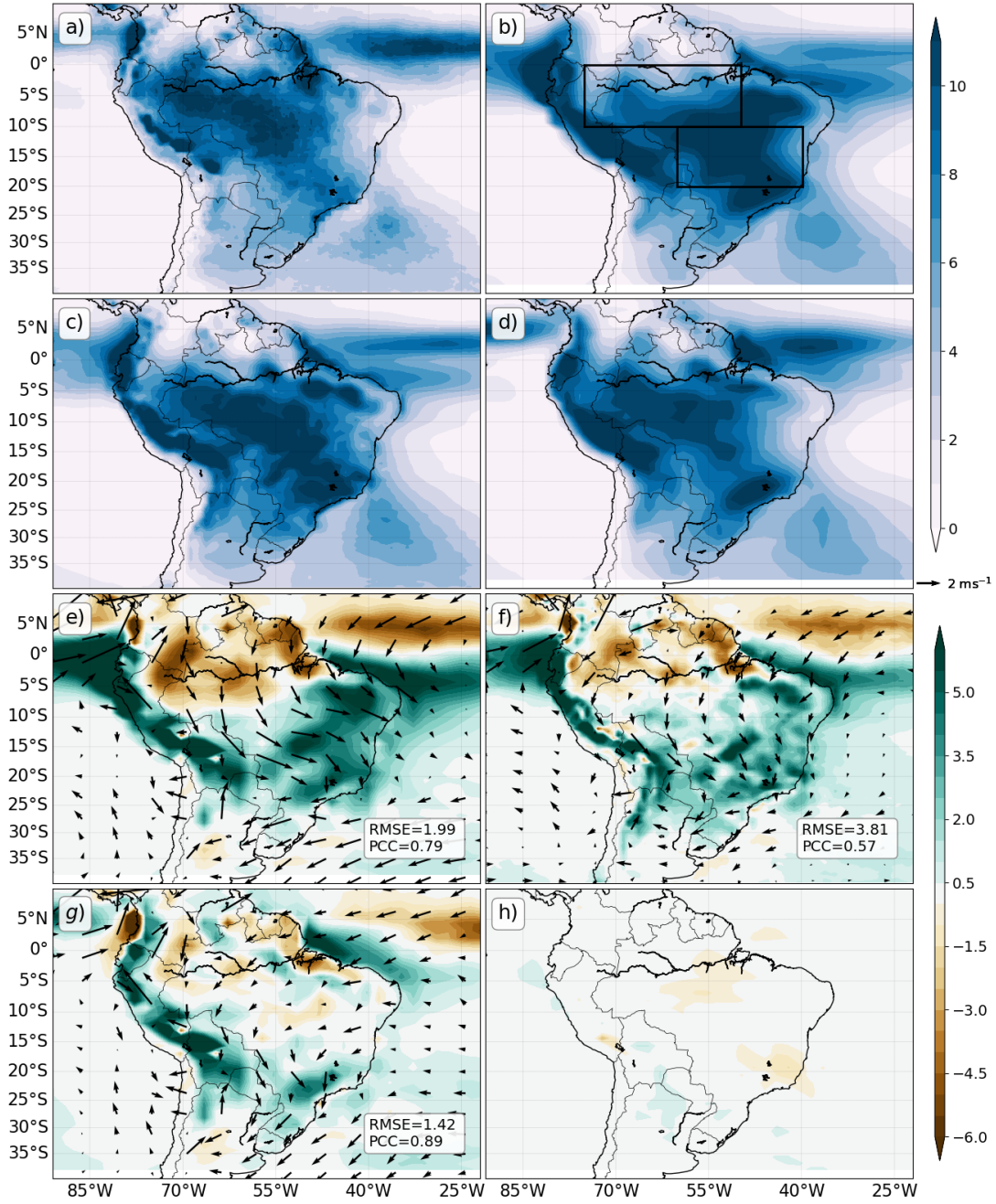


**Figure 4.7:** DJF mean rainfall [mm day<sup>-1</sup>] from (a) TRMM, (b) UKESM1-historical, (c) GC3 N216-pi and (d) GC3-amip. (e, f, g) show the statistically significant differences between panels (b, c, d) and (a) TRMM, respectively. (h) Precipitation difference between UKESM1-historical and UKESM1-pi, only statistically significant differences (95%) confidence level is shown. The biases in the 850-hPa winds are shown as vectors.

The coupled simulations show three main biases. Rainfall in the Atlantic ITCZ in these simulations is displaced southwards, observed as positive (+5 mm day<sup>-1</sup>) biases south of the

equator and negative biases ( $-5 \text{ mm day}^{-1}$ ) north of the equator in the Atlantic. Second, the models underestimate rainfall in the core Amazon basin by  $-3 \text{ mm day}^{-1}$  on average, and the third major bias is that rainfall in southeastern Brazil is overestimated by more than  $+5 \text{ mm day}^{-1}$ , approximately  $+100\%$  of the observed rainfall in this region.

The precipitation biases are associated with a stronger northerly flow in South America, transporting moisture from the Amazon into southeastern Brazil and the La Plata Basin. The magnitude of these biases is smaller in GC3 N216 (Figure 4.7f) than in the low resolution simulations, such as UKESM1-hist. The ensemble mean GC3 AMIP (Figure 4.7d) shows a better representation of the austral summer rainfall and circulation patterns, removing the main circulation biases (Figure 4.7g) of the coupled simulations. The response to historical forcing, illustrated by the difference between UKESM1-hist and UKESM1-pi (Figure 4.7h), is much weaker than the magnitude of the biases and is characterized by a weak drying of the Amazon and southeastern Brazil. Therefore, the magnitude of these biases are too large to have confidence in these drying responses to historical forcing.

The modelled and observed JJA mean rainfall and biases for Mexico and Central America are shown in Figure 4.8. The main feature is the East Pacific (EP) ITCZ which extends north to  $15^\circ\text{N}$  near the western coast of Mexico as a broad band of rainfall ( $>11 \text{ mm day}^{-1}$ ). The modelled EP ITCZ (Figures 4.8e, f, g) rainfall is overestimated by more than  $5 \text{ mm day}^{-1}$ , especially in GC3-amip. This wet bias is associated with a westerly bias in the low-level circulation, suggesting a weaker flow from the Caribbean into the East Pacific.

The North American Monsoon can be observed as a band of precipitation across western Mexico. In the core monsoon region, near the Sierra Madre Occidental (Adams and Comrie, 1997; Zhou et al., 2016), the JJA-mean rainfall is higher than  $8 \text{ mm day}^{-1}$ . The distribution of rainfall in the North American Monsoon region is relatively well represented in all the simulations, as only a moderate wet bias ( $+2 \text{ mm day}^{-1}$ ) in western Mexico is observed. The northernmost part of the North American Monsoon (southwestern US) is best simulated by GC3 N216-pi, as the other simulations show a dry bias in this region. The low-resolution simulations (Figure 4.8e) underestimate rainfall ( $-5 \text{ mm day}^{-1}$ ) over land in southern Mexico, Guatemala and Belize. Rainfall in the Caribbean islands and Florida is underestimated ( $-1 \text{ mm day}^{-1}$ ) in all simulations.

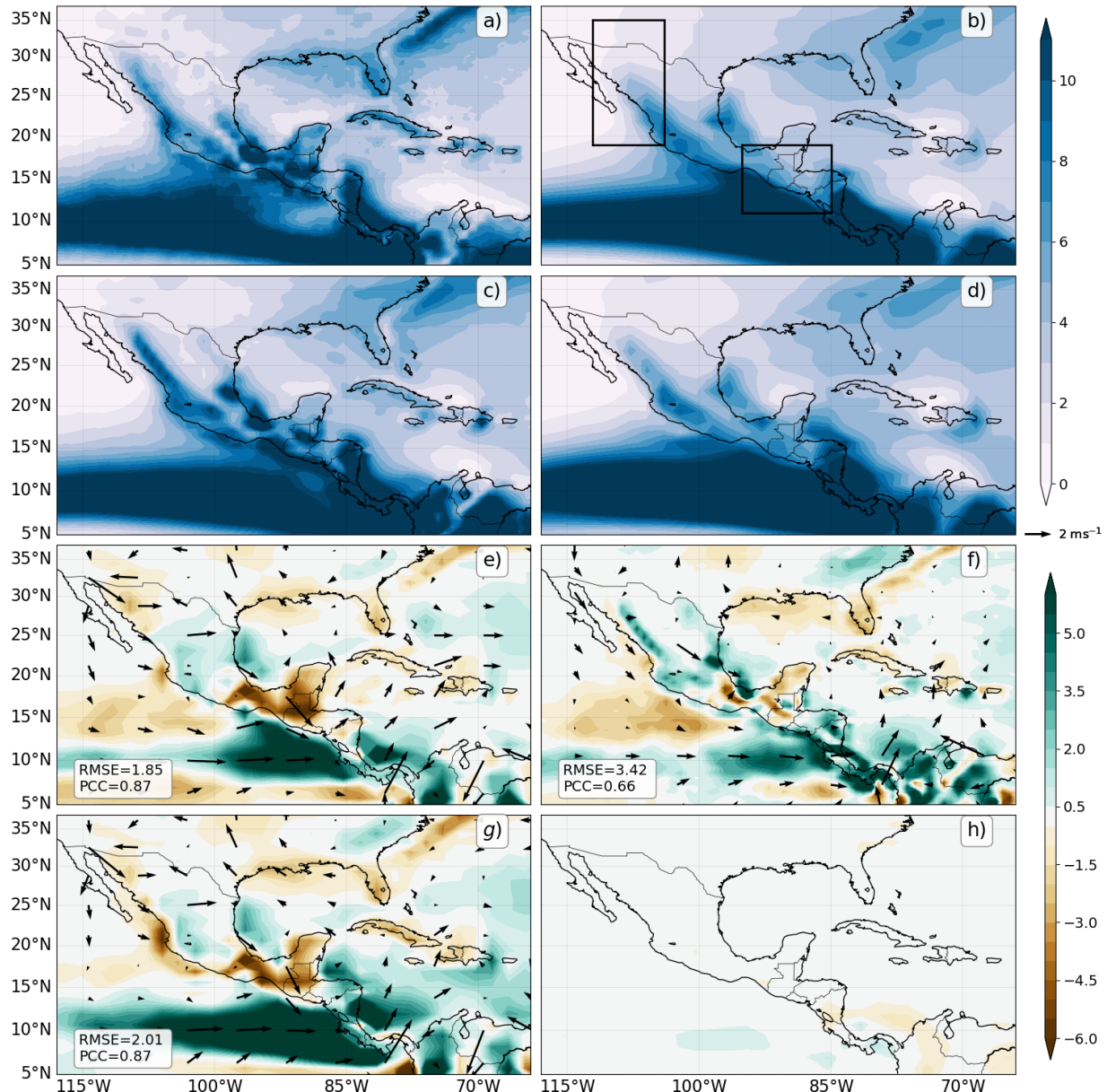


**Figure 4.8:** As in Figure 4.7 but for JJA in the northern part of subtropical America.

In most cases for JJA in this region, the precipitation and wind biases were reduced in the high-resolution simulation (Figure 4.8f) and little-to-no difference was observed between UKESM1-hist and GC3 N96-hist (not shown). The precipitation response to historical forcing is much lower than the biases (Figure 4.8h) with no significant precipitation differences over land due to the historical forcing.

#### 4.5.2 The annual cycle of rainfall

Figure 4.9 shows the seasonal cycle of rainfall at the pentad (5-day) scale over the North American Monsoon, the Midsummer drought (MSD), the Amazon and eastern Brazil regions. The correlation between TRMM and the model and reanalysis data (ERA5) is also shown in each panel. The seasonal cycle of precipitation in the MSD region in the simulations is well represented as all the simulations show the characteristic bimodal distribution, a feature that is uncommon for a climate model to be able to reproduce (Ryu and Hayhoe, 2014).

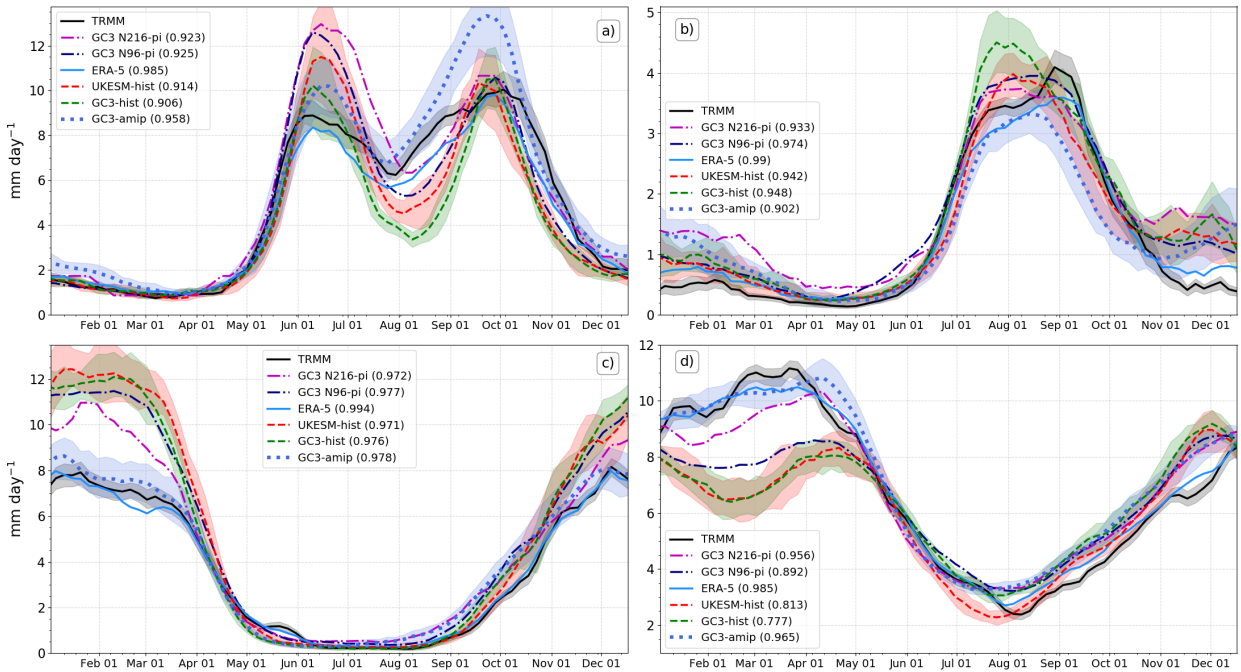


**Figure 4.9:** Annual cycle of pentad-mean rainfall in the regions (a) the Midsummer drought, (b) the North American Monsoon, (c) Eastern Brazil and (d) the Amazon Basin. The regions are defined as in Figure 4.3 and are illustrated in Figure 4.8b and Figure 4.9b. The shaded regions represent observational uncertainty for TRMM and ensemble spread for the historical experiments. The correlation coefficient for each of the simulated seasonal cycles with TRMM is given in brackets in each panel.

However, the characteristics of the simulated MSD are different from observations. For example, the magnitude of the first peak and second peaks in the simulations are different. For instance, most of the first peak simulated magnitudes are higher than TRMM by 4 mm day<sup>-1</sup>, and the AMIP simulation overestimates the second maximum of rainfall by 2-3 mm day<sup>-1</sup>. Similarly, the differences between the first peak and the MSD and between the MSD and the second peak are more pronounced in the coupled simulations. The timing of the MSD period is different in the models, as the simulations show the driest period taking place 10 days after TRMM and ERA5.

In the North American Monsoon (Figure 4.9b), the observed seasonal cycle is characterized by a very long and dry period ranging from the end of November to the start of June, which is followed by a sharp increase of rainfall around mid-June. The timing of the increase of rainfall in models coincides with observations, suggesting that onset timing and strength is well represented in these models. Moreover, the modelled and observed mean precipitation rates during monsoon maturity are 4 mm day<sup>-1</sup>, from mid-July until early September, which suggests notable ability of the models to reproduce the peak monsoon rainfall. The historical simulations show a shorter wet season characterised by an earlier retreat of the monsoon rainfall and, as in all the simulations a positive bias (+1 mm day<sup>-1</sup>) is found during late local fall and early winter, a feature that has been shown in these models in CMIP5 (Geil et al., 2013).

The seasonal cycle of precipitation in eastern Brazil is characterised by a very wet summer ( $\sim 8$  mm day<sup>-1</sup>) compared to a very dry ( $\sim 0.2$  mm day<sup>-1</sup>) winter (Figure 4.9c). Rainfall in TRMM and ERA5 increases steadily from austral spring (September) to a maximum found in early January ( $\sim 8$  mm day<sup>-1</sup>). Rainfall in this region decreases to  $\sim 6$  mm day<sup>-1</sup> by late March as the monsoon migrates northward and then sharply decreases in austral fall.

The models (Figure 4.9c) show a positive bias during monsoon maturity. This bias was found to be of +4 mm day<sup>-1</sup> and +2.5 mm day<sup>-1</sup> for the low and medium resolution simulations, respectively. This positive bias in the maximum rainfall is consistent with the biases shown in Figure 4.7, which showed that rainfall in southeastern Brazil is overestimated, especially in the low resolution coupled simulations. In contrast to the coupled simulations,

GC3-amip shows a very good agreement with the observed maximum summer rainfall and the seasonal cycle ( $r=0.978$ ) throughout the year.

Finally, the seasonal cycle in the Amazon (Figure 4.9d) has a weaker contrast as rainfall greater than  $2 \text{ mm day}^{-1}$  is found year-round. The coupled simulations show a dry bias during austral summer and a good agreement with the observations during austral winter. Rainfall rates in the Amazon from January to March, in both TRMM and ERA-5, is close to  $10 \text{ mm day}^{-1}$ , yet the low resolution simulations show rainfall rates of  $8 \text{ mm day}^{-1}$  in mid-February, particularly the historical experiments. GC3 N216-pi shows a better agreement with observations but still underestimates summertime rainfall by  $1 \text{ mm day}^{-1}$ .

This dry Amazon bias has been a known feature of GCMs, including the MOHC models, since CMIP3 (Li et al., 2006; Yin et al., 2013). In these simulations the dry Amazon bias is only alleviated in GC3-amip whose seasonal cycle and maximum summer rainfall agree well with observations suggesting that the Atlantic SST biases are the key factor for the biases in the Amazon in coupled model simulations. The models, however, represent with reasonable skill the timing of the transition from early austral spring ( $4 \text{ mm day}^{-1}$  in September) to summertime rainfall ( $6 \text{ mm day}^{-1}$  in November). After this description of the spatial and temporal variability of these biases in these models, the next section investigates how the models represent convection through diagnostics that may further

#### 4.5.3 Characteristics of convective activity

The seasonal cycles of outgoing long-wave radiation (OLR), vertical velocity ( $\omega$ ) and specific humidity ( $q$ ) are key features of a monsoon since these quantities characterise the strength and height of deep convection, as well as the moisture within the column. The pentad-mean annual cycle of OLR,  $q$  and  $\omega$  at the 500-hPa level in four regions of the AMS (Figure 4.10) are used as process oriented diagnostics to further evaluate the biases in the spatial distribution and seasonal cycle of rainfall.

For the North American Monsoon the seasonal cycle of OLR,  $q$  and  $\omega$  is relatively well represented in the simulations. During late boreal winter and early spring, OLR increases steadily as a result of surface warming. However, in early June, near the onset date (Douglas et al., 1993; Geil et al., 2013), OLR sharply decreases reaching a minimum

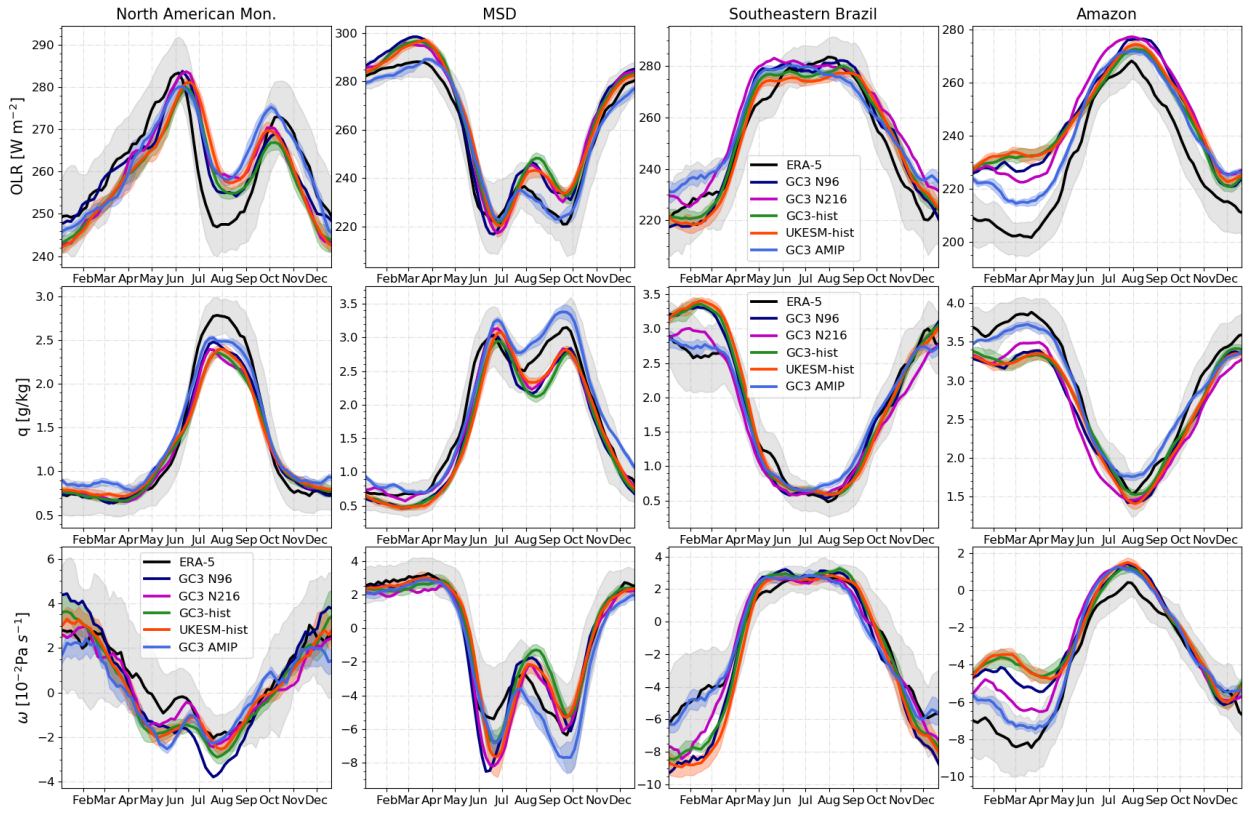


**Figure 4.10:** Pentad-mean (upper) outgoing long-wave radiation (OLR), (middle) specific humidity at 500-hPa and (lower)  $\omega$  500-hPa. These are shown from left to right for the North American Monsoon, the Midsummer drought, southeastern Brazil and the core Amazon. The uncertainty in ERA-5 data, shown as faint gray shading was estimating by bootstrapping with replacement the ERA-5 record 10,000 times.

value of  $246 \text{ W m}^{-2}$  by mid-July. The vertical velocity decreases steadily from January to a minimum in August, indicating ascent from May 1st until September 15th. The models show similar seasonal cycles but overestimate the summertime OLR by  $\approx 6 \text{ W m}^{-2}$  and underestimate mid-level moisture by  $0.3 \text{ g/kg}$  and  $\omega$  by  $0.01 \text{ Pa s}^{-1}$  which is about 5-10% overall. The simulated shallower convection and drier mid-troposphere is seemingly compensated by stronger mid-level ascent.

In the MSD region, OLR and  $q$  show signs of convective activity from mid-April, as OLR sharply decreases and moisture increases. The characteristic MSD bimodal distribution of precipitation can also be observed as two troughs of OLR, and  $\omega$  and two peaks in  $q$ . These periods are separated by a period of relatively higher OLR, lower  $q$  and weaker ascent from June 15 until late August. Although arguably with a small dry bias with shallower

convection after mid-July, the simulations follow closely the observed seasonal cycle.

The simulated conditions during the first peak period show similar OLR and mid-level moisture but stronger ascending motions, which may explain the positive rainfall bias in this period showed in Figure 4.9a. In the period between the first peak and the MSD, the simulated OLR increases more sharply than observations from  $220 \text{ W m}^{-2}$  (June 15) to  $250 \text{ W m}^{-2}$  (early August), with similar behaviour in  $\omega$  and  $q$ , which may also be related to the strong MSD precipitation differences described in the previous section. The period during the second peak of rainfall in September shows signs of shallower convection and a drier mid-level when compared to ERA5.

In southeastern Brazil, the simulations reasonably follow the timings of the annual cycle of OLR,  $q$  and  $\omega$  of the reanalysis, particularly during austral winter. The moisture  $q$  in ERA5 during the dry seasons of austral fall, winter and spring is reasonably simulated by all the experiments. However, during austral summer, the coupled model simulations show significant biases characterised by stronger ascent and increased specific humidity in the mid-levels, although the height of convection (OLR  $225 \text{ W m}^{-2}$ ) is only modestly higher in the simulations.

The simulated OLR,  $q$  and  $\omega$  exhibit the highest biases in the Amazon. During austral summer, particularly January and February, the simulated convective activity is shallower (OLR bias of  $+25 \text{ W m}^{-2}$ ) and weaker (positive  $\omega$  bias  $+0.02 \text{ Pa s}^{-1}$ ) and the mid-level troposphere is drier ( $-0.5 \text{ g/kg}$ ) than in ERA5. All these biases are in agreement with the dry Amazon bias described in the previous section. In spite of biases in the magnitude of OLR,  $q$  and  $\omega$  during peak convective activity, the seasonal variation is very well simulated so that convective activity, as evidenced by these metrics, starts and ends in the simulations within one or two pentads of the reanalysis. The smallest biases in coupled simulations are those of GC3 N216-pi, not just for the Amazon region but for the other regions as well. The simulated OLR,  $q$  and  $\omega$  in GC3-amip in southeastern Brazil and the Amazon show a much better agreement with the reanalysis during austral summer than the rest of the simulations.

This section describes biases in the seasonal cycle of diagnostics intimately related to convection such as top cloud height, vertical velocity and moisture. While precipitation is fairly well represented in the North American monsoon in this region, the models

represent stronger but shallower ascent indicating that competing biases lead to a right representation of precipitation.

## 4.6 ENSO Teleconnections

El Niño-Southern Oscillation (ENSO) teleconnections are the prominent source of interannual variability for the AMS (Vera et al., 2006), as summarized in section 2.4. The response to ENSO events in UKESM1 and HadGEM3 is investigated in this section, which first shows the temperature, sea-level pressure (SLP) and precipitation responses to observed and simulated ENSO events in the AMS, and then analyses of the effect of ENSO flavours on the AMS. Finally, results show a possible influence of the QBO on the teleconnections of ENSO.

### 4.6.1 Canonical teleconnections

The surface temperature and sea-level pressure (SLP) responses to ENSO events are shown in Figure 4.11 for HadGEM3, UKESM1 and ERA5 data during DJF, the season of strongest impact of ENSO events. The characteristic warm anomaly during El Niño events in the East Pacific Ocean does not extend as far east in the simulations as in the HadSST dataset or ERA5. In turn, the cold anomalies during La Niña events in the Central Pacific are colder in the simulations than in ERA5. The teleconnection to southern North America, i.e., colder (warmer) conditions in southern (northern) North America during El Niño events is relatively well simulated. For example, the simulated and observed teleconnection patterns to South America, e.g., the cold anomalies during La Niña events in northern South America are well simulated. However, the low resolution simulations show a broader and stronger than observed negative response in southeastern US to El Niño events.

The SLP response in the north Pacific and North America, known as the Pacific North-American pattern (PNA), is linked with a displacement of the subtropical jet affecting the eastward propagation of wave activity that reaches the North Atlantic (e.g. Bayr et al., 2019; Jiménez-Esteve and Domeisen, 2020). During El Niño events, the Aleutian Low is strengthened in ERA5, with a strong SLP anomaly (-4 hPa) off the coast of California. The models show a similar but smaller SLP response in the same region. El Niño events events are

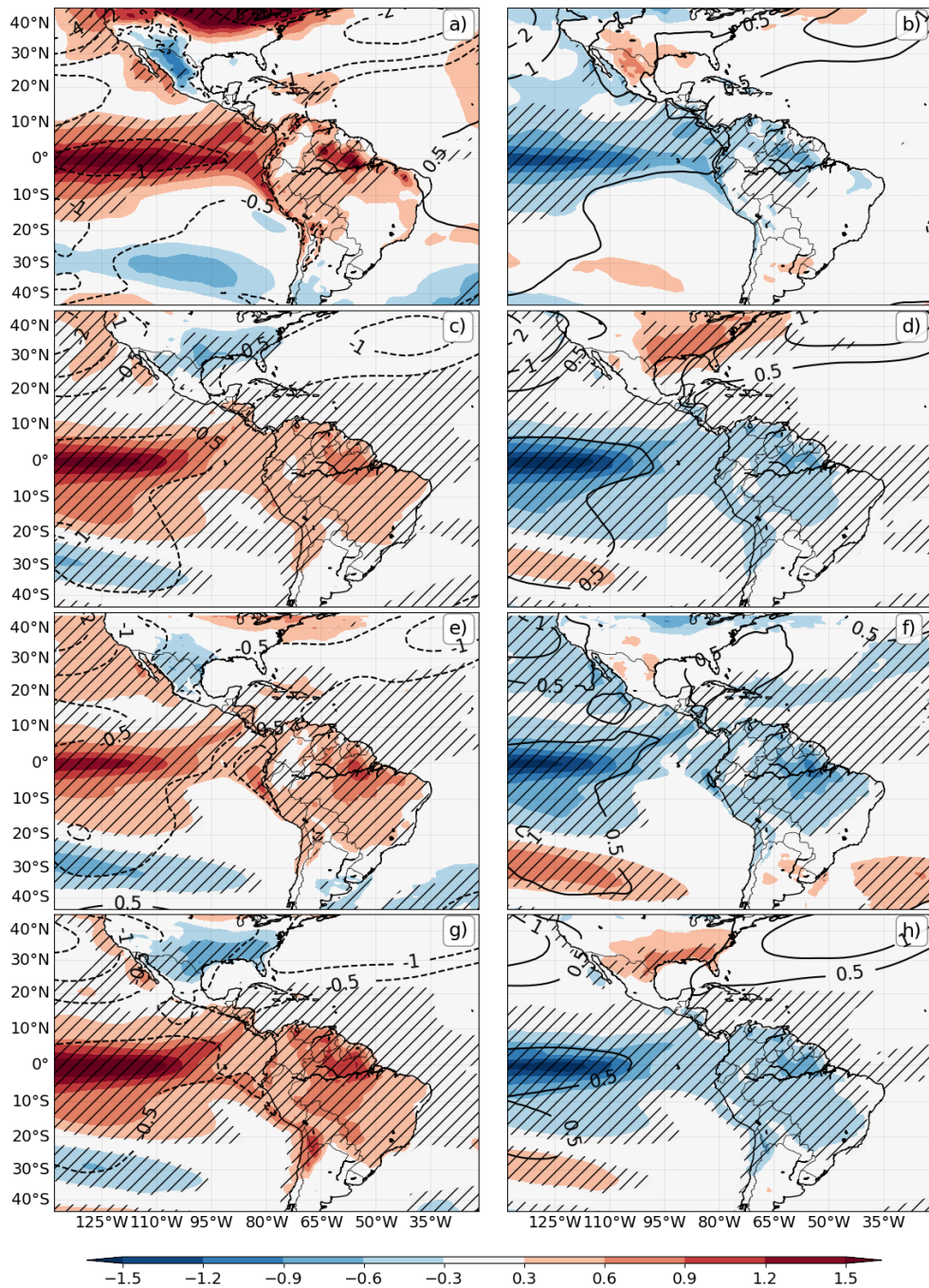


**Figure 4.11:** DJF Temperature anomalies (colour contours in K) and SLP (line contours in hPa) during (a, c, e, g) El Niño and (b, d, f, h) La Niña events. Results are shown for (a, b) ERA-5, (c, d) UKESM1-hist, (e, f) GC3 N96-pi and (g, h) GC3 N216-pi. The hatched regions denote differences between ENSO phases and the climatological state with significance to the 99% confidence level from a Welch t-test for the temperature field.

associated with a negative phase of the North Atlantic Oscillation (NAO), with an opposite response for La Niña events. While the models seem to be able to capture this response of

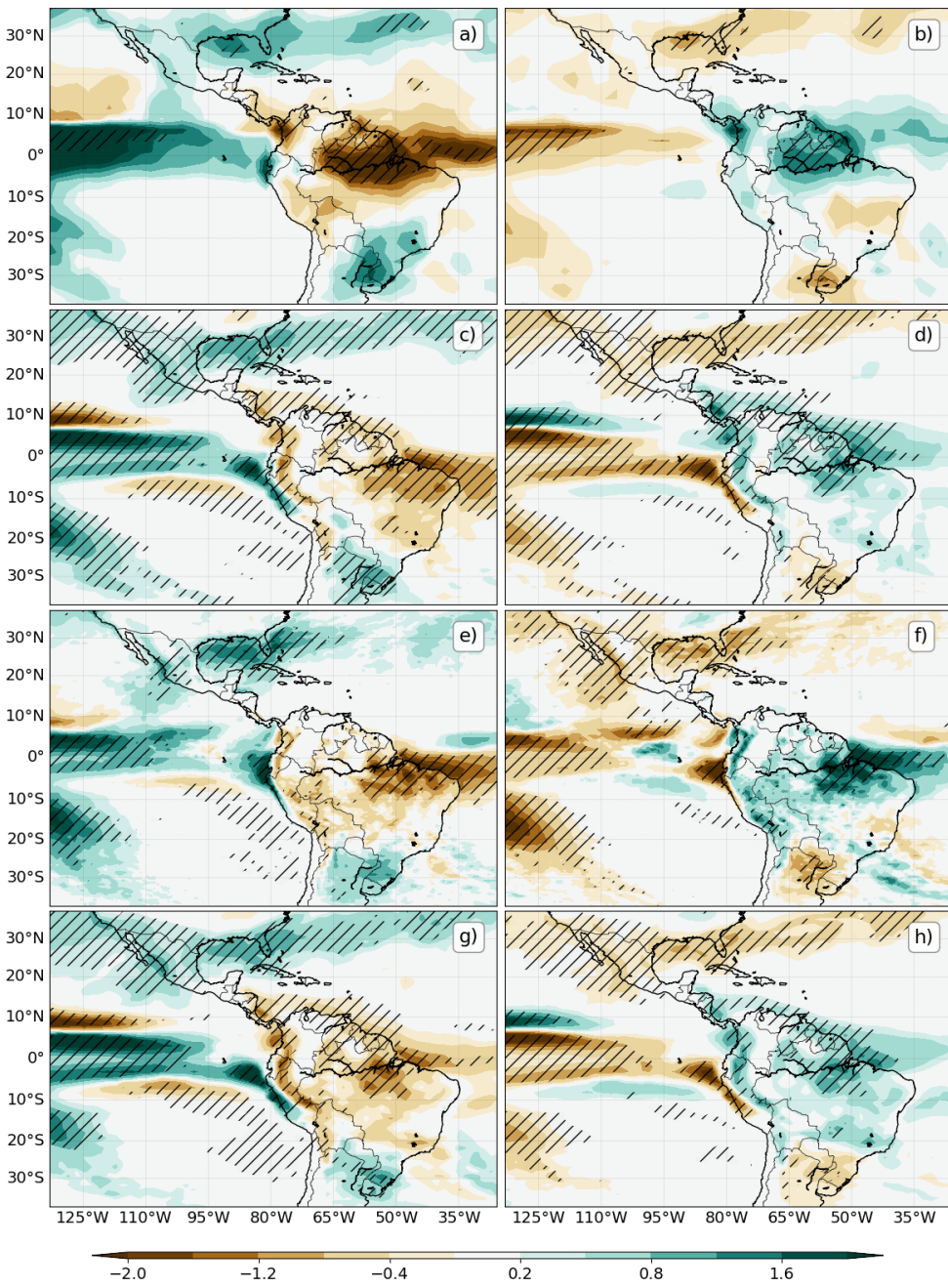


**Figure 4.12:** As in Figure 4.11 but for the rainfall response [ $\text{mm day}^{-1}$ ] using GPCP as the observational dataset.

the NAO, the simulated response is weaker than observed. A sensible representation of the ENSO-NAO tropospheric teleconnection may be relevant to then simulate the effect of the NAO on Central American and northern South American rainfall (Giannini et al., 2000, 2004).

The rainfall anomalies associated with ENSO events are shown in Figure 4.12. Three

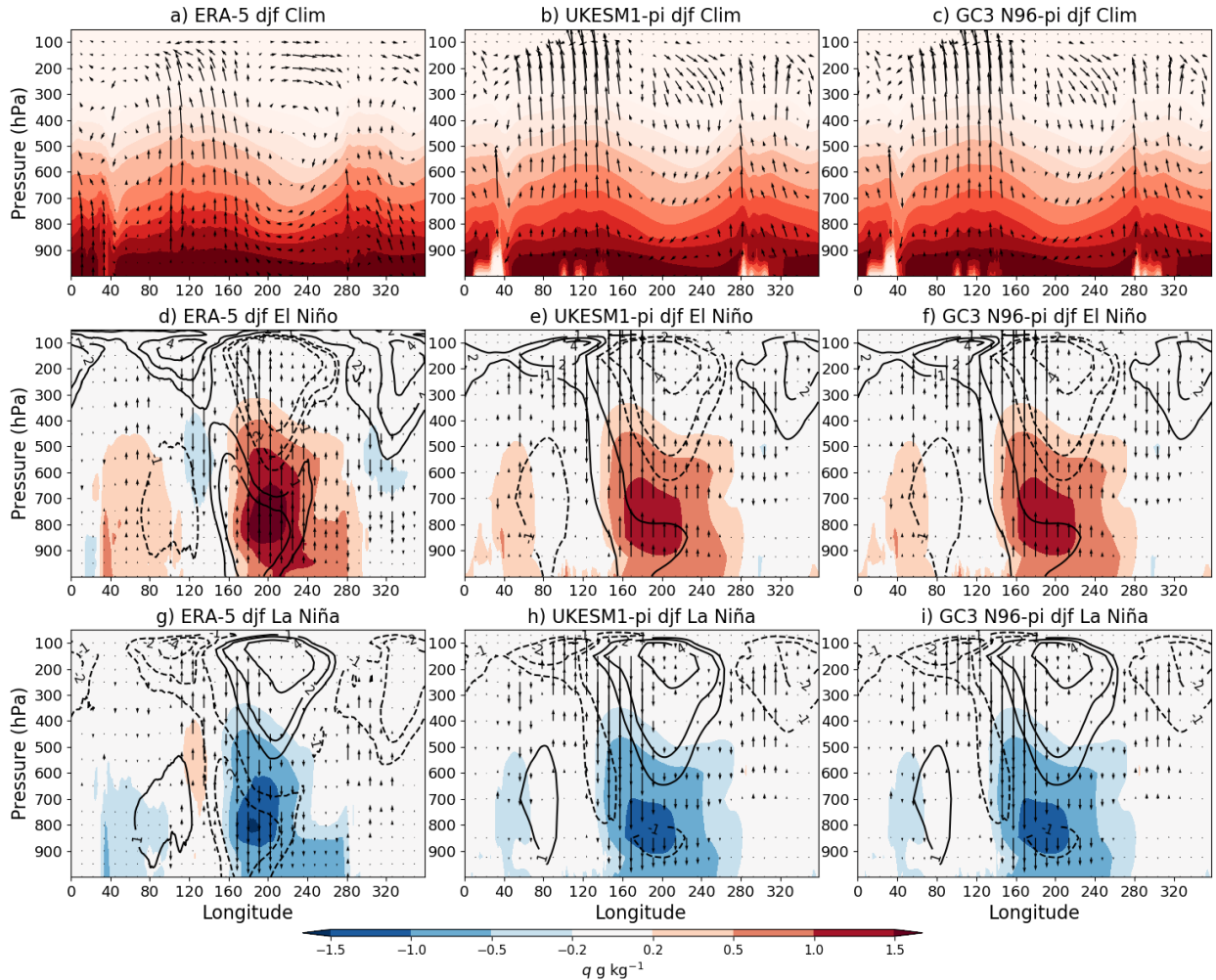


**Figure 4.13:** DJF Longitude-height Walker circulation anomalies of specific humidity (colour-contours),  $\omega$  (vectors) and zonal wind (line-contours) during El Niño events (left) and La Niña events (right). Results are shown for ERA-5 (upper), UKESM1-pi (middle) and HadGEM3 piControl (lower).

regions in the AMS have a significant precipitation response to ENSO events in the observations and simulations. In southern North America, rainfall increases (decreases) during El Niño (La Niña) events due to the effects of the PNA pattern on the subtropical jet, which influences the frequency and latitude of propagation of wintertime midlatitude disturbances which are the main source of rainfall in the region during the dry season (Vera et al., 2006; Bayr et al., 2019).

The GPCP dataset (Figure 4.12a, b) shows significant boreal winter rainfall increases in southeastern US and the Gulf of Mexico during El Niño events, and an opposite response to La Niña phases. All the simulations reproduce this teleconnection rainfall pattern. The

models also simulate the observed response in southeastern South America (SESA) of positive anomalies during El Niño and negative anomalies during La Niña events. This teleconnection to SESA is associated with the effect of ENSO on the sub-tropical jet in the Southern Hemisphere, the South Pacific and Atlantic Convergence Zones.

The anomalies in the Amazon show the strongest response to ENSO events in the observations. Significant positive (negative) rainfall anomalies during the negative (positive) phase of ENSO in northern South America are observed in GPCP. All the simulations show a very similar and statistically significant response. This teleconnection works through the coupling of ENSO with the Walker circulation (Vera et al., 2006; Cai et al., 2019), which is illustrated in Figure 4.13.

The climatological Walker circulation during DJF shows strong ascent in the 100-160°E and the 280-310°E regions, which correspond to the maritime continent and South America (Figure 4.13a). During El Niño events, there is increased specific humidity throughout the lower troposphere in the Central and Eastern Pacific, associated with ascending motions in this region and negative low-level wind anomalies and positive upper-level wind anomalies (Figure 4.13d). In other words, an eastward shift of the Walker circulation. The wind, vertical velocity and specific humidity anomalies are the opposite during La Niña events, indicative of a stronger Walker circulation, slightly shifted to the west. The models seem to broadly reproduce the observed changes to the Walker circulation during ENSO events (Figure 4.13).

Figure 4.14 shows the observed and simulated precipitation responses in four regions of the AMS to different magnitudes of ENSO events, by binning events for their magnitude of the EN3.4 index and the corresponding precipitation anomaly from the climatology in each region. This figure aims to show the degree of linearity of ENSO teleconnections to the AMS. While the observed response shows some degree of linearity for El Niño events in South America (panels c, d), the majority of the observed responses, particularly to La Niña phases, are not linear.

However, the simulations show several signs of linearity. For instance, consider the historical experiments, UKESM1-hist and GC3 N96-hist, which show that the precipitation responses in southwestern North America, SESA and the Amazon increases roughly linearly

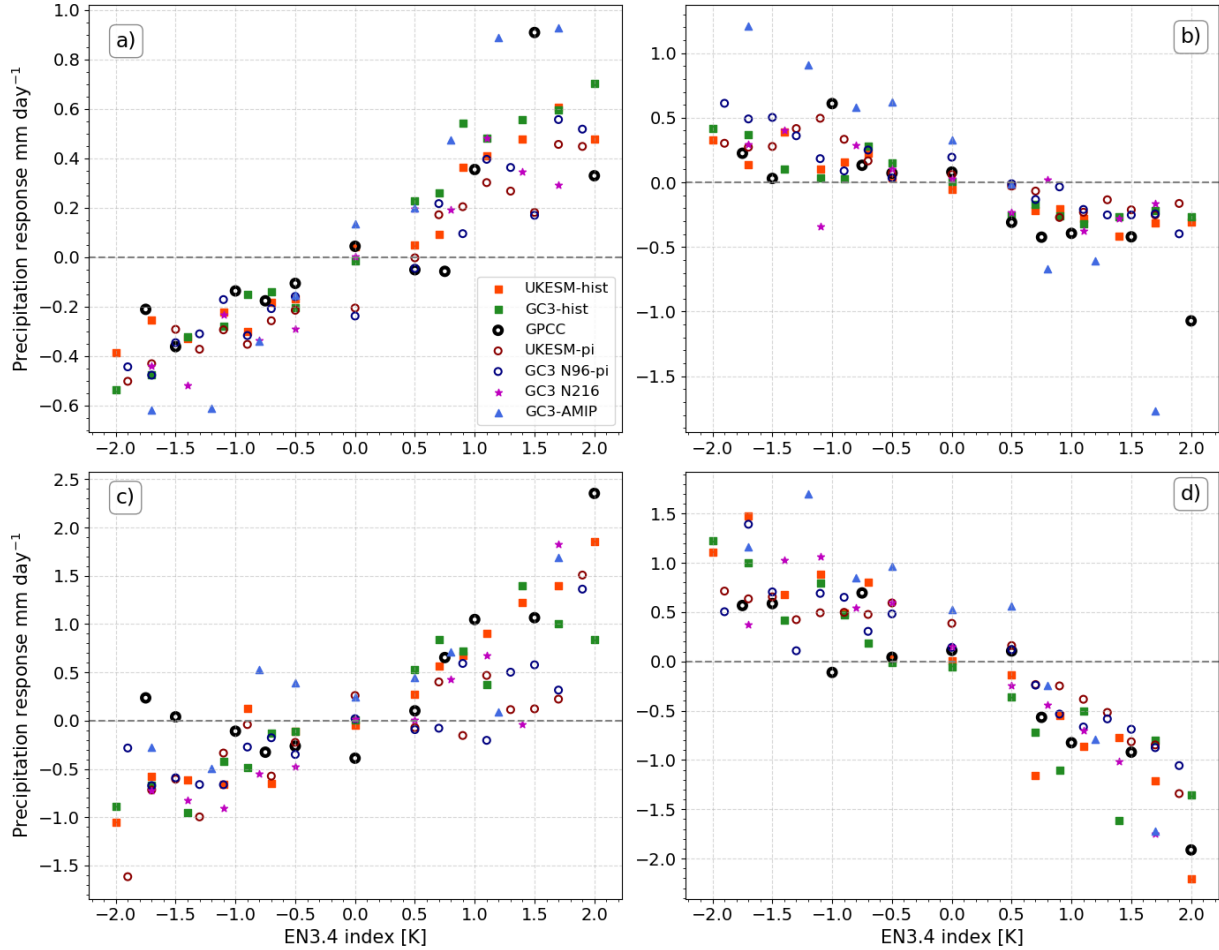


**Figure 4.14:** Precipitation response [ $\text{mm day}^{-1}$ ] as a function of the El Niño 3.4 index (see text) for (a) southwestern North America [ $20\text{-}37^\circ\text{N}, 112\text{-}98^\circ\text{W}$ ], (b) Central America and southern Mexico [ $5\text{-}19^\circ\text{N}, 95\text{-}83^\circ\text{W}$ ], (c) South Eastern South America [ $35\text{-}25^\circ\text{S}, 60\text{-}50^\circ\text{W}$ ], and (d) the Amazon [ $10\text{-}0^\circ\text{S}, 70\text{-}45^\circ\text{W}$ ]. The observation scatter points are from GPCC in the period of 1940–2013.

as the magnitude of SST anomaly increases. In contrast, some other simulated responses, e.g. to La Niña phases in South America in the piControl simulations, show signs of non-linearity.

#### 4.6.2 The role of ENSO flavours

As described in section 2.4, not all ENSO events are observed with the same SST anomaly pattern in the Pacific Ocean. These different SST patterns for each ENSO event are considered to be a source of non-linearity of ENSO impacts over South America (Sulca et al., 2018; Cai et al., 2020). Principal component analysis has shown that ENSO events may be separated into two categories: Central Pacific (CP) and East Pacific (EP) events (Cai et al.,

2020), which highlight where the peak SST anomaly is found in the Pacific Ocean. Figure 4.15 shows that both UKESM1 and GC3 reasonably simulate the observed SST patterns associated with EP and CP El Niño events, although the simulations show CP SST patterns to spread further to the east than the HadSST dataset. The simulations are also able to replicate very broadly the observed differences in the frequency of each event as CP La Niña events are more frequent than EP La Niña events, while the opposite is true for El Niño events.

Furthermore, Figure 4.16 compares the precipitation anomalies for each type of ENSO event in observations with three simulations: GC3 N96-pi, GC3 N216-pi and GC3-amip. The

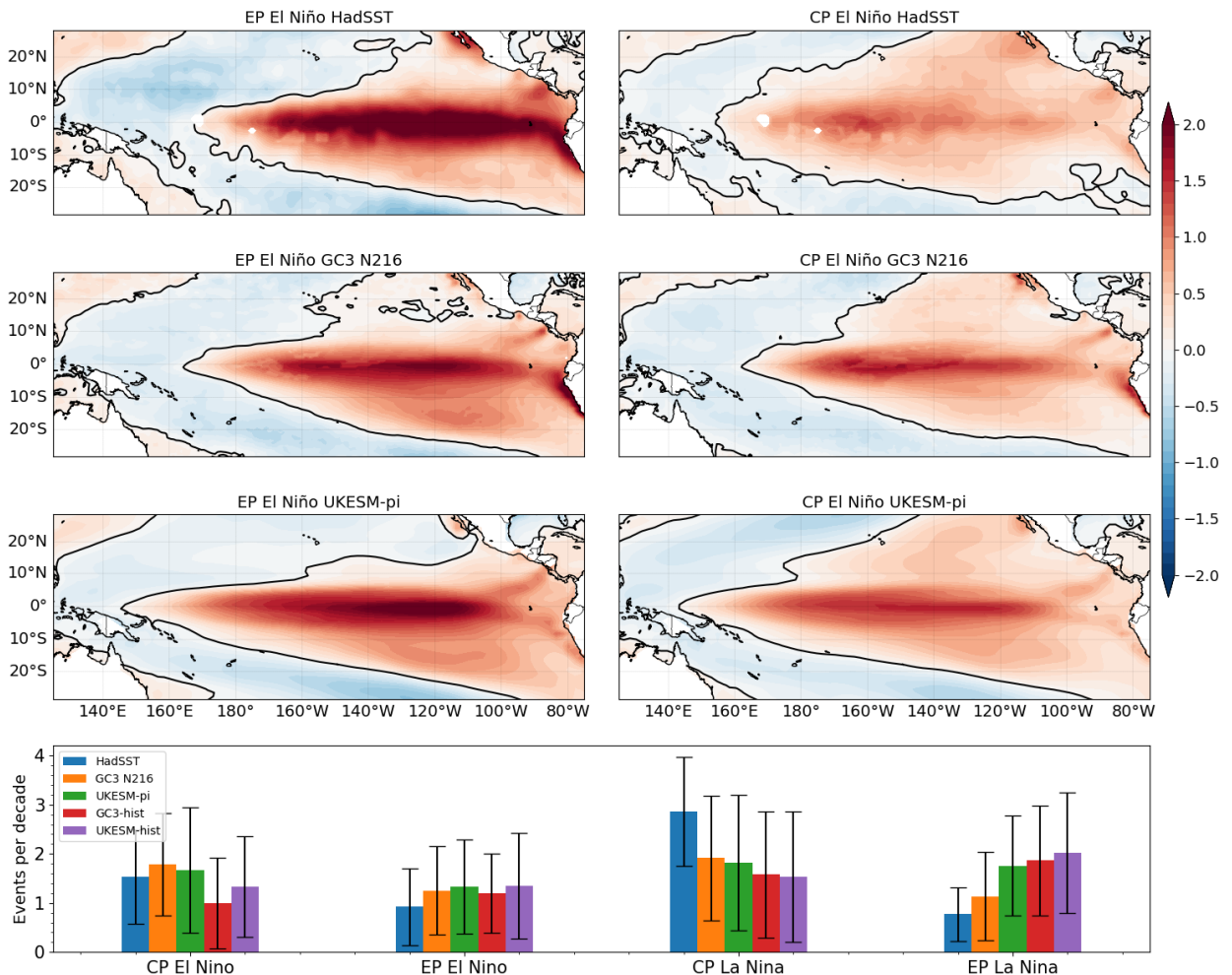


**Figure 4.15:** SST anomalies [K] for East Pacific (EP) and Central Pacific El Niño events in HadSST, GC3 N216 and UKESM piControl. EP (CP) events were defined where the E-index (C-index) was greater than 1. In the bottom panel, the frequency of events per decade (with standard deviation as error bar) is shown for HadSST and the simulations used in this study. The E-index is computed from  $(PC1 - PC2)/\sqrt{2}$  and the C-index from  $(PC1 + PC2)/\sqrt{2}$ .

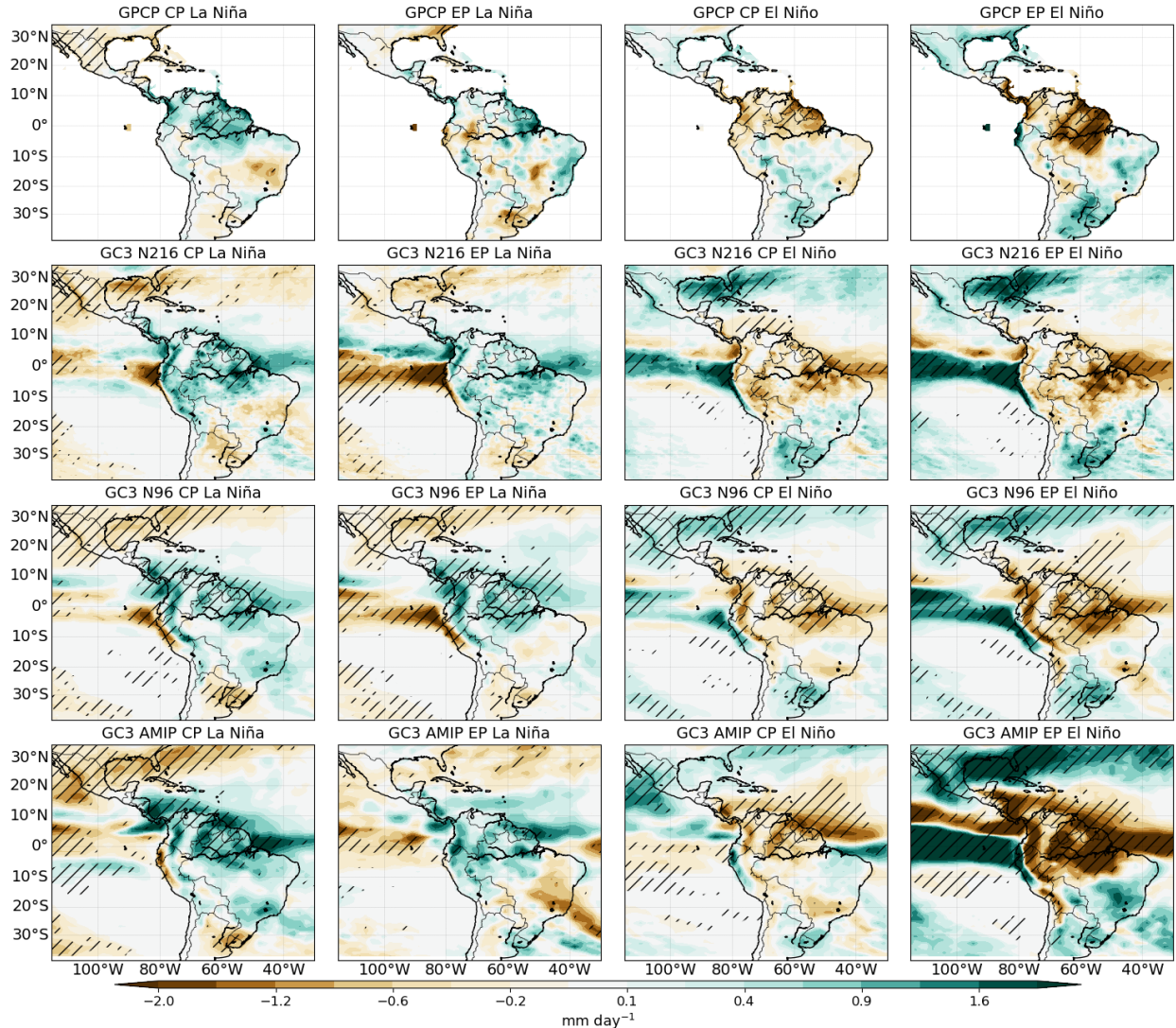


**Figure 4.16:** Precipitation anomalies in GPCC 1940-2013, GC3 N216-pi, GC3 N96-pi and GC3 AMIP for the four different types of ENSO events, as defined by Cai et al. (2020). Statistically significant anomalies (95% confidence level) are hatched.

observed precipitation response in the GPCC dataset to EP La Niña over equatorial South America is not significant and is smaller than the strong positive response to CP La Niña events in the same region. However, the simulated response in GC3 N96-pi and GC3 N216 during La Niña events appears to be more independent of the type of event. In contrast, the GC3-amip simulations shows different magnitudes of responses to different types of La Niña events, in particular a positive, and significant, anomaly for CP La Niña events in the Amazon and weaker but not significant anomalies during EP events, which agrees with observations.

The observed response to El Niño events in GPCC is also dependent on the type of

event. EP El Niño events show significant negative anomalies over the Amazon and positive anomalies over SESA whereas CP events only show significant anomalies ( $-1 \text{ mm day}^{-1}$ ) over northeastern South America. While the coupled models (GC3 N96-pi and GC3 N216) do show a stronger response to EP El Niño events than to CP events, the patterns of the response are very similar. In contrast, the response in GC3-amip agrees with observations, as stronger negative responses to EP El Niño events are observed in the Amazon compared to CP events in which the response is much weaker and is only significant in northeastern South America. In other words, GC3-amip agrees well with the observed non-linear teleconnection patterns whereas the teleconnections in the coupled models do not seem to depend on the type of ENSO event.

#### 4.6.3 A possible influence of the QBO on tropical ENSO teleconnections

Section 2.5 discussed the observational and modelling evidence of the effects on deep convection associated with the stratospheric quasi-biennial oscillation (QBO). In particular, some evidence suggest that the QBO may play a role to determine interannual variability of the Walker circulation and monsoons (Giorgetta et al., 1999; Collimore et al., 2003; Liess and Geller, 2012).

This section evaluates whether the simulations analysed in this chapter, as well as observations, show signs of an influence of the QBO on the AMS. In particular, the analysis aims to understand whether the QBO may be a source of non-linearity for the teleconnections of ENSO associated with deep convection and the Walker circulation. In all cases, the phases of the QBO were defined using a 70 hPa zonal mean zonal wind index, with a threshold of  $+2 \text{ m s}^{-1}$  for the westerly phase (QBOw) and  $-2 \text{ m s}^{-1}$  for the easterly phase (QBOe).

Composites of the precipitation response to La Niña (LN) events in Figure 4.17 show that the phase of the QBO may determine the strength and location of the teleconnection. While the precipitation difference in the western Pacific is relatively similar during QBOe than during QBOw in observations and simulations, the teleconnections to Australia, South America and the maritime continent are notably different depending on the QBO phase. In the GPCP dataset, the composite difference QBOe-QBOw during LN events suggests

that the characteristic positive precipitation response during LN events in the Amazon, is largely associated with QBOw phases, whereas LN events during QBOe appear to have

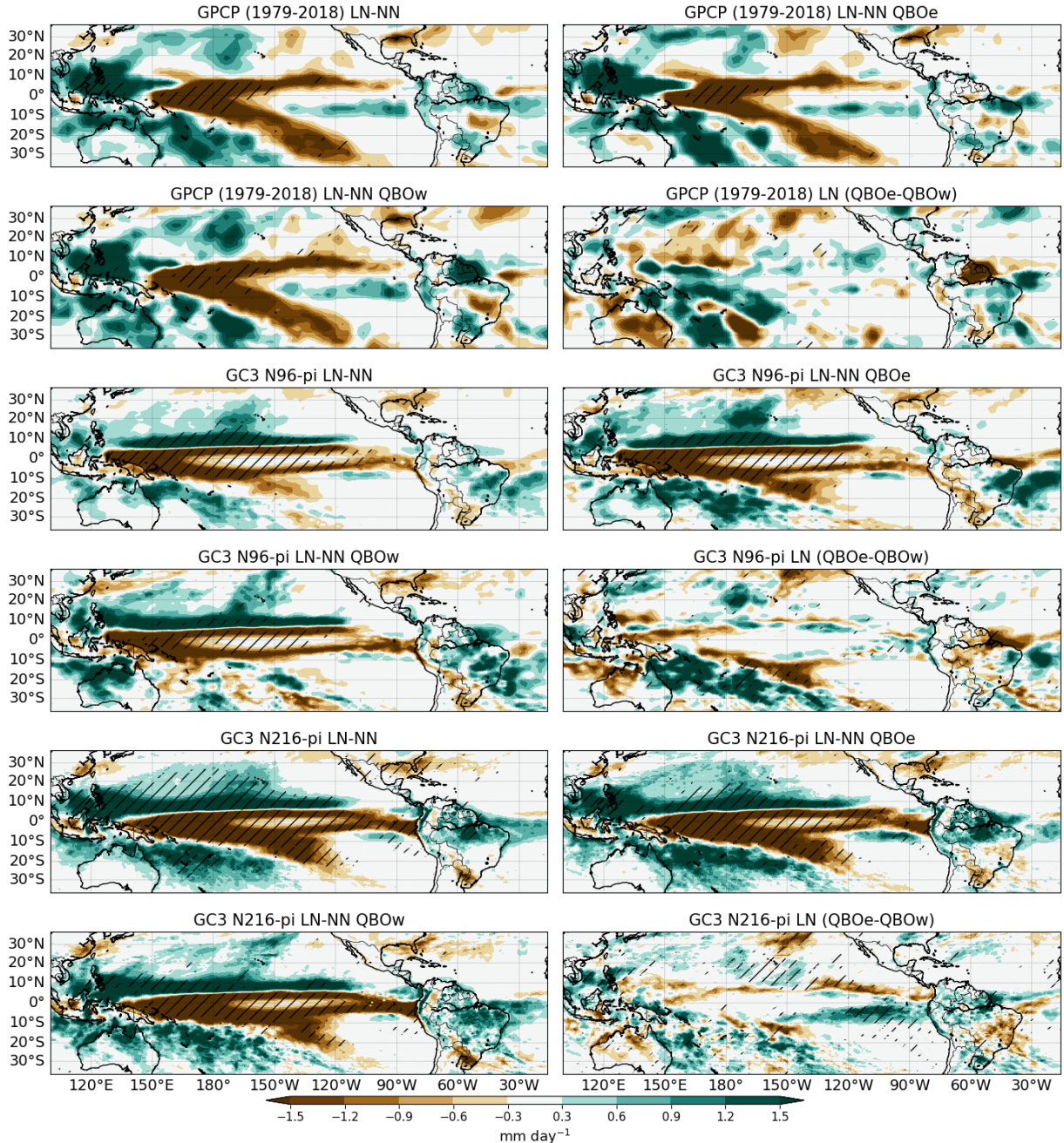


**Figure 4.17:** Composite precipitation differences during JFMA in GPCP (1979-2018), GC3 N96-pi and GC3 N216-pi between (top) La Niña and Neutral ENSO conditions. The two middle panels show a subset of the top panel, by separating the La Niña composite based on the phase of the QBO. The lower panel shows the differences QBO E-W during La Niña periods. Statistically significant anomalies (95% confidence level) are hatched.

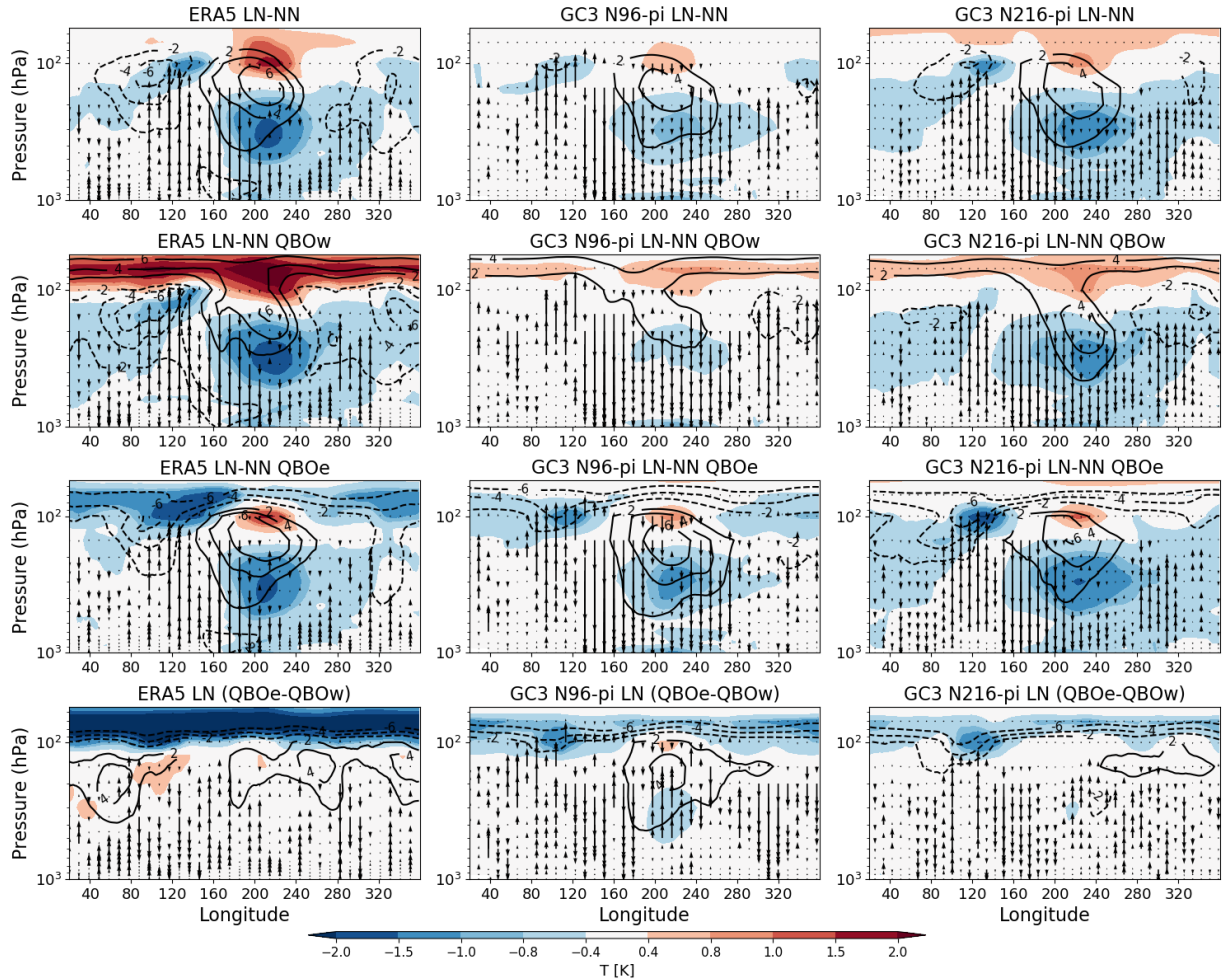


**Figure 4.18:** Longitude-height differences (JFMA) of equatorial (10S-10N) air temperature (color shading), zonal wind (contours) and vertical velocity ( $\omega$  - vectors). The differences shown from top to bottom are between all La Niña (LN) periods and Neutral conditions (NN), between LN and NN during QBOw, LN-NN during QBOe, and the difference between LN events on different QBO phases (LN QBOe-QBOW).

little effect over South America. A similar result is obtained for GC3 N96-pi.

These precipitation responses are further investigated by changes in the overturning circulation (Figure 4.18). As depicted in Figure 4.13, La Niña events are associated with a westward shift in the Walker circulation with a strengthening of the low-level easterlies in the Pacific Ocean. Figure 4.18 shows that during LN the tropical troposphere cools and the UTLS region in the Central Pacific warms. These temperature anomalies are weaker in the simulations than in ERA5.

The zonal wind anomalies in the upper-troposphere associated with LN events show

different patterns and strengths during QBOw than during QBOe. The mean teleconnections during LN show positive upper-tropospheric anomalies above the Pacific Ocean, but these anomalies are stronger during QBOe than during QBOw in ERA5 and the two simulations shown. In ERA5, most of the upper troposphere shows positive zonal wind differences in the QBOe-QBOw panel.

There are three regions where ascending and descending motions are more greatly affected by LN events: the maritime continent, the Pacific Ocean and South America. The observed effect of the mean LN teleconnection is the following: anomalous ascent is seen in the maritime continent and in South America, in agreement with a stronger Walker circulation, whereas anomalous descending motions is observed in the Central and eastern Pacific associated with a westward shift of the Walker circulation.

The effect of LN over ascending and descending motions is seemingly also affected by the QBO phase, according to the bottom panels of Figure 4.18. In ERA5 and the simulations, the anomalous ascent observed in South America during LN events is mostly associated with QBOw, whereas only small anomalous ascent is observed during QBOe. However, ERA5 disagrees with the simulations in the western Pacific region (140-180E), as the simulations suggest larger anomalous descent during QBOe than during QBOw, whereas in ERA5 these descending anomalies are larger during QBOw.

A similar analysis was conducted to evaluate the effect of the QBO during the positive and the neutral phases of ENSO. These results are not shown because, although tentative suggestions were found that the QBO may play a role during these other phases of ENSO, there was little agreement between the models and ERA5/observations. Furthermore, the QBO representation in these CMIP6 models is biased in the UTLS region. In particular, the temperature signal associated with circulation of the QBO, most clearly seen in the bottom panels of Figure 4.18, is much weaker in the models.

As suggested by the literature summarised in section 2.5, this temperature signal could be the key aspect of any effect of the QBO on deep convective systems, and as such, the evidence from a short record (ERA5) or models with key biases in possible processes involved presented in this chapter warrants both caution and more work. This topic will be investigated in the next chapters.

## 4.7 Summary and discussion

This chapter assessed the MOHC models, HadGEM3 and UKESM1, in their pre-industrial control, historical and AMIP experiment contributions to CMIP6 with specific emphasis on the AMS and associated large-scale tropical circulation. These CMIP6 experiments allow the assessment of the effect of including Earth System processes or increasing resolution for representing regional monsoon rainfall. A schematic in Figure 4.19 shows the primary components of the AMS climate and summarises the main biases found in these simulations and this chapter.

Rainfall in the North American Monsoon was particularly well simulated by the models. The seasonal cycle, peak monsoon rainfall rates and timings of monsoon onset and retreat in the simulations agreed well with TRMM. The historical experiments overestimate the mean temperature in most of the Americas by 1.5 K, but particularly in boreal summer in southwestern North America (+4 K). In spite of this warm bias, the temperature seasonal cycle is well represented by these models.

These results suggest model improvement of the simulation of the North American Monsoon from previous versions of the MOHC models (Arritt et al., 2000), and most of the model cohorts of CMIP3 and CMIP5 (Geil et al., 2013). For example, most of CMIP5 models showed a very wet bias during monsoon maturity whereas rainfall during monsoon maturity in all the experiments of this chapter are within less than 1 mm day<sup>-1</sup> of observations, during the maturity stage. However, these models continue to show biases during monsoon retreat as rainfall does not decrease as sharply as in observations after mid-September, which suggests a continued bias in the winter-time precipitation associated with cold-fronts (Adams and Comrie, 1997). Further research into variability of the North American seasonality may be explored using these models given their skillfull representation fo the seasonal cycle.

The Midsummer Drought (MSD) of southern Mexico and Central America is a regional feature of precipitation that most of CMIP5 models had difficulty capturing, with the MOHC models being amongst the few exceptions (Ryu and Hayhoe, 2014). The MSD in UKESM1 and GC3 continues to be relatively well represented; however, the experiments analysed

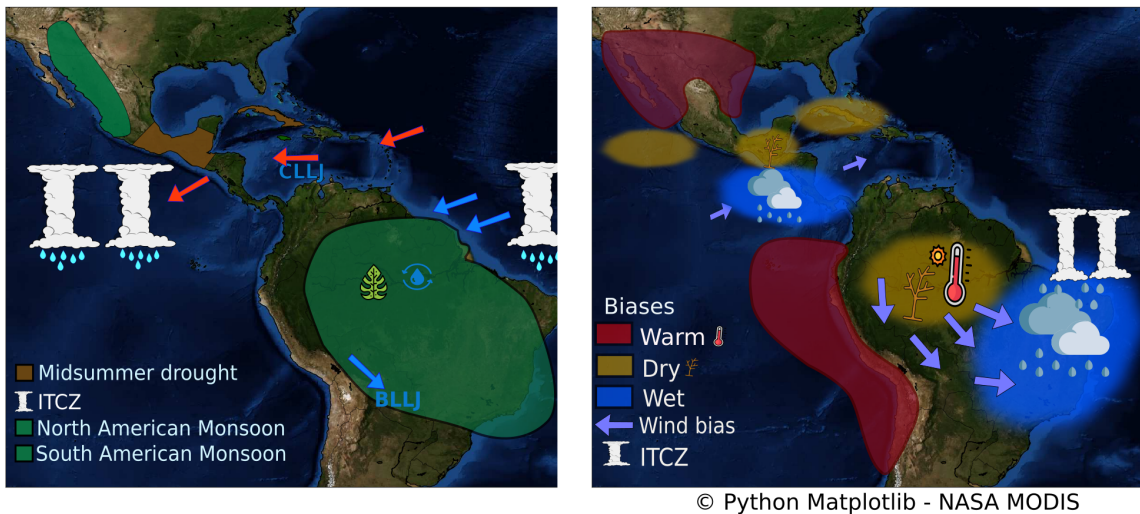


**Figure 4.19:** Schematics of (a) the main features in the AMS and (b) the main biases in UKESM1 and HadGEM3. In (a) the boreal summer easterlies (red) and austral summer circulation (blue) are shown with the Caribbean and Bolivian Low-level Jets (CLLJ and BLLJ, respectively). In (b) the biases are shown for the respective northern and southern Hemisphere summers. The ITCZ bias in (b) refers to the southward displacement bias of the Atlantic ITCZ in the simulations.

in this chapter showed various differences in the timing and strength of the bimodal cycle when compared to observed gridded-datasets and ERA5.

The models simulate a wetter-than-observed first peak of precipitation and a drier MSD period, therefore simulating a larger difference between the first peak and the dry period. While in observations this difference between the first peak and the MSD period ranges between  $2\text{-}3 \text{ mm day}^{-1}$ , in the simulations the difference is closer to  $6 \text{ mm day}^{-1}$ . Rainfall during the first peak has been too wet in these models since CMIP3, suggesting a persistent wet bias in this region, likely associated with the bias in East Pacific ITCZ also shown in this chapter and in recent studies (Ryu and Hayhoe, 2014; Mulcahy et al., 2018). In contrast, the so-called second peak of precipitation, observed in late August, is simulated in close agreement with TRMM, except in the AMIP experiment, which has a wet bias of  $2 \text{ mm day}^{-1}$  at this stage.

The skill of UKESM1 and HadGEM to simulate the MSD's bimodal regime of precipitation makes these simulations ideal to understand the mechanisms underpinning the MSD and why the MOHC models are able to represent a MSD regime but other models fail. Furthermore, section 2.3 discusses several open questions regarding the mechanisms that cause the observed

MSD. These simulations will then be used in future chapters to address the evaluate previous hypotheses of the causes for the MSD.

The East Pacific ITCZ migration and position was shown to be relatively well represented by the models (Figs. 4.4 and 4.5). However, the models showed an overestimation of boreal summer rainfall near the coast of Central America (Figure 4.9). These biases are associated with an easterly wind bias at low-levels, suggesting a bias in the flow from the Caribbean Sea into the Eastern Pacific (Herrera et al., 2015; Durán-Quesada et al., 2017). The simulations also showed a biased Atlantic ITCZ that was displaced south of the observed ITCZ position during boreal winter (Figure 4.5), particularly in the low resolution coupled simulations.

In the Amazon, the simulations showed a warm bias (+2 K) during austral spring and summer, a bias that existed since CMIP5 (Jones and Carvalho, 2013), and a colder than observed southeastern Brazil. These biases were linked with decreased cloud cover and less rainfall over the Amazon and more convective clouds and rainfall in southeastern Brazil (Figures 4.8 and 4.10). The low cloud cover, warm and dry Amazon biases are intertwined with the low-level circulation from the Atlantic into the South American continent. The biases in the circulation during austral summer were observed as a northerly flow anomaly over the central and southern Amazon, a feature that has been associated with a stronger moisture transport away from the Amazon (Marengo et al., 2012; Jones and Carvalho, 2018).

During the period of maximum rainfall rates in February, the simulations overestimate rainfall by 3 mm day<sup>-1</sup> in southeastern Brazil and underestimate rainfall in the Amazon by a similar rate. The historical experiments show a small drying response to historical forcing in the Amazon therefore slightly increasing the magnitude of this dry bias compared to the unforced piControl experiments. The AMIP simulation with the SST biases removed improved the representation of the Atlantic ITCZ and the precipitation, cloud cover and temperature biases over the South American Monsoon. The improvement in the circulation and precipitation biases in the AMIP simulation suggest that the origin of the dry Amazon bias are the biases in the Atlantic SSTs.

The canonical teleconnection responses of temperature, SLP and precipitation in the AMS to ENSO events are well represented in these models. For example, the simulated spatial patterns and strength of the positive (negative) precipitation anomalies observed

in northern Mexico and South Eastern South America during El Niño (La Niña) agree well with observations and reanalysis. Similarly, the teleconnection to the Amazon is well represented for both phases of ENSO, in spite of relevant biases in the mean state of the South American monsoon discussed above.

ENSO teleconnections in these simulations were found to be approximately linear, i.e., the precipitation response is linearly related to the magnitude of the SST perturbation in the EN 3.4 region. These experiments also show signs of symmetric teleconnections as positive and negative phases produce the opposite and equivalent precipitation response in the AMS. In contrast to observations and the GC3 AMIP simulation, the precipitation response in the coupled models appears to be independent of the type or flavour of ENSO events, i.e., between Central and East Pacific events. The fact that these models show a reasonable representation of ENSO diversity in SST patterns but the models do not replicate the observed non-linear dependance to ENSO events warrants further analysis.

The QBO appears to be a source of non-linearity for ENSO teleconnections to the Amazon. La Niña canonical teleconnections in the Amazon are characterized by a stronger ascent associated with a stronger Walker circulation. This teleconnection pattern occurs in observations and these simulations primarily during the westerly phase of the QBO, whereas the teleconnection during the easterly phase is much weaker and barely different from the climatological mean-state. Whether the stratospheric QBO poses such an important control of the main source of interannual variability (ENSO events) for monsoon rainfall in the Amazon merits a separate chapter of this thesis.

The main biases (Fig. 4.19), in these experiments are generally smaller in the medium resolution GC3 N216 compared to the low resolution experiments (N96), which suggests improved model performance with increased horizontal resolution. In contrast, including Earth System processes in the UM model only affects the surface temperature response to historical forcing and not the dynamical biases that drive the precipitation and ITCZ biases. In short, the main dynamical biases in UKESM1 are very similar to those in GC3 N96 as these two models share the same dynamical core; only when resolution is increased are these biases reduced notably.

A noteworthy difference between UKESM1 and GC3 is that warming over the historical period in Mexico and the Amazon is higher in UKESM1 than in GC3. In general, UKESM1-hist shows a stronger temperature response to forcing than GC3 N96-hist, as UKESM1 has been reported to have a greater climate sensitivity than GC3 N96 (Andrews et al., 2019a; Sellar et al., 2019). This differential warming may be a consequence of the land-use change in these regions playing a role in the UKESM1 representation of soil-atmosphere feedbacks.

The improvement in the medium resolution simulation compared to the low-resolution simulations may be attributed to the improved dynamics of the ocean or the atmosphere. For example, the Atlantic ITCZ biases have been shown to be directly affected by processes in the convective scheme (Bellucci et al., 2010), such as the treatment of entrainment and moisture-cloud feedbacks (Oueslati and Bellon, 2013; Li and Xie, 2014). The resolution of the ocean model has been shown to impact the eddy heat flux parametrisation and the associated heat uptake and transport of the ocean (Kuhlbrodt et al., 2018). The improvement in the Atlantic SSTs and ITCZ and the associated dynamics in GC3 N216-pi also improves the associated circulation biases and moisture transport in the South American Monsoon. In other words, the oceanic resolution may play an important role in the cross-equatorial heat and moisture transport which largely control the SST gradients over the equatorial Atlantic. The SST biases in the Atlantic are found to be dominant factor to accurately simulate the spatial distribution of rainfall in South America.

# 5

## A wavelet transform method to determine monsoon onset and retreat

This chapter describes a new method to determine monsoon onset and retreat timings using wavelet transform methodology applied to precipitation time-series at the pentad scale. The use of the method is illustrated for the North American Monsoon and the Indian Monsoon using four different precipitation datasets and climate model output. An extension of the method is used to identify the timings and strength of the Midsummer Drought of southern Mexico, Central America and the Caribbean. The advantages and shortcomings of the method are discussed at the end of the chapter.

### 5.1 Introduction

The timing and strength of the rainy season are key aspects of the climate of monsoon regions as the onset or start and the retreat or end of the monsoon rainfall greatly influences sectors such as agriculture (Sultan et al., 2005; Gadgil and Rupa Kumar, 2006; Jain et al., 2015; Harvey et al., 2018) and water management (Turner and Annamalai, 2012; Bussmann et al., 2016). Scientific and societal motivation has led climate and weather research to objectively determine onset and retreat dates for purposes such as the characterisation of variability

and trends, and forecasting (e.g. Kitoh and Uchiyama, 2006; Cook and Buckley, 2009; Lucas-Picher et al., 2011; Nieto-Ferreira and Rickenbach, 2011; Htway and Matsumoto, 2011).

For this reason, a wide range of methods exist to diagnose the onset and retreat dates from a number of variables and datasets. Bombardi et al. (2020) provides a recent review of these methods and highlights the technical differences and purposes of each. Methods can be divided into those that evaluate monsoon onset and retreat on a regional scale (e.g. Webster and Yang, 1992; Fasullo and Webster, 2003; Garcia and Kayano, 2013) or at a local or grid-box scale (e.g. Liebmann and Marengo, 2001; Cook and Buckley, 2009).

Threshold methods are the most commonly used local-scale methods that typically diagnose onset and retreat from a precipitation time-series (Bombardi et al., 2020). These methods evaluate the accumulated (Liebmann and Marengo, 2001) or daily/pentad-mean rainfall rates (Geil et al., 2013) and determine the onset and retreat dates when the time-series exceeds or falls below a pre-defined value (threshold) for a given amount of time (persistence). The persistence parameter aims to decrease the effect of noise of precipitation in the calculation. The threshold parameter can be a statistical measure of the seasonal cycle such as the total annual mean rainfall (Arias et al., 2012) or tuned to a specific dataset (e.g. Geil et al., 2013).

In other words, for a given purpose each threshold method is tailored to a monsoon region using a specific dataset and a specific variable. This characteristic of the threshold methods poses various shortcomings. Firstly, practical shortcomings of the threshold methods, particularly rigid thresholds, include false hits (Moron and Robertson, 2014) or some years not meeting the threshold and persistence criteria (Arias et al., 2012) requiring further relaxation of the parameters. Secondly, given that threshold methods are tailored to a specific dataset in a given region, statistical corrections are needed to implement the same threshold method in a different dataset or in another region.

The Coupled Model Intercomparison Project (CMIP) assessments of monsoon onset and retreat typically use precipitation threshold methods due to the lack of high temporal or vertical resolution output from all models to estimate vertically integrated quantities required for some methods (e.g. Geil et al., 2013; Zou and Zhou, 2015; Ha et al., 2020). Threshold methods have multiple shortcomings for CMIP assessments as the persistence and

threshold parameters are tuned for observations with a specific seasonal cycle but models have a range of biases in the seasonality, magnitude and spatial distribution of rainfall (Pascale et al., 2019; García-Franco et al., 2020). The use of pre-defined threshold values may also not be suitable to compare different model experiments with changes in forcing where the climatological mean rainfall or the seasonal cycle may change within the model run. These shortcomings are relevant because a proper diagnosis of the seasonal cycle in CMIP assessments is key to understand and diagnose current and future changes to monsoon seasonality as a result of greenhouse forcing (Zhou et al., 2016; Wang et al., 2017).

The objective diagnosis of shorter time-scale rainfall variability, such as bimodal regimes and active and break phases of a monsoon, also requires methods that can separate relatively drier and wetter periods within the rainy season. For example, for the MSD of Central America and the Caribbean (section 2.3) the objective determination of the strength, spatial distribution and robustness of the bimodal signals is not straightforward. For example, the global method used in Bombardi et al. (2020) fails to diagnose the region of southern Mexico, Central America and the Caribbean as a bi-modal regime.

The majority of existing methods to diagnose bimodal signals in the MSD region use geometric or statistical measures of the monthly-mean rainfall that measure the difference between the months of maximum rainfall and the drier months. However, this approach fails to capture the shorter-scale changes that have been shown to occur in both observations and model data, as the MSD does not start or end exactly on given calendar months (Magaña et al., 1999; García-Franco et al., 2020). Zhao and Zhang (2021) review and compare several methods to detect and measure the MSD, finding that using monthly-mean data and prior assumptions of the dates of the first and second peaks can lead to errors.

Only a handful of methods exist that can determine the characteristics of the MSD in Central America on sub-monthly timescales. Anderson et al. (2019) analysed the pentad-mean time-series from the Climate Hazards Infrared Precipitation with Stations (CHIRPS) dataset. After a double temporal smoothing of the time-series, Anderson et al. (2019) determined the MSD timings through a threshold method with parameters tailored to the CHIRPS dataset. In turn, Zhao et al. (2020) used daily-mean time-series and determined the two-peak structure through linear-regression analysis. However, more general methods

that may be applied to multiple datasets on the daily-mean scale could provide useful to understand variability and trends in the seasonality of precipitation in the region.

In short, multiple methods exist to diagnose monsoon onset and retreat as well as bimodal signals, each with various parameters fit for different purposes, but these methods present shortcomings for studies that compare results from multiple datasets or investigate model experiments where the climatological rainfall and the seasonal cycle are non-stationary. Both the objective determination of monsoon onset and retreat and the timings of bimodal regimes require a method that can analyse temporal changes to precipitation on several scales and that can be used on any gridded dataset.

The purpose of this chapter is then to present an objective approach that is more portable across datasets, regions, less prone to false-hits and robust for various purposes. This chapter introduces a wavelet transform method to determine monsoon onset and retreat dates using pentad-mean precipitation time-series. Wavelet algorithms have been extensively used in atmospheric research for multiple purposes, such as the detection of the boundary layer height (e.g. Brooks, 2003), as well as to analyse time-frequency features of a signal (e.g. Whitcher et al., 2000; Dimdore-Miles et al., 2021). In fact, Allen and Mapes (2017) used a wavelet analysis to determine monsoon onset and retreat using daily OLR data. The remainder of this chapter is organised as follows: section 2 describes the methods and datasets. Section 3 shows the results of applying the method to the Indian and North American Monsoons and the MSD. Section 4 summarises the method and discusses the results.

## 5.2 Data

### 5.2.1 Precipitation datasets and reanalysis data

This chapter uses three gridded precipitation datasets described in chapter 3: the TRMM v7 3B42, the CHIRPS, and the CMAP datasets. These three precipitation datasets are merged products, TRMM and CMAP mainly use microwave satellite measurements complimented by several other sensors and calibrated with rain-gauge data whereas CHIRPS uses several products from TRMM, as well as high-resolution station data. These datasets also differ in their end-product horizontal resolutions.

The precipitation output from the latest ECMWF reanalysis, ERA5, is used, which has been shown to exhibit a relatively good representation of the temporal characteristics of rainfall in the AMS in chapter 4. Other variables from ERA5 used to diagnose changes to the circulation associated with monsoon onset were daily-mean geopotential height at 500 hPa and wind speed ( $\vec{u}$ ) at several vertical levels.

### 5.2.2 Model data

Daily precipitation data from the CMIP6 archive are used and retrieved from: <https://esgf-index1.ceda.ac.uk/projects/cmip6-ceda/>, to illustrate the method using standard climate model output. In particular, we use results from the piControl and historical simulations of HadGEM3 GC3.1 and UKESM1, described in chapter 3. The daily precipitation data were converted to pentad-scales.

## 5.3 The wavelet transform method

Wavelets are band-limited wave-like functions with specific mathematical properties that include a finite energy and zero-mean (Whitcher et al., 2000; Addison, 2017). The wavelet function is defined using two parameters, a dilation (a width or temporal scale) and a translation (centroid in time/space).

Wavelet transforms are the result of the inner product (convolution) of a wavelet function with a time-series or a signal (Addison, 2017). The wavelet transform (WT) can be thought of as a local comparison between the wavelet function and the observed signal for different frequencies. The information provided by a WT largely depends on the characteristics of the wavelet function, such that different wavelet functions are used for different purposes (Addison, 2017). For the purpose of finding the onset and retreat dates, the wavelet based on the Haar function is useful as this wavelet finds sudden changes in a signal, in a way acting as a temporal filtering of the data (Addison, 2017; Brooks, 2003). The Haar wavelet is defined as the non-continuous piece-wise function:

$$\psi\left(\frac{t-b}{a}\right) = \begin{cases} 1 & b \leq t < b + \frac{a}{2} \\ -1 & b - \frac{a}{2} \leq t < b \\ 0 & elsewhere, \end{cases} \quad (5.1)$$

where  $a$  is the dilation coefficient,  $b$  is the centre of the wavelet or the translation coefficient and  $t$  is the time coordinate.

The wavelet covariant transform is then the inner product of the Haar wavelet with a timeseries (Brooks, 2003), as follows:

$$W_f(a, b) = \frac{1}{a} \int_{t_i}^{t_f} pr(t) \psi\left(\frac{t-b}{a}\right) dt, \quad (5.2)$$

where  $pr(t)$  is a time-series of precipitation, either on daily or pentad scales and  $W_f(a, b)$  is the matrix of the covariant transform and  $t_i$  and  $t_f$  are the start and end time-points. No statistical treatment, normalization or anomaly, *a priori*, is calculated on the precipitation time-series  $pr(t)$  so the units of  $W_f$  are the same as the precipitation time-series (e.g. mm d<sup>-1</sup>).

Monsoon timings can be observed as sharp changes to precipitation, i.e., rainfall sharply increases at onset and sharply decreases at retreat. However, measuring these changes can be difficult since precipitation time-series are typically noisy. The Haar wavelet is useful in these cases for signal detection since the WT is interpreted as gradients across different temporal scales and can smooth out the high-frequency variability using sufficiently large dilation scales. In other words, the wavelet covariant transform ( $W_f(a, b)$ ) filters the time-series  $pr(t)$  using a temporal scaling of  $a$ , or measures gradients on a scale  $a$  for each time-step ( $b$ ).

Figure 5.1 shows the Haar wavelet and one year of observed precipitation in the North American Monsoon from the CMAP dataset. Figure 5.1a illustrates how the wavelet function compares the observed signal in the interval  $b < t \leq b + \frac{a}{2}$  with the values of the signal in the interval  $b - \frac{a}{2} \leq t < b$  where  $b$  in this case is a pentad time step. The WT coefficient for dilation  $a = 20$  pentads at the translation of  $b = 35$ , i.e., pentad 35, is a measure of the precipitation difference between the sum of the observed rainfall 10 pentads after pentad 35 and the sum of the observed rainfall 10 pentads before pentad 35 as illustrated in Figure 5.1b.

Figure 5.2 shows an example of the WT application using the observed climatological precipitation in the North American Monsoon in four different precipitation datasets. The

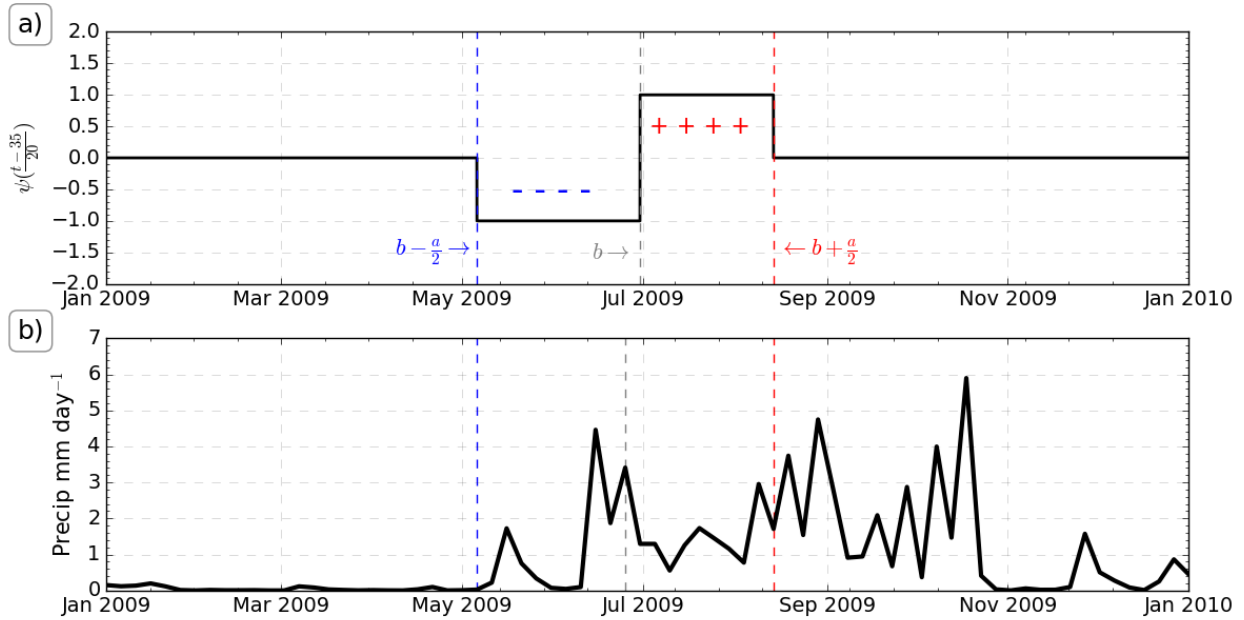


**Figure 5.1:** (a) Haar wavelet at a dilation  $a = 20$  and translation  $b = 35$ , which is the 35th pentad around June 22. The positive and negative parts of the wavelet are highlighted in red and blue, respectively. (b) CMAP precipitation in 2009 in the North American Monsoon [20-27°N, 110-103°W].

mean climatological rainfall rates (upper panel) differ in their peak summer rainfall rates but qualitatively show similarities in the start and end dates of the rainy season. The WT coefficients ( $W_f(a, b)$  in the middle panel) for a small dilation  $a = 4$  are relatively noisy but show a clear maximum and minimum that correspond well with the maximum and minimum of longer dilations ( $a = 14, 20$ ). The sum of these four coefficients at each translation or pentad  $b$ , highlight a maximum found around June 22 and a minimum found around September 21, which agree well with previous results of mean onset and retreat dates in the North American Monsoon (e.g. Arias et al., 2012; Geil et al., 2013).

### 5.3.1 Identification of Monsoon Onset and Retreat

Local maxima in the WT highlight positive steps in the precipitation time-series with a coherent scale of  $a$  pentad steps. This interpretation is then extended to diagnose monsoon onset. The pentad ( $b^*$ ) corresponding to the maximum of the sum of the transform over

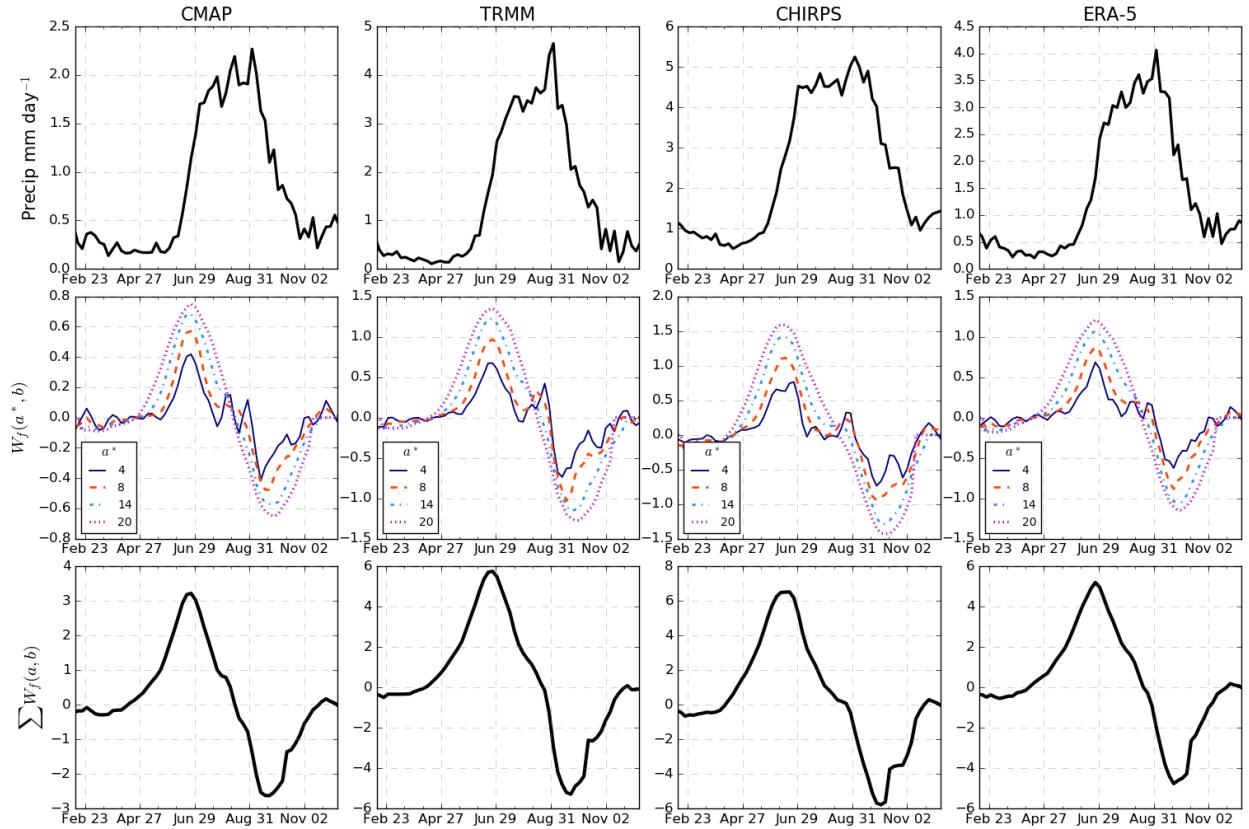


**Figure 5.2:** (upper) Climatological pentad-mean precipitation in four different observational datasets in the North American Monsoon [19–35°N, 110–103°W]. (middle) The wavelet transform coefficients ( $\text{mm d}^{-1}$ ) for four different dilations  $a$ . (lower) The sum of the WT coefficients ( $\text{mm d}^{-1}$ ) over dilations  $a = 4, 8, 14, 20$ .

a set of scales is defined as monsoon onset (MO), i.e.:

$$MO = b^* \Leftrightarrow \sum_{a_0}^{a_f} W_f(a, b^*) = \max \left( \sum_{a_0}^{a_f} W_f(a, b) \right). \quad (5.3)$$

where  $a_0$  and  $a_f$  are the limits of the pentad scales, i.e., the dilation coefficients,  $b^*$  is the pentad of maximum  $\sum W_f(a, b)$  and the monsoon onset pentad. Similarly, the monsoon retreat pentad is found at the minimum of the sum of the WTs, i.e.,

$$MR = b^* \Leftrightarrow \sum_{a_0}^{a_f} W_f(a, b^*) = \min \left( \sum_{a_0}^{a_f} W_f(a, b) \right). \quad (5.4)$$

In other words, we seek to find monsoon onset and retreat using the maximum and minimum the wavelet power spectrum over a range of temporal scales. Several sensitivity tests were performed with different dilation coefficients ( $a$ ) in the different observational datasets, models and regions and a set or vector of dilation scales was found to be optimal.

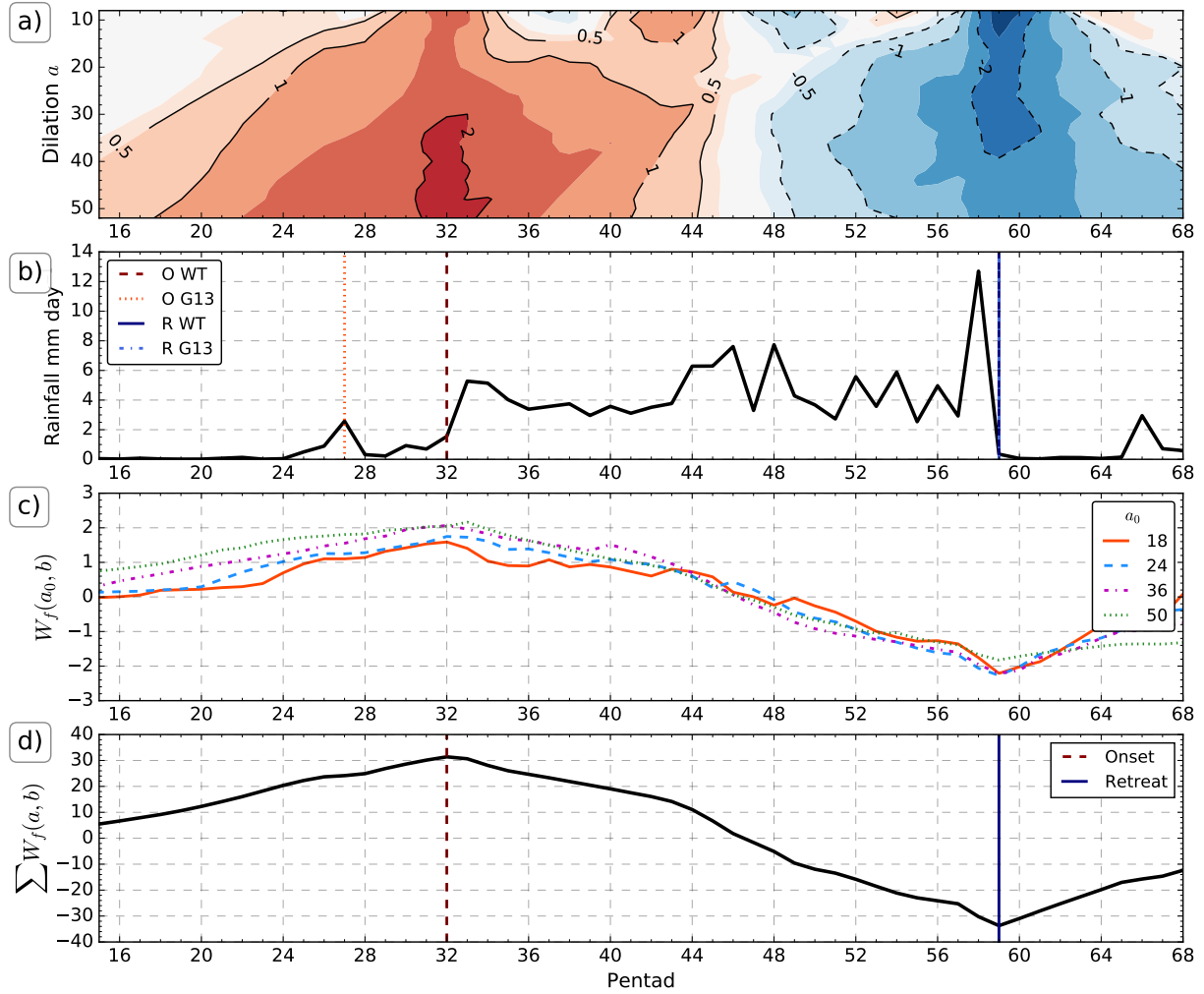


**Figure 5.3:** Example determination of monsoon onset and retreat dates for the North American Monsoon [20-27°N, 109-103°W] in the TRMM dataset for 2009. (a) WT coefficient matrix ( $\text{mm } d^{-1}$ ) as a function of time and dilation coefficient  $a$ . The shading is from -3 to 3  $\text{mm } d^{-1}$  with an interval of 0.5  $\text{mm } d^{-1}$ . (b) Observed precipitation, the onset and retreat dates as determined by the WT method (dashed) and the threshold method of Geil et al. (2013) (solid) are shown. Note that the date of retreat is diagnosed to be the same between the two methods. (c) The WT coefficients for different dilations. (d) The sum of the WT ( $\sum W_f(a, b)$ ) ( $\text{mm } d^{-1}$ ); the maximum and minimum are shown in red and blue, representing onset and retreat pentads, respectively.

The set of dilation coefficients  $\vec{a} = (28, 30, \dots, 54)$  was found to be robust, i.e., was able to capture the onset and retreat dates in all the datasets.

Monsoon onset is defined as the maximum sum of wavelet coefficients, capturing positive gradients within the scales of 14 to 27 pentads (half of the elements of vector  $a$  defined above). Monsoon Retreat has a similar definition, capturing the greatest negative gradient of precipitation over the same pentad scales.

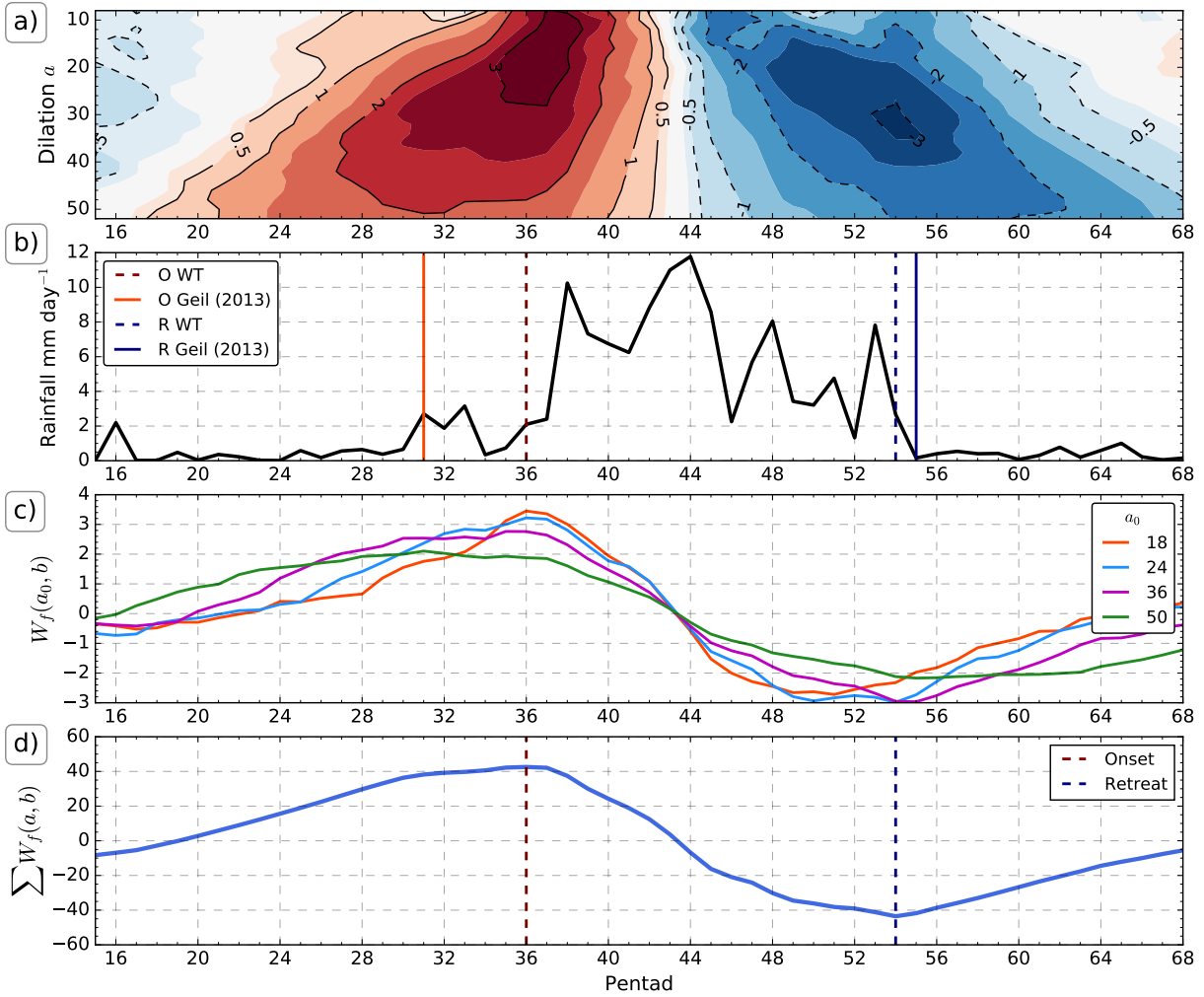


**Figure 5.4:** As in Figure 5.3, but for a year (1875) in the HadGEMGC3.1 N216 pre-industrial control simulation.

For example, Figure 5.3 illustrates the method in the North American Monsoon in the TRMM dataset for 2009. Figure 5.3a shows the WT coefficient matrix, showing the changes in precipitation for dilations ranging from 10 to 50. A clear signal of positive coefficients is observed between pentads 28 to 34 and a similar negative signal observed in pentads 56 to 60. Figure 5.3b shows the time-series of the observed precipitation, which suggests that monsoon onset occurs sometime between pentads 28 and 34. Observed rainfall rapidly decreases after pentad 59 suggesting that monsoon retreat can be diagnosed around this pentad.

Figure 5.3c shows the WT coefficients as a function of pentad for several dilations ( $a_0$ ). The coefficients for all scales seem to follow a very similar behaviour, increasing during

spring to reach a maximum around pentad 32 and thereafter decreasing to a minimum around pentad 59. When the sum of the wavelet transform coefficients across the dilations is computed (Figure 5.3d) this behaviour becomes much clearer. The maximum and minimum are found at pentads 32 and 59, respectively and these pentads define the onset and retreat times. For comparison, the results from the method of Geil et al. (2013) are shown in Figure 5.3b, indicating that this method may have found an earlier onset.

As a proof of concept, Figure 5.4 shows a similar example using precipitation area-averaged in the same region but using model data from the piControl simulation of HadGEM3 GC3.1 N216. The results show that the WT method can capture the onset and retreat dates with relatively high skill and that these dates are different from the dates computed using the method of G13, with the threshold method suggesting an earlier onset and a later retreat.

### 5.3.2 Extension for Application to the MSD signal

The wavelet method can be extended to characterise the shorter scale variations of precipitation of the MSD in Central America and the Caribbean. First, the monsoon onset and retreat dates are determined in the time-series from the area-averaged precipitation in the MSD region via the approach described in the previous section. Once the onset and retreat dates are established, an additional wavelet analysis determines the dates in which the MSD starts and ends. The onset and end of the drier period of the MSD can be found by computing the wavelet transform again but using smaller dilations and over a limited temporal range. In particular, the WT is only calculated in the 20 pentads before and after the dates defining monsoon retreat and onset, respectively. The MSD Onset (MSDO) and MSD End (MSDE) are defined as the minimum and maximum, respectively, of the sum of the wavelet transforms (equations 5.3 and 5.4) using dilation coefficients  $\vec{a}^* = (10, 12, \dots, 24)$ . The diagnosis of the onset and end of the MSD is also robust to using other dilation coefficients of similar magnitude.

Figure 5.5 illustrates the use of the WT method to determine the dates of MSDO and MSDE for the precipitation of 2017 in ERA-5. Figure 5.5a depicts the wavelet covariant transform matrix, showing the  $W_f$  coefficients for each dilation  $a$  at each pentad  $b$ . The onset of rainfall is diagnosed around the time-steps of highest positive  $W_f$  coefficients –

around pentads 24 to 32 for almost all dilations. These positive coefficients are followed by a period of negative values from pentad 32 to pentad 40, which represent the decrease in precipitation, or relative drought, in the midsummer. The MSD is followed by another period of positive coefficients from pentad 44 to pentad 52, illustrating the so-called second peak of precipitation and, finally, a period of negative coefficients associated with monsoon retreat.

The coefficients of the wavelet transform ( $W_f(a_0, b)$ ) for selected dilations  $a_0$  (Figure 5.5c) show that the smaller dilations are more sensitive to smaller scale variations in the time series and longer dilations better highlight the long-term change of the time series. For example  $a_0 = 18$  shows signs of a MSD by showing two local maxima and two local minima, whereas  $a_0 = 54$  only shows a local maximum and a local minimum associated with onset and retreat.

The maximum and minimum of the sum over all dilations (Figure 5.5) depict the rainfall onset and retreat dates, respectively. The second wavelet transform  $W_f(a^*, b)$  is computed over smaller dilation coefficients ( $a^*$ ) near the onset and retreat dates as described above to highlight the MSDO and the MSDE. Figure 5.5e shows the sum of the wavelet transform coefficients  $W_f(a^*, b)$  and the pentad of the MSDO, 34, and MSDE, 49, corresponding to the minimum and maximum of the sum of these wavelet transform coefficients, respectively.

The strength of the MSD can be measured through the maximum and minimum sum of the coefficients  $\sum W_f(a^*, b)$  used to define the start and end dates of the MSD. For example, in Figure 5.5e the minimum of the  $\sum W_f(a^*, b)$  was  $-20 \text{ mm d}^{-1}$  found at pentad 35 and an opposite local maximum of  $+20 \text{ mm d}^{-1}$  at pentad 49. These two values, hereafter *coef1* and *coef2*, provide a quantitative measure of the strength of the MSD for this year in this dataset and will be used to measure the spatial and temporal variability of the magnitude of the MSD in the different datasets.

### 5.3.3 Comparative Methodologies

For validation purposes, the wavelet transform method is compared with existing methods which determine onset and retreat in the North American and Indian monsoons. The threshold methods of Geil et al. (2013) (hereafter G13) and Arias et al. (2012) (hereafter A12) are compared to the results of the wavelet transform in the North American Monsoon. G13 used a threshold of  $1.3 \text{ mm day}^{-1}$  for at least 3 days for onset and 7 days for retreat for

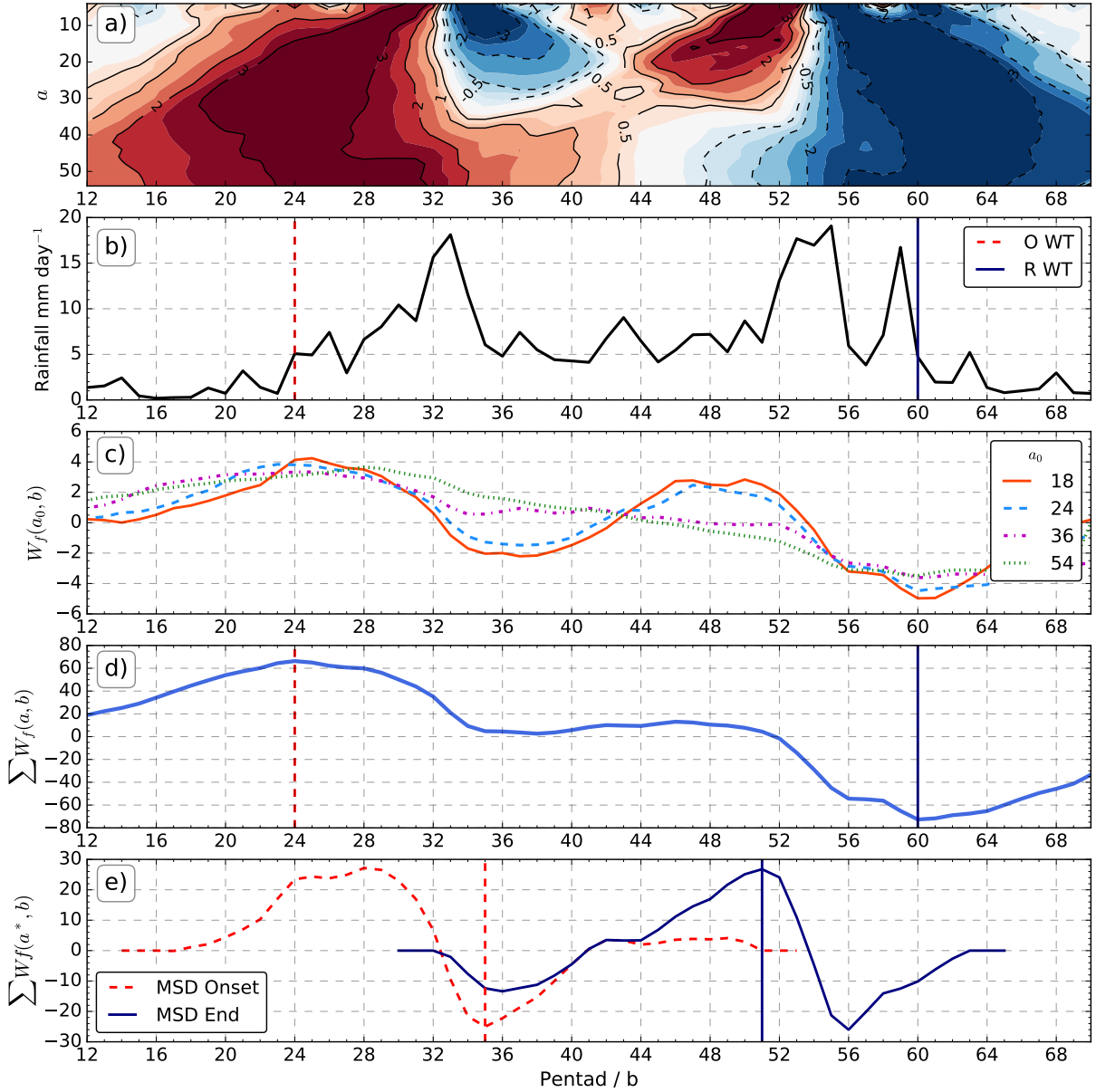


**Figure 5.5:** Example characterisation of the MSD [11-19°N, 95-85°W] using ERA-5 data for 2017. (a) Wavelet transform spectra, (b) observed precipitation with the onset and retreat pentads shown in red and blue, respectively. (c) Wavelet transform coefficients for four different dilations ( $\text{mm d}^{-1}$ ). (d) The sum of the wavelet transform coefficients ( $\text{mm d}^{-1}$ ) for  $a = 28, \dots, 51$ . (e) The sum of  $W_f(a, b)$  ( $\text{mm d}^{-1}$ ) for dilation coefficients  $a = 12, \dots, 24$  showing the start (MSD Onset) and end (MSD End) of the midsummer drought.

daily TRMM observations. This study, in contrast, analyses most of the data on the pentad-scale, so we adapt this method for TRMM to the same threshold value, but the onset pentad is the first pentad above the threshold whereas for retreat, we require rainfall to be below the

threshold for two consecutive pentads. The method of A12 defines onset with two conditions. The first condition to find the onset pentad is that six out of the eight subsequent pentads must have rain-rates above the annual-mean climatological rainfall. The second condition is that at least six out of the eight previous pentads must be below the annual-mean climatological rainfall. The opposite definition is used to determine the pentad of monsoon retreat.

In relation for the Indian Monsoon region, a commonly used metric is the hydrological onset and withdrawal index (HOWI) which is based on moisture transport over the Arabian Sea (Fasullo and Webster, 2003; Sahana et al., 2015; Chevuturi et al., 2019). To compute the HOWI index, first, the vertically integrated moisture transport ( $\chi$ ) is computed from daily ERA-5 data in the Arabian sea, as described by Fasullo and Webster (2003), i.e.:

$$\chi = \frac{1}{g} \int_{p_0}^0 q \mathbf{V} dp, \quad (5.5)$$

where  $g$  is the gravitational acceleration,  $p$  are the pressure levels,  $q$  is the specific humidity and  $\mathbf{V}$  is the wind vector. The VIMT is then normalized using the transformation:

$$HOWI = 2 \left( \frac{\chi - \min(\bar{\chi})}{\max(\bar{\chi}) - \min(\bar{\chi})} \right) \quad (5.6)$$

where  $\chi$  is the unnormalized time-series,  $\bar{\chi}$  is the mean seasonal cycle of the unnormalized index and HOWI is the normalized index. The onset date is defined as the first day of each year where the HOWI index is greater than zero and the retreat date is the first day after the onset date that the HOWI index is negative (Fasullo and Webster, 2003; Sahana et al., 2015). The necessary daily data of moisture and wind speed on sufficient vertical levels to compute the HOWI index in the MOHC submissions to CMIP6 was not available, so the HOWI index can only be computed using ERA5 and will be compared to the WT method used on the observational gridded datasets.

## 5.4 Results

The monsoon onset and retreat dates were determined for each year in each observational and model dataset for the Indian, North American and MSD regions using the methods described in the previous section. The calculations were performed for area-averaged precipitation

time-series representative of the core regions defining these monsoons. Calculations were also made at grid-box scales to illustrate the spatial distribution of the onset and retreat dates.

### 5.4.1 The North American Monsoon

Table 5.1 shows the mean onset and retreat dates estimated using the G13, A12 and WT methods for precipitation time-series averaged over the North American monsoon. The table reports the results for three observational datasets, ERA-5 reanalysis and five climate model experiments. The observations agree that the onset date is found at pentad 33 (around June 15), according to the WT and the method by G13. However, the method of G13 reports a mean retreat date that is one pentad later than the WT method, i.e., around October 7th for G13 method and October 2nd for the WT. The method by A12 disagrees with G13

**Table 5.1:** Mean (standard deviation) pentads of monsoon onset (O) and retreat (R) in the North American Monsoon [110°-103°W, 20°-27°N] for observational datasets, reanalysis and model output with the wavelet transform method WT, G13's and A14's method. Pentad 34 corresponds to the period between June 17-22 and pentad 54 to the period Sep 27 - Oct 1. The results from the WT method in the model experiments which are statistically different to both the CMAP and CHIRPS results at the 95% confidence level, according to a Welch's t-test, are shown in bold.

Dataset / Experiment	WT O	WT R	G13 O	G13 R	A12 O	A12 R
TRMM	33.3 [±1.8]	55.8 [±1.9]	33.0 [±1.7]	56.6 [±1.4]	30.4 [±1.7]	53.8 [±2.0]
CMAP	33.2 [±1.6]	55.0 [±2.1]	36.0 [±3.3]	55.7 [±1.8]	31.7 [±3.0]	54.5 [±3.3]
CHIRPS	32.5 [±1.5]	54.7 [±1.9]	33.6 [±1.7]	56.1 [±1.4]	30.1 [±1.7]	53.6 [±2.5]
ERA-5	33.5 [±1.8]	55.5 [±2.0]	33.6 [±1.8]	56.4 [±1.4]	30.9 [±1.7]	53.3 [±2.3]
GC3 N216-pi	33.7 [±2.0]	55.1 [±1.8]	32.6 [±2.5]	55.9 [±2.3]	32.4 [±2.5]	53.8 [±3.8]
GC3 N96-pi	33.7 [±2.2]	55.0 [±2.1]	32.7 [±2.9]	56.3 [±2.0]	31.9 [±2.6]	54.1 [±4.1]
GC3-hist	33.8 [±2.3]	55.1 [±2.1]	33.3 [±2.9]	56.0 [±2.2]	31.9 [±2.6]	53.7 [±4.0]
UKESM-pi	<b>34.5</b> [±2.1]	54.8 [±2.1]	34.1 [±2.9]	56.1 [±1.9]	33 [±2.6]	53.9 [±4]
UKESM-hist	<b>34.3</b> [±2.2]	54.3 [±2.2]	34.4 [±3.2]	55.6 [±2.1]	33.1 [±3.0]	53.2 [±4.2]

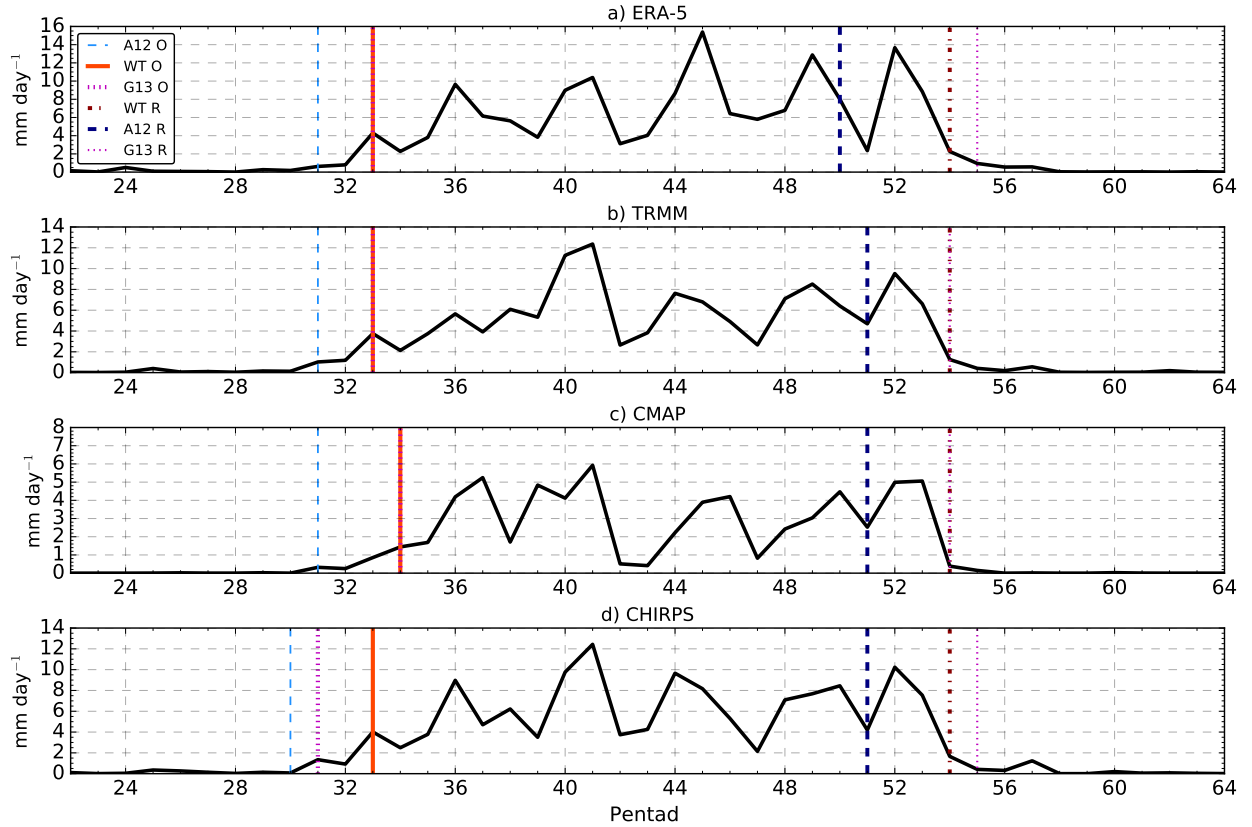


**Figure 5.6:** Pentad-mean precipitation for the North American Monsoon in 2010 in four precipitation datasets showing the onset and retreat pentads as diagnosed by the WT, the A12 and G13 methods. The area used to average the precipitation is illustrated in in Figure 5.7b).

and the WT methods for both onset and retreat mean pentads, in both cases finding an earlier onset (pentad 30) and retreat (pentad 54) for all the observational datasets.

The climate models reasonably represent the mean onset and retreat dates, as only the onset dates from both experiments of UKESM1 are statistically different to the results of CMAP and CHIRPS. The similarities in onset and retreat dates confirm that the seasonal cycle in the North American monsoon is very well represented by these models, as suggested by chapter 4. In the results of the simulations, A12 also produces an earlier onset and retreat dates when compared to the other two methods of about 1.5 pentads, but this difference is within the uncertainty range given by the interannual variability of the model data which is largest for A12.

Figure 5.6 compares the estimated onset and retreat dates using the three methods for the 2010 North American Monsoon using the three observational datasets and ERA5. A12

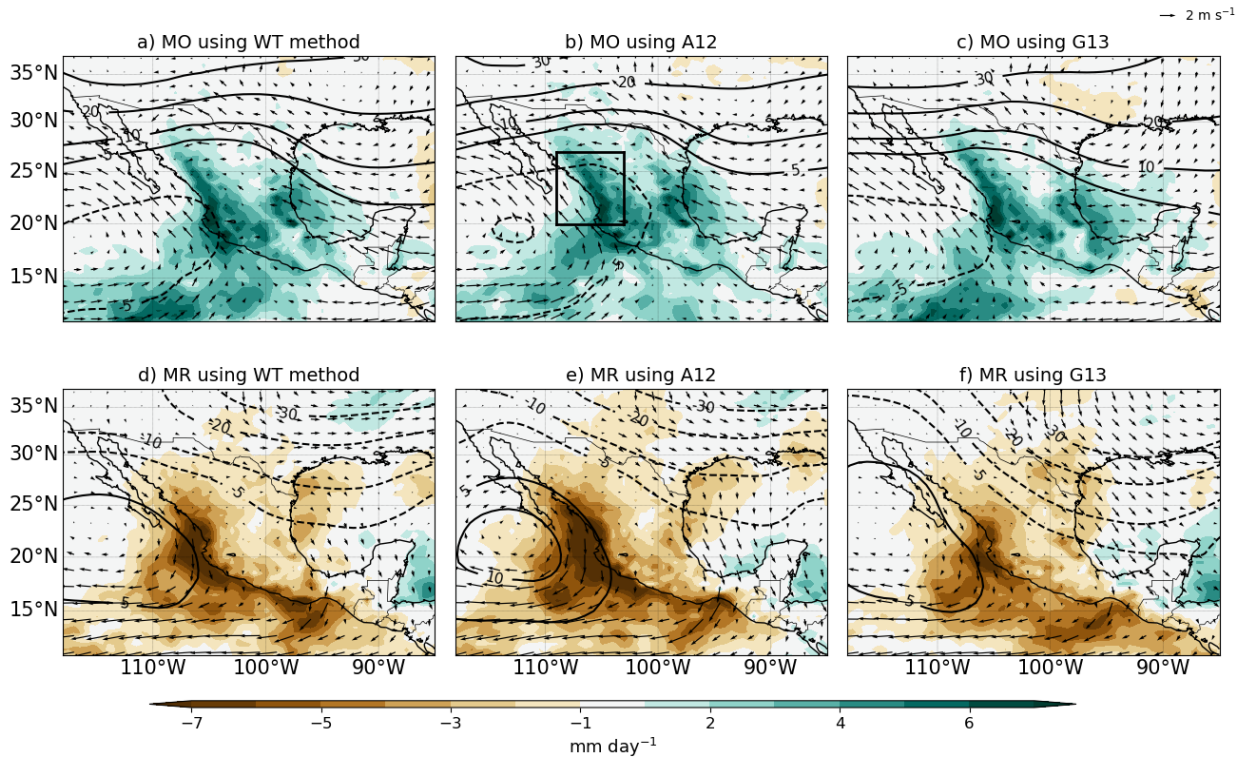


**Figure 5.7:** Precipitation (color contours), low level wind at 850-hPa and geopotential height (line contours) at 500 hPa anomalies for (a, b, c) the difference between the 10 days after monsoon onset and 10 days prior to onset (MO) using onset dates from (a) the WT (b) Arias et al. (2012) and (c) Geil et al. (2013). (d, e, f) are as in (a, b, c) but for monsoon retreat. The data and dates are obtained from ERA-5, and the area for the average is shown in the box in b).

shows an earlier onset and retreat in all the datasets compared with the WT and G13 which agree in almost every dataset. The WT method is the only method that estimated the same retreat date for all the four datasets and the same onset date in three of the four datasets, with the CMAP datasets showing an onset date one pentad later than the others.

The meteorological changes associated with onset and retreat of the North American Monsoon (Figure 5.7) are illustrated as the composite differences of the precipitation, wind and geopotential changes 10 days prior to and after onset and retreat. These changes to the circulation and precipitation are reasonably similar for all the three methods. The impact of monsoon onset in precipitation is diagnosed to be slightly stronger by A12 compared to WT or G13. The WT method shows a very similar pattern and magnitude of the circulation and precipitation anomalies of onset and retreat when compared to the other two methods. The method by G13 produces the weakest anomalies, particularly

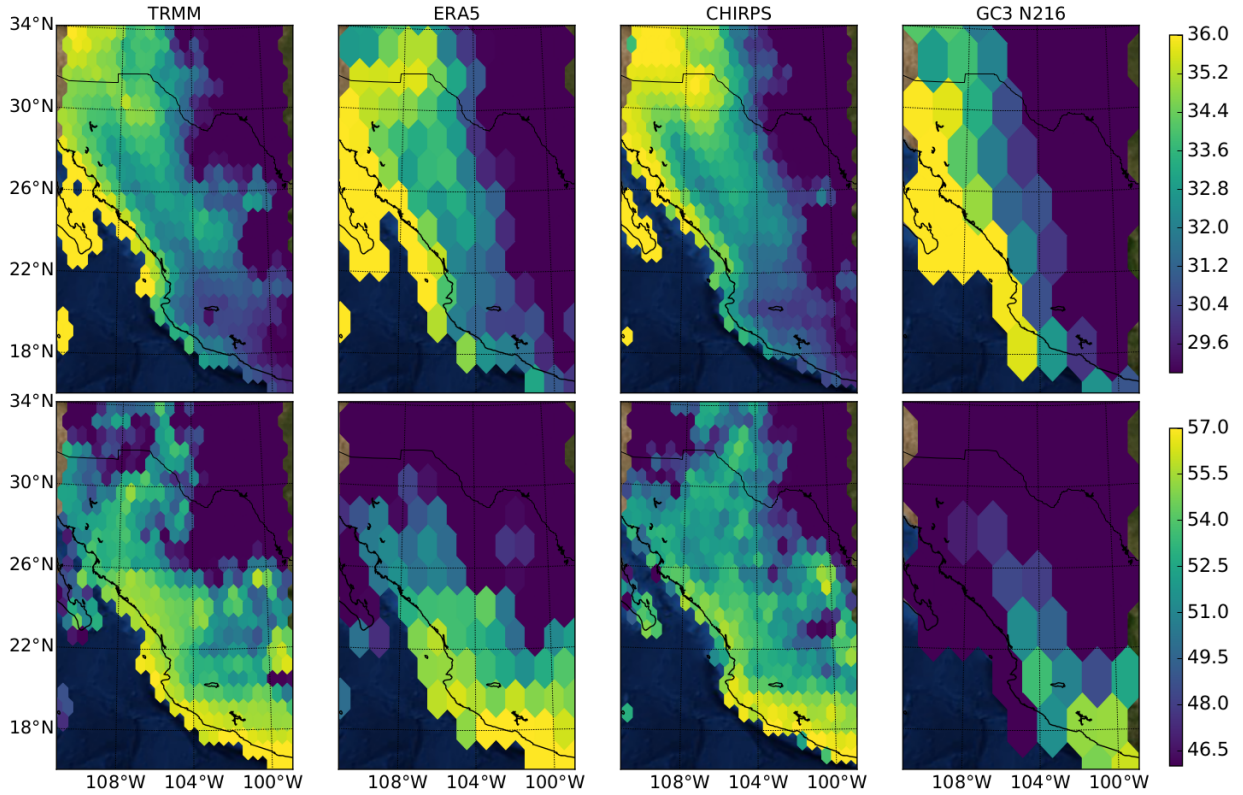


**Figure 5.8:** Rainfall onset (upper) and retreat (lower) mean pentads in the North American Monsoon for observations and a climate model output using the WT method.

of precipitation whereas the method by A12 produces the strongest precipitation and geopotential anomalies, particularly at retreat.

Figure 5.8 shows the spatial distribution of the mean onset and retreat dates in the North American Monsoon region for various datasets. There is high agreement between TRMM, CHIRPS and ERA5 on the spatial pattern of mean onset and retreat dates. Onset in western Mexico is around pentad 31 (around June 1st), whereas in Chihuahua and Sonora the rainy season begins shortly after pentad 35 (June 22). The pattern in the medium-resolution simulation GC3 N216 piControl is consistent with observations, particularly during onset. However, the spatial pattern of the mean retreat dates in the northern regions of the monsoon show an earlier than observed retreat, possibly associated with the dry bias in this region in these models (see chapter 4).

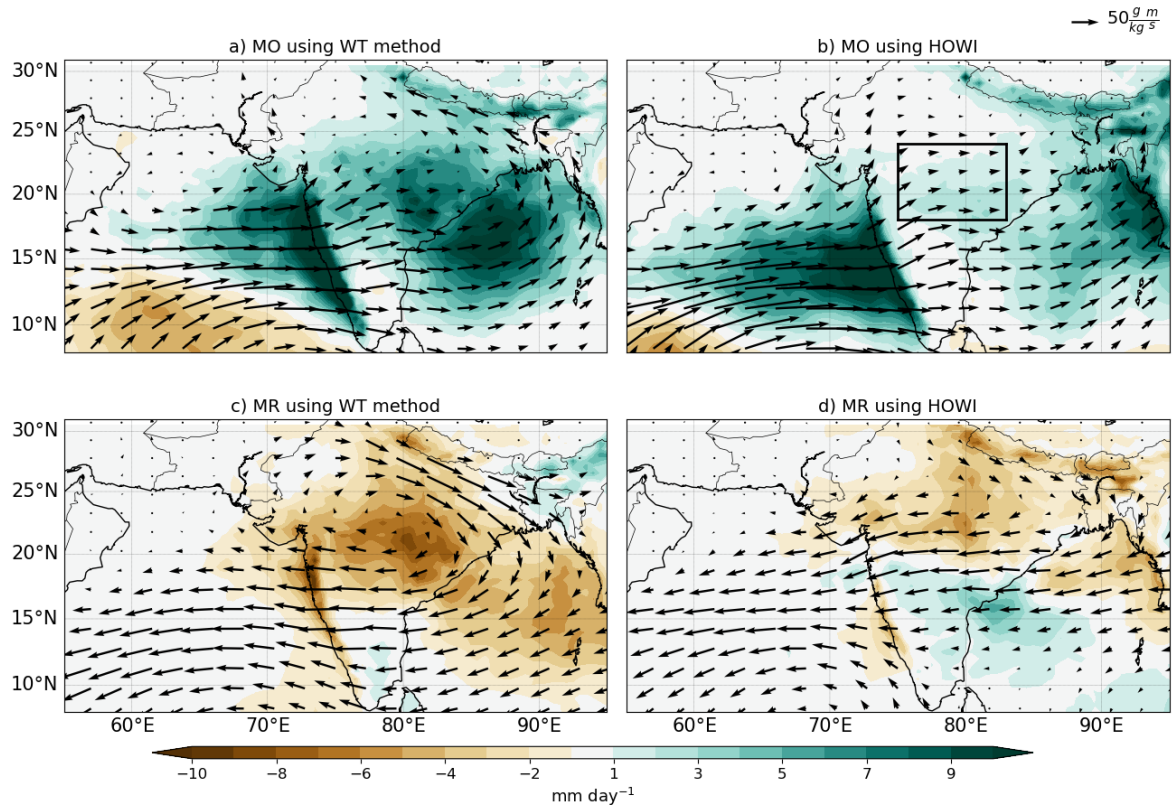
### 5.4.2 The Indian Monsoon

Table 5.2 compares the mean onset and retreat dates of the Indian Monsoon as computed from the HOWI index using ERA5 data, and the WT used for gridded precipitation datasets. The onset and retreat dates from the HOWI index were converted from the daily to the pentad-scale to compare with the WT. The mean onset date for the HOWI index is May 27th between pentads 29 and 30, and retreat is between pentads 49 and 50, around September 3rd. The mean onset date found using the WT method for the four observational datasets was pentad 32, about two pentads later than the HOWI index. The mean retreat date for the WT method (pentad 53) was two pentads later than the HOWI results.

Overall, the models exhibited later than observed onset (+4 pentads) and earlier retreat (-2 pentads) dates. The differences between the hydrological determination of onset and retreat dates, through HOWI, and the WT method on gridded precipitation datasets is statistically significant, according to a Welch's t-test comparing the HOWI and all the gridded datasets. These differences may be due to the different regions where each method is defined, i.e., HOWI is defined over the whole of the Arabian Sea where an earlier onset would be expected when compared to rainfall over mainland India, where the WT method was applied.

**Table 5.2:** Mean (standard deviation) pentads of monsoon onset (MO) and retreat (MR) in the Indian Monsoon using the WT method on observed, reanalysed and modelled time-series as well as for the HOWI index. The region over which precipitation was area-averaged for the WT method was [75°-83°E, 18°-24°N]. The mean onset and retreat dates that are significantly different to the 99% confidence level to the CMAP dataset are shown in bold.

Dataset	MO	MR
TRMM	31.6 [ $\pm 1.8$ ]	53.2 [ $\pm 1.9$ ]
CMAP	31.8 [ $\pm 1.6$ ]	53.3 [ $\pm 2.6$ ]
CHIRPS	31.5 [ $\pm 1.4$ ]	53.4 [ $\pm 1.9$ ]
ERA-5	31.8 [ $\pm 1.9$ ]	52.7 [ $\pm 2.6$ ]
GC3 N216-pi	<b>34.4</b> [ $\pm 1.3$ ]	<b>50.5</b> [ $\pm 1.9$ ]
UKESM-pi	<b>36.1</b> [ $\pm 3.1$ ]	<b>51.9</b> [ $\pm 3.2$ ]
UKESM-hist	<b>36.0</b> [ $\pm 3.9$ ]	<b>51.8</b> [ $\pm 3.3$ ]
GC3 N96-pi	<b>35.5</b> [ $\pm 1.8$ ]	<b>51.8</b> [ $\pm 2.3$ ]
GC3-hist	<b>35.7</b> [ $\pm 2.1$ ]	<b>51.5</b> [ $\pm 2.8$ ]
HOWI (ERA5)	<b>29.5</b> [ $\pm 2.3$ ]	<b>49.3</b> [ $\pm 2.4$ ]



**Figure 5.9:** Precipitation anomalies (color contours) and the moisture flux vectors calculated from the product of specific humidity ( $q$ ) and wind ( $\vec{u}$ ) at 850 hPa. (a, b) shows the difference between the 10 days after monsoon onset and 10 days prior to MO using (a) the WT and (b) the dates estimated using the HOWI index. (c, d) are as defined in (a, b) but for MR. The dates are calculated from ERA5 data averaged over the box in panel b).

Figure 5.9 shows the differences between the WT (based on ERA5 precipitation) and HOWI methods in their characterisation of the meteorological changes associated with onset and retreat. The comparison of precipitation and moisture fluxes at 850 hPa anomalies 10 days prior to and following monsoon onset and retreat show that the HOWI index better captures the moisture transport in the Arabian Sea whereas the WT method best captures precipitation differences over mainland India. The HOWI index characterisation of the moisture flux in the Arabian Sea may be out-of-phase with precipitation over mainland India, and this lag could possibly explain some of the results of Table 5.2.

The WT method is also able to capture onset and retreat dates and the associated anomalies within the climate model output. Figure 5.10 shows the precipitation and moisture transport anomalies around the onset and retreat of the Indian monsoon in

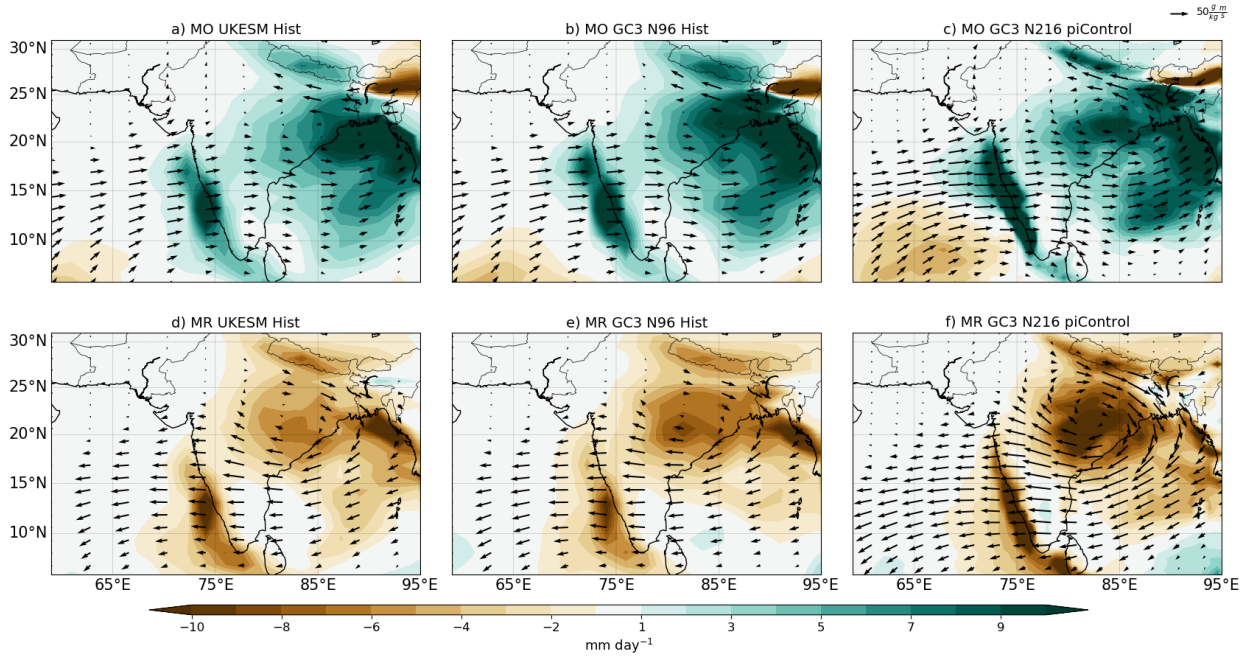


**Figure 5.10:** As in Figure 5.9 but showing onset and retreat for three different climate model experiments: (a, d) UKESM1 historical, (b, e) HadGEM3 GC3.1 N96 historical, (c, f) HadGEM3 GC3.1 N216 piControl.

three different climate model experiments. While the models show significant biases in the timings of the monsoon, according to a Welch's t-test (Table 5.2), the patterns of rainfall and moisture transport anomalies to the observations around both onset and retreat agree well with reanalysis.

The spatial distribution of the mean onset and retreat dates of the Indian monsoon as characterized by the WT method (Figure 5.11) shows that the mean onset and retreat dates vary greatly spatially on the southern tip of the subcontinent. While most of northern India has a mean onset date around pentad 33, the western coast shows an earlier onset by about one or two pentads. There is high agreement in the onset date between the three observational datasets and the reanalysis over mainland India and between TRMM and ERA5 over the western coast of India. The earliest onset is found on the western coast around pentad 25-27 and extending to central India by pentad 31. The GC3 N216 simulation, however, shows a later onset than observed by about two pentads in most regions. In contrast, the spatial pattern for the mean retreat date shows higher spatial variability between the western and eastern coasts of India. CHIRPS shows the latest retreat dates

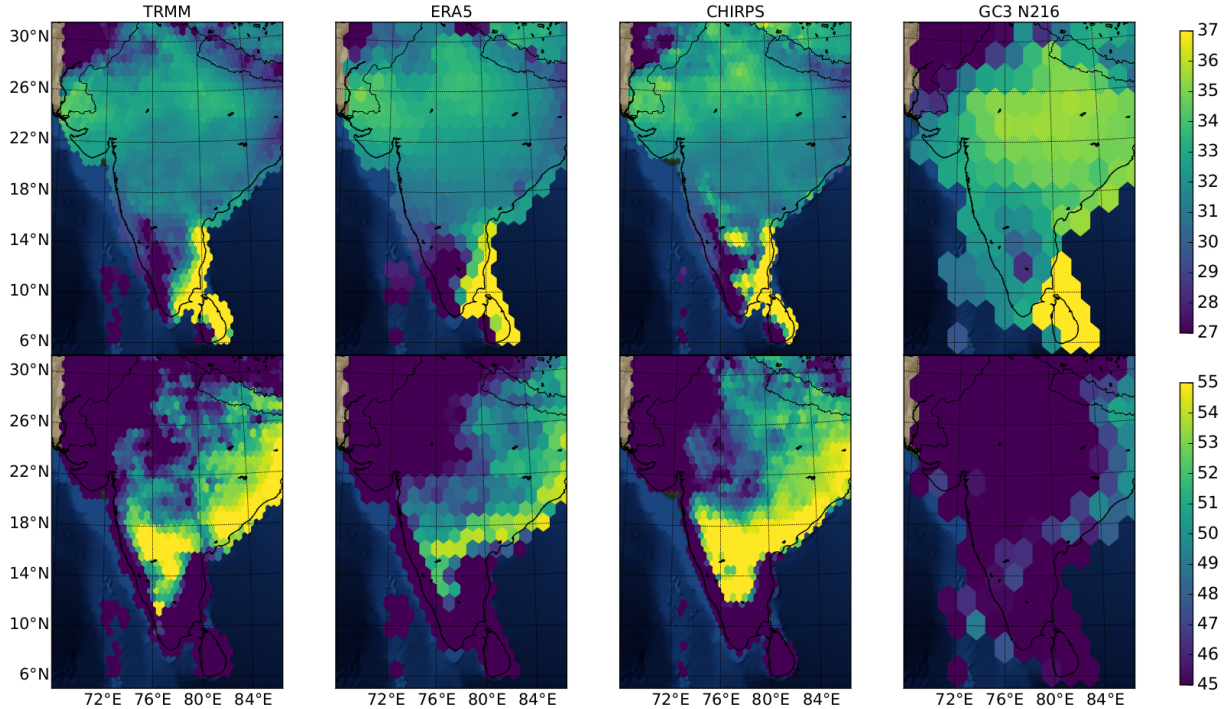


**Figure 5.11:** As in Figure 5.7 but for the Indian Monsoon.

over the south-central states when compared to TRMM and ERA-5.

### 5.4.3 The midsummer drought

Results from the application of the wavelet transform to the MSD, including the mean onset and retreat dates as well as the start and end dates of the MSD period, are reported in Table 5.3. The mean onset date in the observations is around pentad 27 (May 14), whereas the retreat date is around pentad 61 (October 31). The end of the so-called first-peak period, or start of the relatively drier period (MSD), referred to in this thesis as MSD onset (MSDO) is consistently found in all the observed datasets to be around pentad 36 (around June 29). The end of the drier period or start of the second peak, referred to in this thesis as MSD end (MSDE) is also consistently determined to be between pentads 48 to 49 in the four observational datasets. In other words, the MSD has a mean duration of 12 pentads, or around two months, from late June to late August. In the MOHC simulations, the MSD starts slightly later than observed by about two pentads, and ends about one pentad later than observed around September 10.

**Table 5.3:** Mean pentads of monsoon onset (MO), rainfall retreat (MR), MSD Onset (MSDO) and MSD End (MSDE) in the MSD region [11-19°N, 95-85°W, illustrated in Figure 5.12a.] estimated through the WT method. Pentad 35 corresponds to the period between June 22-27 and pentad 52 to the period Sep 13-18. The model dates shown in bold are statistically different from CMAP and CHIRPS results to the 99% confidence level according to a Welch's t-test.

Dataset	MO	MR	MSDO	MSDE	coef1	coef2
TRMM	25.8 [±2.2]	61.6 [±3.1]	35.9 [±2.4]	49.0 [±4.1]	-9.5 [±4.2]	10.4 [±5.4]
CMAP	26.7 [±1.9]	60.6 [±3.3]	36.5 [±2.6]	48.0 [±4.2]	-7.1 [±4.2]	7.7 [±4.3]
CHIRPS	26.7 [±2.3]	61.4 [±3.1]	36.5 [±2.7]	48.3 [±3.5]	-4.7 [±2.7]	5.5 [±3.2]
ERA-5	26.5 [±2.2]	61.8 [±3.2]	36.1 [±2.7]	48.8 [±3.5]	-10.7 [±5.4]	11.8 [±6.6]
UKESM-pi	27.4 [±2.4]	61.9 [±3.2]	<b>38.2</b> [±2.7]	<b>49.1</b> [±2.7]	-18.2 [±8.7]	14.6 [±8.0]
GC3 N96-pi	26.9 [±2.6]	62.3 [±3.5]	<b>37.8</b> [±2.1]	<b>49.9</b> [±3.1]	-21.7 [±9.4]	16.8 [±8.0]
GC3 N216-pi	26.9 [±2.3]	62.2 [±3.5]	<b>38.4</b> [±2.1]	<b>50.0</b> [±2.7]	-23.5 [±8.0]	14.1 [±6.7]
GC3-hist	26.9 [±2.7]	<b>62.8</b> [±3.7]	<b>37.8</b> [±2.4]	<b>50.3</b> [±2.6]	-19 [±8.7]	17.1 [±8.4]
UKESM-hist	<b>28.5</b> [±2.7]	<b>62.8</b> [±3.5]	<b>38.7</b> [±2.8]	<b>50.1</b> [±2.7]	-20.3 [±10.1]	14.9 [±8.3]

Figure 5.12 shows the rainfall anomalies associated with the different periods (stages) of the rainy season in southern Mexico and Central America. These include monsoon onset and retreat, and the start and end of the MSD, the MSDO and MSDE, respectively. For each stage, we compared the anomalies computed by separating the stages using the WT method or the dates of the climatological monsoon onset, retreat, MSDO and MSDE as found in Table 5.3. In this way, the ability of the WT method to characterise rainfall variations is tested against a first best guess – the climatological mean dates.

Overall, using the dates for MSDO and MSDE from the climatological dates results in weaker anomalies than compositing via the specific dates for each year obtained with the WT method. Even though the area-averaged signal used to diagnose the different MSD stages focuses on a small region of southern Mexico and northern Central America, the anomalies associated with the onset and end of the MSD (Figures 5.12f, h) extend

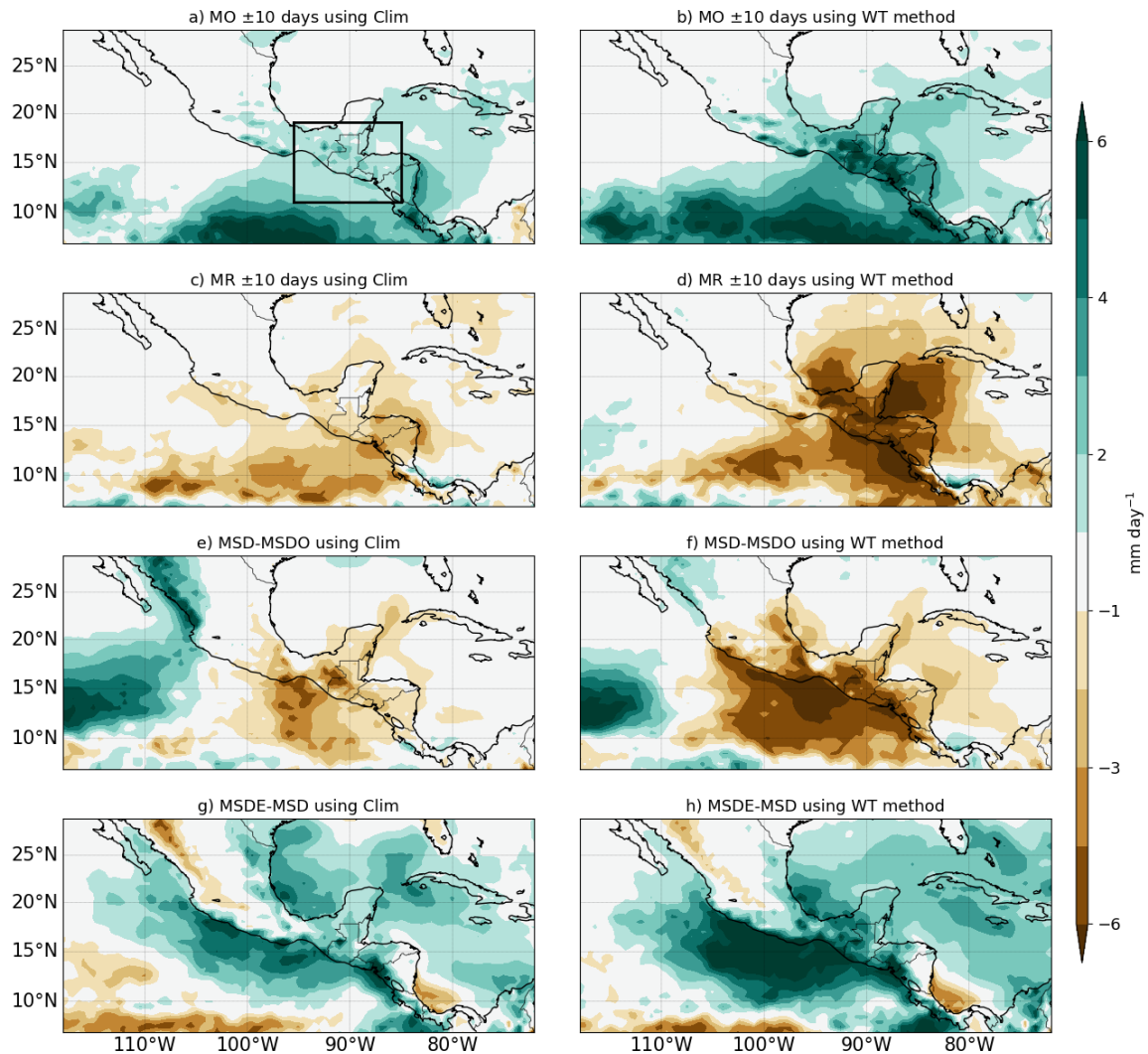


**Figure 5.12:** Precipitation anomalies for (a, b) the difference between the 10 days after monsoon onset and 10 days prior to onset (MO) using (a) the climatological dates of onset and (b) the dates estimated using the WT method. (c, d) are as in (a, b) but for monsoon retreat. (e, f) Difference between the Midsummer Drought (MSD) and the 10-day mean prior to the onset of the MSD (MSDO). (g, h) as in (e, f) but showing the difference between the end of the MSD (MSDE) and MSD. The data and calculations are from ERA-5. The black rectangle in a) shows the MSD area used to average the precipitation throughout this study.

across the East Pacific warm pool, most of the western coast of Mexico and into to the Caribbean Sea and Cuba. This result suggests that the MSD is part of a regional-scale process on the result of local-scale processes.

The analysis of individual years of observed precipitation in the selected area-averaged time-series showed that not all years showed a bimodal signal in the area-averaged pre-

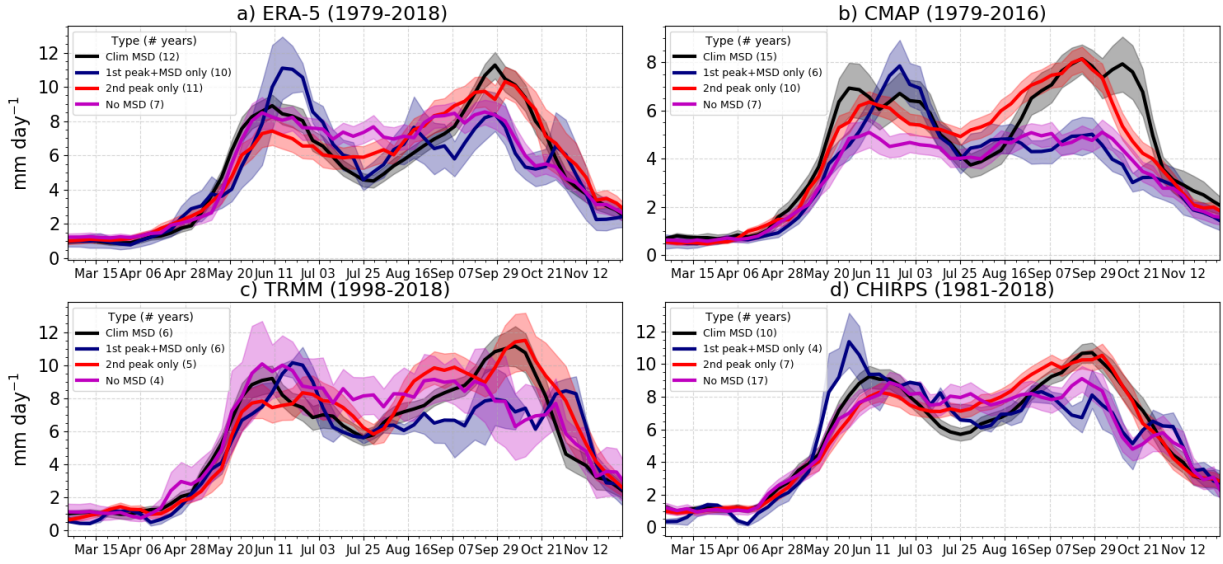


**Figure 5.13:** Pentad-mean precipitation in years differentiated by MSD characteristics in four datasets: (a) ERA-5, (b) CMAP, (c) TRMM and (d) CHIRPS. The shading for each line represents first to third quantile of the distribution provided a bootstrapping with replacement all the years in each composite 10000 times.

cipitation (Fig. 5.13). In fact, a given year could be classified as having (1) a canonical two-peak structure separated by an MSD, (2) only having a first peak and an MSD but no second peak, (3) only having a second peak but no clear MSD or (4) a plateau-like monsoon season with no MSD-type variations (see Fig. 5.13).

Due to this year-to-year variability in the characteristics of the seasonal cycle, an objective measure was defined to determine whether a signal presented a robust MSD-bimodal seasonal cycle. For this purpose, the WT algorithm was applied to randomly generated precipitation time-series. The random time-series are constructed by randomly sampling observations in the wet and dry seasons. The pentad-mean onset and retreat dates from Table 5.3 were used to composite the observations into dry and wet distributions.

For a random time-series that aims to mimic one year of precipitation, the rainfall values for each pentad in the year are randomly selected from the dry or wet distributions, depending on the pentad. In this way, the value of a given pentad of the random time-series may have been observed at a different pentad; the only constraint is that the random values come from pentads that were observed in the same season: dry or wet. The logic behind this approach is that in most monsoon regions, the peak monsoon rainfall should

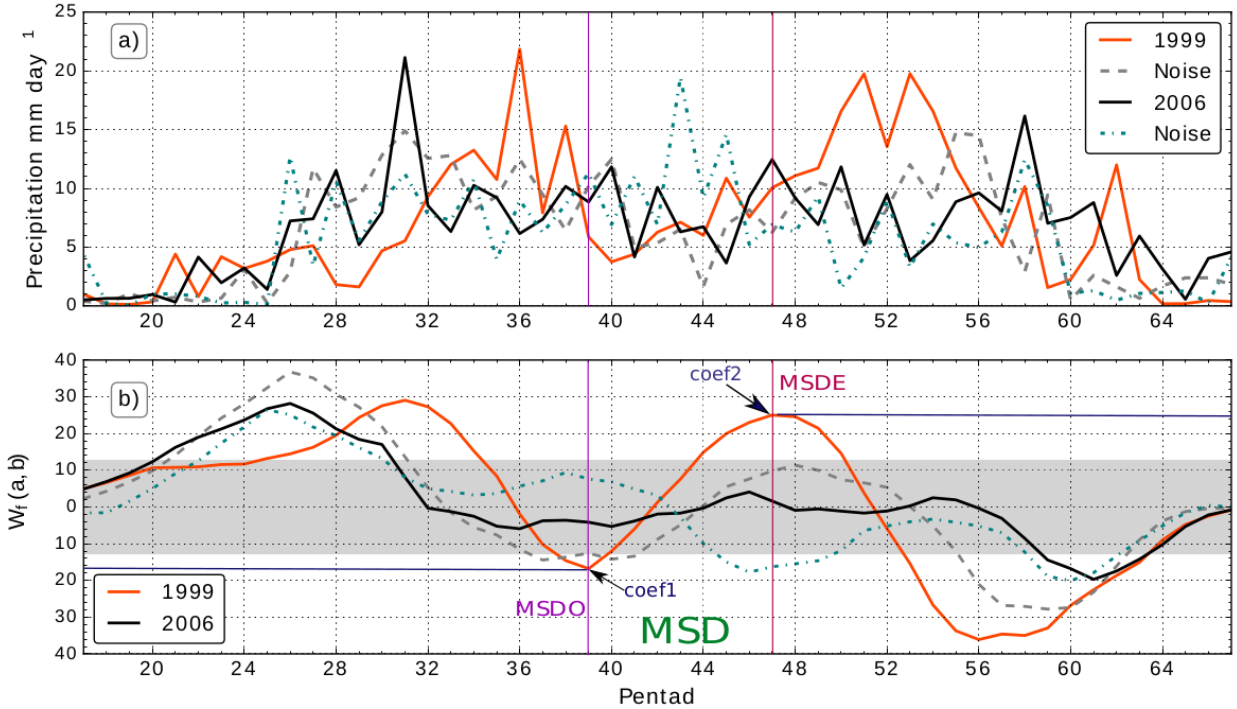


**Figure 5.14:** (a) Pentad-mean precipitation in two years of TRMM data: 1999 and 2006 and two randomly generated precipitation time-series (see text). (b) Sum of the wavelet transforms of the time series in (a). The shaded region in gray in (b) corresponds to the interval between the first quantile of  $coef1$  and the third quantile of  $coef2$  of 10,000 random timeseries constructed with TRMM data. The onset (MSDO) and end (MSDE) of the relatively drier period, as well as the location and values of  $coef1$  and  $coef2$  for 1999 are labelled in (b).

follow a plateau, see for example the North and South American monsoons in Figure 4.9 in the previous chapter. However, a bimodal regime would show a notable decrease in precipitation in the middle of the rainy season, such that it cannot be explained by the inherent short-scale variability of rainfall.

This approach has two advantages. First, that the random time-series impose a monsoon-like feature with a sharp wet-dry season contrast but secondly, the random selection in the wet season removes the possible signal of the MSD in the climatological rainfall. The random time series are then constructed by randomly drawing values at each pentad from the wet or dry season distributions of each dataset. Then, the WT method was used on 10,000 of these random-time series. This approach rendered a distribution of coefficients ( $coef1$  and  $coef2$ ) essentially representing the variability of the WT method applied to noise.

Figure 5.14 shows the pentad-mean time-series from two years in the TRMM dataset,

and two randomly generated time-series. The coefficients  $coef1$  and  $coef2$ , illustrated in Figure 5.14b, measure the difference in precipitation between the first peak and the MSD period and the MSD and the second peak, respectively. The first quantile of  $coef1$  and the third quantile of  $coef2$  provide a measure of robustness for the observed  $coef1$  and  $coef2$ . In other words, for a year to be classified as having a robust MSD signal, the resulting  $coef1$  and  $coef2$  of the WT procedure must be lower and higher, respectively, than those obtained for a random time-series. The analysis of  $coef1$  then determines the existence of a first-peak MSD type variability and  $coef2$  determines the robustness of a possible second-peak for that year. By this procedure, a given year could fit into four categories:

- Canonical MSD:  $coef1$  lower than the first quartile (25%) of random  $coef1$  and  $coef2$  higher than the third quartile (75%) of random  $coef2$ .
- 1st peak+MSD:  $coef1$  lower than the first quartile of random  $coef1$  but  $coef2$  lower than the third quartile of random  $coef2$ . In other words, the second peak is not distinguishable from noise.
- 2nd peak only:  $coef1$  higher than the first quartile of random  $coef1$  but  $coef2$  higher than the third quartile of random  $coef2$ . In other words, the second peak is distinguishable from noise, but there is no first-peak + MSD structure.
- No MSD:  $coef1$  higher than the first quartile of random  $coef1$  and  $coef2$  lower than the third quartile of random  $coef2$ . In other words, the precipitation time-series shows no robust signal of an MSD regime, with a first or second peak.

Figure 5.13 shows how separating years into these categories affects the pentad-mean seasonal cycle of precipitation in southern Mexico and Central America in four observational datasets. This figure also validates the above procedure as the WT method is able to robustly separate years into the different categories.

For each dataset we determine those grid-points showing a robust MSD. We use the method outlined above to construct the random time-series for each grid-point and estimate the random values of  $coef1$  and  $coef2$ , repeating the procedure 10,000 times. A given

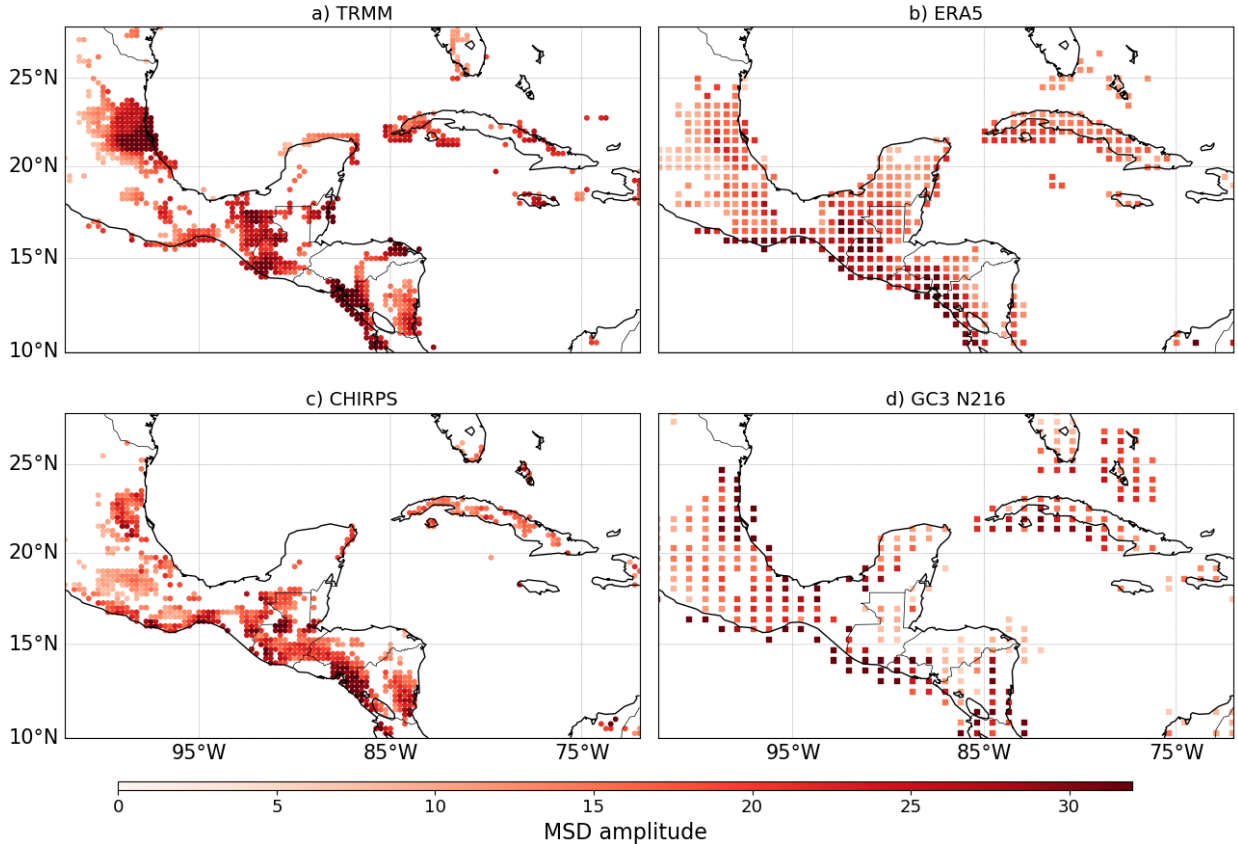


**Figure 5.15:** Grid points where the MSD is significantly different, i.e. outside the first and second quartiles of the random distribution, from noise (see section 3.3) for a) TRMM, b) ERA5, c) CHIRPS and d) GC3 N16-pi. The magnitude of the MSD, measured as  $coef2 - coef1$  is shown in colour shading.

grid-point is diagnosed to have a robust MSD when the value of  $coef2 - coef1$  is higher than the third quartile of the PDF of the random time series. The value of  $coef2 - coef1$  is a measure of the magnitude of the MSD since  $coef2$  measures the relative strength of the second-peak compared to the MSD and therefore positive in an MSD grid-point and  $coef1$  compares how dry the MSD is relative to the first-peak and thus negative if an MSD regime is observed at that grid point.

Figure 5.15 shows the regions where the climatological rainfall shows a MSD signal that is distinguishable from noise, i.e., regions where the values of  $coef2 - coef1$  exceed the third quartile of the distribution composited with random time-series, as well as the magnitude of the MSD for the TRMM, ERA5, CHIRPS and the GC3 N216 piControl simulation. Cuba, western Central America and most of southern and central-eastern Mexico exhibit a robust

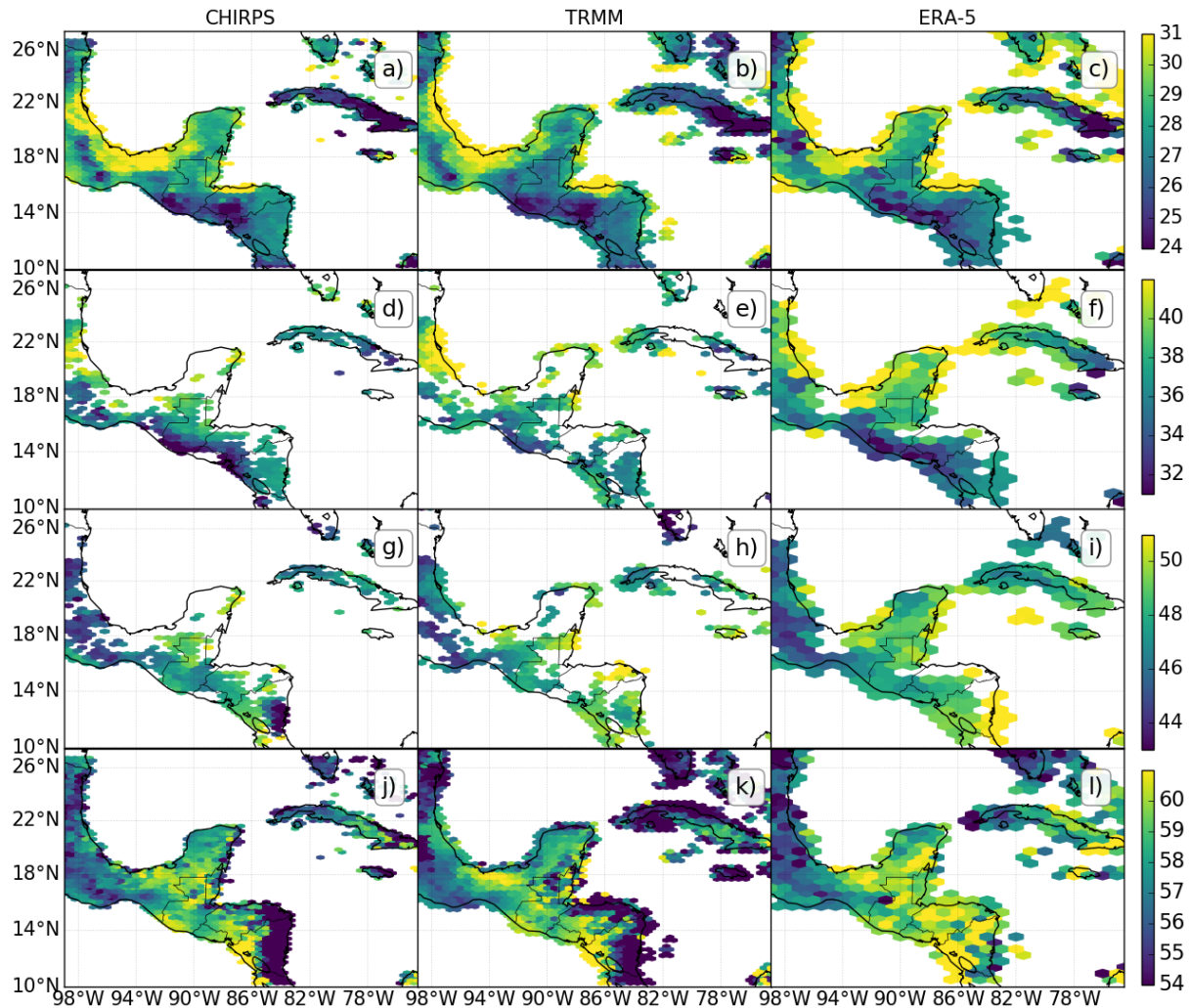


**Figure 5.16:** Spatial distribution of pentad dates of the timings of the summer rainfall season in the MSD region, showing (a-c) MO dates and (d-f) MSDO dates, (g-i) MSDE and (j-l) MR for (left) CHIRPS, (middle) TRMM and (right) ERA-5.

MSD signal. This map also shows that the strongest MSD signal is found on the western coast of northern Central America and northeastern Mexico. The high correspondence between the three observational datasets shows that the method is robust across datasets. These results agree well with previous studies on the spatial distribution of the MSD (Magaña et al., 1999; Perdigón-Morales et al., 2018; Anderson et al., 2019; Zhao and Zhang, 2021). In particular, the method is able to replicate the previously reported MSD signal in the Pacific Mexican coast and the stronger MSD signal in northeastern Mexico.

Figure 5.16 shows the spatial distribution of the mean onset and retreat pentads and the

start and end of the MSD, in the grid-points where the signal is significant as in Fig. 5.15. The earliest rainfall onset is found on the western coast of southern Mexico, Guatemala and El Salvador, as well as in Cuba, at pentad 25, whereas onset in the Yucatan peninsula is found at pentad 28 and even later, around pentad 31, in the eastern states of Mexico. In contrast, the retreat date seems spatially more homogeneous as northern Central American has a mean retreat date around pentad 59 and central Mexico around pentad 54. The MSD coherently starts over the western coast of Guatemala and Chiapas around pentad 33. In contrast, the MSD on the eastern Mexican states of Veracruz and Campeche begins after pentad 40. The earliest MSD end (Figs. 5.16h-j) is found in central and northeastern Mexico, around pentad 42 whereas the MSD in Guatemala ends around pentad 48.

## 5.5 Summary and discussion

The assessment of the AMS in the MOHC submissions to CMIP6 in Chapter 4 lacked a robust analysis of the representation of the timings of the monsoon. The principal reason for this shortcoming was the lack of a robust, wide-spread method to diagnose onset and retreat dates in the various regions of the AMS with the various datasets available. This chapter aimed to address this issue by developing a new method to compute onset and retreat dates for the purpose of intercomparison between multiple observational and model data.

The novel method described in this chapter uses pentad-mean precipitation data to compute a wavelet transform over multiple temporal scales from which a set of coefficient and diagnostics are used to determine onset and retreat dates. The wavelet function used is the Haar wavelet, a wavelet typically used to find abrupt changes in signals. Onset is defined as the maximum of the sum of the coefficients of the wavelet transform computed over a range of temporal scales or dilations. These dilations were found to provide the best results in a range from 28 to 54 pentads. Monsoon retreat is similarly defined but using the minimum of this sum of wavelet transform coefficients. The use of this method is illustrated using multiple observational datasets and climate model output. The method is compared to existing methods to find onset and retreat dates in three monsoon regions.

The method performs favourably to existing methods that use precipitation thresholds in the North American Monsoon, as shown by the anomalies of precipitation, wind and geopotential around the onset and retreat dates. The spatial distribution of monsoon onset and retreat in this region was found to be sensibly captured by the wavelet algorithm, illustrating the earlier onset in central western Mexico and the later onset in northwestern Mexico, Arizona and New Mexico. The spatial distribution of onset and retreat dates was diagnosed to be very similar between the TRMM, CHIRPS and ERA5 datasets, which suggests that the method produces similar results in datasets with different resolutions and climatologies. This result also suggests that the method is robust to be used at the grid-box scale, and not just for region-averaged time-series.

The WT method also compares well to a hydrologically defined index (HOWI) in the Indian Monsoon, although the WT better captures the precipitation variations whilst HOWI betters captures changes to the moisture transport. However, the WT method is also able to capture strong differences in moisture transport around the onset and retreat dates, in both models and observations. The WT method obtains a later onset and retreat as compared to the HOWI index, which is possibly associated with a lag between the moisture transport about the Arabian Sea (as diagnosed by HOWI) and the precipitation over mainland India (as measured by the WT method). The spatial distribution of onset and retreat dates in the Indian Monsoon region, diagnosed using the WT method seems to be relatively consistent and coherent amongst the observational datasets, as the mean onset date in mainland India was found at pentad 32. Onset is earliest on the western coast of India and the onset date appears to be very homogeneous in central India.

The WT method was extended to characterise the timings and strength of the Midsummer Drought (MSD), using the same principle as for determining onset in the Indian monsoon, but computing the WT over smaller dilations around the onset and retreat dates. By using randomly-generated time-series, the spatial distribution of grid-points displaying a robust MSD signal was found in Cuba, the northwestern coast of Central America and several regions of south and north-eastern Mexico. The MSD in southern Mexico and northern Central America is found to start around pentads 35 and 36 (last week of June) and end around pentad 48 (mid-August) in most observational datasets and the ERA5 reanalysis.

To our knowledge, this extension of the WT method provides one of the very few methods for characterising the MSD on sub-monthly scales.

The WT method is in many ways similar to the agronomical and threshold methods (e.g. Liebmann and Marengo, 2001; Moron and Robertson, 2014), as the implementation of the method uses a subjective determination of the dilation scales; these scales are comparable to the persistence and window parameters of the threshold methods. However, the WT method presented has three main advantages over most threshold methods. First, the method produces robust results for the Indian and North American monsoon of onset and retreat, and spatial distributions comparable to previous methods (Moron and Robertson, 2014) while not being subject to 'false-hits' nor years without an identification of the onset and retreat dates. In other words, the method provides robust results without requiring further treatment of years with false-hits or undetermined years.

The second advantage of the method is portability, or utility, as the method shows robust and consistent results for three observational datasets, a reanalysis and climate model experiments with varying climate forcing but without any constraint or treatment of the data beforehand and in three different regions with different seasonal cycles. In other words, this method is robust across datasets and regions. In contrast to rigid threshold techniques (e.g. Liebmann and Marengo, 2001), the identification of onset and retreat for each time-series, e.g. at each grid-point, is based upon coherent temporal changes within each precipitation time-series while not using parameters determined '*a priori*' specifically for a region. The WT method then, can be used in any time-series, regardless of the origin of the time-series, without any further change or consideration than those established by the dilations scales determined in section 2.2.1. The portability of the method also means that the method can be implemented as a 'local-scale' method applied at the grid-box scale for high-resolution datasets such as CHIRPS as well as for regional scales using area-averaged time-series.

Third, and in contrast to typical threshold methods, the wavelet method can be applied to climate model output straightforward using the same configuration of dilation scales, a feature of the method that is illustrated by our analysis of several experiments using the Hadley Centre models. The treatment of the data does not require any normalisation or statistical treatment even when used for grid-point time-series for different regions or

experiments with varying forcing where the seasonal cycle or total annual rainfall may change notably within the model time-series.

This chapter follows up on some missing details of the previous chapter by analysing the timings of the North American monsoon and the Central American MSD in the MOHC models by objectively computing the onset and retreat dates with the WT method. The results confirm that the CMIP6 MOHC models reasonably simulate the seasonal cycle of rainfall in North American monsoon and the MSD regions. Moreover, this chapter provides the main tool to be used in the following chapter, which aims to better understand the physical mechanisms behind the MSD, a question that would be difficult to address without the existence of a robust method for determining the timings of the MSD on the pentad-scale.

# 6

## The Midsummer drought in the MOHC CMIP6 experiments

This chapter investigates the mechanisms associated with the bimodal seasonal cycle of precipitation, also known as Midsummer drought (MSD), of southern Mexico and Central America using CMIP6 experiments produced by the Met Office Hadley Centre. The chapter evaluates three theories for the MSD that exist in the literature: SST and cloud-radiative feedbacks, the double crossing of the solar declination angle and the moisture transport associated with the Caribbean Low-Level Jet (CLLJ). The wavelet transform method, introduced in the previous chapter, is used to evaluate the timings of the monsoon in the region and characterise the physical changes that are relevant for the MSD.

### 6.1 Introduction

A bimodal signal in the climatological seasonal cycle of precipitation has been documented in several regions of southern Mexico, Central America and the Caribbean; most commonly referred to as Midsummer drought (MSD Mosiño and García, 1966; Magaña et al., 1999; Gamble et al., 2008; Perdigón-Morales et al., 2018; Zhao et al., 2020). Since the first observational descriptions of the MSD, research has aimed to understand the physical mechanisms that cause the two-peak structure of precipitation (e.g. Hastenrath, 1967;

Magaña et al., 1999; Curtis, 2002; Herrera et al., 2015; Maldonado et al., 2017; Straffon et al., 2019; Perdigón-Morales et al., 2019; Zermeño-Díaz, 2019). Section 2.3 summarises the literature on mechanisms for the MSD, concluding that all the proposed mechanisms have shortcomings and have received criticism that question the extent to which these theories can explain the spatial and temporal variability of the bimodal signal.

Moreover, most global climate models from the CMIP5 cohort struggle to reasonably reproduce the seasonal cycle of precipitation in the region (Rauscher et al., 2008; Ryu and Hayhoe, 2014) which has limited their use to better understand these mechanisms and leading other studies to focus on regional models (Fuentes-Franco et al., 2015; Cavazos et al., 2020). Less attention has been given as to why some GCMs reproduce the bimodal seasonal cycle; for instance, Ryu and Hayhoe (2014) analysed how biases in large-scale features of CMIP3/5 models such as the North Atlantic Sub-tropical High could influence the representation of the MSD. Chapters 4 and 5 show that the CMIP6 MOHC simulations reproduce the timings and strength of the bimodal signal of precipitation with reasonable skill (Figure 6.1), albeit with a stronger first peak and a later onset of the MSD.

The lack of agreement in the literature on the leading mechanism for the bimodal seasonal cycle of precipitation and the good representation of the spatial and temporal characteristics of the MSD in the MOHC CMIP6 experiments are the main motivation for this chapter. This chapter aims to increase our understanding of the physical mechanisms associated with the MSD of southern Mexico and northern Central America, also referred to as Mesoamerica, by diagnosing relevant processes that are represented in these MOHC CMIP6 experiments.

Three leading hypotheses (section 2.3) are investigated for the MSD of southern Mexico and Central America: the SST-cloud-radiative feedback proposed by Magaña et al. (1999), the solar declination angle hypothesis (Karnauskas et al., 2013) and the CLLJ as a modulator for moisture transport and convective activity in Mesoamerica (Herrera et al., 2015; Zermeño-Díaz, 2019). The main features of the three mechanisms are illustrated in Figure 6.2. Briefly, the cloud-radiative feedback mechanism (Fig. 6.2a) proposes that the peaks and trough of precipitation in the seasonal cycle are a result of a similar seasonality in the East Pacific SSTs and surface humidity. During the first peak of precipitation, cloud radiative effects block shortwave solar radiation from reaching the surface in addition to increased latent

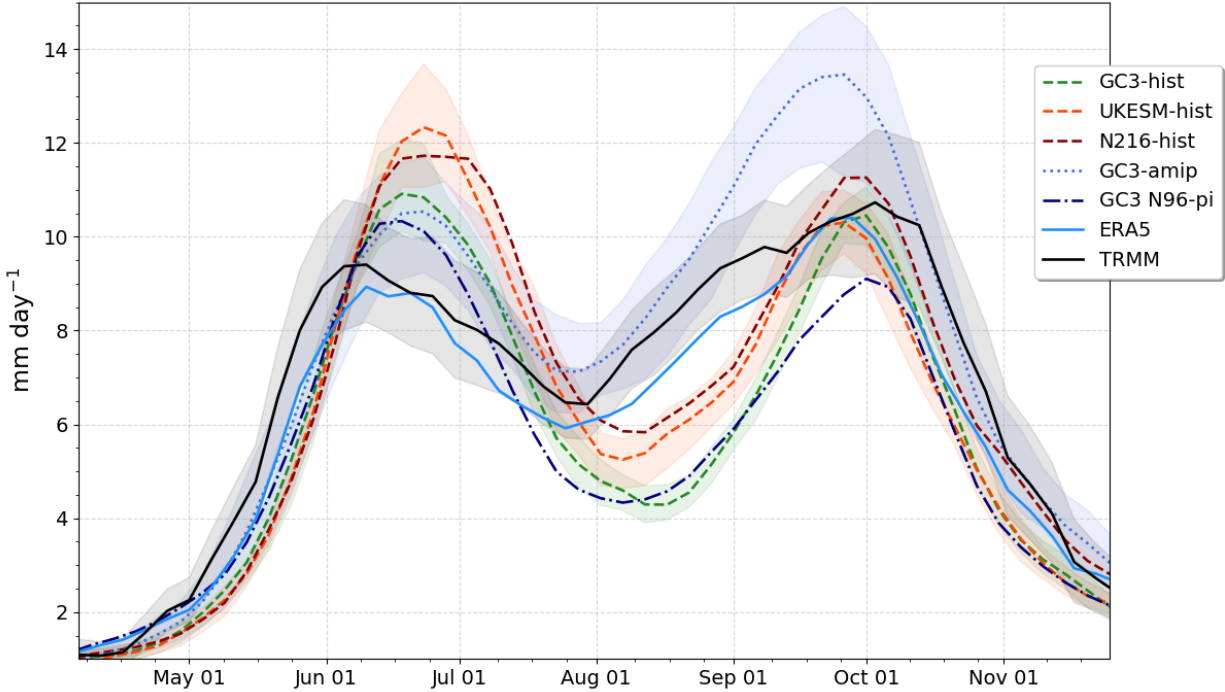


**Figure 6.1:** Pentad-mean precipitation in southern Mexico and northern Central America [95–86°W, 11–19°N]. The shading for the TRMM dataset is a measure of observational uncertainty obtained by bootstrapping the interannual variability whereas the shading for the CMIP6 experiments show the ensemble spread where multiple ensemble members were available.

heat fluxes from the ocean to the atmosphere cooling the SSTs and leading to a decrease in convective activity and precipitation in the MSD. During this drier period, incoming shortwave increases again and raises East Pacific SSTs above 29°C and surface humidity leading to the second peak of precipitation.

The solar declination angle hypothesis (Fig. 6.2b) argues that total shortwave radiation absorption at the surface is the key element that controls the surface energy balance and the strongest control of the seasonal cycle of incoming shortwave is the solar declination angle. The total shortwave absorption by the surface modifies the surface moist static energy, specifically the surface moisture, which in this framework is the ultimate control of precipitation. In Central America, the solar declination angle crosses twice during the summer, once at the start and once at the end, and evidence by Karnauskas et al. (2013) suggests that precipitation follows the solar declination angle and surface moist static energy with a lag of a few weeks.

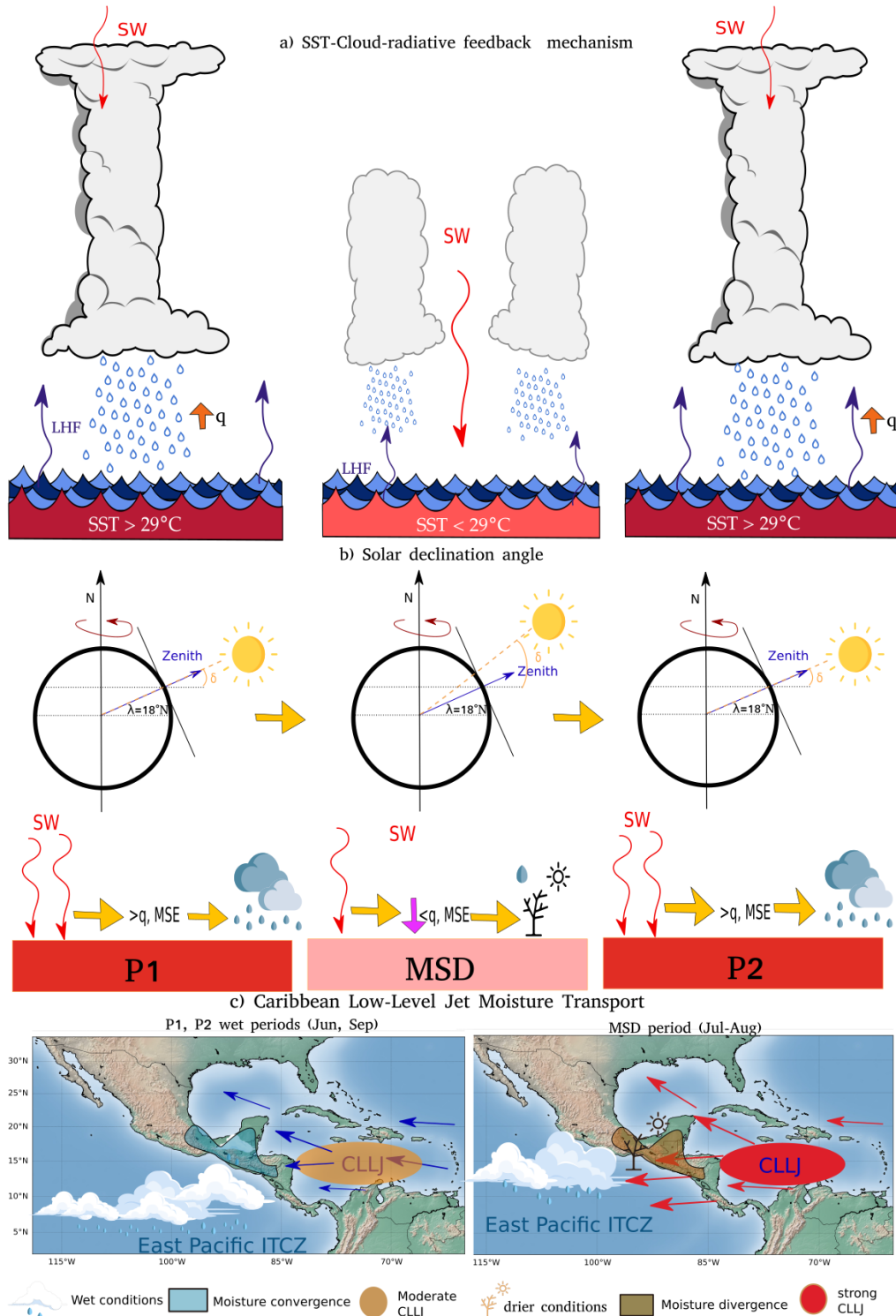


**Figure 6.2:** Schematic of the three mechanisms analysed in this chapter, a) the SST cloud-radiative mechanism, (b) the solar declination angle and (c) the moisture divergence mechanism driven by the CLLJ. In all panels, three stages of the MSD are represented (left) the first peak period, (middle) MSD and (right) the second peak period.

Finally, the third mechanism investigated in this chapter argues that the seasonal cycle of the CLLJ, possibly influenced by the seasonal variations to the North Atlantic Subtropical High, modifies moisture transport in the region (Fig. 6.2c). In particular, studies have noted that the increase in the jet strength at the midsummer coincides with a reduction of rainfall over mainland, the MSD. This argument appears more frequently in studies to explain the MSD of the Caribbean (e.g. Martinez et al., 2019), but suggestions have also been made that the CLLJ variations could control the total moisture transport over the continent (Herrera et al., 2015). Specifically, the hypothesis is that, in July, the strengthening of the CLLJ decreases the convergence of moisture over the continent and the total water content over western Central America, which ultimately explains the slight decrease in precipitation during the MSD.

The remainder of this chapter is presented as follows. Section 2 describes the observational data and the CMIP6 experiments used in this chapter and an overview of how the WT method is implemented to diagnose the timings of MSD. Then, section 3 evaluates the representation of the key features of the regional climate in the CMIP6 experiments and in ERA5. Then, the roles of the East Pacific SSTs (section 4), cloud-radiative effects and surface shortwave absorption (section 5) and the CLLJ and moisture transport (section 6) are investigated using composite and regression analysis. Finally, a short investigation of the MSD using the moist static energy budget is given in section 7. A summary and discussion is presented in the final section of this chapter.

## 6.2 Data and methods

### 6.2.1 Observations and reanalysis data

All the data used in this chapter are described in chapter 3. In particular, this chapter uses the gridded precipitation datasets of TRMM and CHIRPS. However, the main precipitation dataset will be the reanalysis ERA5. The remaining diagnostics are taken from ERA5 at the  $0.75^\circ$  resolution and for the period 1979-2019. ERA5 precipitation data is used throughout this chapter to compare against the models, and not observed datasets, because of two reasons. Firstly, observational (satellite or surface station) data of all diagnostics are not

available on long periods at the daily resolutions required for this study, for example of the wind flow or moisture profiles over the ocean region. Secondly, ERA5 precipitation in the MSD region closely follows TRMM and CHIRPS (Fig. 6.1), and the previous chapter shows that ERA5 reasonably reproduces the mean timings for the MSD compared to TRMM and CHIRPS. Therefore, ERA5 can be compared to the simulations as another model; one that is more realistic as the reanalysis is partially driven by the observed state of the atmosphere through the assimilations of radiosondes taken in the region as well as satellite data of various quantities (Hersbach et al., 2020).

### 6.2.2 CMIP6 data

This chapter uses the output from realizations of the HadGEM3 GC3.1 run at two resolutions at N96 and N216 and from UKESM1. These experiments are described in section 3.2.2 and summarised in Table 3.2. This chapter follows the terminology and acronyms outlined in section 3.2.2. In addition to the pre-industrial, AMIP, and historical experiments used in previous chapters, this chapter uses experiments from the Cloud-Feedback MIP (CFMIP) (Webb et al., 2017) and ScenarioMIP (O'Neill et al., 2016) activities of CMIP6 (see Table 3.2). These are the GC3-amip lwoff, amip-p4K and amip-m4K from CFMIP, all run at N96 resolution for HadGEM3, and SSP1, SSP2 and SSP5 from the ScenarioMIP for UKESM1, HadGEM3 N96 and N216.

### 6.2.3 Determination of the timings of the MSD

Chapter 5 describes a wavelet transform (WT) method that can determine the timings of the MSD in observational gridded datasets, reanalysis and climate model precipitation time-series. This chapter uses the WT method to determine the onset (MO) and retreat (MR) of the monsoon rainy season, as well as the onset (MSDO) and end (MSDE) of the MSD. To summarise, MO and MR are determined by the maximum and minimum sum of WT coefficients computed from a dilation scale vector ranging from 24 to 54 pentads. After MO and MR are determined, a second WT is computed with dilation scales from 10 to 24 pentads and the minimum sum of the WT coefficients corresponds to the onset of the MSD and the maximum to the end of the MSD (MSDE). Similarly, the timings of the first (P1) and second

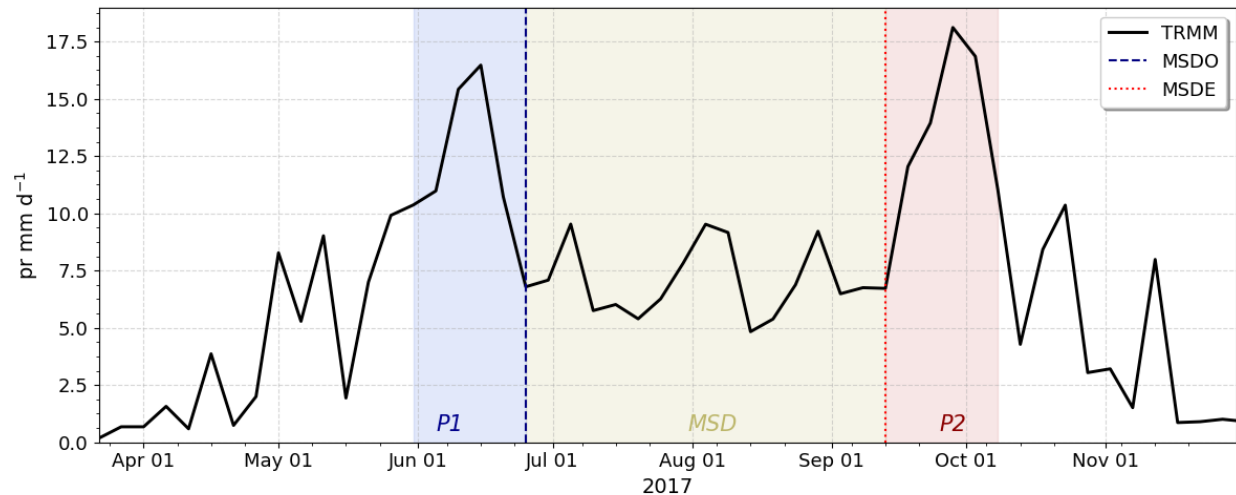


**Figure 6.3:** Pentad-mean precipitation averaged over the study region [95-86°W, 11-19°N] in the TRMM dataset for the summer of 2017. The timings of the onset (MSDO) and end (MSDE) of the MSD, as well as the first (P1) and second (P2) peak periods and the MSD periods are highlighted.

(P2) peaks of precipitation are determined from the results of the WT method: P1 is defined as the period between the MSDO and the preceding 4 pentads or 20 days, whereas the second peak is defined as the period between the date of MSDE and the subsequent 4 pentads.

An example of this separation of the MSD timings for each year is given in Figure 6.3, for precipitation observed from TRMM in 2017 over the study region. The area of study of this chapter is in southern Mexico and northwestern Central America (depicted in Figure 6.4) a region with strong and robust MSD signals (see Chapter 5). The WT method was applied to the TRMM, CHIRPS and ERA5 datasets and in the model precipitation time-series area-averaged over the study region.

### 6.3 Climatological features

The seasonal cycle of precipitation in the MSD region (Figure 6.1) is reasonably well simulated by the CMIP6 experiments and by ERA5, as shown in previous chapters. The two-peak structure of the MSD is observed in TRMM and ERA5 as two precipitation maxima, the first peak found during early to mid-June and the second peak at the end of September, separated by a drier period that spans from late June to late August. The

precipitation in ERA5 agrees well with the seasonal variation of TRMM and the mean rates during the first peak, the MSD and second peak periods.

The MSDO in the CMIP6 experiments is diagnosed one or two pentads after TRMM and ERA5 (see the mean values in the previous chapter) and shows a stronger variation of precipitation between the first peak and the MSD. A noteworthy feature is that most experiments simulate a drier MSD period but wetter peak periods. In particular, the pre-industrial control experiments show a higher magnitude of precipitation during the first peak and the MSD period whereas GC3-amp experiments are characterized by a wetter second peak.

The climatological distribution of precipitation and the temporal differences within the MSD timings in ERA5 agrees well with TRMM and CHIRPS (Figure 6.4). ERA5

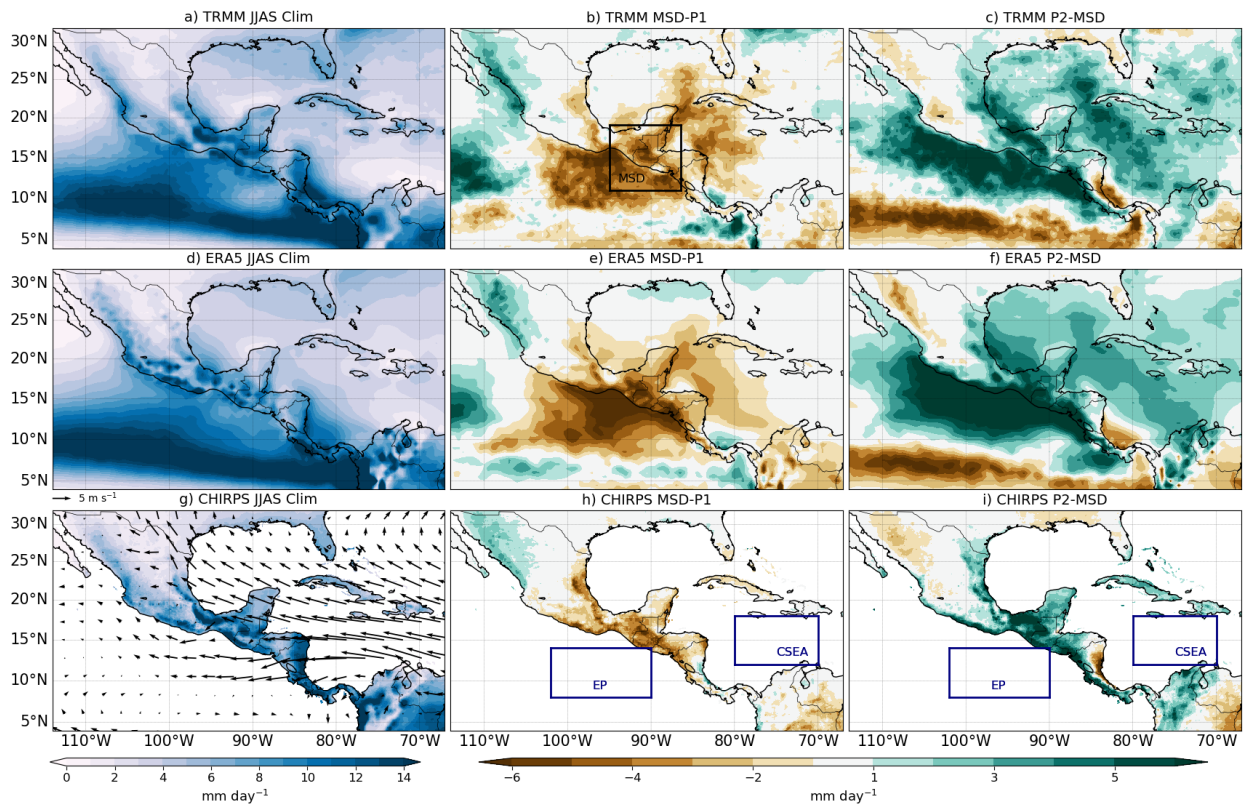


**Figure 6.4:** (a, d, g) Climatological JJAS rainfall and the difference between (b, e, h) the midsummer drought and the first peak (MSD-P1) periods and (c, f, i) between the second peak and the midsummer drought (P2-MSD) periods for (a-c) TRMM, (d-f) ERA5 and (g-i) CHIRPS. The climatological low-level winds (at 850 hPa) for JJAS in ERA5 are shown in c). The boxes in panels b, h and i show the definitions of the MSD, EP and CSEA regions that are used throughout this chapter.

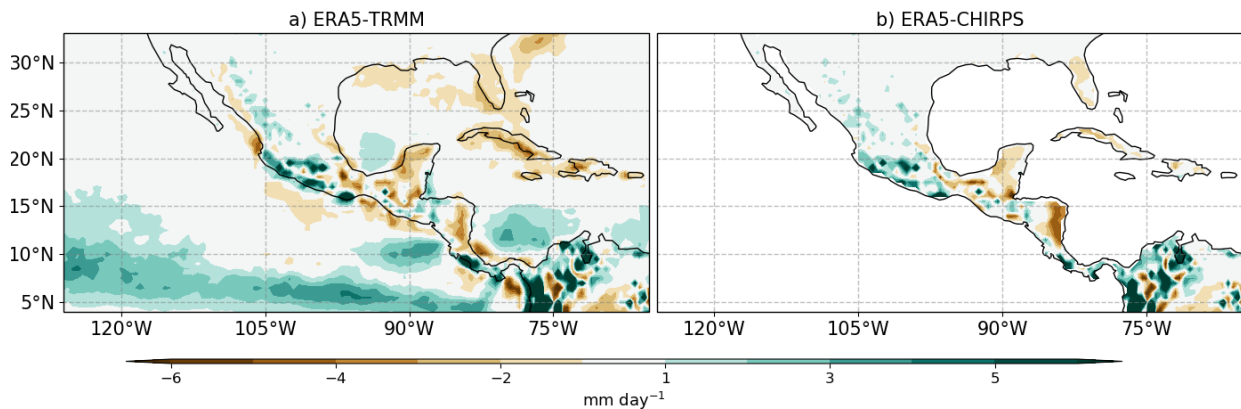


**Figure 6.5:** (a, b) JJAS precipitation biases in ERA5 when compared to (a) TRMM and (b) CHIRPS.

reasonably captures the climatology of precipitation over land but also captures the strength and position of the East Pacific ITCZ, as shown by the precipitation maximum in the easternmost Pacific (panels a, d). Specifically, the biases of JJAS-mean precipitation in ERA5 (Figure 6.5) are positive over the East Pacific Ocean and western Mexico, and negative over land in southern Mexico and Central America.

The patterns of the MSD-P1 and P2-MSD differences in ERA5 (Fig. 6.4) also agree well with TRMM. These two panels show that precipitation differences associated with the MSD measured by the area-averaged precipitation within the box in Figure 6.4b extends outside of the study region all over the Intra-Americas Seas comprising the easternmost Pacific Ocean, the entrance to the Gulf of Mexico and western Caribbean Sea, particularly in the P2-MSD panel. Notably, the strongest differences for both panels are found on the western coast of Mesoamerica.

The simulations (Figure 6.6) have important biases in the magnitude of the precipitation in the East Pacific ITCZ with a positive bias of  $3\text{-}6 \text{ mm day}^{-1}$  depending on the simulation as well as a dry bias over southern Mexico and Central America, as shown in chapter 4. These biases are much larger than the biases between ERA5 and TRMM and CHIRPS. The simulations capture the spatial patterns associated with the MSD stages, which also show the strongest differences are found on the west coast of the Mexican state of Chiapas, Guatemala and El Salvador. The negative differences in the MSD-P1 and positive differences in the P2-MSD extend to the Caribbean Sea, northeastern Mexico and the Gulf of Mexico. In

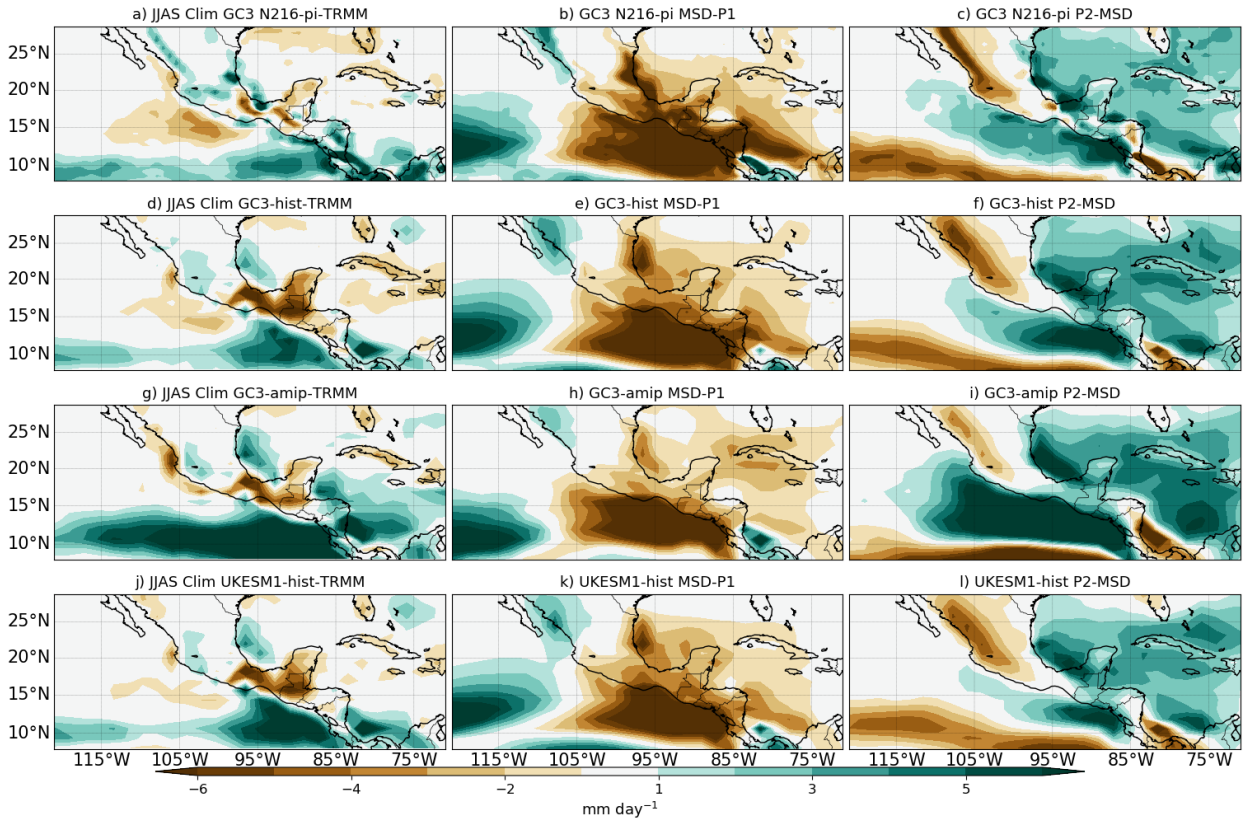


**Figure 6.6:** (a, d, g, j) JJAS model bias compared to TRMM and the difference between (b, e, h, k) the midsummer drought and the first peak periods and (c, f, i, l) between the second peak and the midsummer drought periods for four different simulations.

agreement, with ERA5 and TRMM, the simulations show that the precipitation differences in the MSD region are always opposite to that of the North American monsoon region, e.g., in Figures 6.4 and 6.6 the North American monsoon is wetter when the MSD period begins and Mesoamerica is drier.

The mean rainfall observed in the three periods (P1, P2 and the MSD) in the simulations varied notably between experiments done with different model configurations and with external forcing (Figure 6.7). The scatter of the first and second peak and the MSD mean rainfall rates shows, first, that the mean rainfall in each stage is not linearly related to another, i.e., a larger magnitude of the first peak of precipitation does not necessarily imply a wetter or drier MSD period. The atmosphere-only runs, GC3-amip, is a good example of this behaviour as the mean rainfall during P1 is roughly the same as in the rest of the simulations but the mean rainfall during the MSD is slightly larger than in the rest of the

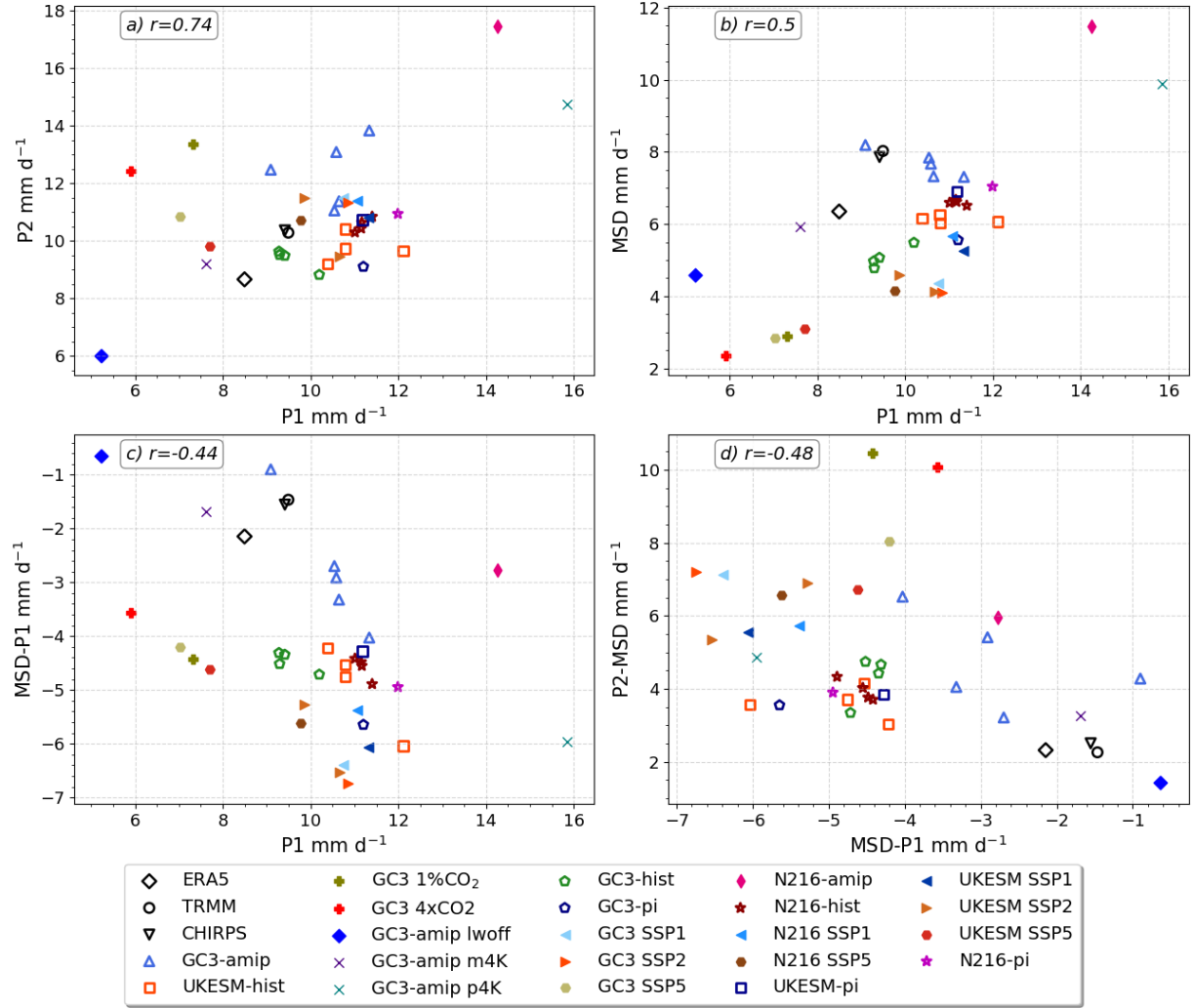


**Figure 6.7:** (a, b) Scatter plots of the mean values of precipitation [ $\text{mm day}^{-1}$ ] for TRMM, ERA5, CHIRPS and the CMIP6 experiments (see 6.2.2) during the first peak (P1), the MSD and the second peak (P2) periods and (c, d) the precipitation differences between the three periods. The region used for this averages is illustrated in Figure 6.4.

simulations and the P2 precipitation is largest in GC3-amip.

Second, the magnitude of the first decrease in rainfall (MSD-P1) and the late-summer increase (P2-MSD) also show a significant spread amongst experiments, which also suggest that there is only a modest relationship between the magnitude of the MSD and the magnitudes of the two peaks of precipitation in these simulations. The scatter of ERA5 in all panels is notably close to that of TRMM and CHIRPS, which is further evidence that the timings and strength of the MSD is well represented by this reanalysis. In contrast, the high resolution atmosphere-only run (N216-amip) shows the highest bias in precipitation

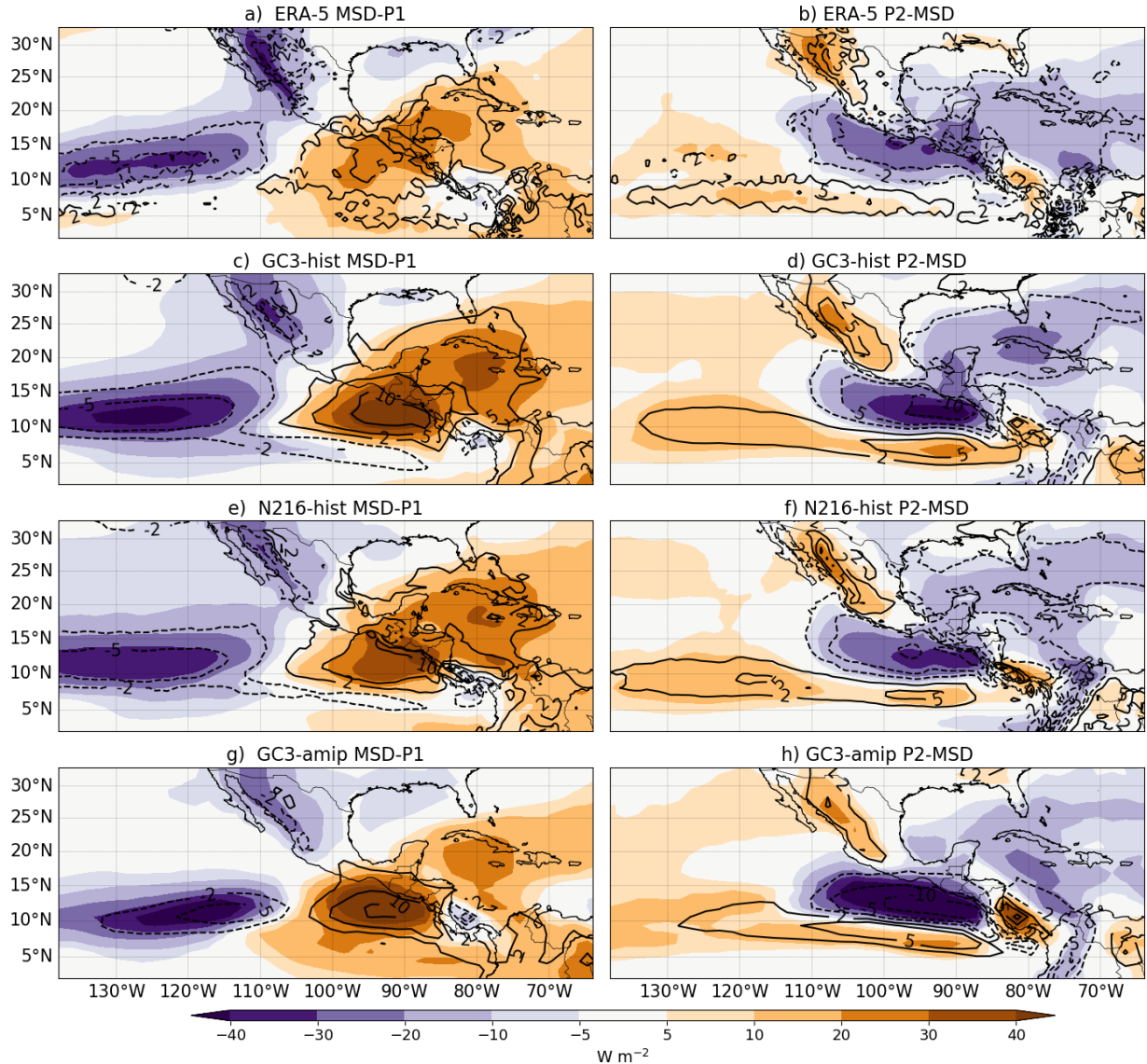


**Figure 6.8:** Outgoing long-wave radiation (OLR) [ $\text{W m}^{-2}$ ] (shaded) and  $\omega$  500-hPa [ $10^{-2} \text{ Pa s}^{-1}$ ] (line contours) differences between the MSD and first peak and the second peak and MSD.

throughout the three stages of the wet season. This result is noteworthy because this configuration uses the medium-resolution configuration, i.e., a higher resolution than GC3 N96 and is forced by observed SSTs, yet the simulation cannot capture the observed precipitation rates and is strikingly the worst simulation overall.

The outgoing long-wave radiation (OLR) and vertical velocity ( $\omega$  at 500 hPa) differences associated with the MSD were computed using the WT method for each dataset (Figure 6.8). These composite results show that the MSD is not a local-scale feature but convective

activity varies coherently in neighbouring regions. From the first peak period to the MSD, OLR and  $\omega$ , increase in the easternmost Pacific, southern Mexico and northern Central America and extend into the Caribbean islands and Sea; because  $\omega$  is defined as  $\omega = DP/Dt$  these positive anomalies are indicative of weaker ascent.

In contrast, two regions show opposite responses to the MSD. A region several degrees west into the East Pacific Ocean ( $125^{\circ}\text{W}$ ) and another region north of the study region, i.e., the North American monsoon region, show signs of negative OLR and  $\omega$  anomalies, in the MSD-P1 panels. These negative anomalies are indicative that, simultaneously to the onset of the MSD, convection is observed stronger and deeper in the North American Monsoon region and in the Pacific region west of the continent. Note that several of these features have been described previously Herrera et al. (2015).

The OLR and  $\omega$  variations associated with the end of the MSD show a relatively opposite picture to the MSD-P1 differences (Fig. 6.8). OLR and  $\omega$  decrease all across the central and south western coast of Mexico and northern Central America extending into the Caribbean Sea whereas positive differences are found in the North American Monsoon region and in the Pacific Ocean at around  $125^{\circ}\text{W}$ . These composites agree with the results of Herrera et al. (2015) that argues that ascending and descending anomalies in the MSD are closely related to ascent and descent elsewhere.

The literature suggests that a number of climatological features of the region play key roles for the MSD (Section 2.3). These climate features include the seasonal cycle of the East Pacific (EP) SSTs, the Caribbean Sea SSTs, the EP zonal wind flow and the CLLJ (Magaña et al., 1999; Amador, 2008; Herrera et al., 2015; Straffon et al., 2019; García-Martínez and Bollasina, 2020). The seasonal cycle of these features in ERA5 and the simulations (Figure 6.9) shows that the models are able to replicate the seasonal variations of the SSTs and the zonal wind flow of the region.

The seasonal cycle of EP SSTs (Figure 6.9a) show that the maximum SSTs are found in late May, prior to the first peak of precipitation in Mesoamerica. In contrast, the Caribbean SSTs peak in early fall, about five months later, during late September. After the peak SST period in the EP, SSTs decrease to a local minimum found in July both for ERA5 and the simulations. The models show a cold bias in the SSTs in both regions,

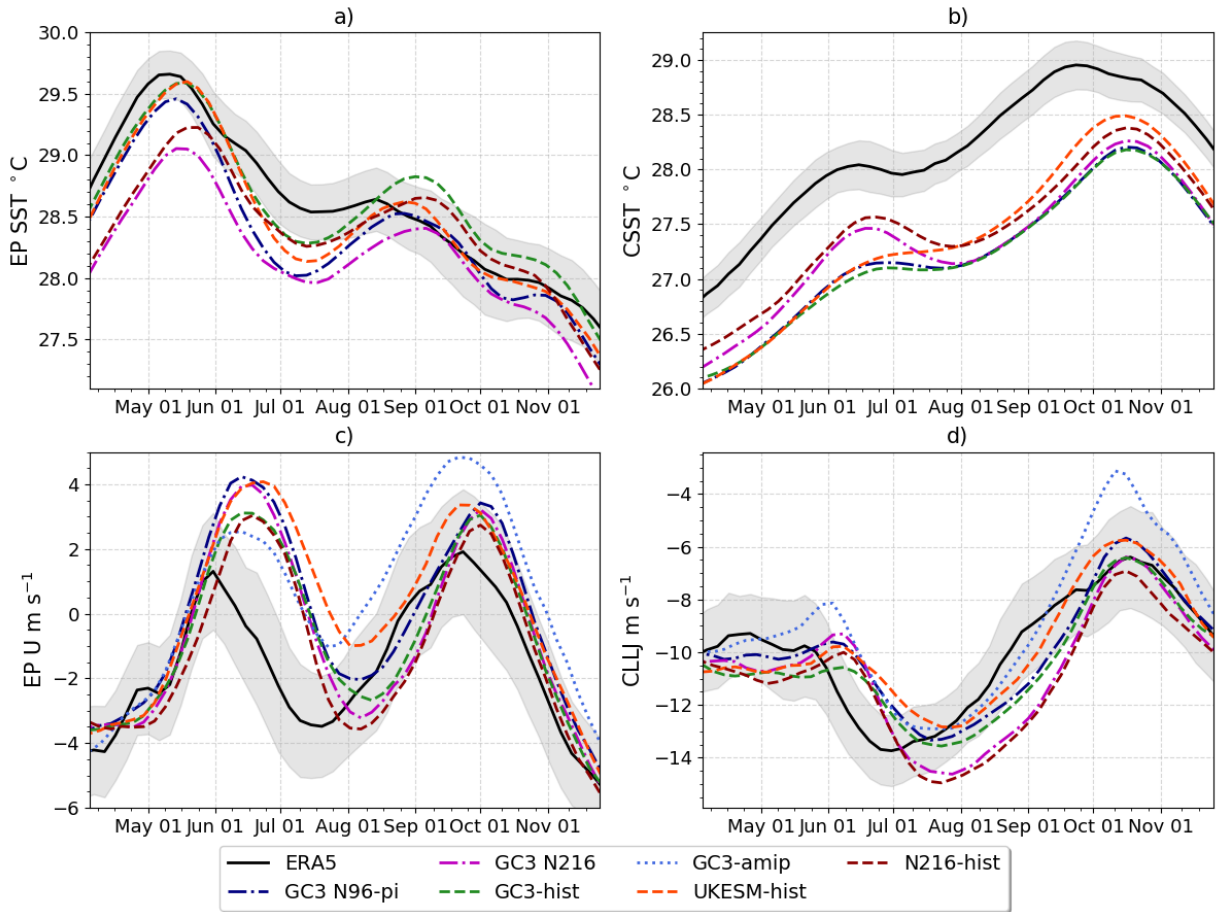


**Figure 6.9:** Pentad-mean seasonal march of the (a, b) SSTs [°C] and (c, d) the low-level (925-hPa) zonal wind flow [ $\text{m s}^{-1}$ ] in (a, c) the easternmost equatorial Pacific and (b, d) the Caribbean Sea. The transparent shading is as in Figure 6.1. The regions used for EP and CSEA averages are illustrated in Figure 6.4h.

but this bias is most pronounced in the Caribbean Sea where throughout the wet season the SSTs in the models are colder than in ERA5.

The low-level wind flow in the EP shows a bimodal seasonal cycle in ERA5 and the simulations (Figure 6.9c). The easterly flow in the EP during the spring becomes weaker turning westerly at the end of May and reaching a local maximum in early June in ERA5 and mid-June in the simulations. This local maximum then decreases during June and early July as the zonal wind becomes easterly again. The easterly flow peaks in mid July in ERA5 and two to three weeks later in the simulations. The strength of this easterly flow magnitude is more different between experiments during the July and August than in other months. After the easterly flow peaks in the midsummer, or zonal wind local minimum,

the zonal wind becomes westerly again peaking at the end of September-early August in both ERA5 and simulations. This seasonality of the zonal wind in the EP is similar to the seasonal cycle of precipitation in the region, and the difference in the phase of ERA5 and the models is also the same between the zonal wind and precipitation.

The CLLJ seasonal cycle (Figure 6.9d) is reasonably replicated by the simulations, compared to ERA5, although the peak strength of the CLLJ, which is found during the last week of June in ERA5, is delayed in the simulations by about three weeks, as the simulated CLLJ peaks in mid-July in all the simulations. The simulations follow closely the late summer and fall seasonal cycle and magnitude of the CLLJ, except for a notable bias in GC3-amip in Oct-Nov characterised by a weaker than observed zonal wind.

## 6.4 The role of East Pacific SSTs

The EP SSTs are a key element of the radiative-convective feedback mechanism of Magaña et al. (1999), which argues that the EP SSTs, surface moisture, cloud radiative effects and surface fluxes are part of a feedback mechanism that explains the two peak structure of the seasonal cycle of precipitation in Mesoamerica. A key prediction of this mechanism is that EP SSTs, surface moisture and turbulent fluxes exhibit a bimodal seasonal cycle in which EP SSTs and surface fluxes decrease during the first peak period and increase during the Midsummer drought period. In other words, this hypothesis predicts that the EP SSTs should also exhibit a bimodal signal, similar to that observed for precipitation but out-of-phase, with the SSTs leading the precipitation. This section aims to evaluate these predictions for ERA5 and for the CMIP6 experiments.

According to the radiative convective feedback mechanism, the EP SSTs should cool down during or slightly prior to the onset of the MSD and then increase during the local minimum of rainfall, i.e., during the MSD period which would lead enhanced precipitation and cause the second peak of precipitation in late summer. However, in ERA5 the EP SSTs only very slightly increase during the MSD (Jul-Aug) and instead of increasing in late summer rather cool again in late August and September. In fact, the EP SSTs in

ERA5 decrease after mid-August, in synchrony with the second peak in deep convection and precipitation (Figs. 6.1 and 6.9a).

In the models, however, there is indeed a second peak in EP SSTs in late summer found in early September and therefore nearly synchronous to the second peak of precipitation. While EP SSTs clearly lead precipitation in May-June, the SST-precipitation relationship in mid and late summer is less obvious. In the models, the second peak of SSTs is nearly synchronous to the second peak in precipitation, which seems to contrast with the predictions of the

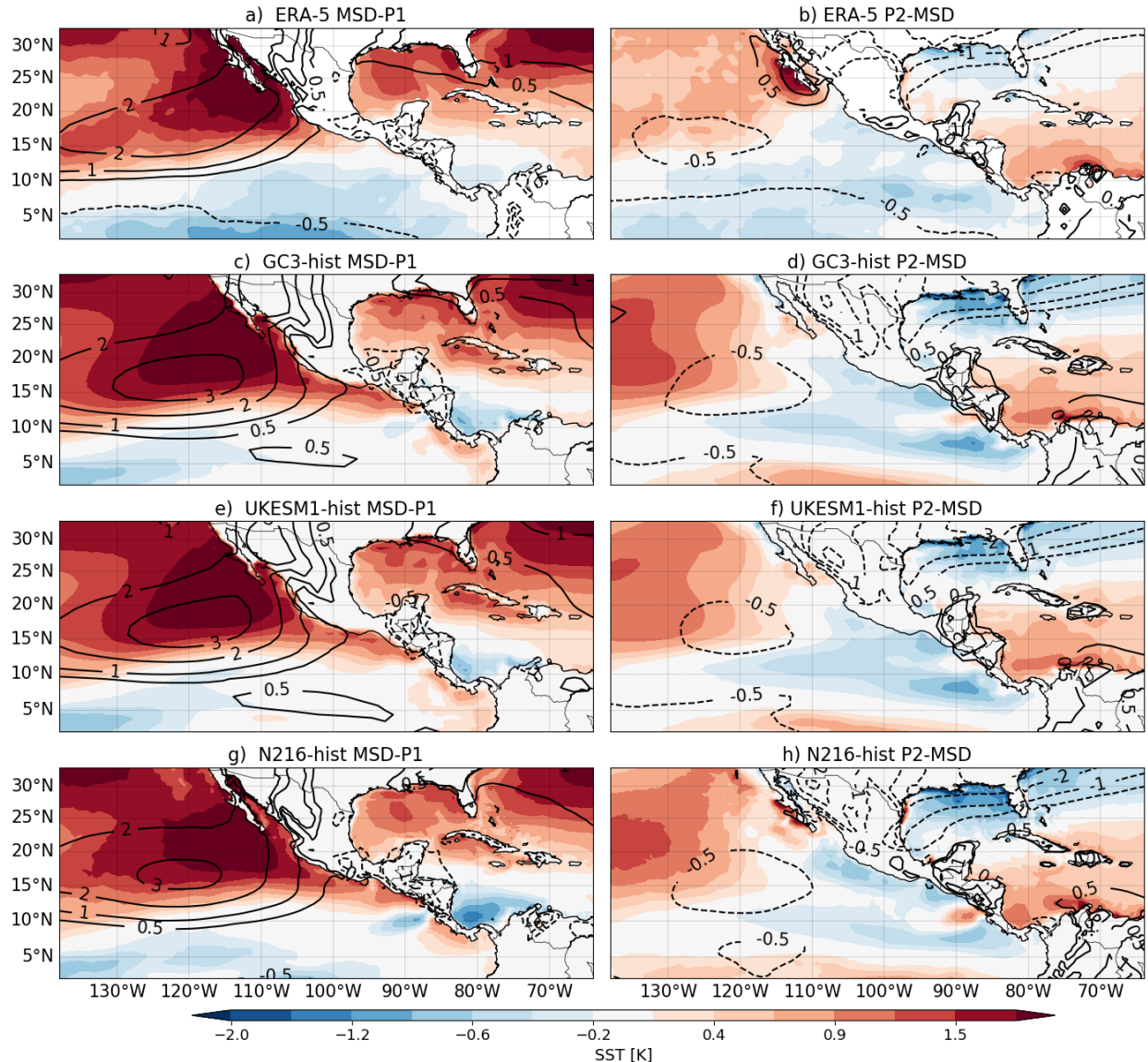


**Figure 6.10:** As in Figure 6.8 but the anomalies are shown for SSTs [K] (contours) and surface humidity [ $\text{g kg}^{-1}$ ] (line-contours).

radiative-convective feedback mechanism.

In order to better understand the relationship between EP SSTs and precipitation over the MSD region, the WT method is used to composite SSTs and surface humidity in the P1, MSD and P2 periods. The spatial distribution of SST and surface humidity changes associated with the MSD (Figure 6.10) suggest that the EP SSTs south of 10°N cool slightly between the first peak (P1) and the MSD periods, meanwhile the Gulf of California and the northern eastern Pacific significantly warms. At the end of the MSD (P2-MSD), the EP SSTs decrease in both ERA5 and the simulations. The P2-MSD panels show that the Caribbean SSTs increase, associated with the peak Caribbean SSTs at the end of the summer (Fig. 6.9b).

The historical simulations generally agree with the composite differences of ERA5, with no appreciable warming in the EP region in the MSD-P1 panels, and cooling in the EP and the Gulf of Mexico and warming in the Caribbean Sea in the P2-MSD panels. These results suggest that while the seasonal cycle of EP SSTs show a bimodal signal, when the timings of the MSD in each year of each simulation are examined more closely using the WT method, the EP SSTs do not synchronously warm during or after the MSD, contradicting the radiative-convective feedback mechanism.

Another element of the convective-radiative feedback mechanism is that the SST variability would force changes to the surface humidity and surface humidity would modify precipitation. The surface humidity in the EP and MSD regions, however, is unchanged (less than 0.5 g kg<sup>-1</sup>) during the various stages of the MSD (Figure 6.10), even though precipitation varies notably during these periods. Instead, the greatest variations in surface humidity are observed west of Baja California from the P1 to the MSD, and this region of increased surface humidity extends into the North American Monsoon region. Similarly, at the end of the MSD, the most notable variations in surface humidity is the drying of the North American monsoon region. The surface humidity variations in the simulations also agree well with those of ERA5 and are very similar amongst the realizations.

If the EP SSTs play a dominant role in the timings and strength of the MSD, as implied previously (Magaña et al., 1999; Magaña and Caetano, 2005; Herrera et al., 2015), then the simulations with imposed SSTs taken from observations, e.g., the GC3-amip experiment, may be further explored to evaluate the links between the timings or strength of the MSD

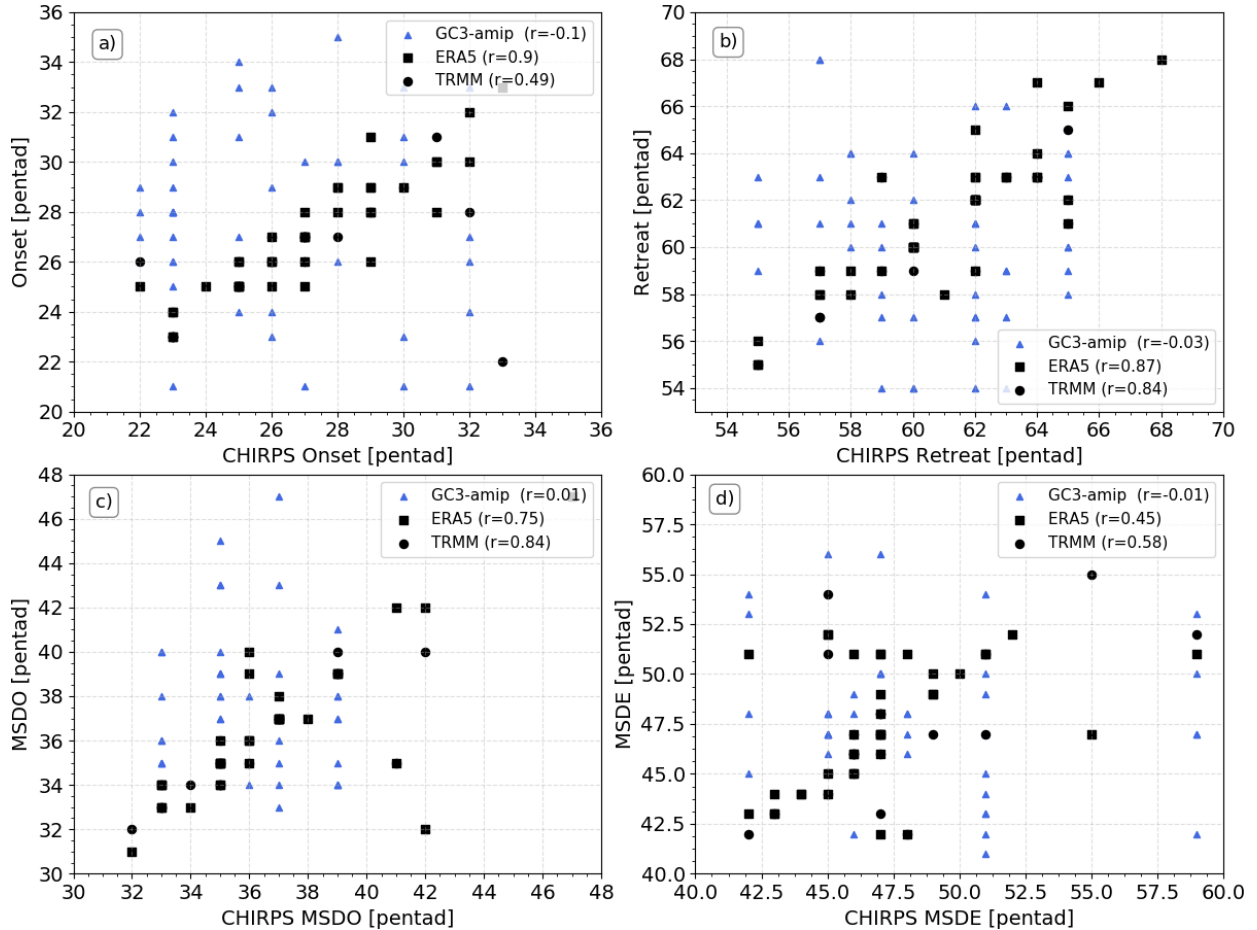


**Figure 6.11:** Scatterplots of the pentads diagnosed by the WT method as the dates of (a) monsoon onset (MO), (b) monsoon retreat (MR), (c) MSDO and (d) MSDE where the results of the CHIRPS dataset, on the x-axis, are compared with ERA5, TRMM and the GC3-amip simulation, on the y-axis. The legend shows the Pearson  $r$  coefficient for each comparison.

in GC3-amip and ERA5. A scatter plot of the dates (pentads) of the MO, MR, MSDO and MSDE (Figure 6.11) for matching years between the CHIRPS dataset and TRMM, ERA5 and the five ensemble members of GC3-amip shows that the timings of the MSD in GC3-amip are unrelated to CHIRPS and ERA5. ERA5 produces MSD timings that agree very well with the CHIRPS and TRMM datasets. This evidence would suggest that the SSTs forcing the model in GC3-amip are not the dominant factor controlling the timings of the MSD in these atmosphere-only runs.

Alternatively, the interannual variability in ERA5 and the differences amongst the MOHC CMIP6 experiments may be further explored to understand whether the changes to the SSTs are related to changes in the precipitation. For this purpose, composite

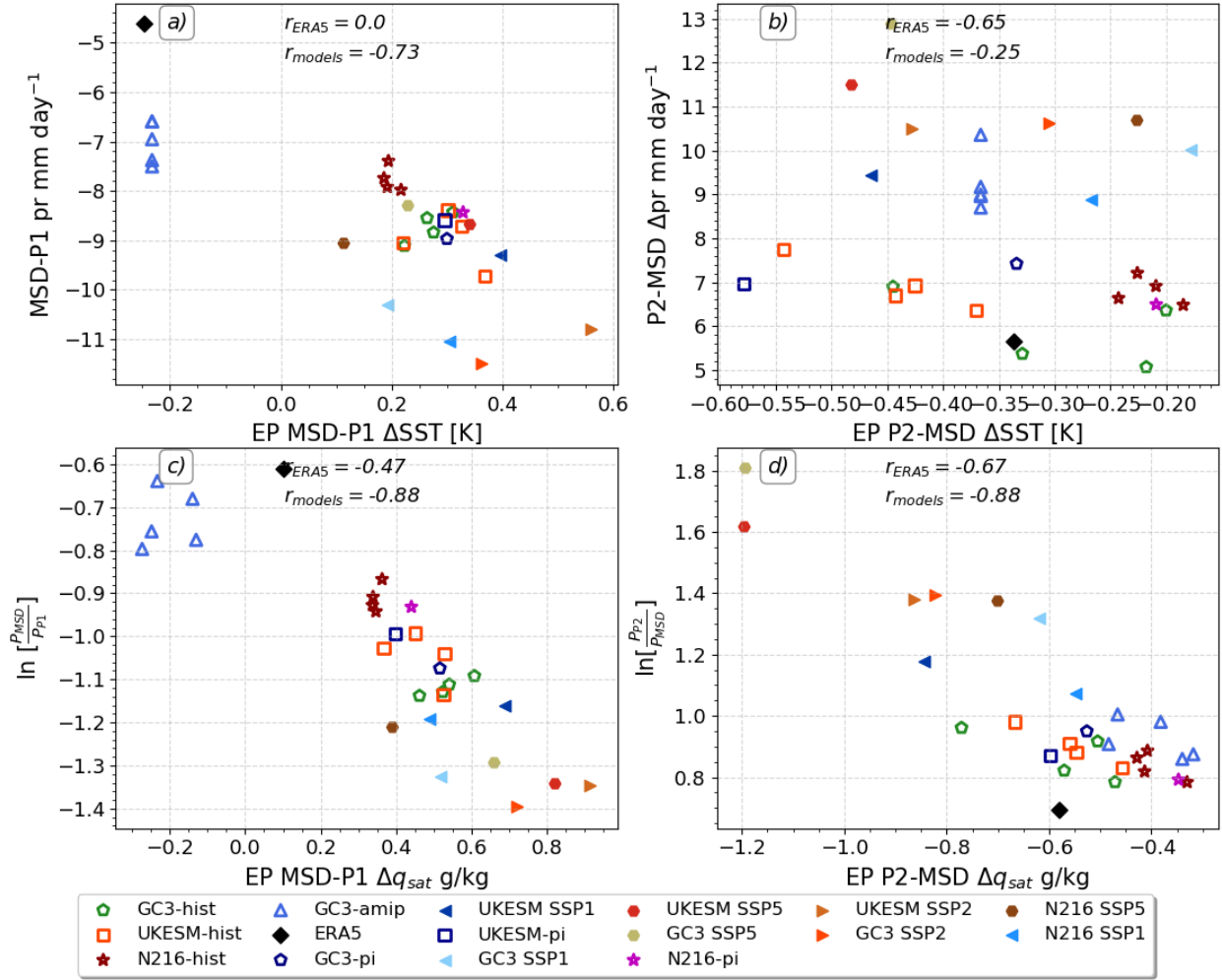


**Figure 6.12:** Scatterplots of the mean changes in the East Pacific (a, b) sea-surface temperatures (SSTs) and (c, d) surface saturation specific humidity  $q_{sat}$  in the x-axis with respect to precipitation variations in the MSD region on the y-axis for the (a, c) MSD-P1 and (b, d) P2-MSD periods. The correlation coefficient of the interannual spread in ERA5 and the multi-experiment correlation coefficient are shown in each panel.

differences between the P1, MSD and P2 periods were computed for each variable for each year in each dataset and then averaged to provide a mean value that relates changes in precipitation to different diagnostics in different stages of the rainy season. These results are presented in scatter plots that aim to diagnose emergent properties that explain the different representations of the MSD in the various simulations.

For example, the mean difference in SSTs (Figure 6.12a) between the P1 and the MSD periods, show a cooling difference for ERA5 associated with a smaller precipitation reduction. In contrast, the coupled model simulations show a positive SST difference (warming)

associated with a greater precipitation reduction during MSD compared to the P1 period. The slight warming signal in the MSD-P1 difference (Figure 6.12a) in the coupled-model experiments agrees with the seasonal cycle (Fig. 6.9) and suggests that in the model, as precipitation decreases during the MSD, the EP SSTs warm by 0.2 K.

During the second peak, the EP SSTs cool (Figure 6.12b) associated with a positive increase in precipitation, suggesting an inverse relationship between EP SSTs and precipitation. However, the relationship does not seem to explain the inter-experiment spread or the inter-annual variability in ERA5 as the correlation coefficients are low and not significant, i.e., a stronger second peak is not associated with a cooler EP SSTs in late summer.

The feedback mechanism of Magaña et al. (1999) suggests that one of the main consequences of the SST changes would be changes to evaporation and surface humidity. Furthermore, evidence shows that the surface saturation specific humidity  $q_{sat}$ , which measures the maximum moisture that a parcel can hold, provides a strong link between precipitation and SSTs on seasonal time-scales over tropical oceans (Yang et al., 2019; Good et al., 2021). For these reasons, Figure 6.12 also shows the relationship between the saturation specific humidity at the surface and precipitation.

The temporal changes to  $q_{sat}$  associated with the MSD timings (Figure 6.12c,d) are not positively related to changes in the precipitation over the MSD region. Although the inter-annual variability of  $q_{sat}$  changes during the MSD-P1 period in ERA5 shows a positive correlation, the mean changes to  $q_{sat}$  during this stage are very small compared to the differences in the experiments and, furthermore, the relationship for the simulations shows an opposite relationship (negative correlation).

For the P2-MSD differences, there is a negative correlation for both ERA5 and the experiments, which means that the strongest second peaks of precipitation are associated with cooler SSTs. A more direct relationship was examined between the EP  $q_{sat}$  and EP  $pr$ . This analysis (not shown) resulted in a weaker (but still negative) relationship in both regions between  $q_{sat}$  which suggests that changes to  $q_{sat}$  are not strong enough to explain the variability of precipitation.

The previous results have analysed synchronous changes between the EP SSTs, surface humidity,  $q_{sat}$  and precipitation over the MSD region, but the expected relationship may exist

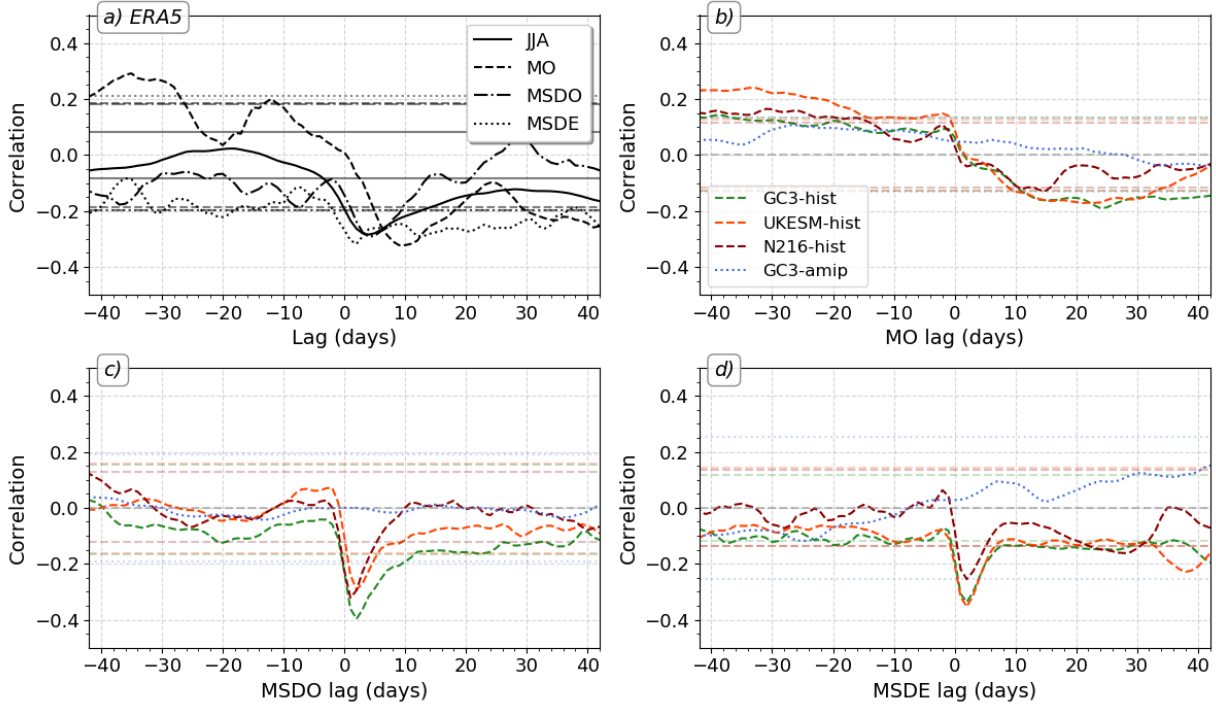


**Figure 6.13:** Lagged correlations between East Pacific SSTs and precipitation in the MSD region for (a) ERA-5 where the lag 0 date was used in four different ways: first, all the boreal summer JJAS SSTs and precipitation pairings, then lag 0 represents the monsoon onset (MO), MSD onset (MSDO) and MSDE dates. (b-d) as in (a) but for the simulations where the correlations are computed with the SST-precipitation timeseries lagged with respect to the b) monsoon onset date, the c) MSDO date and the d) MSDE date.

with some lags, in particular as suggested by the radiative-convective feedback mechanism the SSTs should be leading precipitation. Lag-lead correlations (Fig. 6.13) of the EP SSTs and the precipitation in the MSD region show that only during monsoon onset are these two fields significantly positively correlated at lags of  $\approx$ -35 days in ERA5 and -40 to -20 days in the historical experiments.

In ERA5, the correlation for all the boreal summer (JJAS) sample is only significant for the SSTs leading precipitation region for negative lags from 30 to 40 days and is only significant (negative correlation) at positive lags at lag +5 days, indicative of an inverse SST-precipitation relationship where the SSTs follow precipitation. In the models (Fig. 6.13b-d), very similar results are found where significant positive correlations at negative lags, indicative of SSTs leading precipitation, are only found for the MO panel, whereas for MSDO and MSDE panels, the correlations are only significant at positive lags and for

negative correlations, indicative of the precipitation leading the SSTs on the scale of 3-5 days and SSTs decreasing with increased precipitation.

This section investigated the radiative-convective feedback hypothesis by Magaña et al. (1999). Results in this section show that in observations, the EP SSTs do not exhibit a double-peak seasonal cycle, so the second peak of precipitation over the MSD region cannot be driven by a second peak in EP SSTs in late summer. Furthermore, evidence shows that the variations of precipitation during the midsummer are not statistically related to the seasonal variations in EP SSTs or  $q_{sat}$  in ERA5 or in the CMIP6 simulations.

## 6.5 The role of cloud-radiative effects

The mechanisms proposed by Magaña et al. (1999) and Karnauskas et al. (2013) suggest that the net shortwave energy absorbed by the surface is key in the driving mechanism of the MSD. Magaña et al. (1999) suggests that tall convective clouds influence the timings and net shortwave (SW) flux at the surface and suggests that the cloud-radiative effects (CRE) experience seasonal changes that occur at the same as the MSD and are causally linked to the bimodal signal of precipitation. In turn, Karnauskas et al. (2013) argues that the seasonal march of solar insolation determined by the solar declination angle controls the net SW absorbed by the surface and this absorption of SW energy modulates the seasonal cycle of the surface energy balance and of precipitation. This section evaluates the predictions of these theories regarding CRE and the SW absorbed by the surface.

CRE effects are coupled to the tropical circulation (Bony et al., 2004; Webb et al., 2017) and influence the timing and strength of regional (Guo et al., 2015) and axi-symmetric (Byrne and Zanna, 2020) monsoons. The longwave (LW) CRE plays an important role in the convective heating and moistening of the atmospheric column in tropical regions and the SW CRE affects the surface absorption of energy (Allan, 2011). These studies motivate a deeper investigation of the CRE in the Mesoamerican region, specifically for the timings and strength of the MSD. The surface cloud radiative effect ( $\text{CRE}_{surf}$ ) is computed from daily-mean fields following Allan (2011), as the sum of the LW and SW CREs, i.e.:

$$\begin{aligned}
 CRE_{surf} &= LWCRE_{surf} + SWCRE_{surf} \\
 &= LDS - LUS - (LDS_{cs} - LUS_{cs}) + SDS - SUS - (SDS_{cs} - SUS_{cs}), \quad (6.1)
 \end{aligned}$$

where the fluxes are depicted as long-wave (L) or short-wave (S) and downwelling (D) or upwelling (U) at the surface (S) and the subscript  $_{cs}$  denotes under clear-sky conditions. The long-wave upwelling at the surface (LUS) virtually cancels with the  $LUS_{cs}$  because the long-wave emission from the surface is minimally dependent on the presence of clouds (Allan, 2011). The net CRE at the surface is then given by:

$$CRE_{surf} = LDS - LDS_{cs} + SDS - SUS - SDS_{cs} + SUS_{cs}. \quad (6.2)$$

The net CRE during P1, MSD and P2 periods (Fig. 6.14) is negative and the minimum values are found in the East Pacific ITCZ region. The differences between the MSD timings

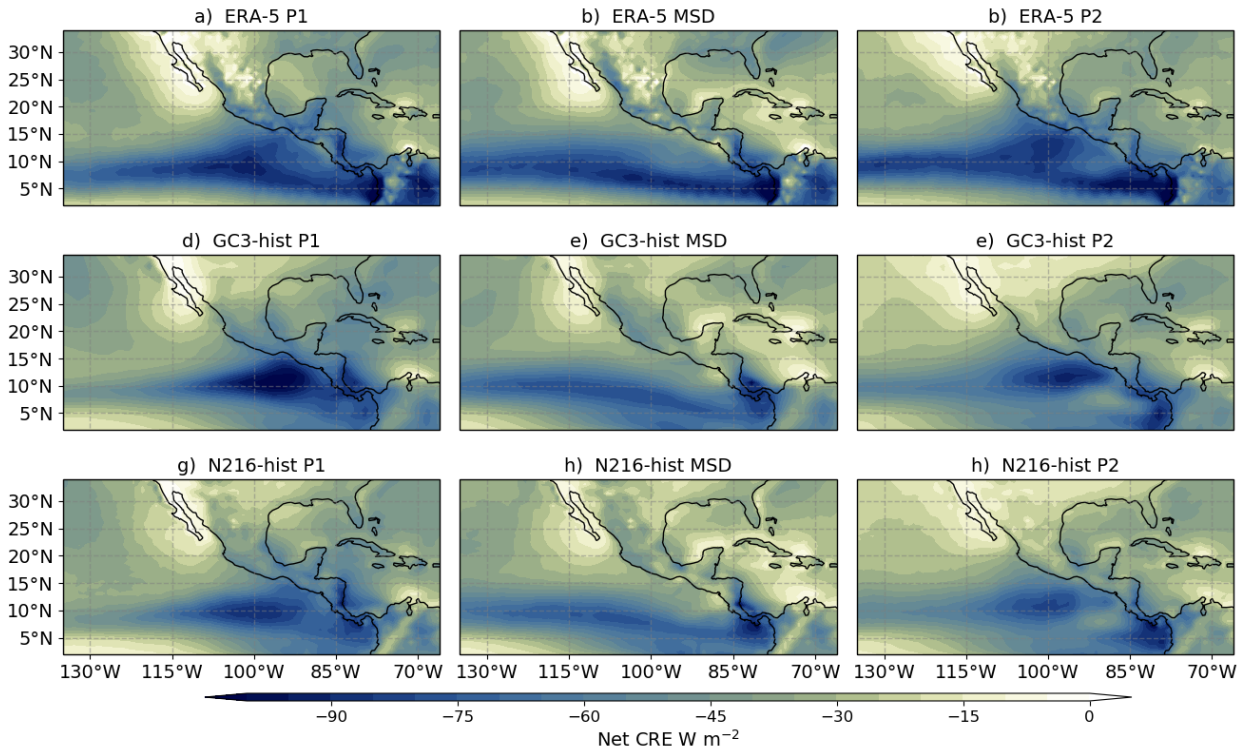


**Figure 6.14:** Composite mean cloud radiative effect (CRE) [ $\text{W m}^{-2}$ ] during the periods of onset of the MSD, the MSD and the end of the MSD for (a-c) ERA5, and the ensemble mean of (d-f) GC3-hist and (g-h) N216-hist.

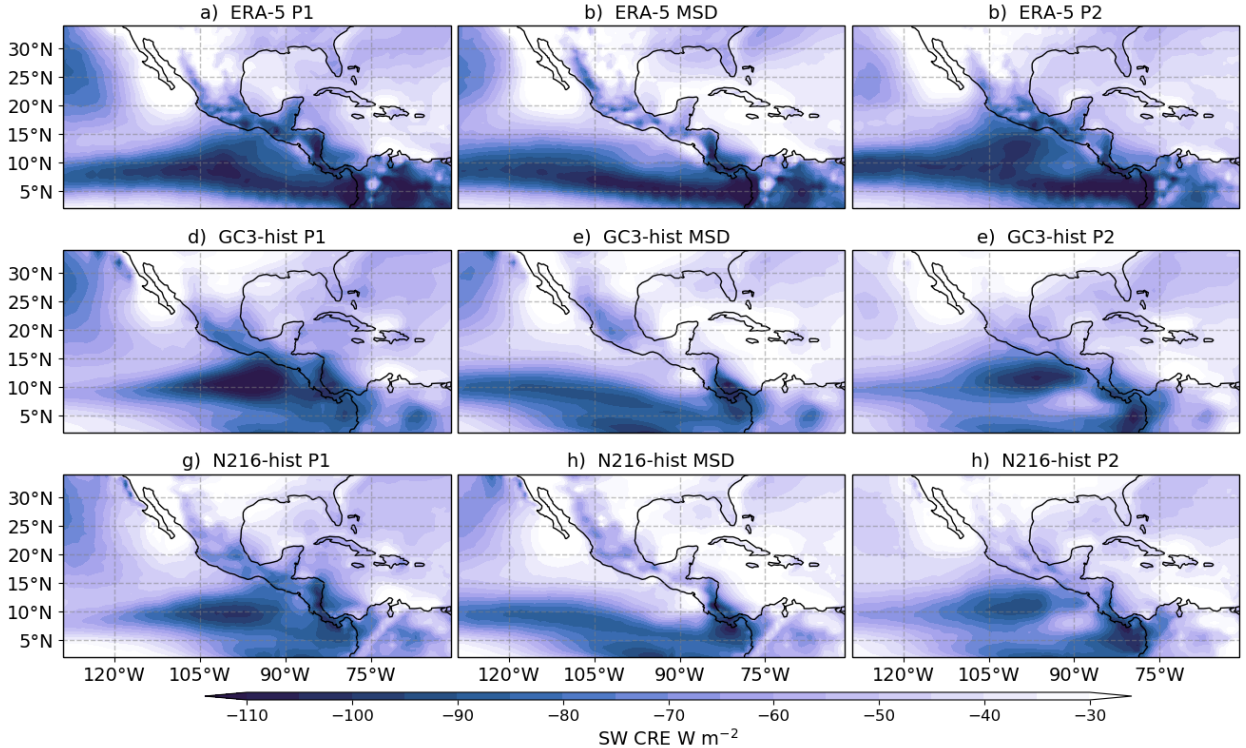


**Figure 6.15:** As in Fig. 6.14 but for the short-wave radiative effect.

closely follow the precipitation changes during these periods as the minimum CRE in the EP and the Mesoamerican region is found during the two peaks of precipitation with a weaker CRE over the Mesoamerican region and nearby basins during the MSD. The smallest CRE is found over the Baja California Peninsula. The results of the two historical experiments closely follow the results of ERA5, and the only notable difference between the lower (GC3) and the higher (N216) resolution historical experiments is that the CRE is stronger in GC3-hist than in N216-hist.

The individual contributions of the SW and LW surface CREs (Figures 6.15 and 6.16) show that the dominant term in the EP and Mesoamerican regions is the SW term. The negative SW CRE is strongest in the EP ITCZ region and the SW CRE varies with the MSD timings in similar fashion to the net CRE, i.e., in the MSD region, the SW term is notably larger ( $<-90 \text{ W m}^{-2}$ ) during the two peak periods of precipitation than during the MSD. The historical experiments also show that the SW CRE is larger in magnitude in the EP ITCZ region and that the SW CRE over the MSD region varies notably in the three stages of the rainy season.

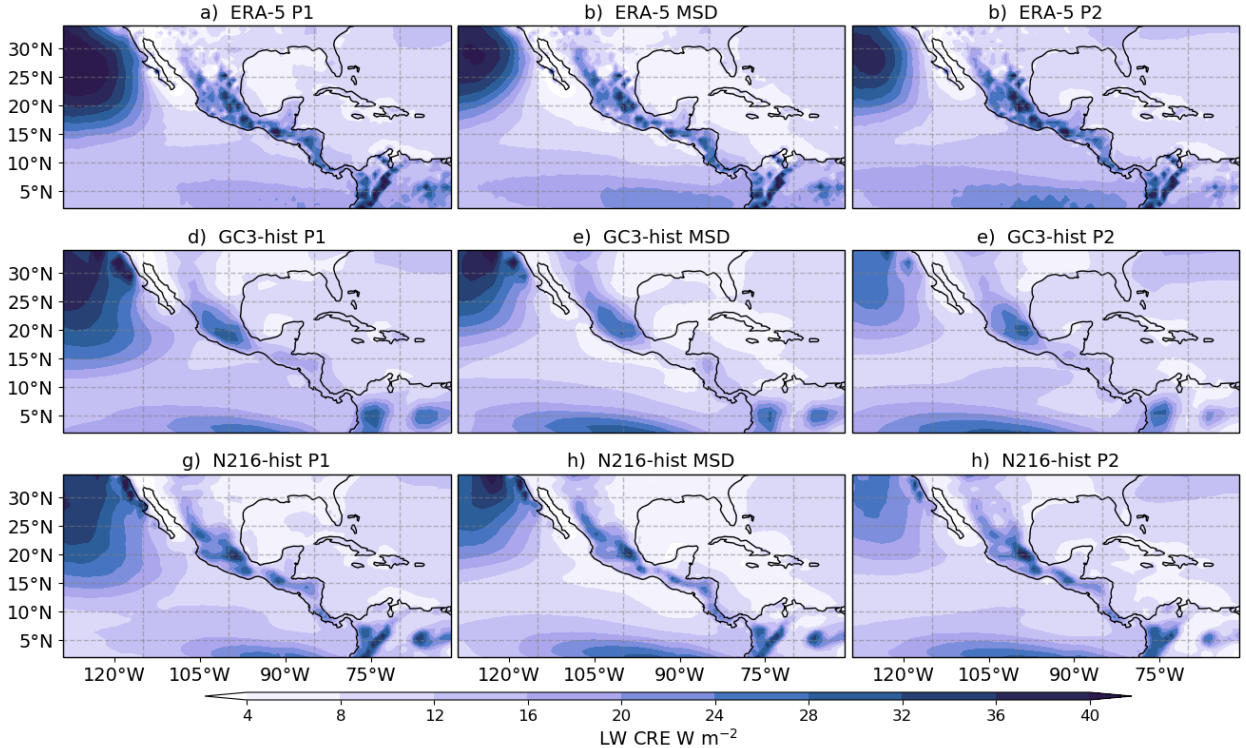


**Figure 6.16:** As in Fig. 6.14 but for the long-wave CRE.

In contrast, the LW term (Figure 6.16), is generally smaller in magnitude than the SW term and is largest over land and in the ocean west of the California. Over the EP and CSEA regions, the LW term shows very small horizontal gradients, indicative of a fairly horizontally homogenous effect of clouds. The differences of the LW between the stages of the MSD are smaller than the SW term variations, but both in ERA5 and the simulations, the LW term over the EP and the CSEA is visibly larger during the two peak periods than during the MSD.

These composites depict how the spatial distribution of the CRE varies with the MSD timings over the larger Intra-Americas Seas region, but how these terms actually within the season in the MSD region is not obvious. The seasonal cycles of the SW, LW and net CREs (Figure 6.17a-c) show bimodal signals characterized by stronger CREs during the two peak periods during June and September and a relative minimum in between found in late July in ERA5 and early August in the simulations. The simulations reasonably simulate the magnitude of the net and SW CRE during the early summer season but overestimate the decrease in the net SW and LW CRE during the midsummer, very likely associated with the underestimation of precipitation over this same period (Figure 6.1).

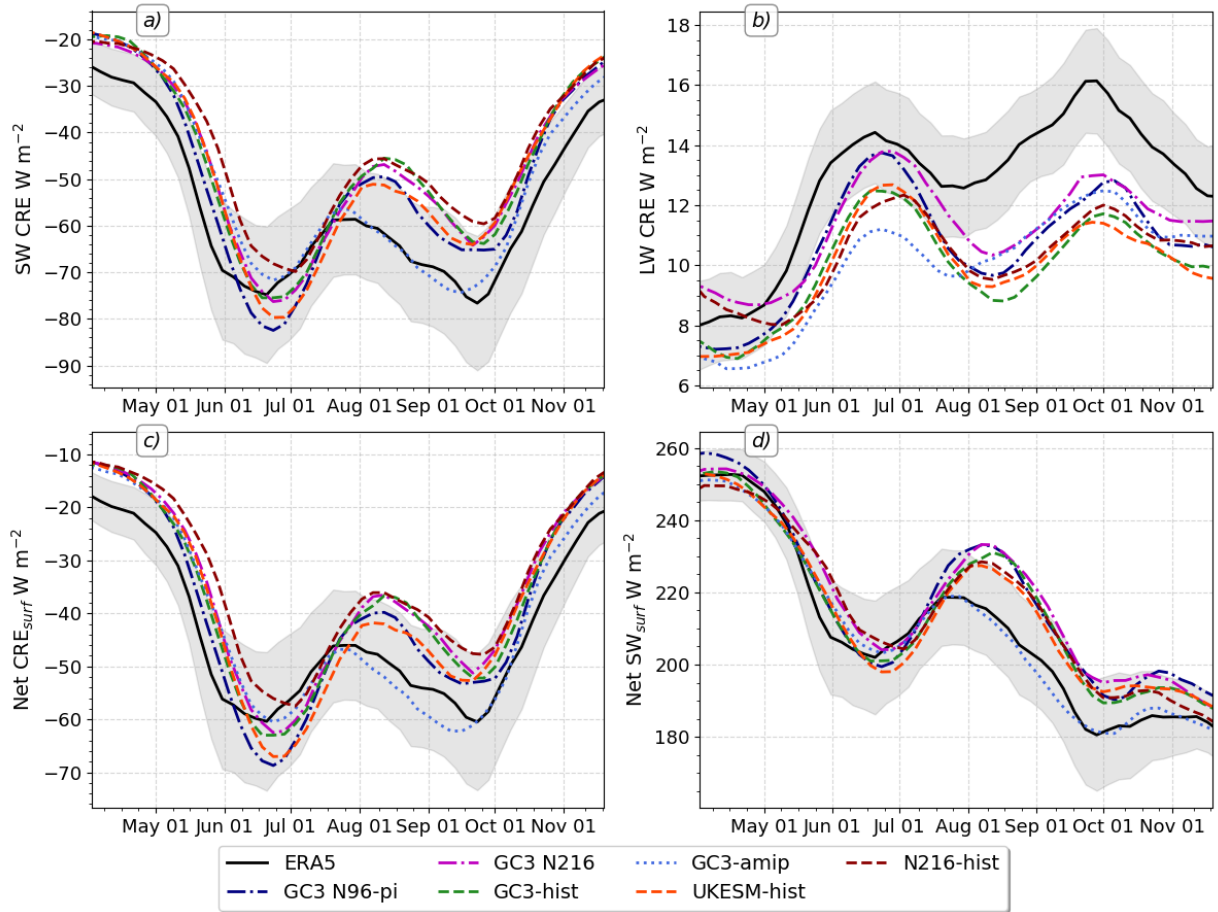


**Figure 6.17:** Pentad-mean seasonal cycle of the (a) SW and (b) LW CREs, (c) the net CRE, and (d) the net SW at the surface, signed positive to indicate surface absorption of SW radiation.

Regardless of CREs, according to Magaña et al. (1999) and Karnauskas et al. (2013), the net SW (the difference between upwelling and downwelling shortwave) at the surface should also present a bimodal seasonal cycle and be related to precipitation. In both ERA5 and the simulations, the net SW (Figure 6.17d) follows a two-peak seasonal cycle characterized by a first peak in late May, which coincides with the peak in East Pacific SSTs. This peak in SW is followed by a local minimum during June which is followed by a secondary increase in July in ERA5 and extending to August in the simulations. After this second local maximum, there is another sharp decrease in the net SW at the surface at the end of the summer, which coincides with the second peak in precipitation and therefore possibly linked with less downwelling SW.

The spatial distribution of changes to the net SW at the surface (Figure 6.18) show that

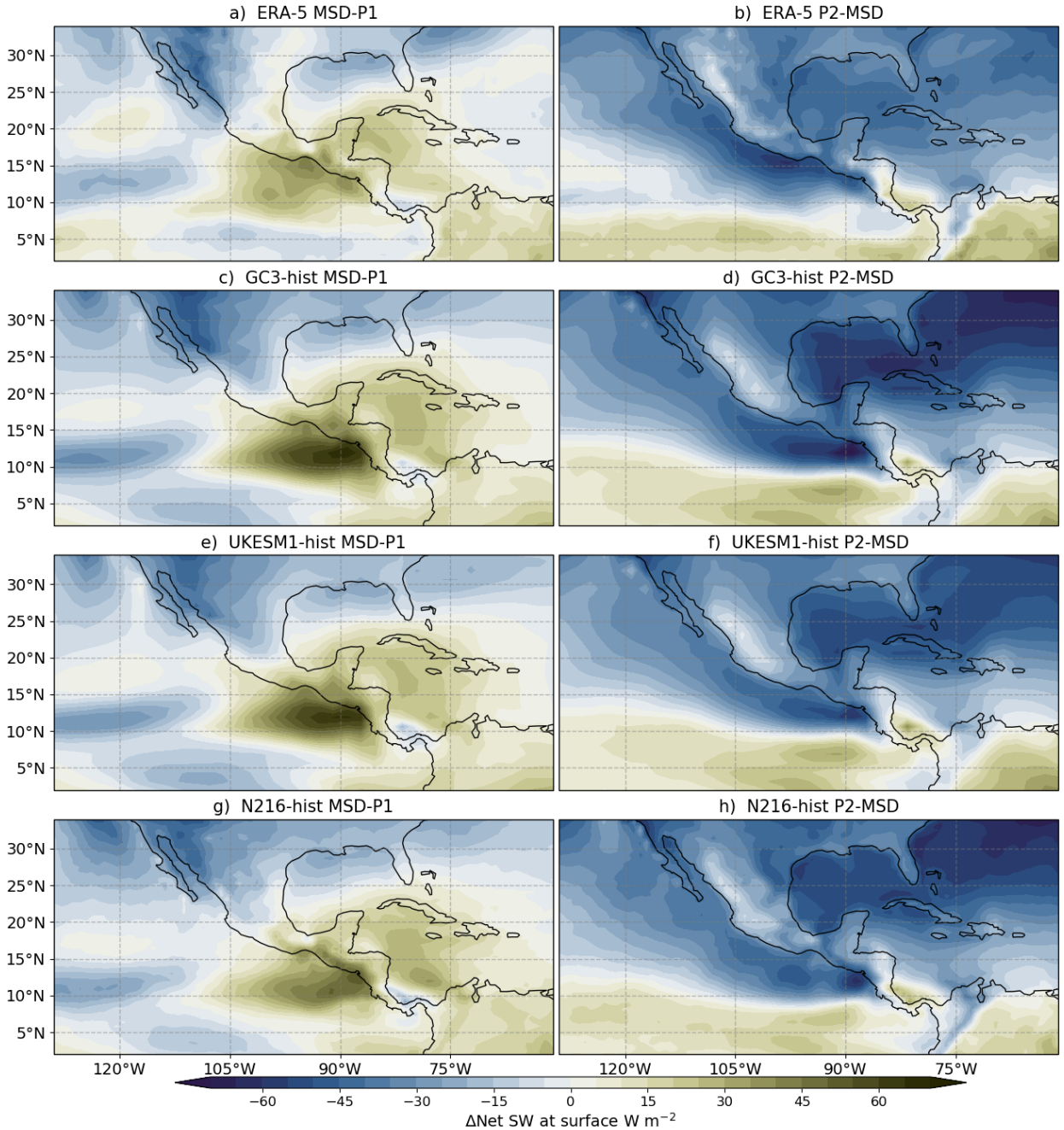


**Figure 6.18:** As in Fig. 6.8, but for the net shortwave radiation [ $\text{W m}^{-2}$ ] at the surface.

from the first peak to the MSD there is a positive difference net SW, indicative of more SW energy absorption at the surface of about  $30 \text{ W m}^{-2}$  in ERA5 and  $40 \text{ W m}^{-2}$  in the simulations. In contrast, for the P2-MSD differences, a notable reduction in net SW energy is observed throughout the North American continent but the maximum reduction is found on the western coast of southern Mexico. One might reasonably then suspect that the increased

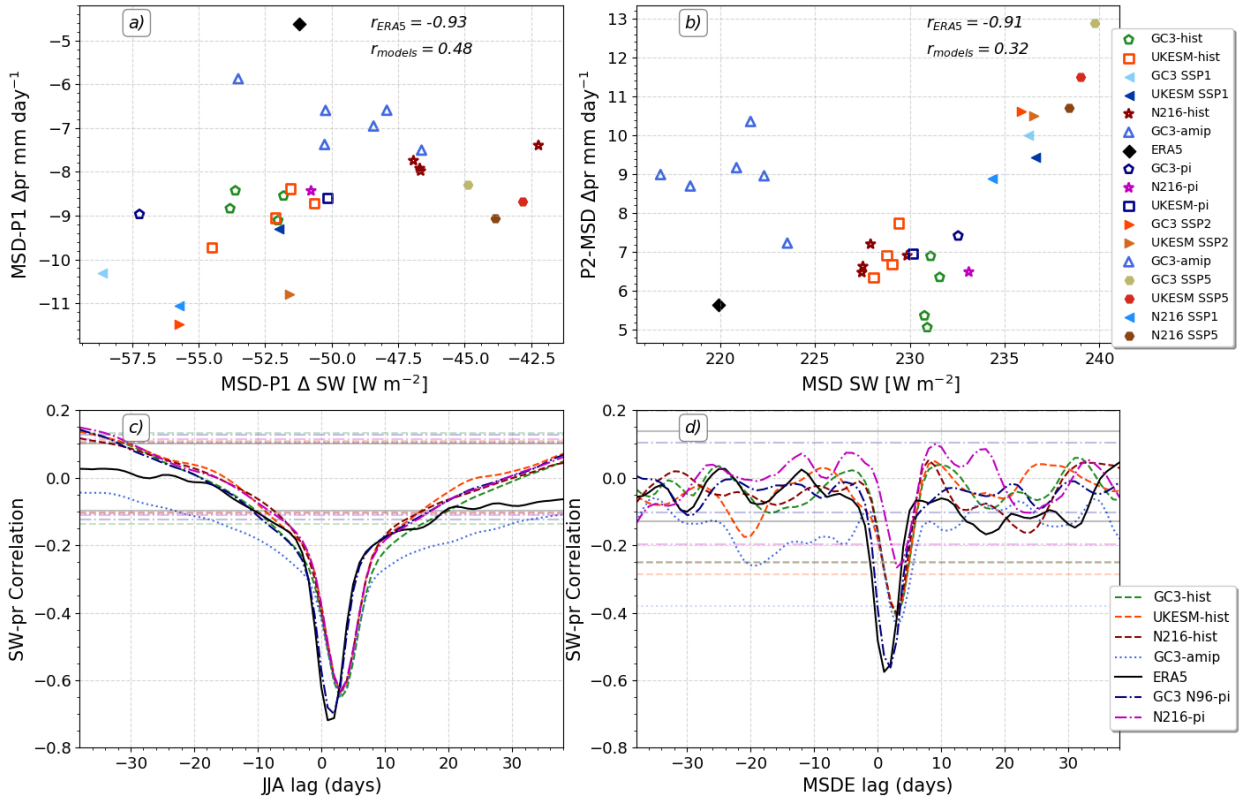


**Figure 6.19:** (a, b) Scatter of the mean changes to the net short-wave (SW) at the surface (abscissa) with respect to changes in precipitation for different MSD stages. (c, d) Lagged-regression coefficients between the net shortwave absorption in the East Pacific and precipitation over the MSD region for the (c) the JJA season and (d) around the MSDE date.

SW absorption during the MSD may indeed be a cause or part of the mechanism for the second peak of precipitation, as suggested by both Magaña et al. (1999) and Karnauskas et al. (2013). However, this could just be a correlation that highlights the coupling between clouds, radiation and precipitation and not necessarily that SW heating is the driving mechanism.

These hypotheses are further tested through scatter and lag-lead regression analysis (Figure 6.19). The changes to the net SW at the surface are unrelated to the interannual variability of the changes to precipitation in ERA5. The reduction in SW in the MSD-P1 periods shows a 0.0 correlation with the changes of precipitation during the same stages, whereas the net SW absorbed in the EP during the MSD period is negatively correlated with precipitation during the second peak. In other words, years where less shortwave is absorbed in the EP is associated with years stronger second peaks in the MSD region, in marked contrast to previous hypotheses.

Furthermore, in the MOHC CMIP6 experiments there appears to be only a modest relationship between net SW and precipitation. The changes to SW during the MSD-P1 are only modestly related to precipitation as simulations that have the smallest changes to net SW in this period do not exhibit the smallest changes to precipitation. Similarly, a very weak relationship between SW and precipitation is found within the different experiments to relate the net SW at the surface during the MSD and the strength of the second peak.

Lag-lead relationships (Figure 6.19c, d) confirm that there is a strong correlation between SW and precipitation but this is a negative correlation at lag 0. This negative correlation illustrates that strong precipitation periods are associated with less shortwave absorbed by the surface, due to the high clouds blocking incoming SW. Correlations are not significant outside of lag -5 to 5 days near the MSDE date, although they appear significant for some coupled simulations at lags of -40 days when the entire JJA season is considered. These results appear contradictory with the argument of Karnauskas et al. (2013) who argued a lagged relationship between shortwave absorption at the surface and precipitation at the end of the MSD.

Finally, while the incoming SW radiation plays an important role in several theories for the MSD, the LW effects have important consequences in general monsoon dynamics (Guo et al., 2015; Byrne and Zanna, 2020). The GC3-amip-lwoff experiment is part of the contributions from the Cloud Feedback MIP (CFMIP) (Webb et al., 2017) to CMIP6. This experiment is identical to the GC3-amip experiment except that the treatment of the LW in the radiation code in the model is not affected by the presence of clouds, in other words all LW fluxes are assumed to be under clear-sky conditions.

The impact of the LW CRE for precipitation in the Mesamerican region is critical (Figure 6.20). When the LW effects of clouds are ignored, precipitation over the whole domain is greatly reduced (50-80%), ascent becomes weaker and the low-level circulation also weakens. These results are in agreement with previous studies (Guo et al., 2015; Byrne and Zanna, 2020) that show that cloud radiative heating strengthens the local and regional circulation in a monsoon. The circulation and precipitation is so diminished in GC3 amip-lwoff that this is the driest simulation found in this chapter (Figure 6.7). The monsoon precipitation is so diminished that small variations between the MSD and the two peak periods of precipitation are almost undistinguishable.

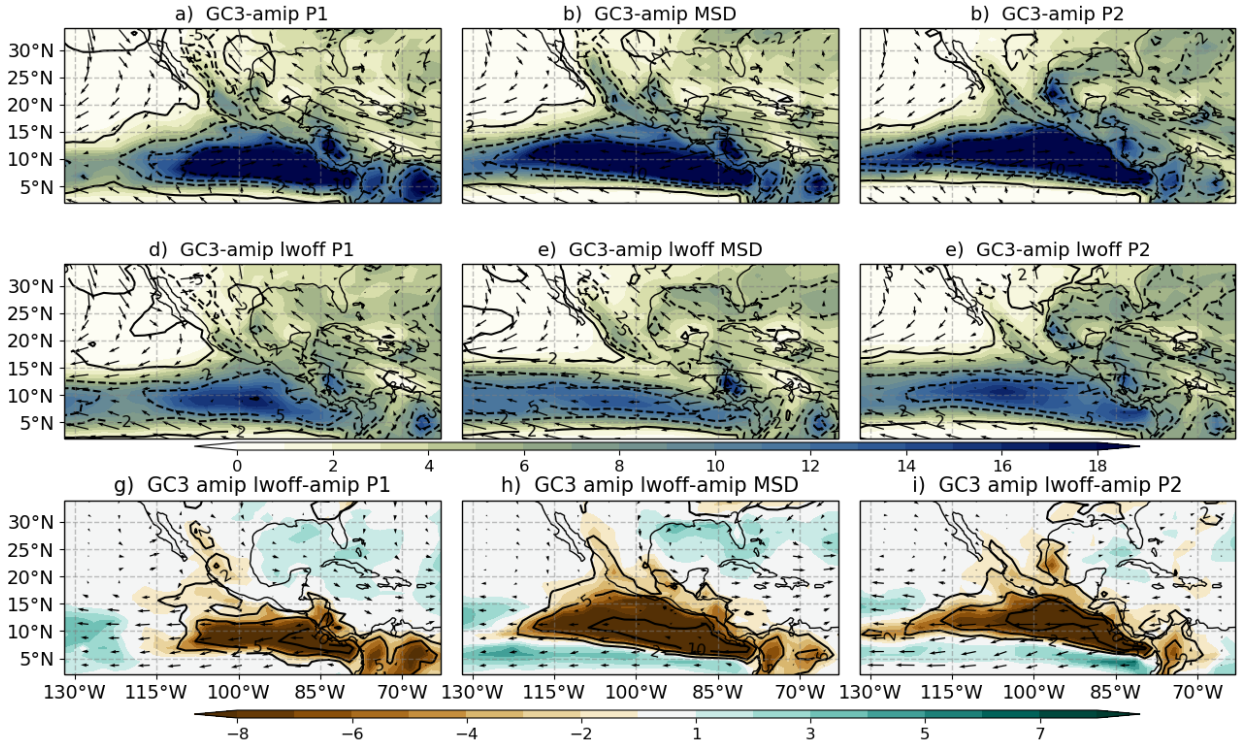


**Figure 6.20:** Composite mean precipitation (shading in  $\text{mm day}^{-1}$ ), vertical velocity (contours in  $10^{-2} \text{ Pa s}^{-1}$ ) and 850 hPa wind speed (vectors) for the P1, MSD and P2 periods in the (a-c) GC3-amip and (d-f) GC3-amip lwoff experiment. (g-i) shows the difference between the lwoff-amip and the amip experiments.

This section diagnoses the seasonal cycle and spatial variability of CRE at the surface as depicted by ERA5 and the CMIP6 simulations. The net CRE at the surface is dominated by the SW term, indicating the strong effect that convective clouds have to block SW radiation from reaching the surface throughout the summer. The total absorbed SW shows a double-peak structure, with the second peak appearing at the end of the MSD period for both ERA5 and CMIP6 simulations, as suggested in the solar declination angle hypothesis Karnauskas et al. (2013). However, the strength and timing of the changes to the SW absorption suggest that the relationship between SW heating and precipitation is more of a correlation than a causal link from the SW to the precipitation.

## 6.6 The role of the Caribbean Low-Level Jet

The previous sections evaluate the radiative-convective feedback and the solar declination angle hypotheses, in addition, this section examines the role of the Caribbean Low-Level Jet

(CLLJ) for the MSD of Mesoamerica. Section 6.3 shows that the seasonal cycle of the low-level zonal wind, i.e., the CLLJ, is well represented by the simulations (see Figure 6.9d), but the timing of the peak magnitude of the CLLJ in the models is delayed by about three weeks with respect to ERA5. The timing of the start of the MSD is notably also delayed in the models by around 10 days, according to Table 5.3 in the previous chapter. This evidence is suggestive that the CLLJ may be playing a role in the timings of the MSD in the simulations, which would be consistent with previous studies (e.g. Herrera et al., 2015; Martinez et al., 2019).

The main dynamical argument that links the MSD in southern Mexico and Central America and the CLLJ is centred around variations in the moisture flux convergence (MFC), and subsequently in the total water content (TWC) (see e.g. Gamble et al., 2008; Herrera et al., 2015; Martinez et al., 2019; Zermeño-Díaz, 2019). For this reason, this section examines the CLLJ magnitude as measured by the 850 hPa zonal wind in the Caribbean Sea (see box in Figure 6.4), and the integrated moisture flux convergence (IMFC) and TWC in the MSD region. The IMFC was calculated using the following equation from daily ERA5 data and daily data from the simulations:

$$IMFC = -\left\langle \nabla \cdot \vec{u}q \right\rangle \quad (6.3)$$

where  $q$  is the specific humidity at each pressure level,  $\vec{u}$  is the wind vector and  $\nabla$  is the horizontal divergence operator and the  $\langle \rangle$  operator denotes column integrals in the troposphere.

The seasonal cycle of the IMFC and TWC (Figure 6.21) averaged over the region of the MSD shows a strong bimodal signal, with two maxima in IMFC and TWC occurring roughly at the same time as the two peaks in precipitation and a minimum found during Midsummer. The simulations follow closely the variations of the seasonal cycle of ERA5, but with a weaker IMFC over the region in all the simulations, particularly after the period of the first peak of precipitation.

The magnitude of the two peaks of IMFC is fairly similar for all the simulations, in contrast with the asymmetry between the first and second peaks of precipitation, e.g., the historical experiments show a wetter first peak than the second peak. The IMFC during MSD, in contrast, shows notable differences amongst experiments, with the SSP1 experiments

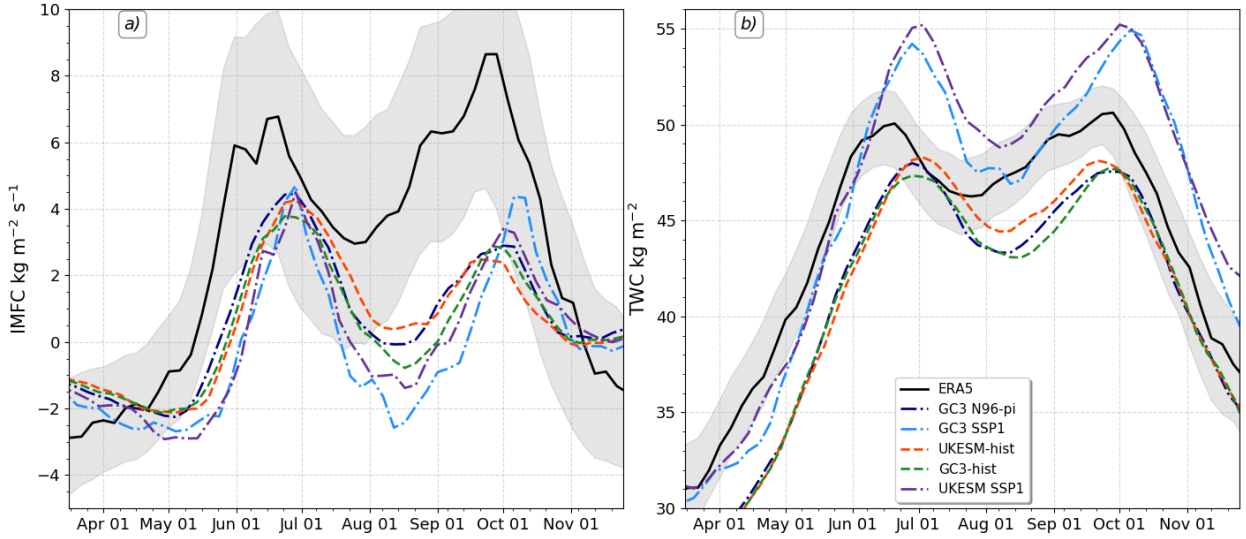


**Figure 6.21:** Seasonal cycle of (a) IMFC and (b) TWC averaged over the MSD region.

showing a smaller IMFC compared to the historical and piControl experiments, in fact in early August the IMFC is negative (indicative of moisture divergence) in the SSP1 experiments.

The magnitude and timings of the two peaks in TWC is fairly similar amongst the piControl and historical experiments and fairly similar to ERA5, however, notable differences exist. Firstly, the drying of the column in the simulations during midsummer occurs weeks after the drying in ERA5, which agrees with the differences in the seasonal cycle of precipitation. Secondly, the low-emission scenario (SSP1) experiment show a higher TWC indicative of a moistening of the column throughout all the seasons for a relatively low greenhouse forcing compared to the historical experiments.

The IMFC, TWC and 850-hPa wind variations associated with the MSD (MSD-P1 and P2-MSD) are shown in Figure 6.22 for ERA5 and two simulations. The patterns observed in the low-level wind vectors associated with the MSD timings follow closely the previously reported "MSD patterns" described by Zermeño-Díaz (2019), which confirms that the WT method is able to extract similar patterns in the low-level wind associated with the MSD to other techniques. The wind flow pattern in the MSD-P1 panel is characterised, both in ERA5 and the simulations, by modest northeasterly anomalies in the Gulf of Mexico and the CSEA and strong easterly anomalies over the EP region. These wind anomalies indicate that as the wetter first peak period transitions to the drier MSD, the wind field changes from

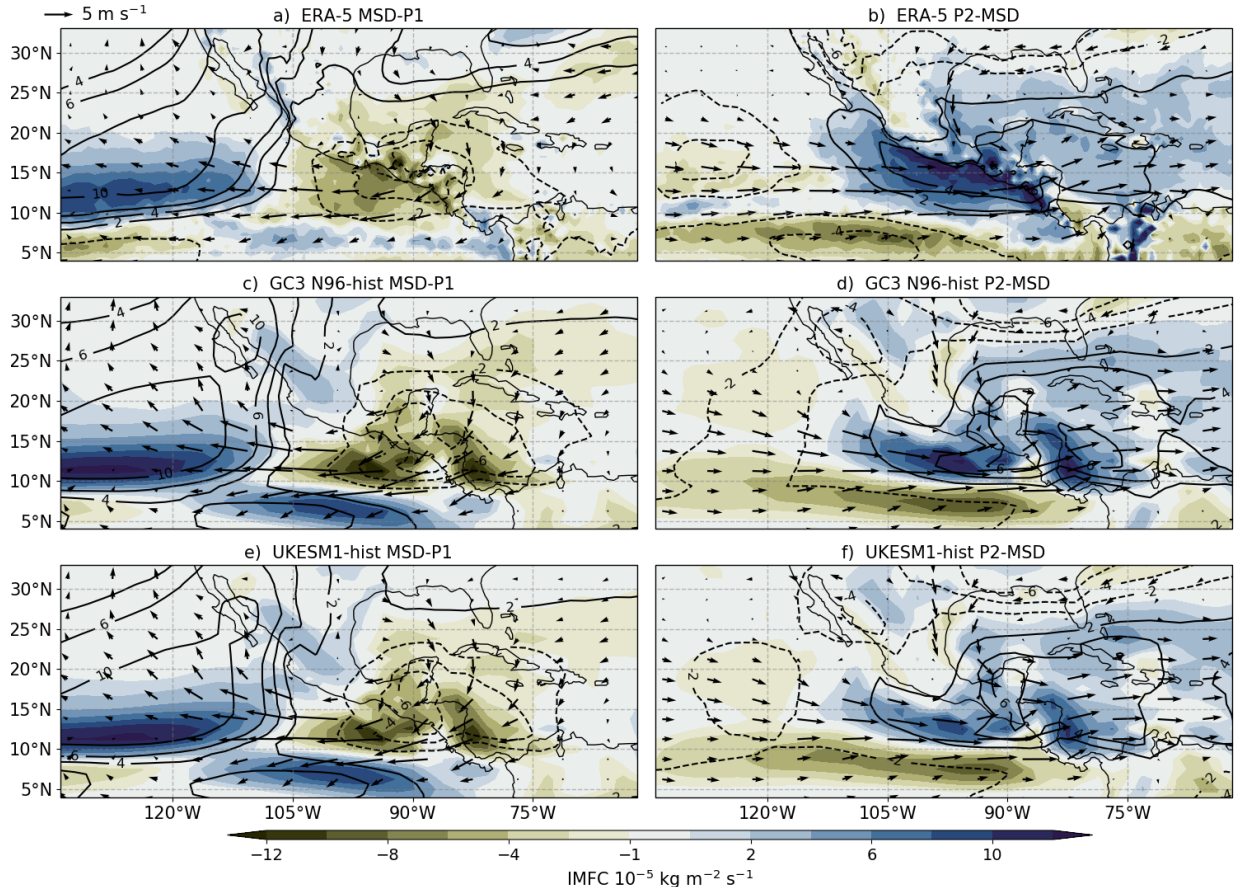


**Figure 6.22:** As in Figure 6.10, but showing variations in the IMFC (shading), TWC (contours in units of  $\text{kg m}^{-2}$ ) and 850-hPa wind (vectors).

a weak low-level westerly wind to an easterly wind (see also Figure 6.9c). At the end of the MSD, the wind direction changes again to a westerly direction in the East Pacific, whereas the wind anomalies in the Caribbean Sea turn to westerlies indicative of a weakening of the CLLJ, coincident with the second peak of precipitation observed in the MSD region.

IMFC and TWC show coherent variations with the timings of the seasonal cycle of precipitation in the MSD region, with less moisture convergence and precipitable water in the column during the drier period compared to the two peak periods. In contrast, west of the coast, at around the  $125^{\circ}\text{W}$ , during the MSD there is increased TWC and IMFC in ERA5 and in the simulations, in agreement with the previous sections which showed increased convective activity in this region. Simultaneous to the drying of southern Mexico and Central America during the MSD, the North American monsoon region moistens as

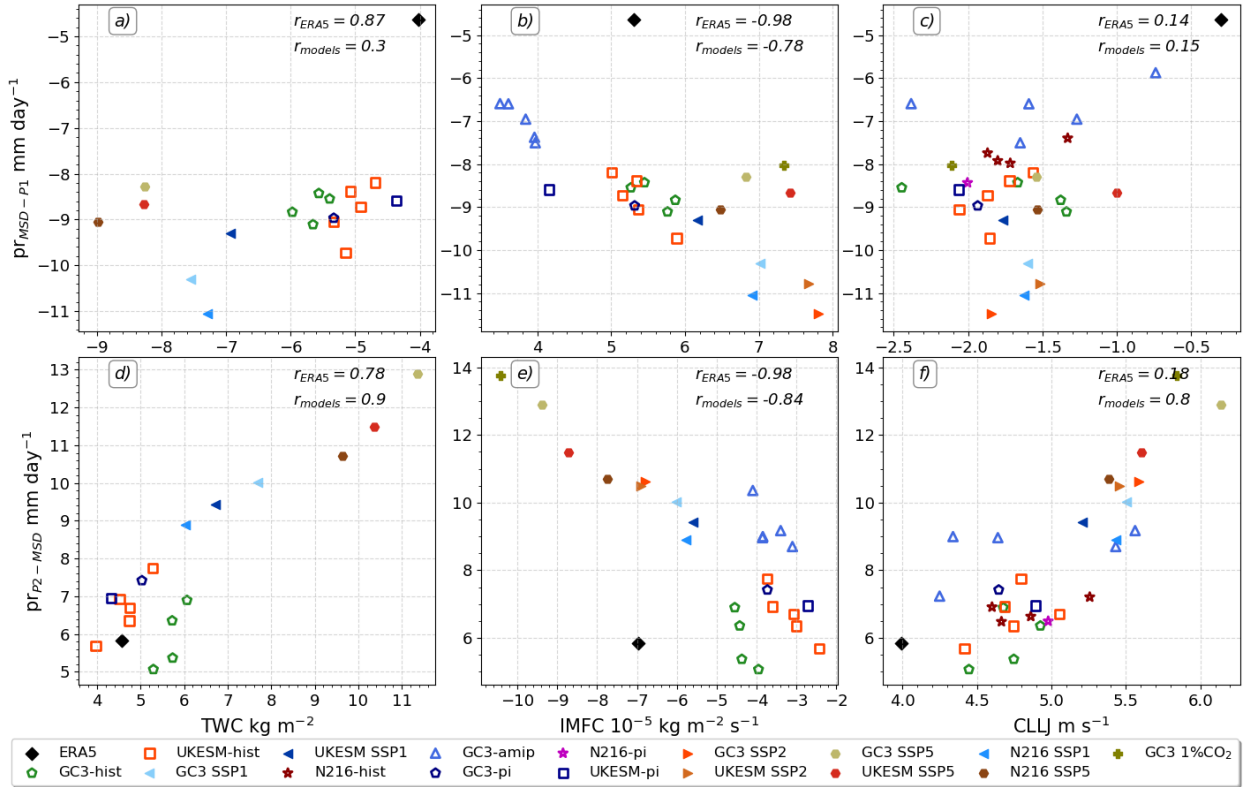


**Figure 6.23:** As in Figure 6.12, showing the scatter of mean changes (a-c) MSD-P1 and (d-f) P2-MSD periods, but using the (a, d) IMFD and (b, e) TWC in the MSD region and the (c, f) CLLJ on the x-axis and precipitation in the MSD region in the y-axis.

shown by the increased TWC and IMFC.

In turn, the IMFC and TWC anomalies associated with the end of the MSD period, depicted by the P2-MSD panel, show positive differences in the MSD region and negative anomalies southward, suggesting increased IMFC and TWC over southern Mexico and northern Central America, in agreement with the secondary increase in precipitation. Positive TWC and IMFC differences extend from the MSD region to the east into Cuba, the Caribbean Sea and the Gulf of Mexico. This moistening coincides with increased moisture divergence to the south of the MSD region in the East Pacific ( $120\text{-}90^\circ\text{W}, 3\text{-}10^\circ\text{N}$ ) and decreased TWC.

Furthermore, a scatter plot of the mean changes to the IMFD, TWC and the CLLJ and their relationship to the synchronous variations in precipitation (Figure 6.23) confirm that these diagnostics are deeply related to the timings and strength of the three stages in the seasonal cycle of precipitation. The interannual variability of the precipitation differences between the first peak and the MSD periods in ERA5 are very well explained by the

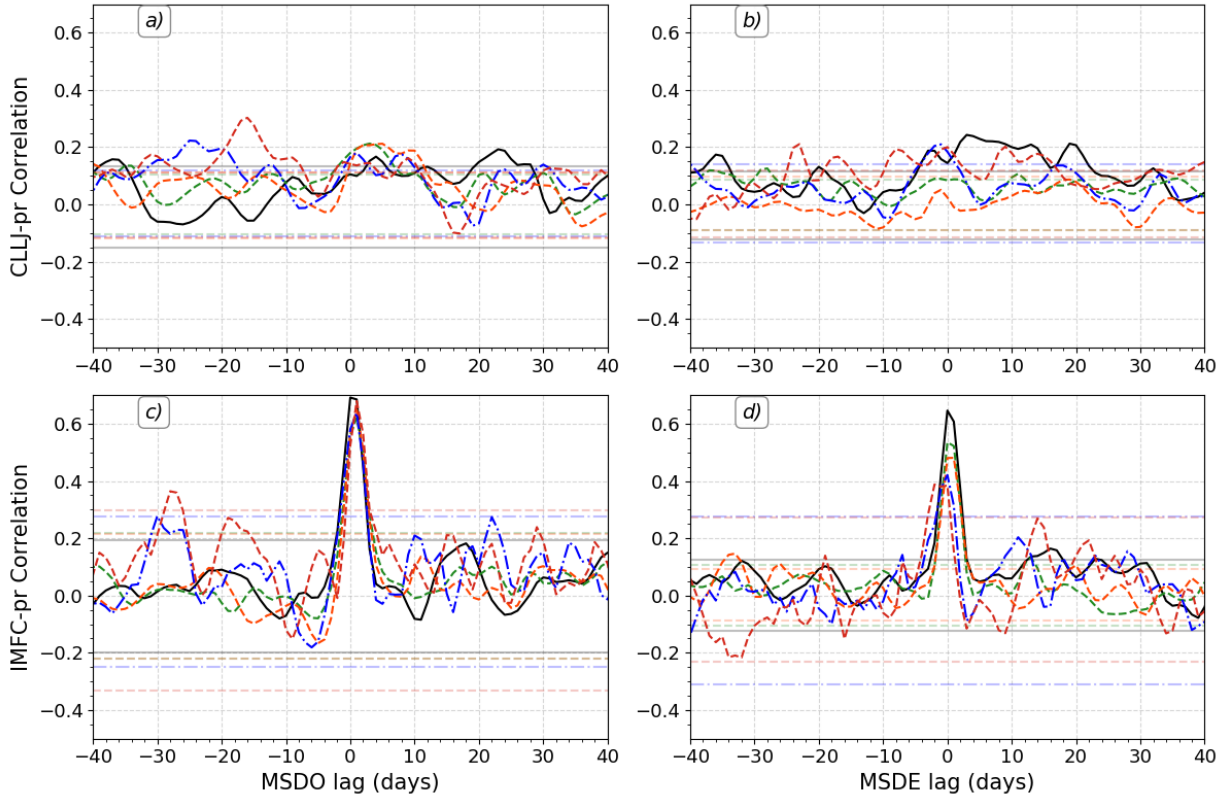


**Figure 6.24:** Lagged correlations between precipitation in the MSD and the (a, b) CLLJ, defined as the 925 hPa zonal wind averaged over the CSEA region, and (c, d) the IMFC over the MSD region. Correlations are shown with lags computed with respect to the (a, c) onset and (b, d) end dates.

interannual variability of the TWC ( $r = 0.87$ ) and the IMFC ( $r = -0.98$ ) but less so by the CLLJ ( $r = 0.14$ ). The inter-experiment variability in the MSD-P1 precipitation differences can largely be explained by the inter-experiment differences in IMFC changes during the MSD-P1 periods ( $r = 0.78$ ). However, the changes in the CLLJ and IMFC in the simulations can not explain the precipitation differences between the runs in the MSD-P1 panels.

The changes from the MSD to the second peak of precipitation (lower row in Figure 6.23) in the simulations are very well explained by the mean variations to the CLLJ, the TWC and the IMFC. However, for the interannual variability of ERA5, only changes to the TWC and IMFC show significant and relatively high correlations. These results would suggest that variability in the CLLJ can explain several differences in the magnitude of the P2-MSD differences in the models, possibly through the modulation of the CLLJ on the TWC and the IMFD over the continent; nevertheless, the observed interannual variability of

the CLLJ cannot explain the interannual variability in the strength of the second peak.

The synchronous relationship found in the previous scatterplot is further tested via lagged correlations, shown in Figure 6.24. These correlations do not show any evidence that the nature of the relationship between the CLLJ or the IMFC with precipitation over the MSD is of a lagged nature. In particular, the correlations of precipitation with the CLLJ are not higher than 0.3 at any lag and only become significant for a few days in some simulations. In particular, around the MSDE date, no correlation at negative lags is notably positive or significant which is at odds with the hypothesis that CLLJ is responsible for the end of the MSD.

However, the strength of the CLLJ may not be the relevant factor, but rather the influence of the CLLJ on the IMFC. The correlation of IMFC with precipitation shows a strong positive correlation, both at MSDO and MSDE in reanalysis and models around lag 0, and similar results are found for TWC-pr correlations (not shown). However, there is little evidence that this relationship is of a lagged nature, as the correlations are not significant far away from the 0 lag.

## 6.7 A short look at the MSD through the lens of the moist static energy budget

The previous sections have tested three leading hypothesis for the Midsummer drought, with results suggesting that only elements of the CLLJ hypothesis can explain the interannual variability in the strength of the MSD in reanalysis, as well as in the differences between the CMIP6 experiments. However, changes to the CLLJ and IMFC appear to be unrelated to the strength and time of the onset of the MSD, which means that other processes are responsible for the start of the drier MSD period. To further explore the processes that control the start of the MSD, the moist static energy (MSE) budget is used in this section to disentangle how the column MSE budget terms vary over the wet season.

The computation of the MSE budget terms is done as described in section 3.3. The budget terms are obtained from daily-mean values at all available levels within the troposphere for reanalysis and climate model output. It should be noted that the radiative heating terms

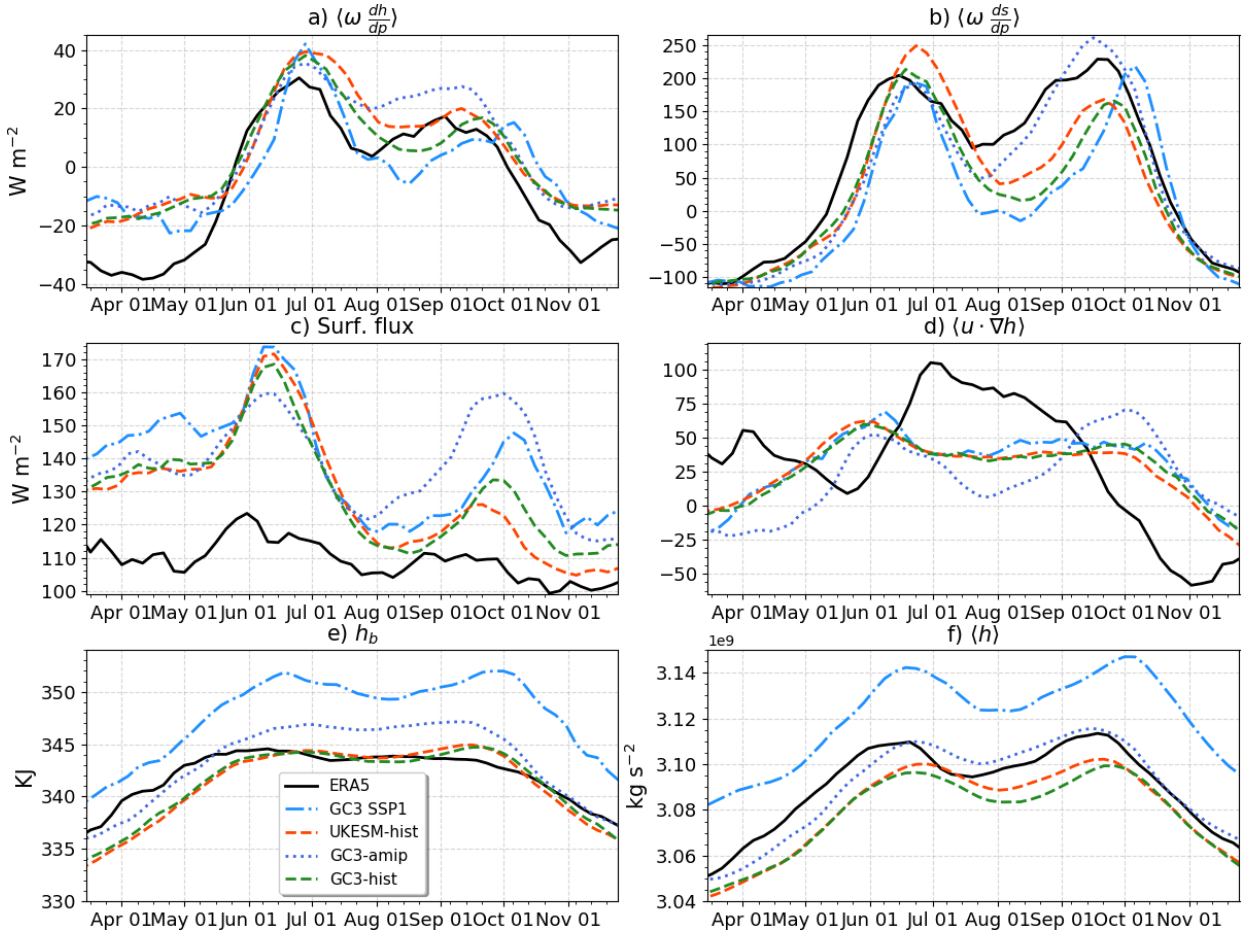


**Figure 6.25:** Pentad-mean seasonal cycle of the moist static energy budget terms. Vertical advection of (a) moist and (b) dry static energy, (c) the sum of the latent and sensible heat fluxes, (d) horizontal advection of MSE, (e) boundary layer MSE ( $h_b$ ) and total column MSE ( $\langle h \rangle$ ). The quantities in panels c,d were averaged over the EP region and the rest of the panels over the MSD region.

are not available from the CMIP archive on daily scales so a full budget was not feasible with model data. In turn, we focus on the vertical and horizontal advection of MSE, the total column MSE, the surface fluxes and the gross moist stability.

First, the seasonal cycle of the column budget terms, as well as the boundary layer or near surface MSE ( $h_b$ ), is shown in Figure 6.25 with some quantities shown for the EP region and others for the MSD region. The vertical advection of dry ( $s$ ) and moist ( $h$ ) static energy shows a clear bimodal seasonal cycle, with two peaks at the start and end of the summer season, separated by a local minimum that occurs at the end of July or early August. The simulated vertical advection of MSE corresponds well with ERA5 during the

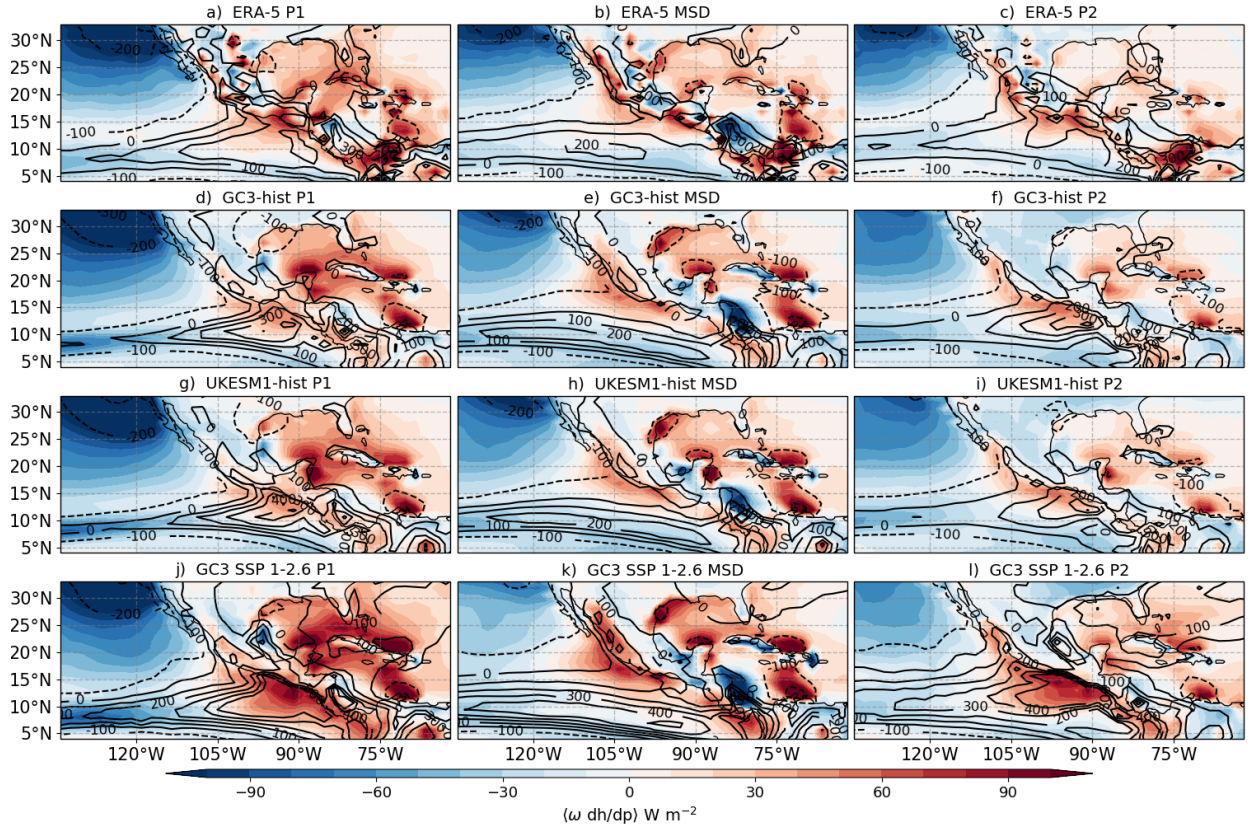


**Figure 6.26:** Composites of mean  $\langle \omega dh/dp \rangle$  (shading in  $W m^{-2}$ ) and  $\langle \omega ds/dp \rangle$  (contours in  $W m^{-2}$ ).

wet season (JAS) for all the simulations, although the vertical advection of  $s$  is smaller in the historical and SSP1 experiments during the MSD and second peak periods. The vertical advection of  $s$  is not underestimated by the GC3 amip experiment during late summer, which has a wetter second peak as shown in previous sections.

The sum of the latent and sensible heat fluxes in the EP region show a clear bimodal signal in the experiments but not in ERA5. The experiments also show very large biases during both periods of peak precipitation in June and Sep-Oct. In late summer, this bias is particularly notable in the GC3 amip experiment. These biases in the surface fluxes in the EP are arguably one of the reasons for the very wet bias found in the EP ITCZ in these models.

One component of the theory by Karnauskas et al. (2013) involved the net shortwave part of the surface energy balance being notably different during the various stages of the MSD. A direct implication from this hypothesis is that the shortwave ultimately influences the surface or boundary layer MSE (Fig. 6.25e). However, in most of the simulations and

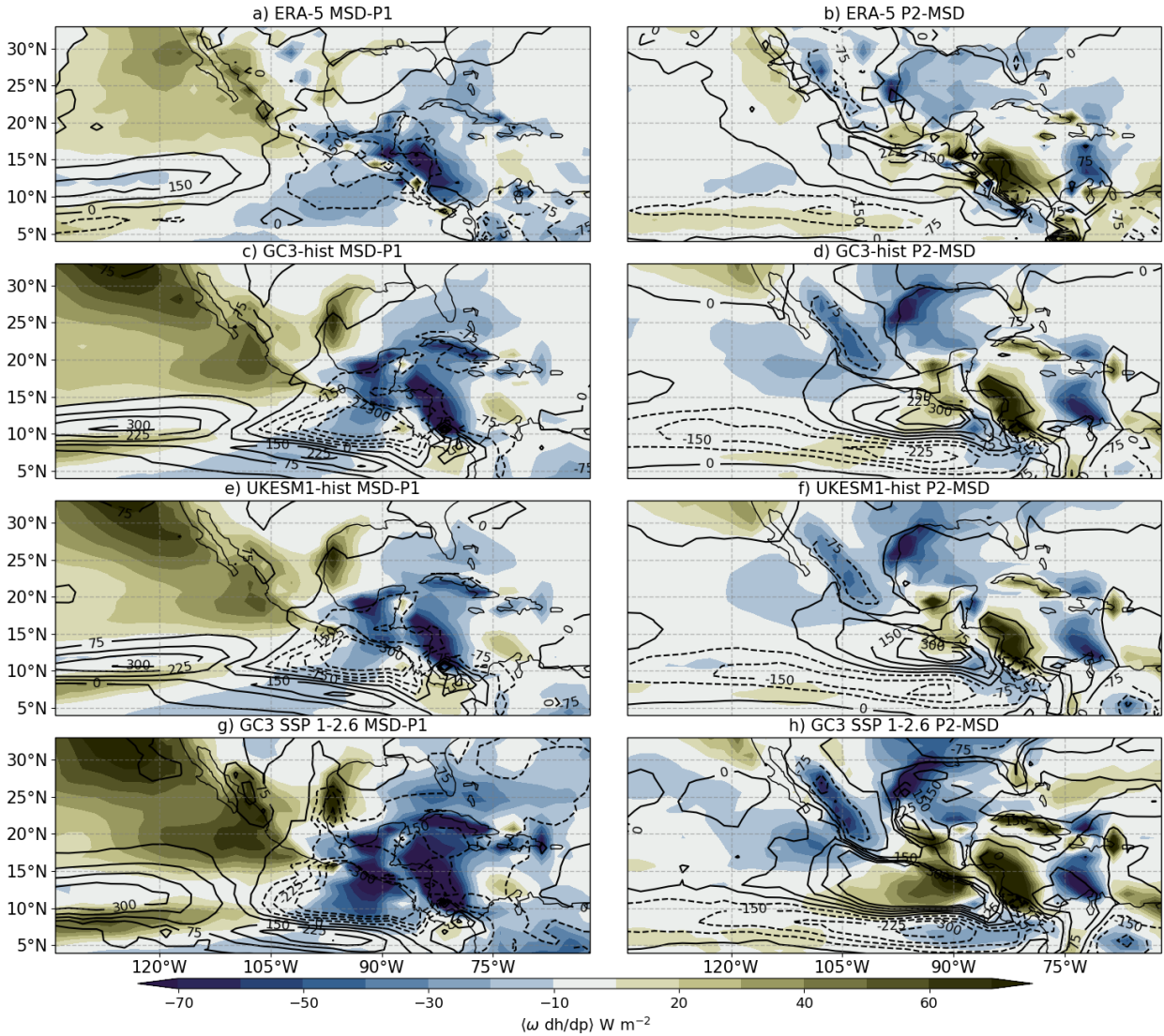


**Figure 6.27:** Composites of the differences (a, c, e, g) MSD-P1 and (b, d, f, h) P2-MSD of  $\langle \omega dh/dp \rangle$  (shading in  $W m^{-2}$ ) and  $\langle \omega ds/dp \rangle$  (contours in  $W m^{-2}$ ).

ERA5,  $h_b$  in the MSD region follows a plateau-like seasonal cycle with a clear increase during spring, a plateau during summer and a sharp decrease in October at the end of the rainy season. The SSP1 experiment shows a decrease in  $h_b$  in August but this is fairly modest compared to the magnitude of the change in  $h_b$  at the end and start of the summer.

Similarly, the total column  $h$  shows a modest bimodal seasonality in reanalysis and simulations, i.e.,  $\langle h \rangle$  decreases at the midsummer. The low-emission scenario shows a notable increase in total column  $h$  compared to historical and pre-industrial experiments, and higher emission scenarios (SSP2 and SSP5) showed that total  $h$  scales with greenhouse forcing (not

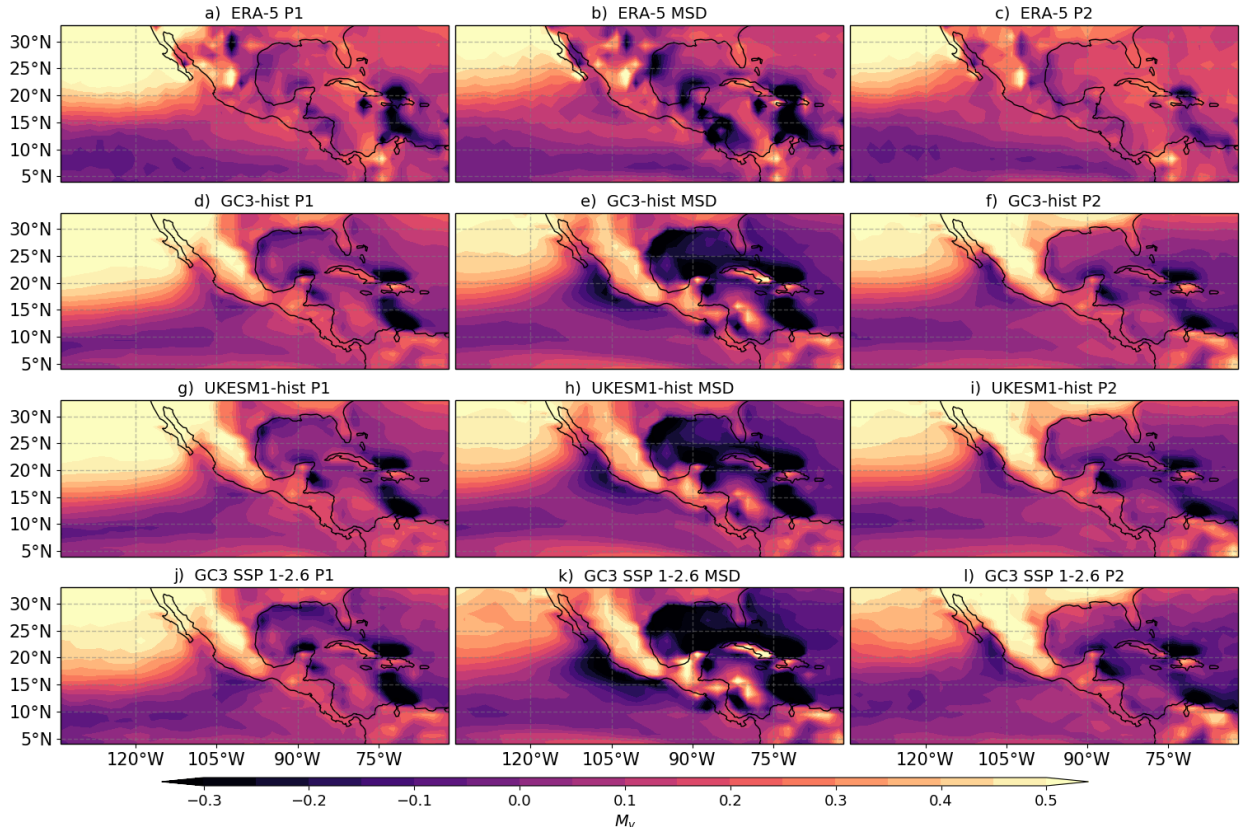


**Figure 6.28:** Composites of vertical gross moist stability ( $M_v$ ) in the three stages of the Midsummer drought for ERA5 and three experiments.

shown). One key aspect of this increase in total column  $h$  is that total precipitation is not increased uniformly over all the stages of the wet season (see Fig. 6.7).

The spatial distribution of the mean  $\langle \omega dh/dp \rangle$  and  $\langle \omega ds/dp \rangle$  (Figure 6.26) during the three stages of the MSD seasonal cycle show a good agreement between the experiments and reanalysis. The highest values of  $\langle \omega ds/dp \rangle$  are found on the western coast of northern Central America, in the easternmost position of the ITCZ. Positive values of  $\langle \omega dh/dp \rangle$  are found in the Caribbean Sea, the Gulf of Mexico and over the Mesoamerican region throughout the three stages of the MSD. Negative values of  $\langle \omega dh/dp \rangle$  and  $\langle \omega ds/dp \rangle$  are found over the coast of California throughout the wet season.

The changes to the  $\langle \omega dh/dp \rangle$  and  $\langle \omega ds/dp \rangle$  during the MSD periods are best illustrated in Figure 6.27, which shows the differences between MSD-P1 and P2-MSD. In the Mesoamerican region,  $\langle \omega dh/dp \rangle$  and  $\langle \omega ds/dp \rangle$  are reduced during the MSD period compared the first peak period, this difference is maximized right at the exit of the Gulf of Tehuantepec, in

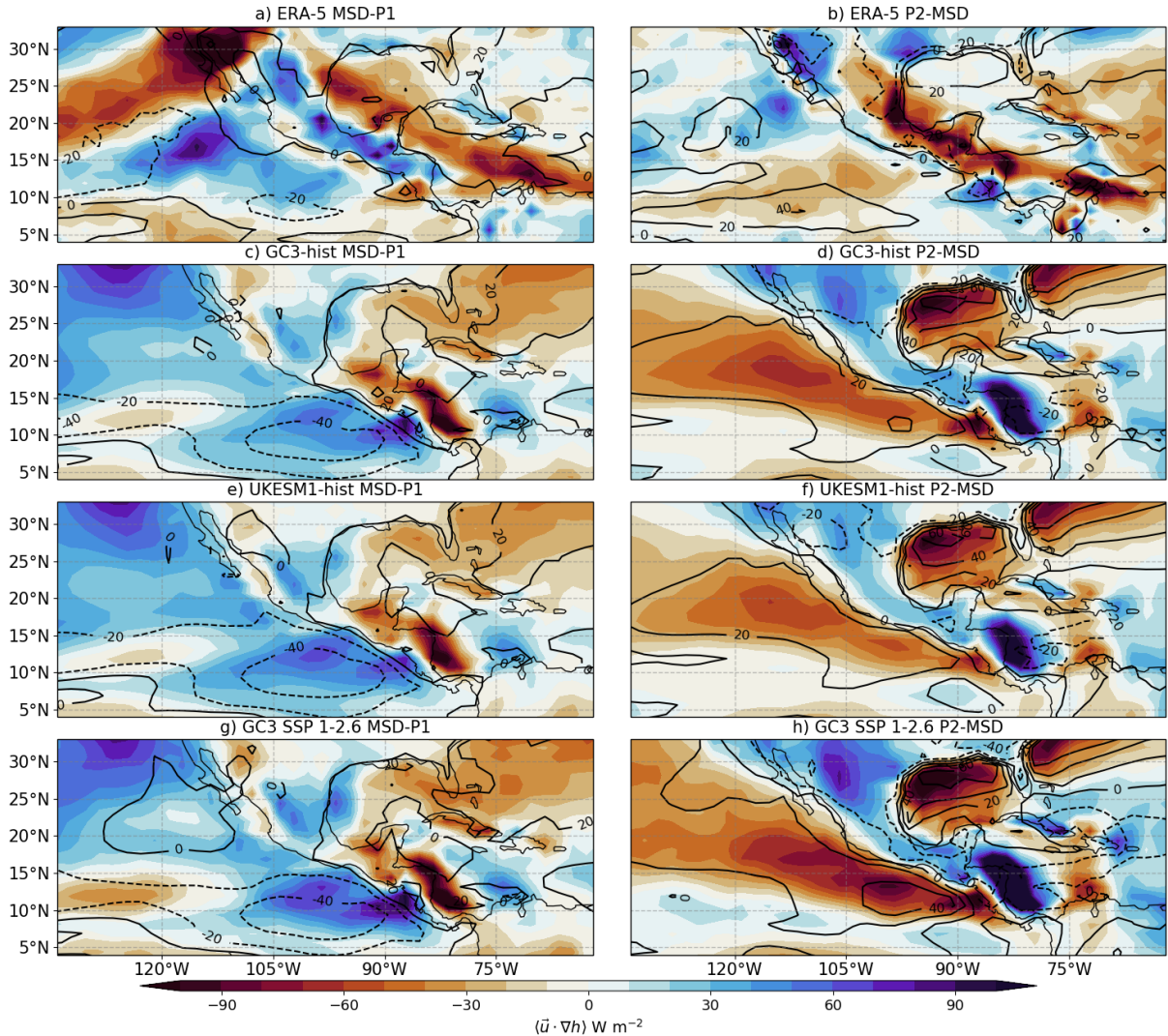


**Figure 6.29:** Composites of the differences (a, c, e, g) MSD-P1 and (b, d, f, h) P2-MSD of  $\langle \vec{u} \cdot \nabla h \rangle$  (shading in  $\text{W m}^{-2}$ ) and total surface fluxes ( $F$ ) (contours in  $\text{W m}^{-2}$ ).

southwestern Mexico. Simultaneously, from the P1 to the MSD period,  $\langle \omega ds/dp \rangle$  notably increases west of the Mesoamerican region near the  $125^\circ\text{W}$  region whereas  $\langle \omega dh/dp \rangle$  increases in northern Mexico and in the Gulf of California.

At the end of the MSD, illustrated by the P2-MSD panels in Figure 6.27,  $\langle \omega dh/dp \rangle$  and  $\langle \omega ds/dp \rangle$  increase notably in the Mesoamerican region. Again, the maximum difference of  $\langle \omega ds/dp \rangle$  is found in the Gulf of Tehuantepec region. The North American monsoon region show a decrease in both  $\langle \omega dh/dp \rangle$  and  $\langle \omega ds/dp \rangle$ . Both for the P2-MSD and MSD-P1 panels, the experiments are able to reproduce the spatial patterns of these changes to these budget terms. Furthermore, the SSP1 experiment shows larger differences between the

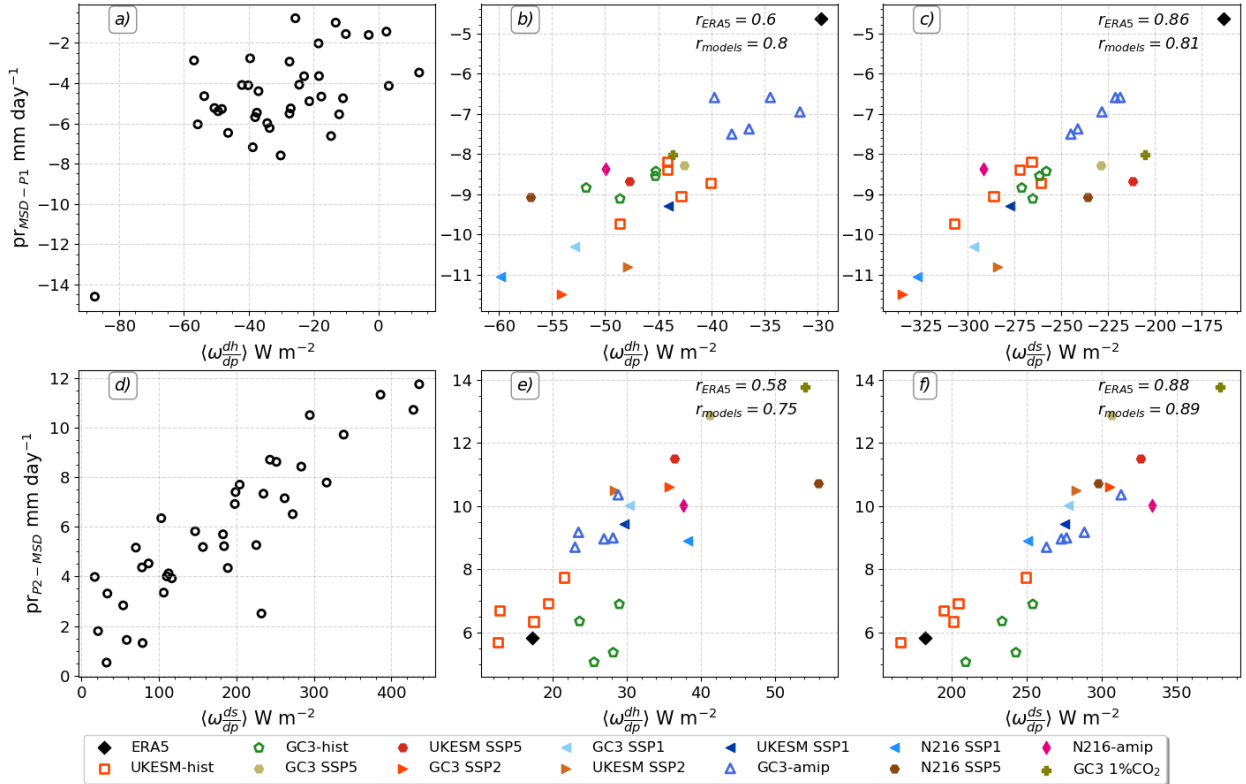


**Figure 6.30:** Scatterplot of the relationship between the area-averaged mean vertical advection of dry and moist static energy and precipitation over the MSD region. In panels a, d, each dot represents the differences in the mean values between a) MSD-P1 and (d) P2-MSD for precipitation in the y-axis and vertical advection of  $h$  and  $s$  in the x-axis. In the rest of the panels, the differences are shown for the dataset-mean for all years in each dataset.

MSD stages compared to the historical experiments.

The normalized gross moist stability (NGMS) is a useful quantity to better understand how convection is redistributing  $h$  vertically (see equation 3.6). Figure 6.28 shows the temporal and spatial variability of the vertical component of the NGMS ( $M_v$ ) during the three stages of the MSD. The reanalysis and the simulations show that  $M_v$  is generally close to 0 in the easternmost Pacific ( $5^\circ\text{N}$ - $15^\circ\text{N}$ ) and into the MSD region, and positive on the western coast of California and over the continental North America.

The most noteworthy variations of  $M_v$  associated with the MSD timings occur over the western coast of Mexico, the Gulf of Mexico and the Caribbean. From the first peak period to the drier MSD period,  $M_v$  decreases in these regions and then increases again from the dry period to the wetter second peak period. Negative and minimum  $M_v$  is then

found during the MSD period over most of the so-called Intra-Americas Seas region. This result is important because these changes point to seasonal variations in the relationship between convection and the large-scale dynamics (Raymond et al., 2009), including the shape of the vertical velocity profile.

The horizontal advection term and the surface fluxes also show notable differences associated with the MSD timings (Figure 6.29). In the MSD-P1 period, decreased surface fluxes in the easternmost Pacific Ocean are observed in the three simulations and, to a lesser degree, in ERA5. These differences suggest that in the models, surface fluxes decrease as precipitation decreases from the wet first peak period to the dry MSD period. In the simulations, these negative surface flux anomalies are collocated with negative differences of the horizontal advection of MSE term.

A key question then is how the MSE budget equation is balanced in the different stages of the seasonal cycle, i.e., which terms balance the horizontal and vertical advection of MSE during the early and late wet periods and in the MSD period. Figure 6.31 shows the mean values of each budget term in the MSD in ERA5 and the simulations. The results in the simulations are shown per month because the radiative heating data from the CMIP6 archive was only available for monthly-mean frequencies.

In ERA5 (Fig. 6.31a), the positive contributions of MSE from the shortwave heating and the surface fluxes are balanced mostly by the negative contribution from the longwave heating (radiative cooling of the column) and to second order by the horizontal and vertical advection terms. The differences in the budget terms between the P1, MSD and P2 periods are most pronounced for the vertical and horizontal advection terms which total contribution increases during the MSD compared to the other two periods. However, from P1 to the MSD stage, the longwave radiative heating notably decreases and increases again from the MSD to P2 periods whereas the shortwave heating term appears to change very little between the stages of the rainy season.

In the CMIP6 simulations (Fig. 6.31b-d), a similar balance is observed with the largest contributions arising from the terms of radiative heating and surface fluxes. From May to September some seasonal variations in each term are observed, for example, stronger longwave cooling in May than in June-July. The vertical advection term also increases notably during

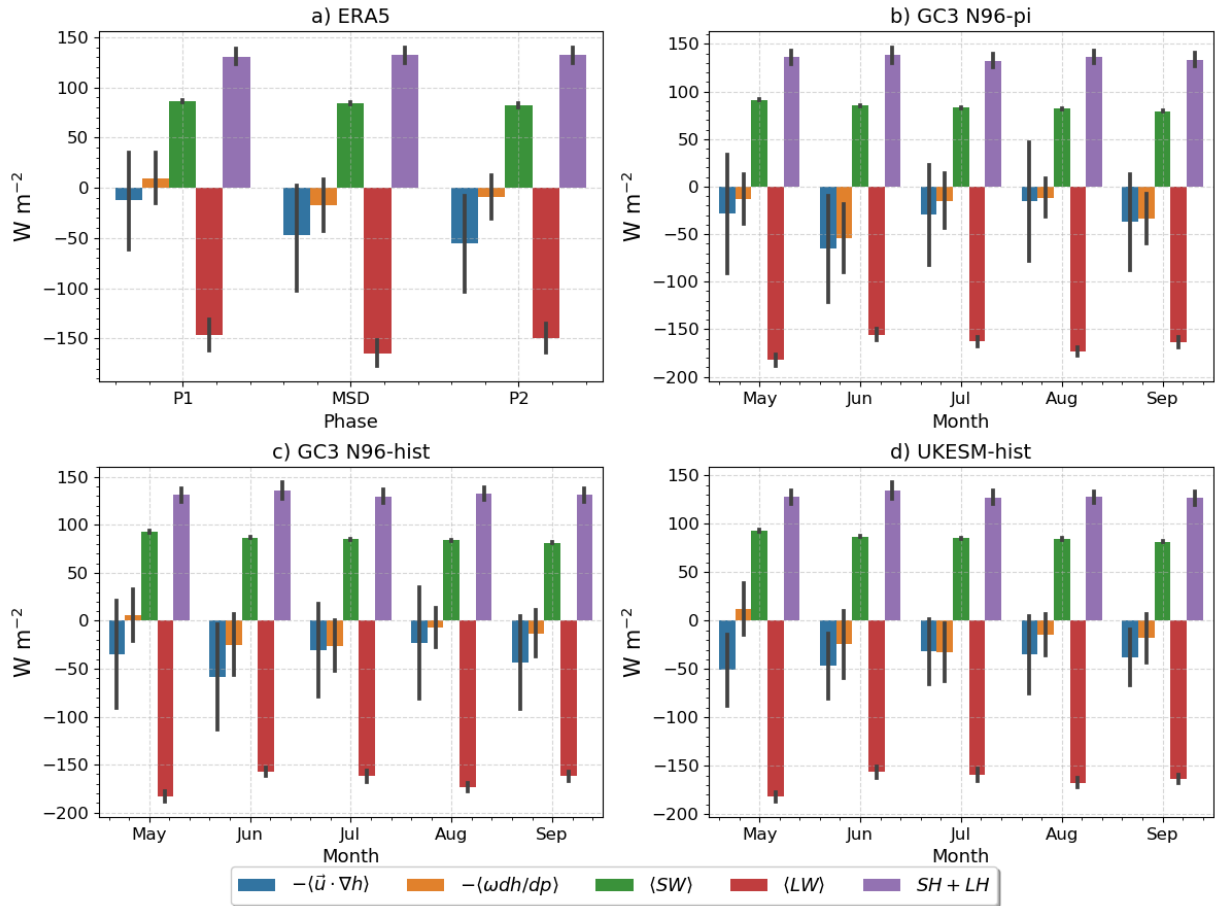


**Figure 6.31:** Barplots of the area and time-averaged MSE budget terms: horizontal advection ( $\langle \vec{u} \cdot \nabla h \rangle$ ) and vertical advection ( $\langle \omega dh/dp \rangle$ ), longwave ( $\langle LW \rangle$ ) and shortwave ( $\langle SW \rangle$ ) and the sum of sensible ( $SH$ ) and latent heat ( $LH$ ) fluxes. (a) shows the budget terms computed from ERA5 in the MSD region in the P1, MSD and P2 periods. (b-d) show the monthly-mean values of the budget terms.

the early rainy season (June-July) compared to the rest of the wet season. As in ERA, the contribution from the vertical advection term increases during the MSD with minima found in June or July in all the simulations. The horizontal advection increases during the months of the two peak of precipitation (May and September) and decreases during the MSD.

The scatter of the relationship between precipitation and the vertical advection of dry and moist static energy during the wet season (Figure 6.30) indicates that the shape of the vertical profile of the vertical velocity is strongly linked to precipitation variations, both in ERA5 as in the simulations. Figure 6.30a, d shows that the interannual variability of vertical advection of dry and moist static energy in ERA5 is strongly related to interannual

variations in the precipitation changes during the MSD. Negative differences of  $\langle \omega dh/dp \rangle$  and  $\langle \omega ds/dp \rangle$  are observed in MSD-P1 panel, in agreement with the previous composite analysis whereas increases of these terms occur from the MSD period to the second peak period in ERA5 and in the experiments. Specifically,  $\langle \omega ds/dp \rangle$  is the term that best explains interannual variability of the strength of the MSD, measured by the difference MSD-P1 in ERA5. The budget analysis shows that the variability of the horizontal advection and longwave heating terms within the rainy season is stronger than for the shortwave heating and surface fluxes. This evidence suggests that LW CRE and moisture transport may be more important than surface fluxes of total shortwave incoming to the troposphere, which supports the mechanism that links the CLLJ to the precipitation in the MSD. These budget terms could also be interpreted as evidence that cloud-radiative feedback mechanism and the solar declination angle are less likely to explain the MSD.

## 6.8 Summary and discussion

The Midsummer drought (MSD) is a key element of past, present and future climates of southern Mexico, northern Central America and the Caribbean with important implications for agriculture and water management (Hellin et al., 2017; de Sousa et al., 2018; Harvey et al., 2018). However, a complete description of the physical mechanisms that explain the spatial and temporal variability of the MSD is not yet clear. This lack of understanding is magnified when investigating the MSD in global climate models that are used for projections of future climate, as little is known as to why only some models can reproduce the MSD (Ryu and Hayhoe, 2014).

This chapter tackled these shortcomings in the literature by investigating the processes that are linked to the MSD in CMIP6 experiments of the MOHC models, an investigation that was motivated by the two previous chapters which showed that these models reasonably reproduced the main features of the MSD signal. The first contribution of this chapter is the diagnosis of MSD timings and patterns on a sub-monthly scale, a step forward from previous studies that diagnosed the MSD on monthly-mean timescales, possibly missing key

information in the process. For this purpose, the wavelet transform method (WT; Chapter 5) was used to determine the timings of the MSD on a 5-day (pentad) scale.

The WT method proved useful to separate the wet season in each dataset into three stages: the first and second peak periods (P1 and P2) and the drier period (MSD). This approach using the WT method was able to reproduce the so-called MSD pattern reported in previous studies (Zermeño-Díaz, 2019; Zhao et al., 2020) using various diagnostics such as OLR,  $\omega$  and the low-level wind flow. This pattern is characterised by strong changes to the zonal wind flow crossing from the Caribbean Sea into the easternmost Pacific Ocean, as well as by anomalous vertical velocities found west of the coast at around 125°W, in agreement with previous findings (Herrera et al., 2015; Zermeño-Díaz, 2019).

The chapter first evaluates key climate features in the region such as the seasonal cycle of the Caribbean Low-Level Jet (CLLJ) and East Pacific SSTs. Results show that the simulations agree well with the observed seasonal cycle and that the experiments show very similar MSD patterns to observations. The following sections in the chapter test three of the leading hypotheses put forth to explain the MSD, this investigation is the second key contribution from this chapter. Each hypothesis is evaluated using the WT method in two different ways. The first question was whether a hypothesis could explain the interannual variability in the strength and timing of the MSD in ERA5. The second approach focused on the CMIP6 experiments and aimed to test whether the elements of each hypothesis could explain the differences in precipitation at each stage of the seasonal cycle between the realizations.

The first mechanism proposed by Magaña et al. (1999) argues that SST-cloud-radiative feedbacks explain the MSD. In this hypothesis, the SSTs in the East Pacific should also exhibit a bimodal seasonal cycle, with a second peak in SSTs found in September. Even though Magaña and Caetano (2005) analysed this for a specific year and found no evidence of a second peak in SSTs, no study to date robustly evaluated whether observations or models confirm their hypothesis. This chapter provides evidence that in ERA5, SSTs not only do not increase at the later stages of the summer but rather decrease. While the seasonal cycle in the simulations do show a two peak structure, the composite analysis shows that as precipitation transitions from the drier MSD to the second peak periods, SSTs decrease in the Pacific

coast of Central America, in contrast to the prediction of the SST-cloud feedback mechanism. No evidence is found that the variability of the East Pacific SSTs is directly associated with the precipitation over the MSD region in ERA5 or in the CMIP6 experiments.

The feedback mechanism also suggests that the second peak is a result of a second increase in downwelling shortwave radiation at the surface that results from cloud cover during the drier MSD. The solar declination angle mechanism of Karnauskas et al. (2013) also suggests that shortwave absorption has two peaks in the seasonal cycle, which leads to the two precipitation peaks. The shortwave absorption at the surface does show a bimodal seasonal cycle in ERA5 and in the simulations, as predicted by these two mechanisms.

However, the interannual variability in ERA5 and inter-experiment differences in the absorbed shortwave at the different stages of the seasonal cycle cannot explain the changes over precipitation. Moreover, no significantly positive correlation is found between the shortwave absorption at the surface and precipitation at any lags but rather a strong anticorrelation signal is found, which is a result of stronger convective activity leading to more cloud cover and less downwelling shortwave at the surface. Therefore, while this chapter found some evidence of strong correlations between SW and precipitation, there is little evidence found that the SW drives precipitation, as argued by the solar declination angle mechanism.

Cloud-radiative effects (CRE) are known to be key for precipitation in monsoon regions and the central argument of Magaña et al. (1999) is that precipitation and CRE (at the surface) are part of a feedback mechanism that explains the MSD. This chapter presents the first regional evaluation of the net CRE at the surface as well as the long-wave and short-wave contributions. The net CRE at the surface over the wet season is negative following the regions of maximum precipitation, i.e., the East Pacific ITCZ and the MSD region reaching values of  $-100 \text{ W m}^{-2}$  over the core ITCZ region in both the models and ERA5.

The net CRE is dominated by the short-wave component that acts to cool the surface due to the effect of cloud cover associated with convection. Over the MSD region, the net, short-wave and long-wave CRE at the surface show a bimodal regime that closely follows the evolution of precipitation. Finally, an experiment part of CFMIP in which the long-wave effects of clouds are turned-off from the radiative scheme shows that the longwave radiative effects are key for monsoon precipitation in Central America and southern

Mexico, where long-wave effects are decoupled from the simulation, shows that the long-wave component of CRE are key for sustaining the monsoon circulation and precipitation irrespective of the bimodal MSD signal.

This section showed that CRE have a strong seasonal cycle associated with the MSD in ERA5 and the MOHC experiments. However, further research into CRE in present and future climates in the region is warranted, for example, further work could include a detailed examination of the CRE at the top of atmosphere and at the surface in the MSD, particularly to understand the relationship between CRE and the large-scale circulation, and how this relationship is different over land in Mesoamerica than over the Caribbean Sea and the East Pacific Ocean.

One alternative hypothesis is that the MSD is caused by the modulation of the transport of moisture by the CLLJ (Herrera et al., 2015; Zermeño-Díaz, 2019; Martinez et al., 2019). The integrated moisture flux convergence and the total column water content are found to better explain observed and simulated differences in precipitation, compared to the previous hypotheses. Evidence is presented that the low-level wind flow variations on the west coast of Central America is linked to the variations in the strength and direction of the CLLJ. Changes to the CLLJ and moisture convergence allow skillful predictions of precipitation changes at the end of the MSD period but these are less skilful for changes at the start of the MSD.

A moist static energy (MSE) budget is implemented to investigate whether this technique could provide additional insight into the mechanisms of the MSD. The total column MSE, as well as the vertical advection terms of the budget show a clear bimodal signal that closely follows that of precipitation. The vertical advection of dry and moist static energy are found to have the strongest relationship to the interannual variability and the inter-experiment differences of precipitation in the MSD region.

In particular,  $\langle \omega_{ds}/dp \rangle$  is able to explain interannual variability in ERA5 as well as the precipitation differences between the range of experiments considered in this chapter. While these results do not directly point to any theory or hypothesis, the strong correlations in reanalysis and simulations indicate that MSE budgets would be useful in future research to better understand the key mechanism underpinning the MSD. Specifically, this result points to a possible modulation of the strength of convection by the shape of the vertical

velocity profile, which is the key modulator of these terms. How the vertical velocity profile changes during the rainy season, and whether there are notable trends in ERA5 or significant changes between historical and Scenario experiments warrants further research.

# 7

## The tropical route of QBO teleconnections in UKESM1 and HadGEM3

Evidence in a previous chapter suggests that the QBO plays a role in tropical ENSO teleconnections associated with the Walker circulation in the CMIP6 experiments of the MOHC models. In this chapter, the influence of the QBO on the tropical mean circulation and teleconnections is more closely examined in these models. An analysis of the CMIP6 experiments from the MOHC shows how the tropical circulation, monsoons and the ITCZ are influenced by the QBO. Results are discussed in the context of existing observational evidence of QBO tropical teleconnections.

### 7.1 Introduction

Long-distance effects or teleconnections associated with the stratospheric quasi-biennial oscillation (QBO) have been well documented in the subtropics and extratropics, for example for the stratospheric polar vortex (Holton and Tan, 1980; Anstey and Shepherd, 2014; Lu et al., 2020), the subtropical jets (Garfinkel and Hartmann, 2011; Hansen et al., 2016) and the North Atlantic Oscillation (Hansen et al., 2016; Gray et al., 2018; Andrews et al., 2019b). Observational and modelling evidence suggests that there is also a tropical route of influence of the QBO to surface climate, for example, over tropical convective phenomena such as

monsoons (Giorgetta et al., 1999; Liess and Geller, 2012), the ITCZ (Gray et al., 2018), tropical cyclones (Gray, 1984; Chan, 1995) and most recently, the Madden-Julian Oscillation (MJO) (Lee and Klingaman, 2018; Wang et al., 2019; Martin et al., 2020), see section 2.5.2.

Several observational and modelling studies have found evidence of QBO-related influence over convective activity in monsoon regions, such as in the South American, East Asian, Australian and Indian monsoons (Giorgetta et al., 1999; Collimore et al., 2003; Liess and Geller, 2012; Gray et al., 2018). In observations, these responses have been found in satellite-derived fields such as cloud height, occurrence and out-going longwave radiation (Collimore et al., 2003; Liess and Geller, 2012), as well as in surface precipitation diagnosed from gridded datasets or from reanalysis (Gray et al., 2018). However, the observational evidence shows zonally asymmetric impacts, indicative that the impact of the QBO depends on longitude, which has been explained (e.g. by Collimore et al., 2003; Liess and Geller, 2012) through a QBO modulation of the Walker circulation.

In models, Giorgetta et al. (1999) finds that boreal summer monsoon regions exhibit a significant response in cloudiness to QBO winds within the GCM ECHAM4. Nie and Sobel (2015) further finds in a modelling framework that the influence of the QBO may depend on the strength of convection and SST forcing, suggesting a non-linear effect of the QBO over a convective profile. In CMIP5/CMIP6 models, only a relatively small number of studies have analysed tropical QBO teleconnections (Serva et al., submitted), as most studies focus on the polar and subtropical routes (Richter et al., 2020; Anstey et al., 2021).

Although the polar and subtropical routes of influence of the QBO to the surface are relatively well established, the impact of the QBO over tropical convective phenomena remains less well understood for various reasons. First, the short observational record limits the confidence in any analysis that seeks to investigate differences between the two QBO phases in a 30-40-yr long dataset. Tropical circulation variability on QBO time-scales is largely dominated by ENSO, which makes it difficult to separate the effects of ENSO and the QBO, other than by multi-variable regression analysis as in Gray et al. (2018). In addition, there is also evidence that ENSO and convection in the Pacific influence the QBO, so there is a two-way relationship that would difficult a separation of cause and effect (Schirber, 2015; Christiansen et al., 2016).

In addition, the specific physical mechanisms through which the QBO could influence tropical convection at the grid-scale or the large-scale tropical circulation are also not well understood. While early studies (Gray, 1984; Collimore et al., 2003) suggest that changes to the vertical wind shear or static stability in the upper-troposphere lower-stratosphere (UTLS) region are the cause of these teleconnections, there is a lack of evidence in the literature to support any mechanism over another. As such, studies have struggled to pin-point direct impacts and mechanisms by which the QBO may modulate any aspect of tropical climate.

This chapter investigates QBO tropical teleconnections in the pre-industrial control experiments of the MOHC UM: GC3 N96-pi, GC3 N216-pi, UKESM-pi. These simulations are ideal to investigate variability associated with the QBO because these experiments are very long integrations where external forcing is kept constant within the simulation and the UM is a model that reasonably simulates the QBO (Richter et al., 2020). The remainder of this chapter is presented as follows. First, the data and methods used are described, after which the results analysing the QBO impacts over the seasonal precipitation and surface temperatures is given. Then, a more detail investigation on the effects on the East Pacific and Atlantic ITCZs is presented and finally, the impacts over ENSO, the Indian Ocean and the Walker circulation are given. A discussion is given at the end of the chapter.

## 7.2 Methods and data

The observational datasets and reanalysis (ERA5) used in this chapter are described in section 3.1 and consist of the HadSST3 dataset for SST, GPCP for precipitation and ERA5 for the rest of the diagnostics that include the zonal and meridional winds, air temperature, etc.

### 7.2.1 CMIP6 data

The three pre-industrial control experiments of the MOHC submitted to CMIP6 are used in this chapter: GC3 N96-pi, GC3 N216-pi and UKESM-pi. UKESM-pi and GC3 N96-pi are run with the same resolution (N96) of  $1.875^\circ \times 1.25^\circ$  and GC3 N216-pi is considered a medium-resolution simulation (N216) with atmospheric resolution of  $0.83^\circ \times 0.56^\circ$ . The period of 1850-2350 is used for GC3 N96-pi and GC3 N216-pi and 2050-2650 for the UKESM-pi.

## 7.2.2 Indices

The indices for ENSO and the QBO are diagnosed exactly as in section 4.2, i.e., the 70-hPa zonal mean zonal wind index is used for the QBO with a threshold of  $2 \text{ m s}^{-1}$  for each phase and the EN3.4 index is used with a threshold of  $\pm 0.65$  to define positive or negative events.

## 7.2.3 Analysis techniques

Composite analysis is the preferred technique used throughout this chapter. For each QBO or ENSO phase, composite samples are drawn for specific seasons using the indices and definitions mentioned above. Statistical significance is estimated in various ways, in some cases through standard Student or Welch t-test's where specified, and in some other cases a randomised resampling or bootstrapping method is also implemented in several sections of the chapter. The bootstrapping method is performed in all cases by drawing random samples from the entire simulation and repeating the process 10,000 times to evaluate the likelihood of obtaining a relationship by chance.

Linear regression analysis has proven useful to understand the effect of one or more aspects of the climate over a region or a time-series, and was used to investigate the surface impacts of the QBO in observations by Gray et al. (2018). A simple linear regression model can be written as:

$$Y(t) = X_0 + X_i(t)\beta_i + \epsilon, \quad (7.1)$$

where  $Y$  is the measured or dependent variable,  $X_0$  is a constant coefficient,  $\beta_i$  is the regression coefficient between  $X_i$  and  $Y$  and  $\epsilon$  represents random error or a residual. A multivariate regression model can be used to study the joint effect of two or more predictors over a variable ( $Y$ ) such that the model can be written as:

$$Y(t) = X_0 + \sum_j^N X_j(t)\beta_j + \epsilon \quad (7.2)$$

where  $X_j(t)$  is any predictor with an associated regression coefficient  $\beta_j$ . As in previous studies (Gray et al., 2018; Misios et al., 2019), the regression coefficient can be rescaled to evaluate the total effect that a predictor ( $X_j$ ) can have on the variance of the measured

variable ( $Y$ ) using the standard deviation ( $\sigma_j$ ) and the maximum ( $X_{j,max}$ ) and minimum ( $X_{j,min}$ ) values of  $X_j$  so that the rescaled coefficient  $\beta'_j$  can be written as:

$$\beta'_j = \beta_j \frac{X_{j,max} - X_{j,min}}{\sigma_j}. \quad (7.3)$$

### 7.3 Teleconnections in the pre-industrial control experiments

Surface impacts of the QBO in the tropics have scarcely been investigated in CMIP models, as most studies focus on the general representation of the QBO (e.g Schenzinger et al., 2017; Bushell et al., 2020), or the extratropical teleconnections (e.g. Anstey et al., 2021; Dimdore-Miles et al., 2021). However, studies that have investigated teleconnections between the QBO and tropical convective phenomena in relatively novel GCMs (e.g. Lee and Klingaman, 2018; Martin et al., 2021; Serva et al., submitted) have found that model biases in representing the variability of temperature and winds in the tropopause layer may hinder a possible interaction between the QBO and tropical convection.

This section examines more closely how the MOHC piControl experiments simulate the effect of the QBO over seasonal-mean precipitation, monsoons and the ITCZ. The three simulations chosen use the same model setup, with constant year 1850 forcing, but differ in their horizontal resolution or the treatment of aerosol-chemistry processes (see section 3.2).

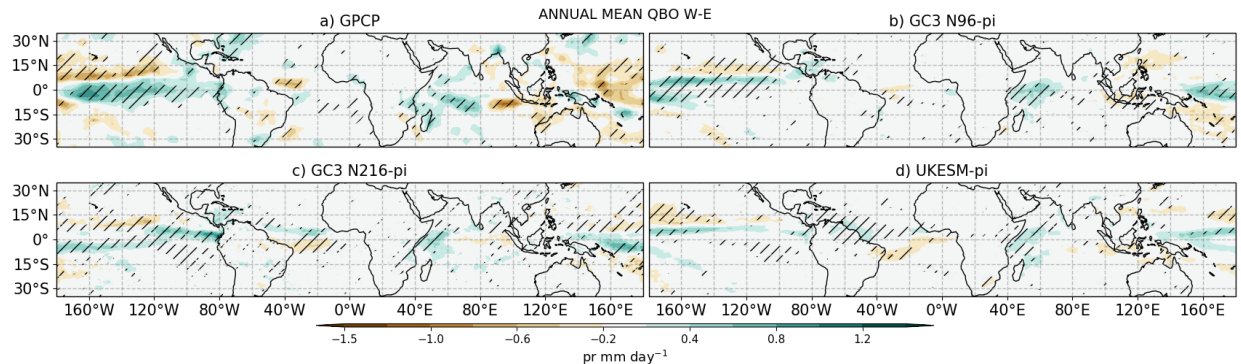


**Figure 7.1:** Annual mean precipitation difference between QBO W-E phases in (a) GPCP, (b) GC3 N96-pi, (c) GC3 N216-pi and (d) UKESM-pi. Hatching denotes statistical significance to the 95% confidence level using bootstrapping with replacement for each composite sample.

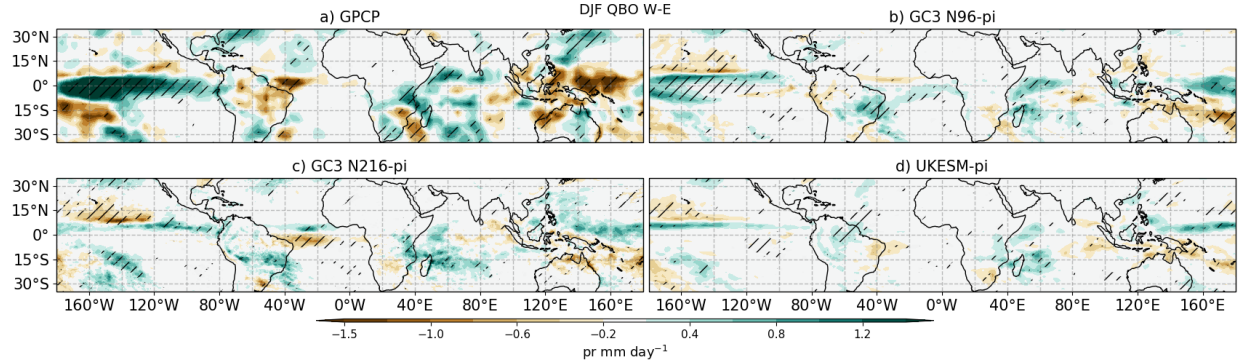


**Figure 7.2:** As in Figure 7.1 but for DJF.

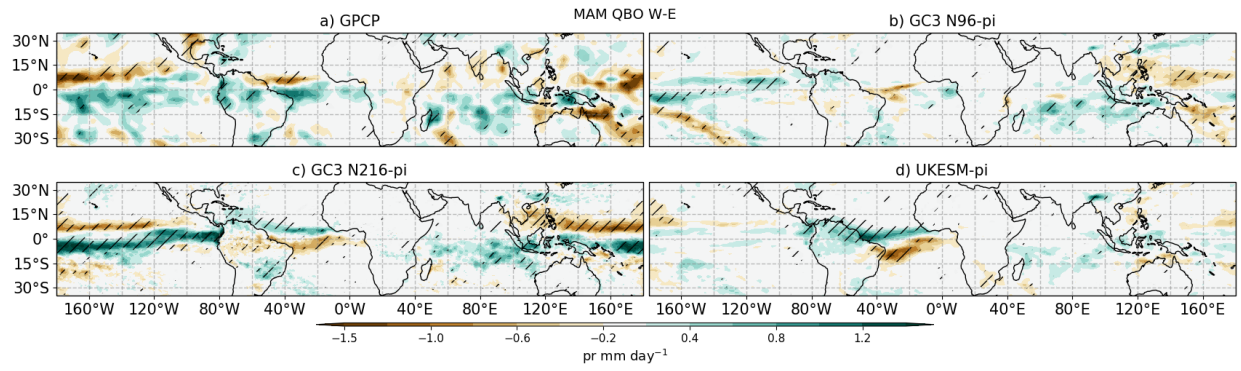


**Figure 7.3:** As in Figure 7.1 but for MAM.

### 7.3.1 Seasonal variability

The composite difference in annual mean precipitation between QBO W and E phases (Figure 7.1) shows that in observations (GPCP) the tropical Pacific, equatorial Atlantic and the Indian Oceans are the regions of possibly largest influence of the QBO, which agrees with previous studies (Liess and Geller, 2012; Gray et al., 2018). The three GCM simulations agree well with the pattern in GPCP, as all three simulations show a positive difference (QBO W-E) in the Central Pacific and the Indian Ocean, albeit the differences are smaller in the simulations. However, the patterns and magnitudes of the impacts become larger when analysed over specific seasons.

For example, during DJF (Figure 7.2), the pattern over the Central Pacific is stronger in GPCP and the simulations relative to the annual mean difference. The positive difference in the western Indian Ocean and the South Pacific Convergence Zone is also observed in this season and is significant in all the datasets. Results in GC3 N216-pi suggest a weakening of

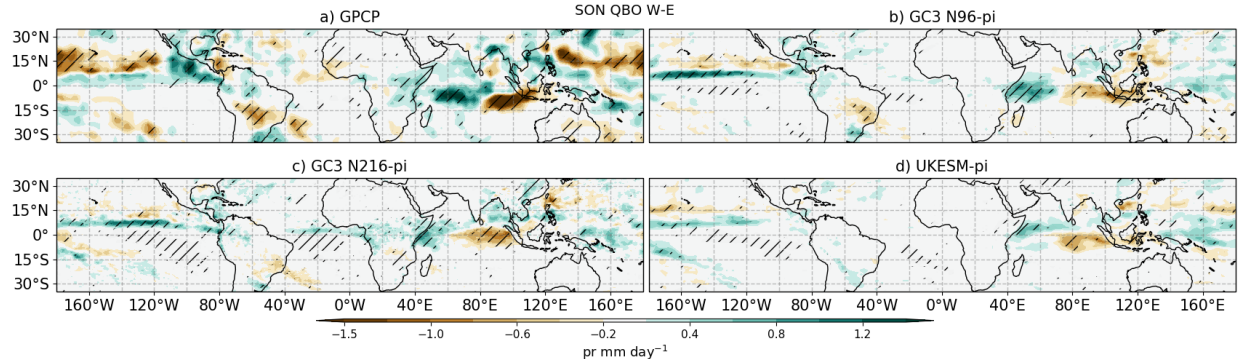


**Figure 7.4:** As in Figure 7.1 but for SON.

the Atlantic ITCZ as in GPCP, whereas UKESM-pi and GC3 N96-pi show little and not significant responses in that region. The response in the East Pacific during DJF matches the results of Serva et al. (submitted), and suggests a southward shift of the ITCZ.

Similarly, during MAM (Figure 7.3), the strongest response arises in the East Pacific and Atlantic ITCZ regions. In GC3 N216-pi the East Pacific ITCZ is shifted southwards whereas in the Atlantic the ITCZ is displaced northward. UKESM-pi agrees with the northward shift of the Atlantic ITCZ and suggests a wetter northern South America during QBO W than E. In GC3 N96-pi, the differences are smaller and the most noteworthy pattern is found in the Western Pacific.

In boreal fall (Figure 7.4), all datasets show relatively large and significant differences in the Indian Ocean, characterized by a dipole of wet anomalies to the west and dry anomalies to the east. These dipole anomalies may be an indication that the QBO influences the Indian Ocean Dipole (IOD), characterized by a zonal gradient of SSTs in the Indian Ocean. In addition, results for GC3 N96-pi and GC3 N216-pi suggest a similar response in the Central and Eastern Pacific as in the other seasons, characterized by a wet anomaly at about 10°N.

Finally, the JJA seasonal mean pattern (Figure 7.5) shows a weak response in GPCP whereas the simulations show a number of significant differences. Specifically, the three experiments suggest a wet anomaly in the Caribbean Sea and the Indian Ocean; the former, likely related to the northward shift of the Atlantic ITCZ observed in the same season particularly in UKESM-pi. West of the Caribbean Sea, in the easternmost Pacific Ocean a seemingly southward shift of the ITCZ is observed with a negative precipitation response on

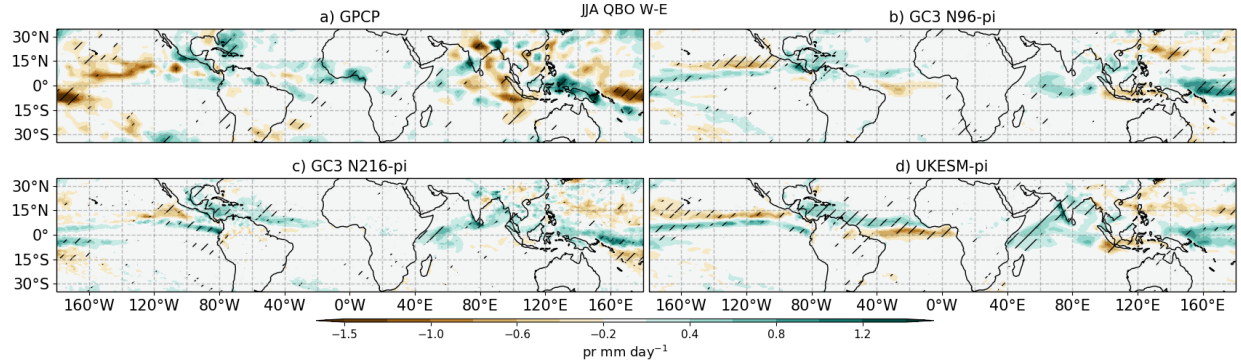


**Figure 7.5:** As in Figure 7.1 but for JJA.

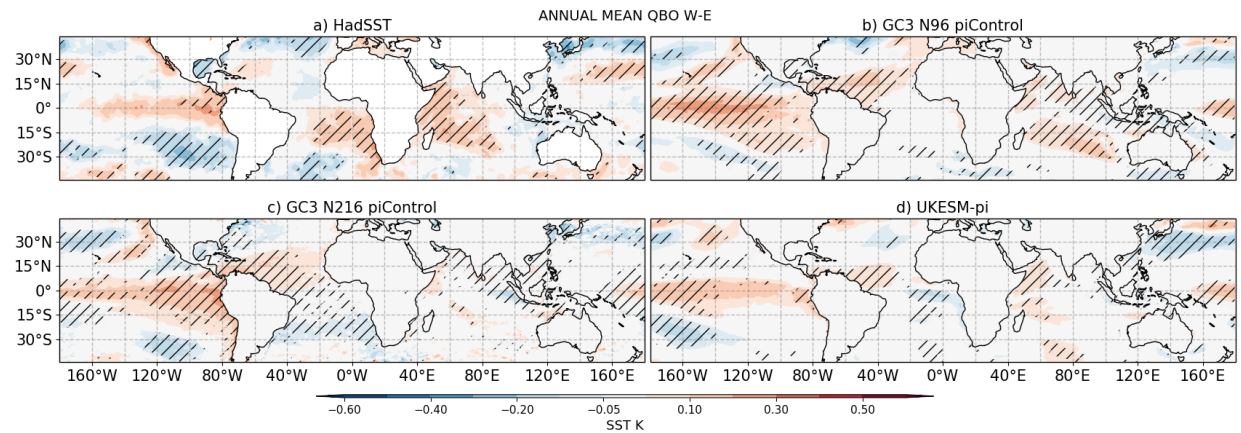


**Figure 7.6:** As in Figure 7.1 but for SSTs.

the western coast of Mexico. A wetter Indian Ocean is observed in all the simulations and in UKESM-pi the wet anomaly extends over land into the Indian monsoon region.

Note that in the annual and seasonal mean patterns there little or no differences over land in most seasons, however, two exceptions are observed in Figure 7.5. A positive and significant response over land is observed in southern Mexico and Central America in all three simulations. Another positive and significant response is observed over the Indian monsoon region, although this signal is only present in UKESM-pi.

The simulated and observed precipitation responses in the Central Pacific resemble an El Niño pattern, especially during DJF. In observations, this pattern is likely a result of the increased frequency of El Niño events for QBOW than in QBOE (Liess and Geller, 2012). For this reason, similar differences are obtained for SSTs (Figure 7.6) which show that the QBO W-E SST appear as an El Niño pattern characterized by increased SSTs

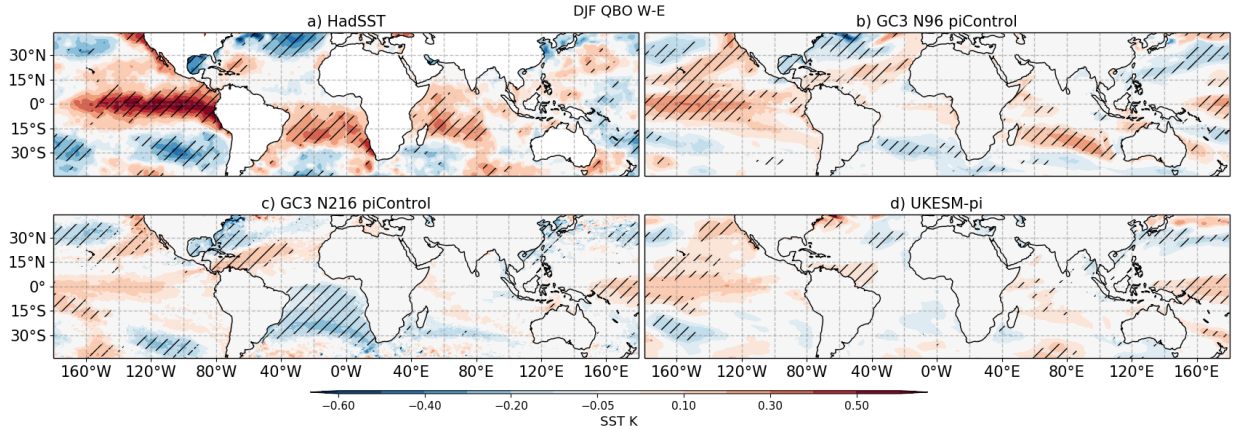


**Figure 7.7:** As in Figure 7.6 but for DJF.

over the Central and Eastern Pacific, extending to the equatorial Atlantic. Although these differences are much weaker than the signal for a typical El Niño event, these differences are significant in all the simulations.

The specific SST pattern for DJF confirms that the SST pattern seen in the annual mean difference is stronger during the boreal winter season, particularly for GC3 N96-pi and for the HadSST dataset. The significant responses in GC3 N96-pi over the North Atlantic and in the Indian Ocean also agree very well with HadSST. Results in GC3 N216-pi and UKESM-pi also show a positive SST difference over the Central Pacific during DJF although not significant. In the case of GC3 N216-pi the strongest SST anomalies over the Central Pacific appear during MAM (not shown) whereas for UKESM-pi the pattern appears during La Niña events with little-to-no response during other phases of ENSO (not shown).

In summary, this section presented the seasonal mean response in precipitation to the phases of the QBO. The main responses in the models were the ITCZ shifts over the Pacific and Atlantic Oceans, but robust signals also suggest wetter conditions in the Indian Ocean and the Caribbean Sea during QBOW compared to QBOE. The results in this section suggest a strong variation of the response with the seasons and with ENSO phase and little overall effect over land regions. For this reason, the following two sections more closely examine the effect of the QBO over the ITCZs in the East Pacific and Atlantic ITCZs, the Indian Ocean Dipole (IOD) and land-averaged precipitation over monsoon regions.

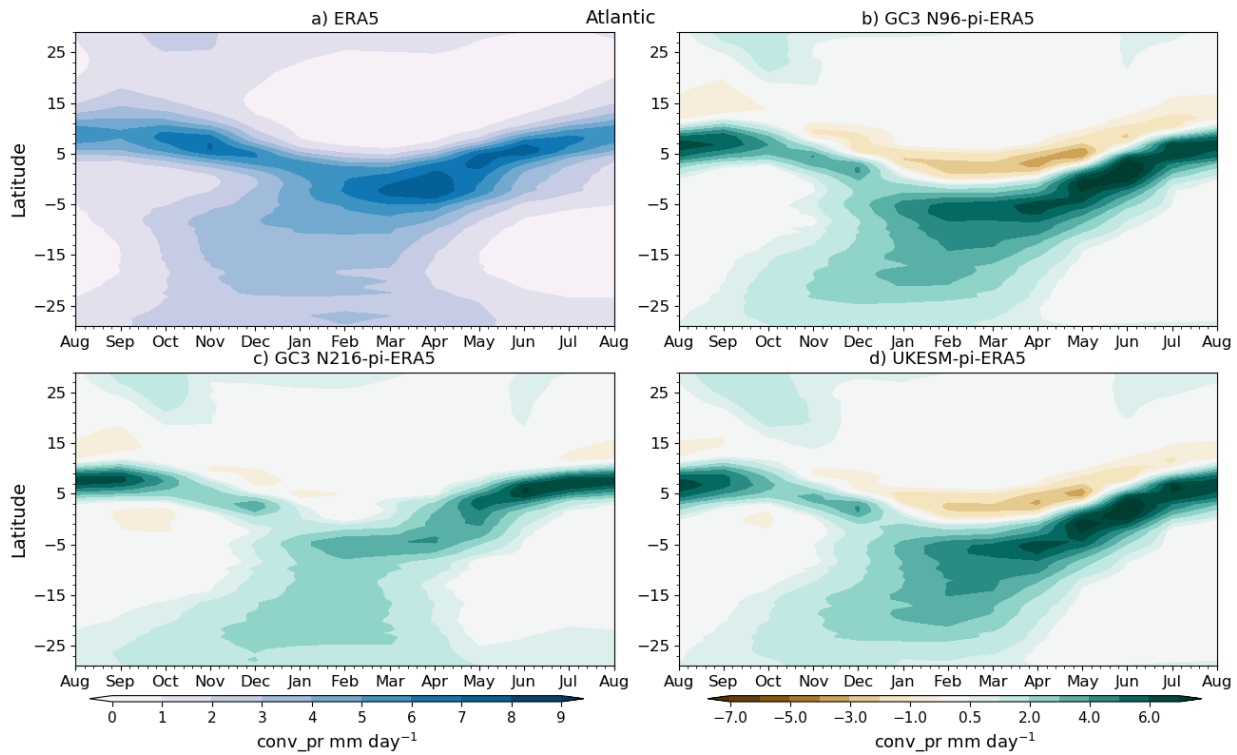


**Figure 7.8:** (a) Monthly and zonal-mean convective precipitation in ERA5 in the Atlantic sector [60°W-20°W]. (b-d) Biases in GC3 N96-pi, GC3 N216-pi and UKESM-pi.

### 7.3.2 Impacts over the ITCZ and the monsoons

This section examines more closely changes to the ITCZ position and strength associated with the phase of the QBO, specifically over the Central Pacific and Atlantic sectors. Note that the biases in the representation of the ITCZ in these models (characterized in Chapter 4) are considerable and could mean that the simulated interaction between the QBO and the ITCZ are different in the model than in the real-world. For example, Figure 7.8 shows the seasonal march of convective precipitation in the Atlantic sector in ERA5 and the biases in the three simulations with respect to ERA5. The Atlantic ITCZ in these simulations is not well represented, as shown in previous sections, as the models show a southward bias particularly in DJF and overestimates the maximum precipitation rate at the ITCZ location. In the Central Pacific sector (not shown), the models do not show a bias in the position of the ITCZ but rather a bias in the magnitude of convective precipitation, as all the models overestimate the amount of convective precipitation throughout all the seasons.

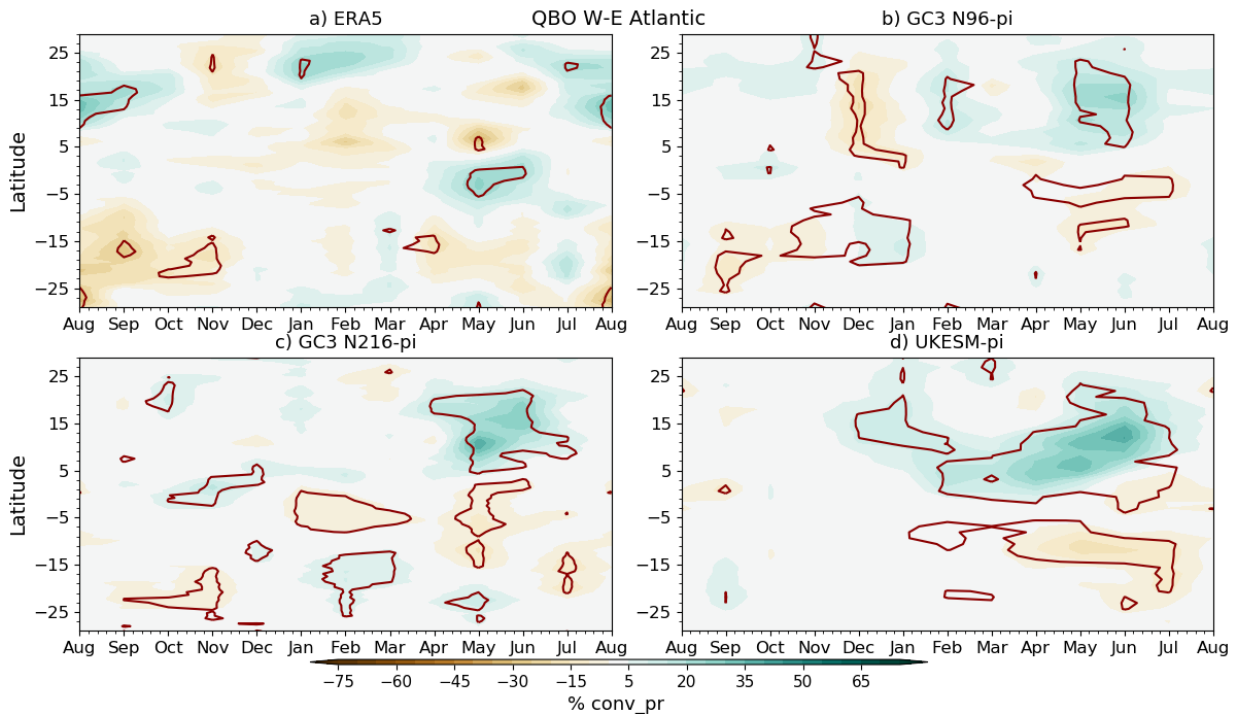


**Figure 7.9:** Zonal mean QBO W-E differences in convective precipitation rates in the Atlantic sector per month, shown as percent (%) where the difference is weighted by the climatological value at each latitude and month. The line-contour (red) depict differences that are statistically significant to the 95% level according to a bootstrapping test.

Figures 7.9 and 7.10 show the time-latitude difference in convective precipitation to the phase of the QBO in the Atlantic and Pacific sectors, respectively. The northward shift of the ITCZ during QBOW in the Atlantic sector highlighted in previous sections is confirmed in Figure 7.9. In all the simulations, but specially in UKESM-pi, there are two significant responses observed from March to July, one wet anomaly north of 5°N and a corresponding dry anomaly south of 5°S. The southern negative difference is weaker (-20%) than the positive response north (+40%). The response in ERA5 shows a relatively less robust response, with few significant patterns.

The southward shift of the ITCZ in the Central Pacific, reported in previous observational studies (Gray et al., 2018), is confirmed by Figure 7.10 which shows that in ERA5 a southward shift of the Central Pacific ITCZ is observed in DJF. The simulations agree well with this southward shift, particularly GC3 N96-pi during DJF. However, the southward shift response of the Central Pacific ITCZ is also observed in other seasons, for example, from May to

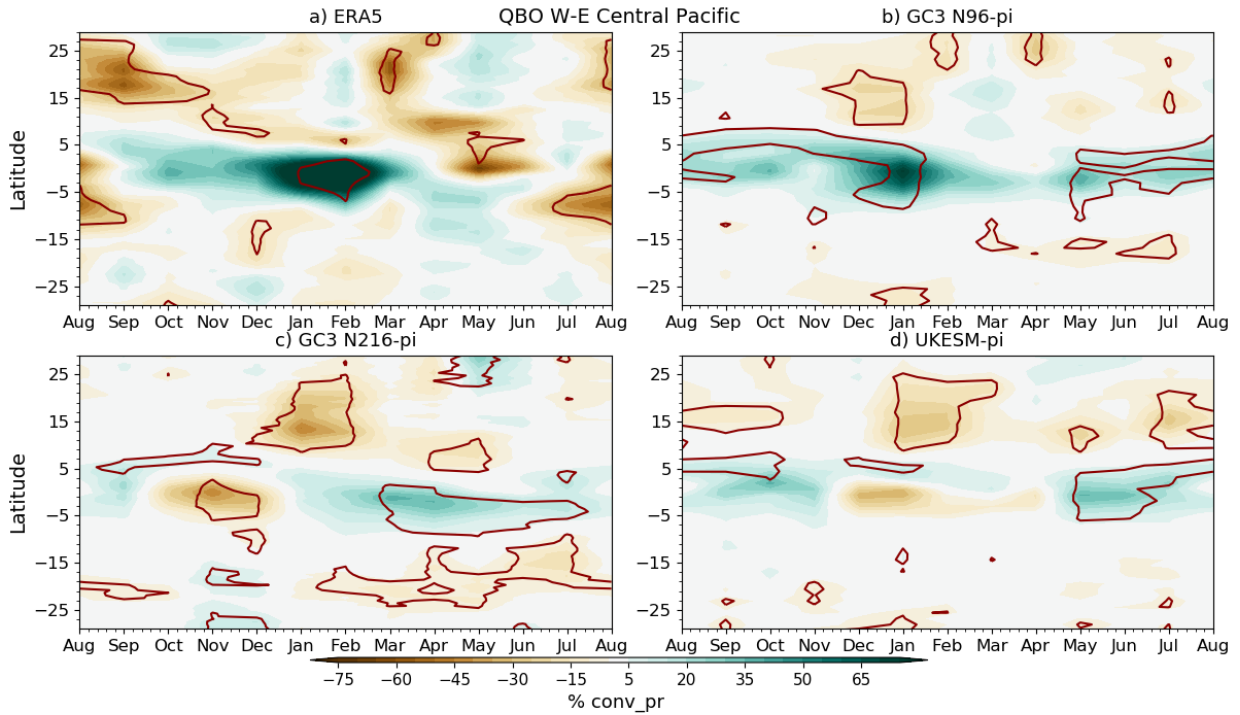


**Figure 7.10:** As in Figure 7.9 but for the Central Pacific sector [180°W-140°W].

September in UKESM-pi and GC3 N96-pi, whereas in GC3 N216-pi the southward shift response is seen from February to July.

These results suggest that the response to the phase of the QBO may depend on the climatological representation of the ITCZ position and strength. Nevertheless, these three simulations which exhibit slightly different representations of the ITCZ as well as of the QBO, agree on the southward shift of the Pacific ITCZ and the northward shift of the Atlantic ITCZ as the main difference between the phases of the QBO.

In spite of the multiple lines of evidence that suggest a modulation of the QBO over convective activity in land monsoon regions, the results in the previous section show little-to-no effect of the QBO on precipitation over land in these simulations. In order to investigate the precipitation response over land more closely, the global monsoon regions are defined within each simulation. A monsoon region is defined as where over 55% of the total annual rainfall is observed or simulated in the respective summer season and the summer-winter rainfall rate difference is higher than  $2 \text{ mm day}^{-1}$  (Wang and Ding, 2008; Wang et al., 2017, 2021).

The local summer convective precipitation differences between QBO phases in monsoon

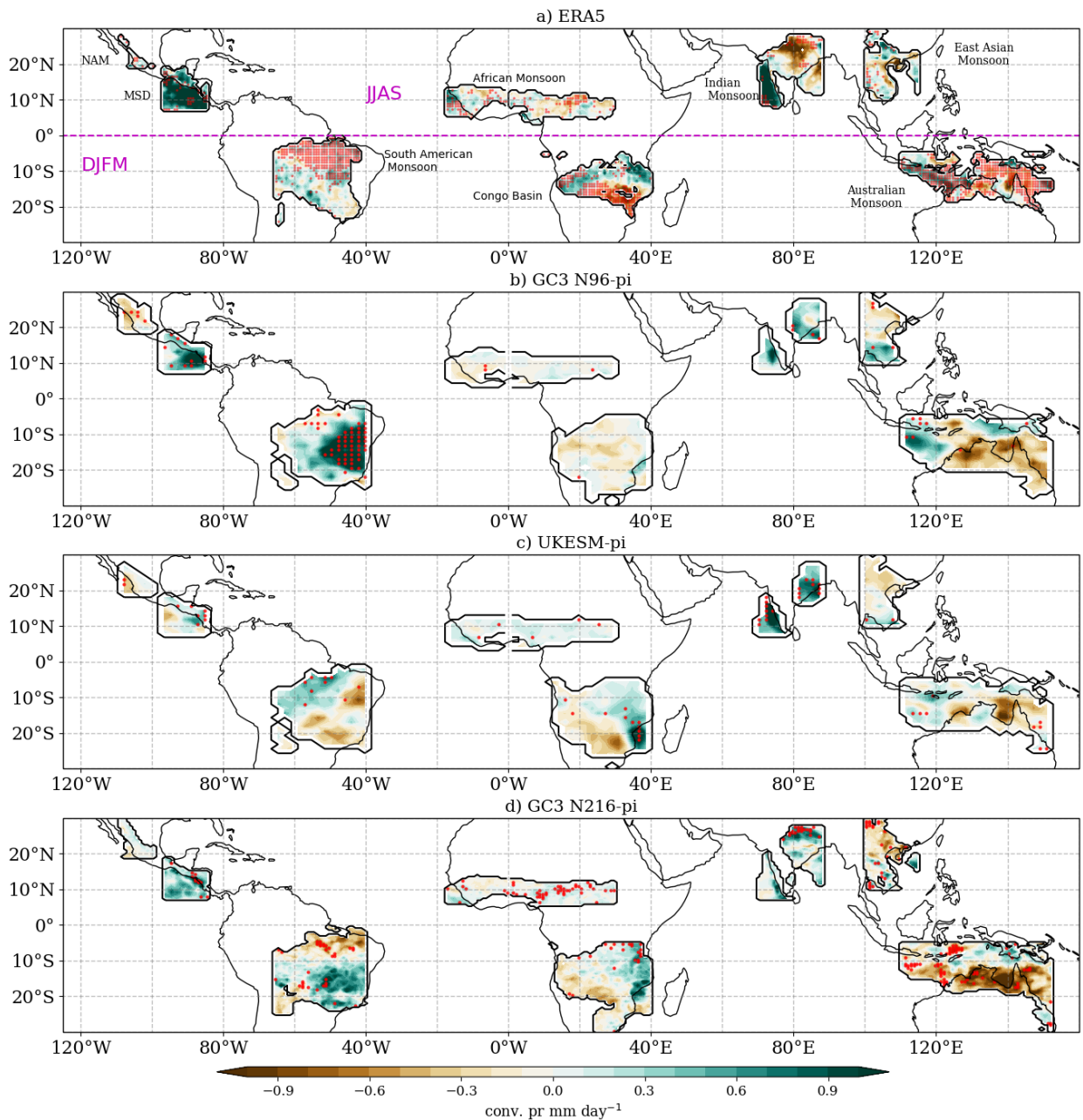


**Figure 7.11:** Convective precipitation differences in monsoon regions between QBO W-E phases during Neutral ENSO months for a) ERA5, b) GC3 N96-pi, c) UKESM-pi and d) GC3 N216-pi. For monsoon regions in the Northern hemisphere, differences are shown for the JJAS period, whereas for Southern Hemisphere monsoons, results are shown for DJFM. Red dots indicate differences that are statistically significant to the 95% level according to the bootstrapping test.

regions (Figure 7.11) shows that there is no region where a clear, robust and region-wide effect is observed, even when the influence of ENSO is removed by considering months where ENSO was in a neutral state. Monsoon regions like the Congo Basin, the East Asian and

Australian monsoons show both positive and negative responses within the domain of their regions, suggesting a rather heterogenous response, and perhaps suggest that the QBO effect over a monsoon region is also modulated by the dynamics of the regional monsoon.

However, some features appear to be robust, as some differences are significant in all three simulations. For example, a positive response is observed in the MSD and northern Indian monsoon regions and a dry anomaly is seen over the Australian monsoon, although the latter is only widely significant in GC3 N216-pi. In the South American monsoon region, a dipole of wet and dry anomalies are observed in UKESM-pi and GC3 N216-pi, but these two simulations show an opposite pattern. The impacts over the southeastern coast of Brazil

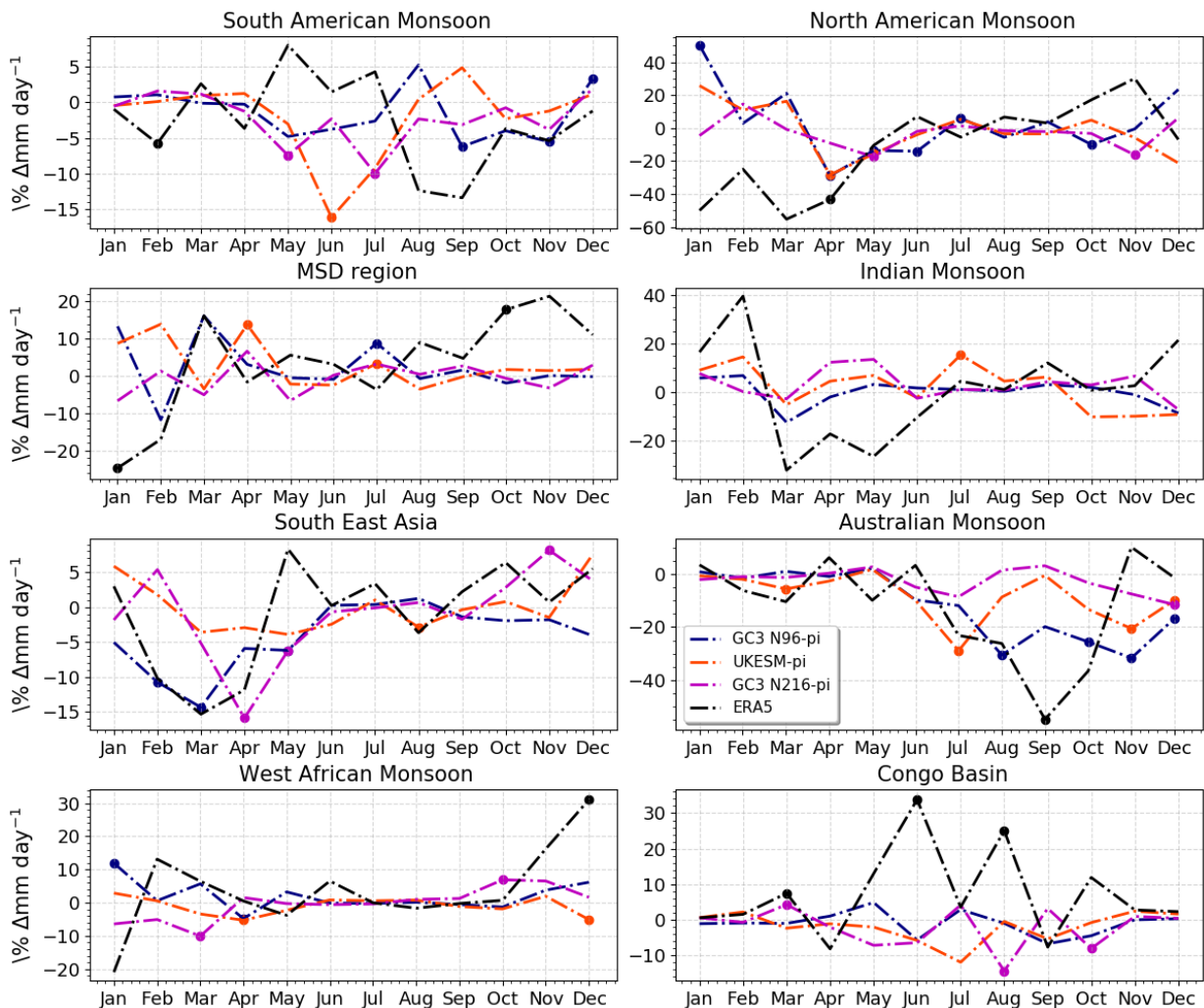


**Figure 7.12:** QBO W-E difference in convective precipitation in monsoon regions separated per calendar month. Dots overlaying lines indicate differences that are statistically significant to the 95% level according to the bootstrapping test.

in all the three simulations may suggest an effect over the South Atlantic Convergence Zone, which may further modify the dynamics of the monsoon. The implication of these results is that feedbacks with the dynamics of the monsoons may be more important than the effects of the QBO over the mass flux and convective activity at the grid-point scale.

To understand the temporal variability of these effects, Figure 7.12 shows the difference in area-averaged convective precipitation between QBO phases for monsoon regions for each calendar month. There is no clear signal of the QBO over any monsoon region for a large part of the year. For example, all three simulations agree in a negative QBO W-E difference in the Australian monsoon region for November and December, and this response is significant; however, the response in Jan-Mar is weak and not significant. This means that the effect of the QBO over the Australian monsoon region is found only in the early local summer season.

Similarly, over the Mesoamerican MSD region, all three simulations agree on a wet anomaly during the local summer, but this response is constrained to the month of July (the drier period of the rainy season) and is only significant in two out of the three simulations. In the Indian Monsoon region, UKESM-pi shows a significant wet anomaly, in agreement with the seasonal mean results found in the previous section, however, the other models show a weak and not significant difference. Significant relationships are found for other monsoon regions in specific months but no consistent relationship is found in any monsoon region across all three models, which agrees with the lack of robust seasonal-mean patterns presented in the previous section.

### 7.3.3 ENSO, the IOD and the Walker circulation

The previous section showed that the strongest precipitation responses to the QBO phase in the tropics are found in the Pacific and Indian Oceans, regions that are connected through the overturning Walker circulation and ENSO teleconnections (Cai et al., 2019). For that reason, this section investigates whether the Indian Ocean state and the frequency of ENSO events varies between QBO phases, as well as whether the mean state or variability of the Walker circulation is impacted by effects related to the QBO.

The Indian Ocean Dipole (IOD) is a coupled ocean-atmosphere feature of the tropical Indian Ocean characterized by a zonal gradient of SSTs that peaks in boreal fall (Saji

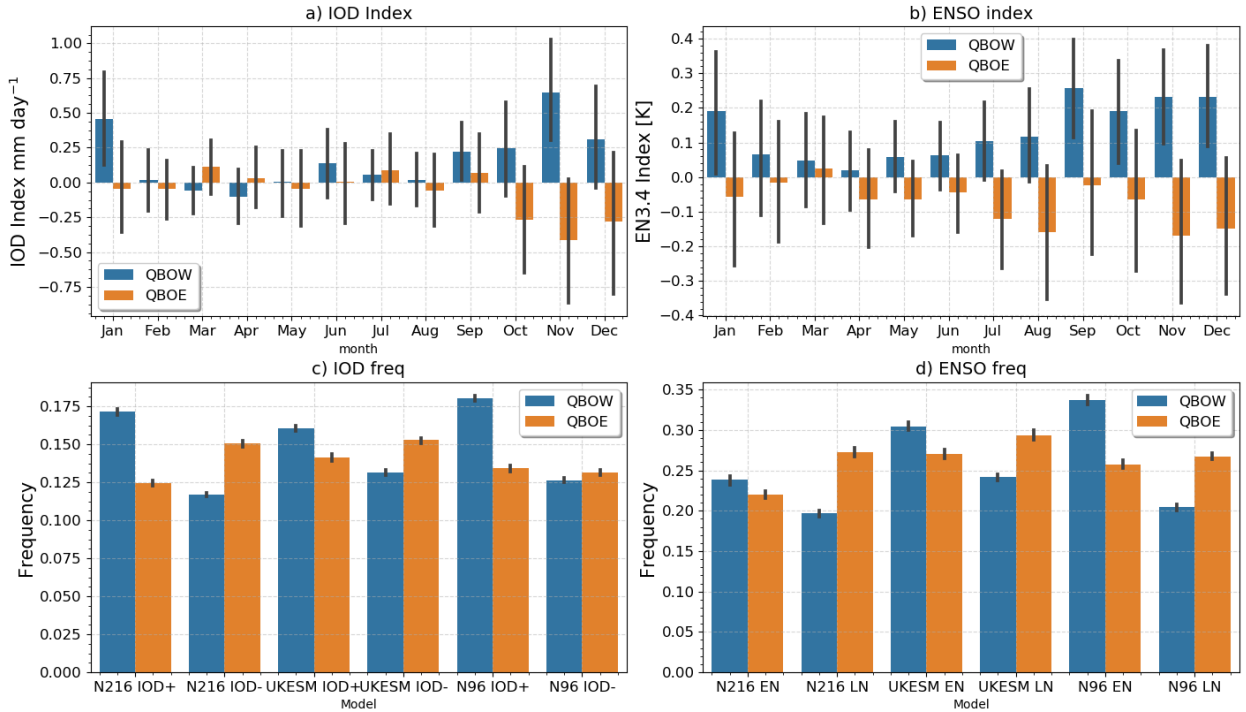


**Figure 7.13:** Monthly-mean (a) IOD-prc and (b) EN3.4 index separated per QBO phase in GC3 N96-pi. (c,d) Bar plots of the frequency of event occurrence for each model for (c) El Niño (EN) and La Niña (LN) and for (d) positive and negative IOD events based on the convective precipitation index. In c,d the count of events in each QBO phase is normalized per total months in each QBO phase so there is no effect associated with an uneven frequency of QBOW versus QBOE events. The error bar show the 95% confidence interval using a distribution obtained using bootstrapping test where 36 year periods were sampled from the entire run period 10,000 times and N216 and N96 labels refer to GC3 N216-pi and GC3 N96-pi, respectively.

et al., 1999; Wang and Wang, 2014; McKenna et al., 2020). IOD events are affected by ENSO events but IOD changes can also have independent long-distance effects through the Walker circulation (Wang and Wang, 2014). The previous section showed a zonal gradient in the precipitation response to the QBO during boreal fall (SON) in the three simulations (Fig. 7.4). However, in these models there was no significant SST response during this to the canonical IOD definition.

The computation of the standard IOD index, a measure of the SST gradient between the western tropical Indian Ocean and the Java-Sumatra region, results in little-to-no correlation with the QBO phase and IOD events defined using this index showed the same frequency under QBOW than during QBOE (not shown). Alternatively, a convective precipitation index of the zonal gradient in the Indian Ocean (convective IOD Index), can

be defined as the difference of the deseasonalized area-averaged convective precipitation between the western [50-70°E] and eastern [80-100°E] equatorial [10°S-10°N]. Using this convective precipitation index, IOD events are defined as in previous studies using a 1 standard deviation to define positive and negative events.

The relationship between the mean ENSO and convective IOD indices, as well as the frequency of ENSO and IOD events, and the phase of the QBO is then investigated, see Figure 7.13. The mean IOD Index and the EN3.4 SST index in GC3 N96-pi are significantly different depending on the QBO phase in GC3 N96-pi. In particular, the mean IOD Index is positive in QBOW and negative in QBOE months from September until January. The EN3.4 index also shows a non-zero mean when separated by QBO phase, with positive mean values found during QBOW and negative values during QBOE. The GC3 N216-pi and UKESM-pi results are very similar (not shown) and the differences are also significant; the only notable difference is the month in which the strongest response in each model is observed for each index.

The frequency of El Niño (EN) and La Niña (LN) months is robustly linked to the QBO phase in the three simulations (Fig. 7.13c). EN months are more frequent during QBOW phases than during QBOE phases, and in contrast, more LN events are diagnosed during QBOE than during QBOW. Similarly, the number of IOD+ events is increased in the westerly phase of the QBO, whereas negative event frequency is increased during QBOE (Fig. 7.13d) for all the three models. The confidence interval in Fig. 7.13c-d is provided by a bootstrapping test sampling the simulations into 36 yr samples and suggest that this result is robust to internal variability within the model.

In addition, several tests were done to evaluate whether changes in the frequency of IOD events were associated with known connections between the IOD and ENSO. Results show that the changes to the frequency of IOD events remain unchanged when only Neutral ENSO months are considered so there is no aliasing with the influence of ENSO on the IOD. Similarly, these changes in the frequency of IOD events are seen in the three simulations in each month from September to January, so there is no aliasing of the seasonality of the QBO within the model and the seasonality of IOD events. Note that these results do no provide any evidence of cause and effect between the QBO and IOD and ENSO indices and only evaluate the nature of these relationships within the model.

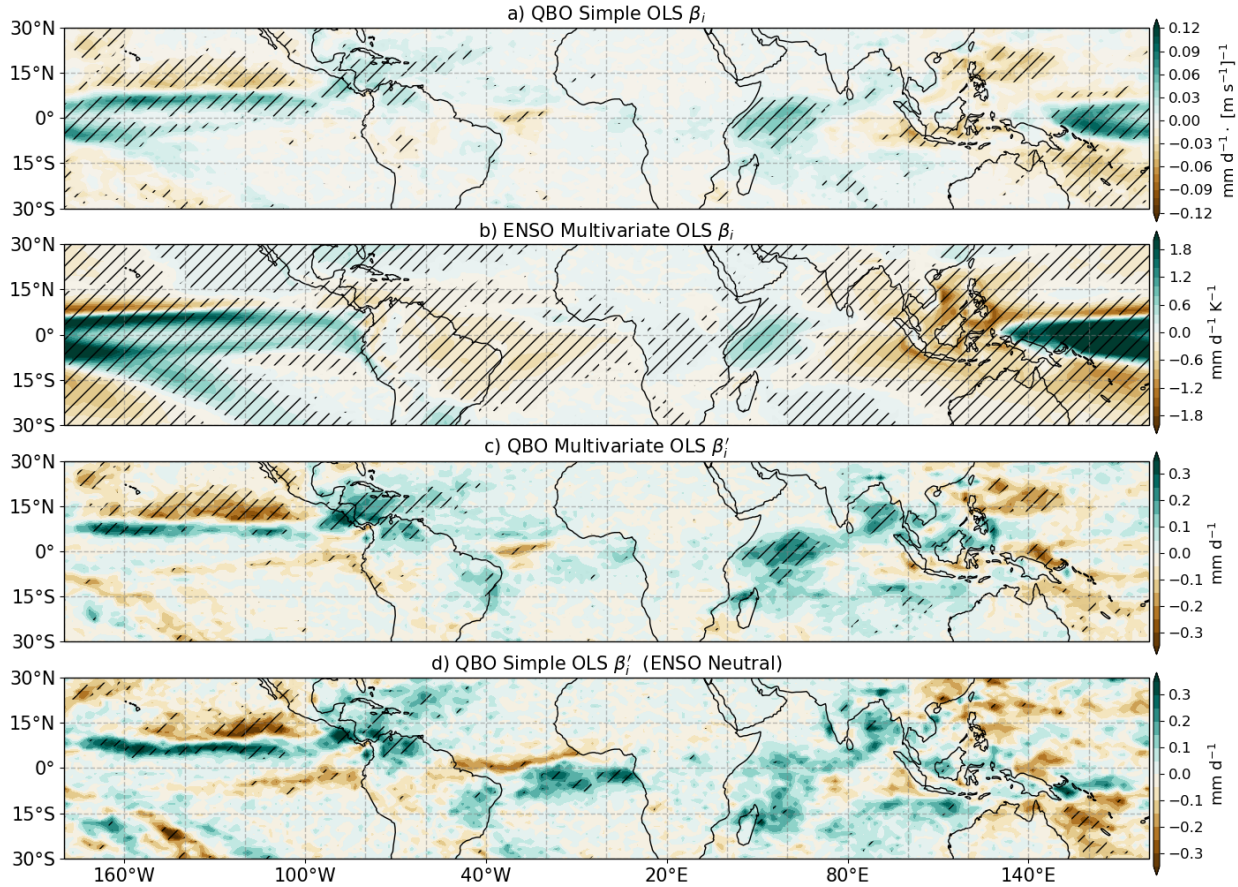


**Figure 7.14:** Regression model results in GC3 N96-pi. (a) Regression coefficients ( $\beta_i$ ) from a simple ordinary least-squares (OLS) regression model with the QBO index, (b, c) the regression coefficients resulting from a multivariate regression model using the ENSO and QBO indices for the (b) ENSO and (c) QBO predictors. In (c) the regression coefficients are rescaled by multiplying the regression coefficients with the ratio of maximum amplitude and standard deviation of the QBO index. (d) Rescaled regression coefficients from a simple OLS model with the QBO index, but using time-series where ENSO was classified as in a Neutral state using the EN3.4 index.

The previous results showed that there is an uneven frequency of ENSO events in the different QBO phases and that within these experiments, the QBO impacts may depend on the phase of ENSO. Linear-regression analysis was used by Gray et al. (2018) to investigate the spatial and temporal variability of the surface impacts of the QBO in tropical precipitation using a multivariate-regression model that accounts for the relationship between ENSO and precipitation. For these reasons, simple and multivariate regression analysis has been performed using the EN3.4 SST index, the 70 hPa zonal wind QBO index and deseasonalized convective precipitation. Other indices such as solar, volcanic and greenhouse forcings are omitted in this analysis because in these runs external forcings are constant.

Figure 7.14 shows results from the regression analysis of GC3 N96-pi. A simple regression model using the QBO 70 hPa index (Fig. 7.14a) shows very similar results to the composite mean differences described in the previous section. The results from the multivariate regression model implemented using the QBO and ENSO indices, show that the spatial distribution of significant regression coefficients for the EN3.4 time-series (Fig. 7.14b) is somewhat similar to results for the QBO in the simple regression model, suggesting the possibility of aliasing between ENSO and QBO indices.

The rescaled regression coefficients for the QBO, obtained using the multivariate regression model (Fig. 7.14c), i.e., the model where the influence of ENSO has been regressed-out, are broadly similar to the simple OLS model, except in the equatorial west Pacific. These regression coefficients suggest that the precipitation response of the QBO is a southward shift of the East Pacific ITCZ, as well as a wetter Caribbean Sea and western Indian Ocean for QBOW phases. A simple regression model using the QBO index during Neutral ENSO months (Figure 7.14d) shows very similar results, except in the Atlantic ITCZ region, confirming that the influence of ENSO needs to be closely examined and removed before analysing the influence of the QBO over the tropics.

The seasonal-mean results could possibly be aliasing effects of ENSO and the regression results have removed the influence of ENSO. A different question, however, is whether the QBO could modify the teleconnections of ENSO in the tropics. An analysis of the DJF

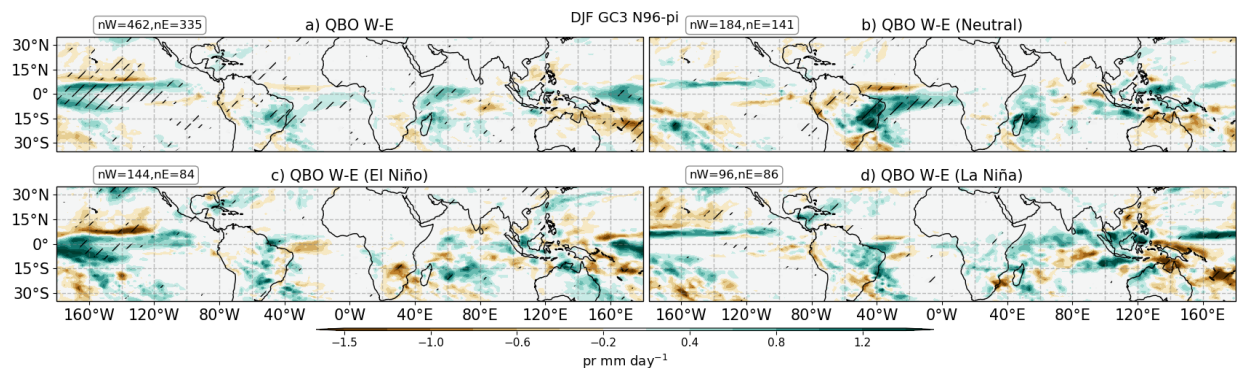


**Figure 7.15:** DJF QBO W-E precipitation differences in GC3 N96-pi for (a) all the events, (b) Neutral ENSO conditions only, (c) El Niño and (d) La Niña conditions. The sample size of each composite is noted in the top left corner of each panel.

mean response to phase of the QBO separated also by ENSO phase (Figure 7.15) shows that the surface response depends on both the QBO and ENSO phase.

The wet anomaly pattern in the southern equatorial ( $15^{\circ}\text{S}$ - $0^{\circ}$ ) Central Pacific observed in the mean DJF response is only observed during El Niño events, not during Neutral or La Niña months. In turn, the dry anomaly in the Central Pacific at  $10^{\circ}\text{N}$ - $20^{\circ}\text{N}$  is observed during both La Niña and El Niño seasons but not during Neutral conditions. Over the Atlantic ITCZ region and eastern Brazil, the strongest response is observed during Neutral conditions, suggesting that the pattern observed in panel a) is likely the closest to a true QBO response independent from ENSO and that this response is characterized by a southward shift of the ITCZ during QBOW.

Similar results are found other seasons (MAM and SON) and simulations, which confirms that within these simulations, the teleconnections of ENSO can be different depending on the QBO phase. One implication of these results may be that ENSO teleconnections are themselves a function of the QBO state and that the impact of the QBO may be different for La Niña than for El Niño, an effect that would be masked by the regression analysis presented above.

Results in Chapter 4 and in this chapter suggest a link between QBO, ENSO and the Walker circulation. For that reason, an analysis of the zonal streamfunction, zonal wind and vertical velocity in the deep tropics is now presented to better characterise whether the QBO has any possible influence on the mean-state and variability of the zonal overturning in the tropics. The zonal streamfunction (Yu and Zwiers, 2010; Bayr et al., 2014) is defined as:

$$\psi = 2\pi \frac{a}{g} \int_0^p u_D dp, \quad (7.4)$$

where  $\psi$  is the zonal streamfunction,  $u_D$  is the divergence part of the zonal wind,  $a$  is the Earth's radius,  $p$  is the pressure coordinate and  $g$  the gravitational constant. The streamfunction is calculated by first averaging in the equatorial band of  $10^{\circ}\text{S}$ - $10^{\circ}\text{N}$  and integrated to the top level within the model.

Results in previous sections show that the boreal winter and early spring exhibit the strongest responses in the Pacific region and in boreal fall in the Indian Ocean. For that

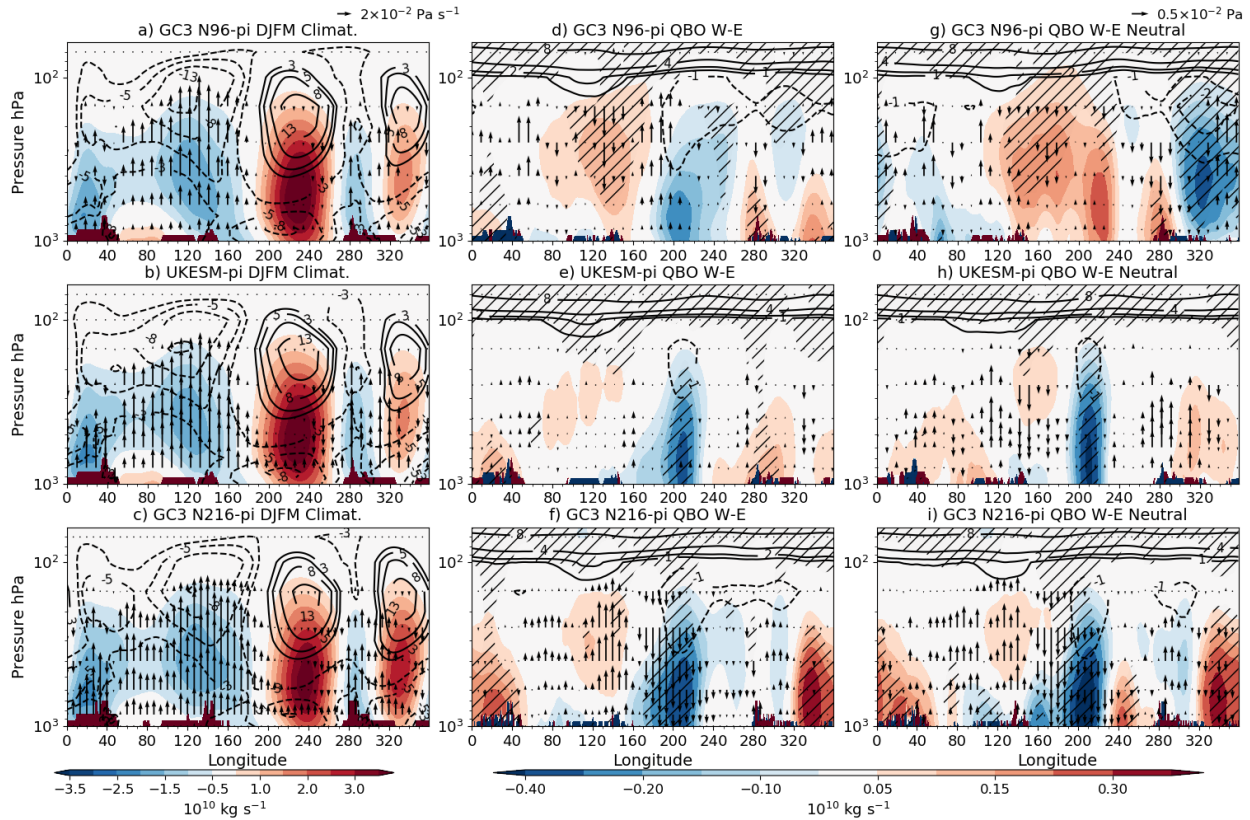


**Figure 7.16:** (a-c) Climatological mean-state of the Walker circulation, depicted through the zonal streamfunction ( $\psi$ ) in shading, the zonal wind (contours), and vertical velocity ( $\omega$  [ $\text{Pa s}^{-1}$ ], vectors) during the DJFM season in the three simulations. (d-f) show W-E composite differences, during DJFM, for the same variables only that hatching represents statistical significance to the 95% confidence level for differences in the streamfunction, and only statistically significant differences in the zonal wind and  $\omega$  are shown. (g-h) are as in (d-f) but considering Neutral ENSO periods only. Example vector for  $\omega$  are given in the top right corners of a and g.

reason, the QBO response of the Walker circulation is illustrated for DJFM and SON in Figures 7.16 and 7.17. The streamfunction mean values are higher in DJFM than in SON, indicative of a stronger Walker circulation during boreal winter.

Composite differences in DJFM show that the streamfunction from 180-240°E is significantly weaker during QBOE than during QBOW in all three simulations. The zonal wind at upper-levels (300-100 hPa) is also weaker during QBOW at 200°E. In GC3 N216-pi, this negative  $\psi$  difference is accompanied by descending motion anomalies in the 190-220°E region, whereas anomalous ascent is observed in the Maritime continent and Indian Ocean. Vertical velocity ( $\omega$ ) anomalies in the other simulations are weaker in the Central-Eastern Pacific. These results suggest a weaker Walker circulation during QBOW compared to QBOE seasons.

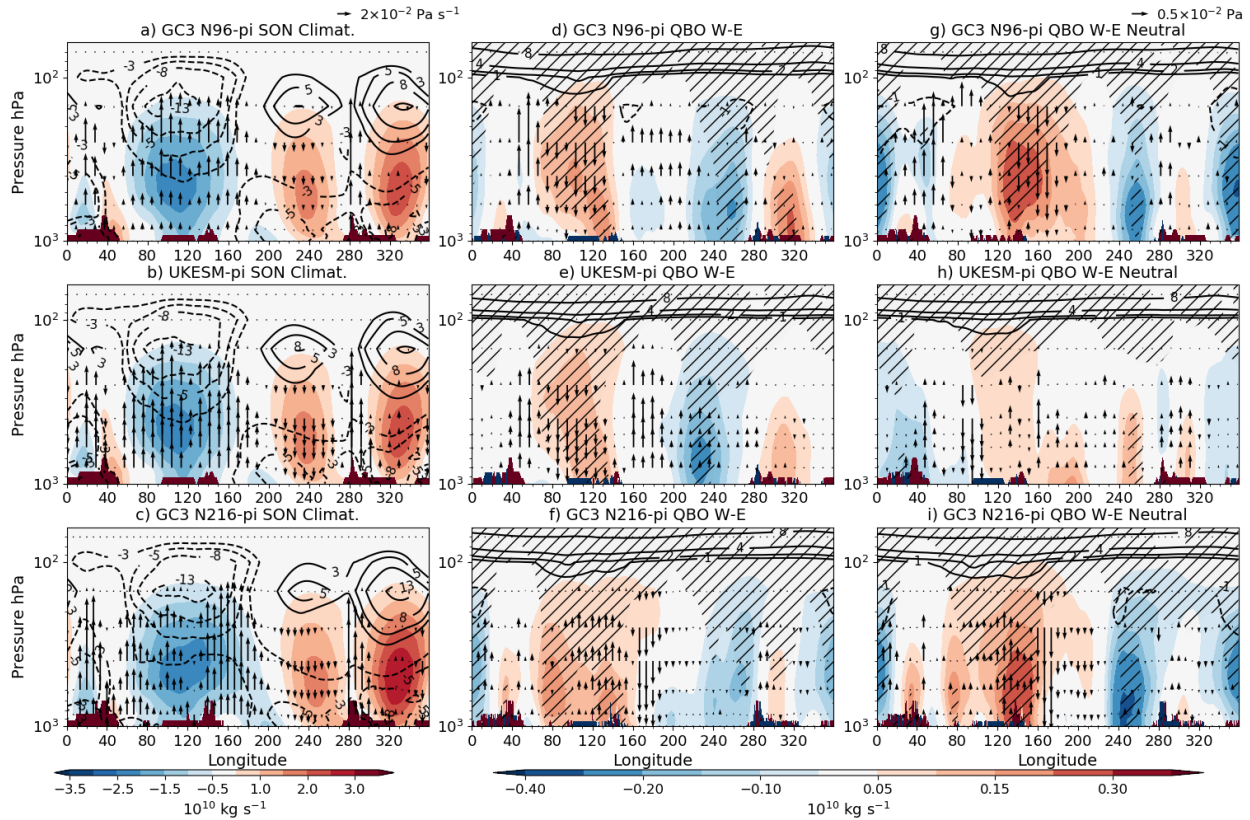


**Figure 7.17:** As in Figure 7.16 but for SON.

The rightmost panels in which only Neutral ENSO months are removed, suggest that this relationship between the QBO and the Walker circulation occurs regardless of ENSO events.

In boreal fall (Fig. 7.17), the mean Walker circulation is weaker and ascent is mostly concentrated in the Indian Ocean and Maritime continent, as well as in South America. Positive streamfunction differences are found to be significant over the Indian Ocean in all three simulations, associated with anomalous descent on the eastern Indian Ocean and ascent over the western Indian Ocean. These results agree well with the results using convective precipitation index for the IOD, described in the previous section, which found more rainfall in the western Indian Ocean than in the east during QBOW than during QBOE.

Furthermore, in SON, significant negative differences in the streamfunction are found in the Eastern Pacific and Atlantic Oceans and positive differences over South America, although in both cases differences in  $\omega$  appear very small or not significant. These results suggest that there are possible links between ascending and descending motion in the Indian

Ocean, as described through the IOD in the previous section, and the Central and Eastern Pacific, and Atlantic Oceans through the boreal fall Walker circulation.

## 7.4 Summary and discussion

This chapter investigates the tropical route of QBO teleconnections in the pre-industrial control experiments of the MOHC from HadGEM3 and UKESM1. Results in this chapter confirm observational evidence (Collimore et al., 2003; Liess and Geller, 2012; Gray et al., 2018) that there is a QBO impact over tropical precipitation, mainly over the tropical ocean in the East Pacific and Atlantic ITCZs.

The position of the East Pacific and Atlantic ITCZs is significantly different between the two phases of the QBO in the three experiments; however, the season of strongest influence varies for each model. For example, the southward displacement of the East Pacific ITCZ in QBOW compared to QBOE phases (as previously reported, e.g., by Gray et al., 2018) is confirmed but in GC3 N216-pi this shift of the ITCZ is strongest in MAM whereas in GC3 N96-pi the most pronounced shift is in the DJF season. The position of the Atlantic ITCZ is found further northward during QBOW than during QBOE periods in all the simulations; the strongest response is found during late boreal spring and early summer in UKESM-pi.

For most land-monsoon regions, little evidence was found of robust impacts on the local summer monsoon precipitation associated with the QBO, in spite of observations from satellite-derived and gridded station data suggesting otherwise (Collimore et al., 2003; Liess and Geller, 2012; Gray et al., 2018; Lee et al., 2019). For example, the South American monsoon region exhibited different responses in eastern Brazil than in the southernmost part of the monsoon. The surface response over land also varied notably from model to model. One hypothesis for the lack of a spatially coherent signal over land is the differences in the representation of the monsoon dynamics and feedbacks between the three models UKESM-pi, GC3 N96-pi, GC3 N216-pi that may represent the land-surface processes and moisture transport differently, so that any grid-scale impact of the QBO on the convective profile may produce different dynamic responses in the lower troposphere.

The influence of the QBO over the Indian and Pacific Oceans was confirmed through multi-variate regression analysis, suggesting an independent effect of the QBO from ENSO in these ocean basins. However, the QBO-related differences over the Atlantic and East Pacific ITCZ appear to also depend on the phase of ENSO, suggesting a non-linear interaction between the ITCZs, ENSO and the QBO which may be confounded when using regression analysis. The observed relationship between the QBO and ENSO is confirmed in this chapter in the CMIP6 experiments, as more frequently El Niño events appear during QBOW than during QBOE and the opposite for La Niña.

A zonal gradient of convective precipitation in the Indian Ocean appeared in all the simulations, and this signal maximised during SON. This zonal gradient was further diagnosed through an index that was found to be significantly sensitive to the QBO phase, the index was found to be positive during QBOW and negative during QBOE, indicative of wetter conditions in the western Indian Ocean than in the eastern Indian Ocean during QBOW and the opposite during QBOE. To our knowledge, these results are the first suggestions of a surface impact of the QBO associated with the IOD during SON.

The zonal asymmetry in the QBO surface impacts in the tropics documented in observations (Collimore et al., 2003; Liess and Geller, 2012; Gray et al., 2018; Lee et al., 2019) is also observed within these simulations. Regional effects that depend on the longitude suggest that there is not a clear single effect of the QBO over precipitation, in contrast to early suggestions (Gray, 1984) that in general more precipitation would be observed during one phase of the QBO. This chapter proves that the relationship between the QBO and tropical convection is not likely only relevant at the grid-box scale, but the large and regional scale dynamics in the tropics play a role such that zonal asymmetries appear when analysing these responses.

The hypothesis that the QBO may influence the mean-state of the Walker circulation suggested by previous observational studies to explain zonally asymmetric responses (e.g. Collimore et al., 2003; Liess and Geller, 2012) is confirmed as the Walker circulation varies up to 10% between QBO phases, even when the effect of ENSO events is taken into account. Specifically, the Walker circulation is found to be weaker during QBOW than during QBOE. In DJF, this anomaly of the overturning circulation in the Pacific is likely

linked to the East Pacific ITCZ shifts, and in SON, the changes to the overturning are likely linked to the ascending and descending motions in the Indian Ocean that generate the IOD response documented in this chapter.

The relationships found between the QBO, the Walker circulation and ENSO frequency could potentially be causally linked with the QBO variability being the driving mechanism. Changes to the mean state of the Walker circulation are known to modify the frequency of El Niño events and La Niña events. A weaker state of the Walker circulation could more likely trigger an El Niño event during QBOW than during QBOE, and similarly, a stronger Walker circulation during QBOE could more likely trigger a La Niña event, which would be consistent with the results of this chapter.

The results of this chapter are one of the few analyses of the tropical route of QBO teleconnections within a fully coupled GCM. The length of the pre-industrial control experiments (500 yr) was useful to adequately evaluate the statistical significance of the relationships between the QBO and tropical climate features. Furthermore, the fact that most of the impacts diagnosed in this chapter are very similar in the three simulations, despite their differences in resolution and inclusion of Earth System processes provides robustness to the results. Nevertheless, the dynamical core of all the simulations is the same, so the parametrisation schemes such as the convective and gravity-wave scheme are identical. Further work needs to evaluate these relationships in different models from CMIP6.

However, the direction of causality cannot be interpreted from the regression or composite analyses presented in this chapter. For example, the ENSO-QBO relationships could be explained by anomalous tropical wave activity associated with ENSO modifying the downward propagation of the QBO (Schirber, 2015) or alternatively, the QBO temperature variability affecting convection in various regions and modifying the tropical circulation. Further experiments are needed to separate the mechanisms that could explain these relationships and that could separate the directions of influence between the tropical stratosphere and troposphere.

# 8

## Tropical Teleconnections of the QBO in the UM with a nudged stratosphere

The previous chapter describes tropical teleconnections associated with the stratospheric quasi-biennial oscillation (QBO) in the MOHC CMIP6 pre-industrial control experiments. One could reasonably hypothesize that those relationships are the result of a control of tropical convection by the QBO. This chapter tests this hypothesis by constraining the zonal winds in the tropical stratosphere, eliminating any possible influence of the troposphere on the stratosphere. The relaxation experiment design is described and results are presented and a discussion on how the nudging modifies the teleconnections found in the free-running CMIP6 experiments is given at the end of the chapter.

### 8.1 Introduction

Surface impacts of the QBO in the tropics have been documented in observational and modelling studies (Giorgetta et al., 1999; Collimore et al., 2003; Garfinkel and Hartmann, 2010; Liess and Geller, 2012; Hansen et al., 2016; Gray et al., 2018; Ma et al., 2021) but the specific processes that link the QBO to the strength and height of tropical convection are less clear. The observational evidence available (e.g. Collimore et al., 2003; Liess and Geller, 2012; Gray et al., 2018) cannot determine the causal links between the QBO and

tropical convection due to the strong influence of ENSO on tropical climate, as well as the short period of observations available. For instance, a relationship between the QBO on the Madden-Julian Oscillation (MJO) amplitude and predictability has been diagnosed in recent years (Son et al., 2017; Wang et al., 2019; Lim et al., 2019; Klotzbach et al., 2019; Densmore et al., 2019) but studies disagree over whether these relationships point to a downward influence from the stratosphere to the tropical troposphere (Klotzbach et al., 2019; Lim et al., 2019) or the observed relationship is due to other processes (Wang et al., 2019).

The use of GCMs to address these questions is also limited due to the fact that only some recent models are able to reproduce a sufficiently reasonable representation of the QBO. Still, some CMIP6 models produce highly unrealistic QBO features and some require a relaxation of the model towards an observed state of the QBO, i.e., artificially generating a QBO (Richter et al., 2020). For example, the observed relationships between the QBO and the MJO have not been found in GCMs (Lee and Klingaman, 2018; Kim et al., 2020) and one reason for these results may be the underestimation of the UTLS temperature variability associated with the QBO in current GCMs.

The leading hypothesis to explain an impact from the QBO on convection suggests that changes to the upper-troposphere lower-stratosphere (UTLS) static stability caused by the QBO residual circulation modifies the strength of convection throughout the column (Liess and Geller, 2012; Nie and Sobel, 2015). However, GCMs simulate a weaker change in the upper-level static stability at the equator due to a weak amplitude of the QBO in the lower stratosphere (Lee and Klingaman, 2018; Richter et al., 2020) which may cause the models to misrepresent teleconnections in the tropics. These biases have led several studies to perform experiments in which the model stratosphere is relaxed towards an observed or idealized state of the stratosphere, also known as nudging, (e.g. Garfinkel and Hartmann, 2011; Gray et al., 2020; Richter et al., 2020; Martin et al., 2021). The nudging technique has proven useful because the relaxation can remove biases, identify causal pathways and test specific hypotheses regarding the mechanisms that play a role in stratosphere-tropospheric coupling.

This chapter investigates tropical teleconnections associated with the QBO in the MOHC UM using relaxation experiments. The remainder of this chapter is presented as follows. First, the chapter provides a scientific rationale for nudging experiments in the context of

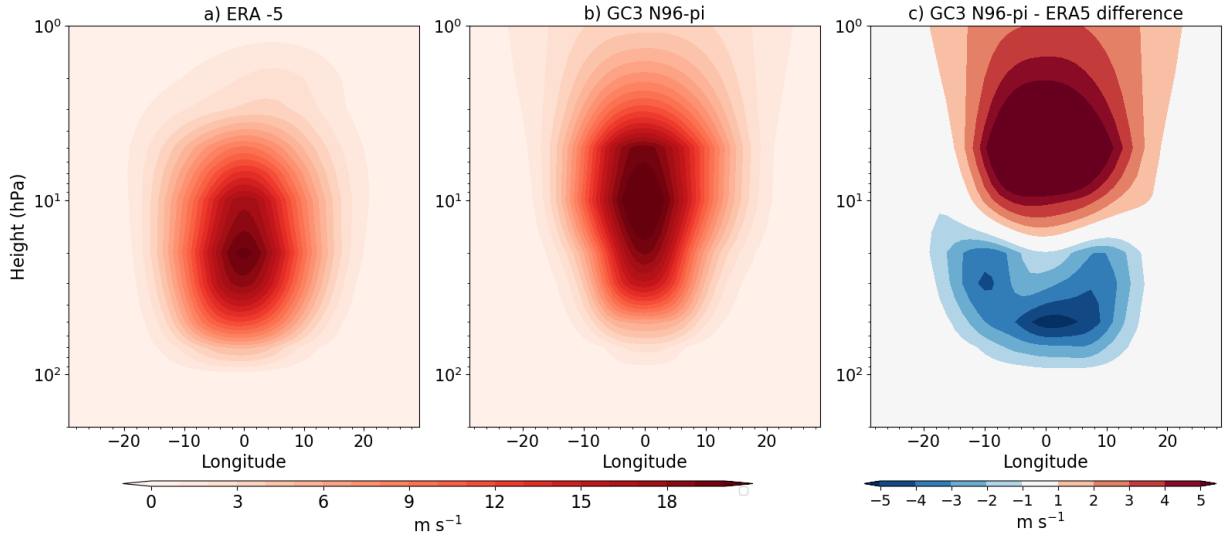


**Figure 8.1:** Latitude-pressure plot of the amplitude [ $\text{m s}^{-1}$ ] of the QBO. Obtained from the zonal mean zonal wind fourier spectrum magnitude within the QBO periods, as in Schenzinger et al. (2017).

QBO tropical teleconnections and then describes the experimental configuration and the goals and hypotheses that we aim to test using these simulations. Afterwards, results comparing runs using the nudging technique versus the free running model are presented and discussed highlighting the possible mechanisms at play for the tropical route of QBO teleconnections.

## 8.2 The nudging protocol

The number of GCMs with a full stratosphere have increased notably from CMIP3 to CMIP6 which means that features such as the QBO are increasingly better resolved with each iteration of the CMIP (Bushell et al., 2020; Richter et al., 2020). Nevertheless, several aspects of the QBO are still not well represented by state-of-the-art climate models, such as the period and amplitude of the QBO (Schenzinger et al., 2017; Richter et al., 2020). These biases increase uncertainty in teleconnections diagnosed from these models, because these biases could make the models misrepresent processes that are observed in the real-world between the tropical stratosphere and troposphere.

### 8.2.1 The importance of biases in the UTLS for stratosphere-tropospheric coupling

One key stratospheric bias in most of the existing climate models relates to the representation of the QBO in the lowermost stratosphere. Figure 8.1 illustrates this bias in GC3 N96-pi by comparing the variation of the QBO amplitude with height and latitude with ERA5; the amplitude is obtained using the method in Schenzinger et al. (2017). The amplitude of the QBO in the lowermost equatorial stratosphere is much smaller and extends to the subtropics less in the model than in ERA5, in agreement previous studies (Schenzinger et al., 2017; Richter et al., 2020; Bushell et al., 2020). The implication of this bias is that if the QBO signal is too weak in the lower part of the stratosphere in the model, the simulated meridional circulation will also be weaker, and any temperature anomaly associated with this residual circulation will also be smaller near the tropopause.

The main hypothesis suggested in the literature to explain observed relationships between the QBO and tropical convective diagnostics is the temperature variability in the tropopause layer and its influence on the upper-level static stability (Collimore et al., 2003; Liess and Geller, 2012; Nie and Sobel, 2015; Gray et al., 2018). Models that simulate a weaker than observed variance of the temperature near the tropopause associated with the QBO may dampen any processes that relate the QBO to tropical convection. Due to the fact that most models underestimate the variability of the temperature associated with the QBO in the UTLS region, several studies have argued in favour of performing numerical experiments with a GCM where the stratosphere is relaxed towards an observed or idealized state (e.g. Lee and Klingaman, 2018; Martin et al., 2021) to correct this bias.

Chapter 7 described a number of robust signals in convective features associated with the QBO within the CMIP6 experiments that have an internally generated QBO. Figure 8.1 shows that the signal that may be responsible for these relationships is too weak within these models. One might reasonably then expect that if the models simulate a stronger temperature variability associated with the QBO, then the surface response to the phase of the QBO would also increase. The remainder of this chapter describes the experimental design and results of simulations that aim to alleviate the biases in the QBO in the lower

stratosphere and compare the surface response in these experiments with those of simulations with a free-running stratosphere with an internally generated QBO.

The following section describes a nudging protocol using the Met Office Unified Model. The aim of these experiments is to investigate how the tropical route of QBO teleconnections is modified when the representation of the QBO is improved, and whether nudging is a good tool for this purpose.

### 8.2.2 The nudging protocol

This section describes the experimental setup for the nudging experiments. The GC3.1 configuration of the UM model is used (model version 11.4), using an atmospheric horizontal resolution of N96 (corresponding to the low-resolution version of the simulations of the MOHC submitted to CMIP6). Both atmosphere-only and ocean-atmosphere coupled experiments were conducted, in all cases spanning the period 1981–2015, using a present-day climate setup where all forcings are set constant to those of the year 2000, so there is no variation in, e.g., greenhouse gases within these simulations.

Nudging refers to the relaxation of a variable within the model to a specified state, and is a technique that has recently been used for several purposes such as investigating the MJO-QBO relationship in a climate model (Martin et al., 2021) and the role of the upper stratosphere for forecasting sudden stratospheric warming events (Gray et al., 2020).

In the UM setup, three variables can be relaxed, air temperature ( $T$ ) and the zonal and meridional components of the wind ( $u$  and  $v$ ). The relaxation is applied towards reanalysis data or towards an idealized state at each grid-point, in contrast to the setup in other models (e.g. Martin et al., 2021) where the relaxation is performed in a zonal-mean sense. Furthermore, the nudging can be performed between specified vertical levels and in selected latitude/longitude regions. To find the experimental setup that resulted in an improvement in the representation of the QBO without over constraining the model’s climatological state we conducted several sensitivity tests using an atmosphere-only setup to test the effect of nudging all  $u$ ,  $v$  and  $T$  compared to just one, as well as the model levels and latitudes where the nudging was applied.

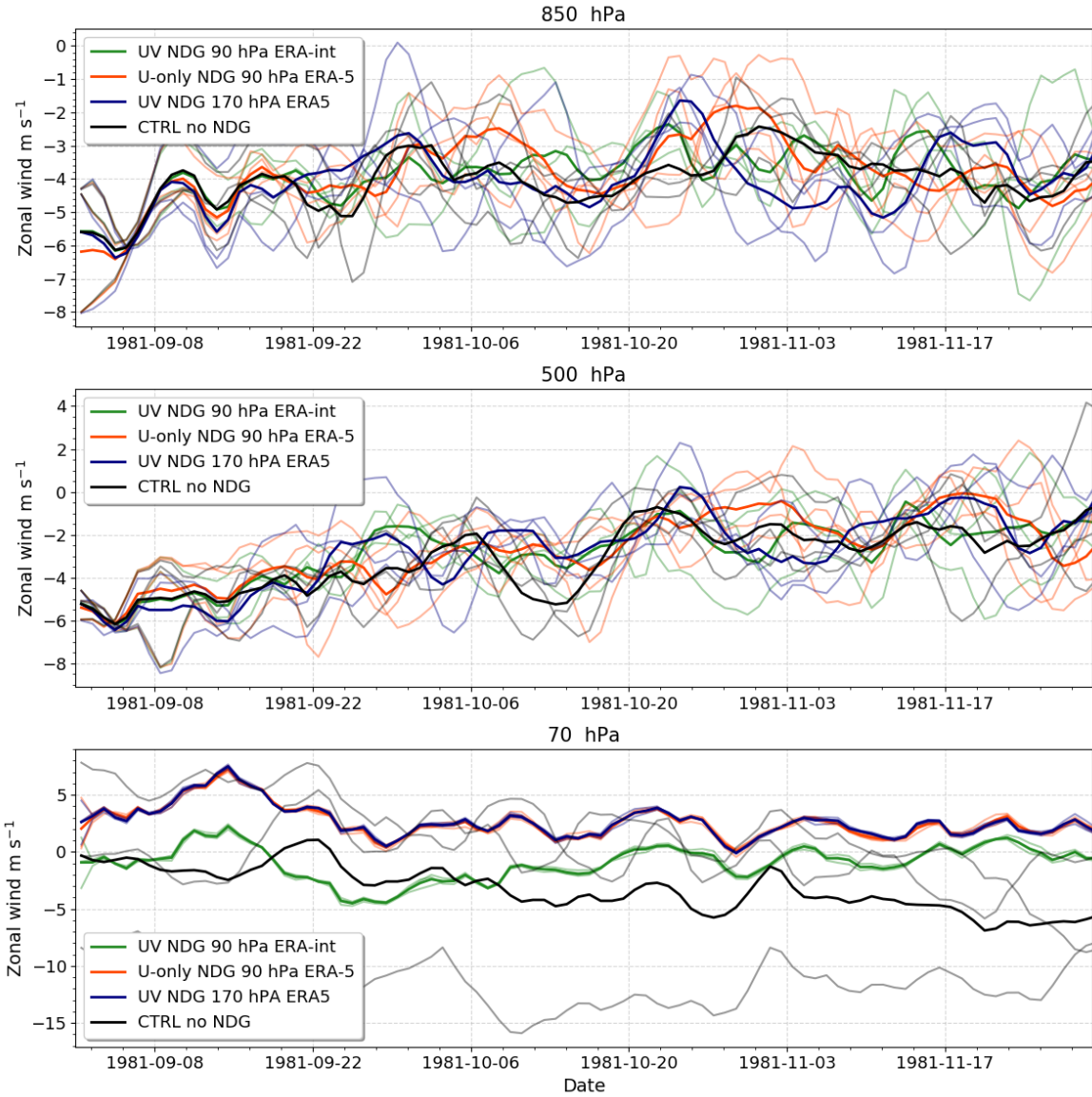


**Figure 8.2:** Time-series of the zonal-mean zonal wind in the  $10^{\circ}\text{S}$ - $10^{\circ}\text{N}$  band at the 850 hPa (upper), 500 (middle) and 70 hPa (lower) levels. Results are from atmosphere-only simulations without nudging (CTRL no NDG), with nudging applied to both  $u$  and  $v$  up between 90 and 4 hPa using ERA-interim data (UV NDG 90 hPa ERA-int), with nudging between 170 hPa and 4 hPa nudging  $u$  and  $v$  using ERA5 data and finally, nudging only  $u$  from 90 to 4 hPa using ERA5 data. For each kind of the simulation, each ensemble member is shown (faint line) and the ensemble mean (solid line) is shown.

Figure 8.2 shows the time-series of the zonal-mean zonal wind at different levels for the different sensitivity experiments performed. Three ensemble members were performed first for a control simulation with no nudging, a simulation where  $u$  and  $v$  were relaxed towards ERA-interim, and two simulations with ERA5 as the nudging data, one relaxing  $u$  between

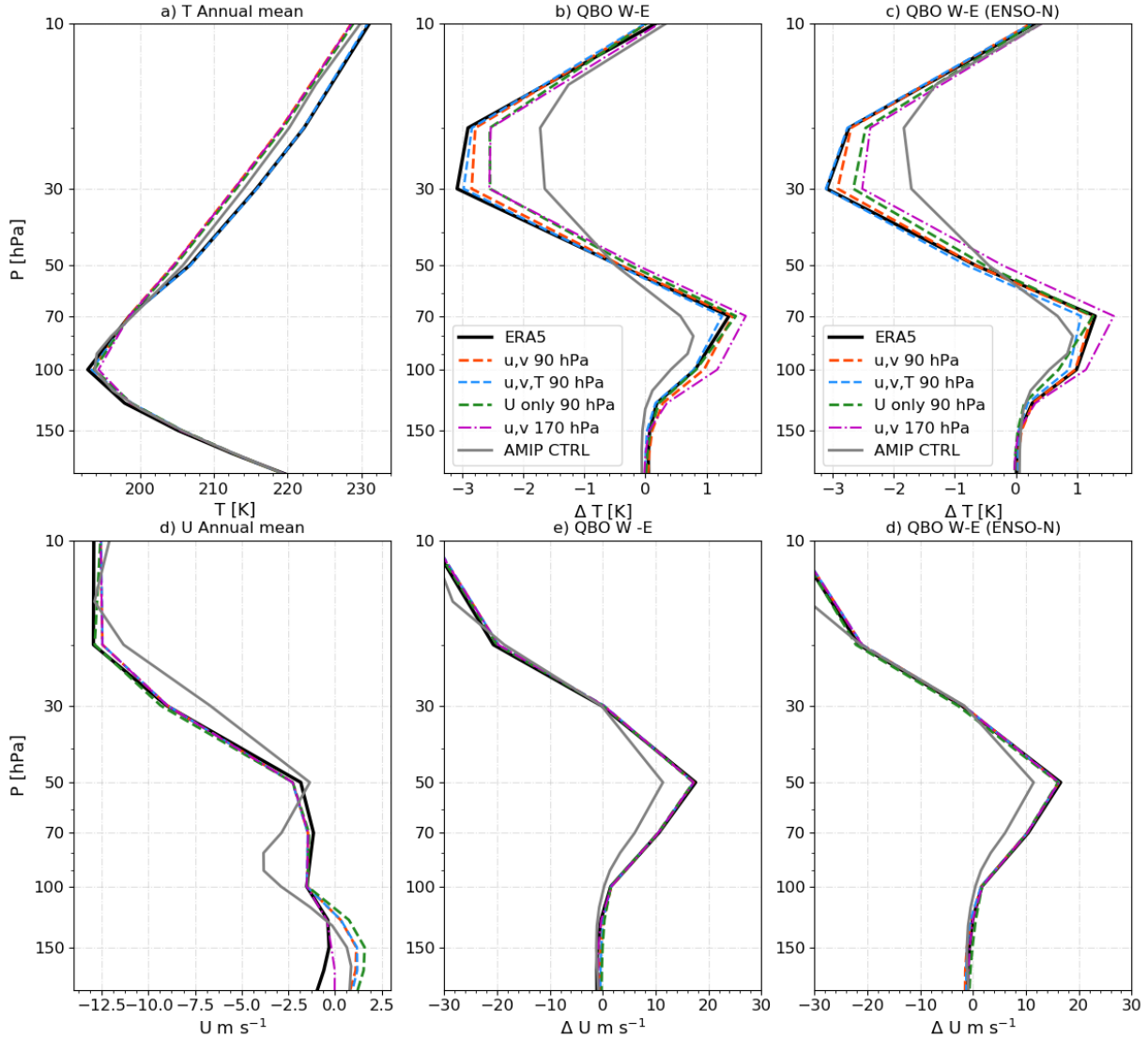


**Figure 8.3:** Vertical profiles of zonal mean temperature (a-c) and zonal wind (d-f) depicting the climatological state (a, d), the QBO W-E difference (b, e) and the QBO W-E difference during Neutral states of ENSO (c, f). In all the simulations with relaxation, the nudging data was ERA5.

90-4 hPa and another relaxing  $u$  and  $v$  between 170 hPa and 4 hPa.

These results show that in the troposphere (850 hPa) all the ensemble members diverge towards different states, whereas in the lower stratosphere, the ensemble members of the nudged simulations converge towards a single state. The nudged simulations at the 70 hPa level differ only due to the nudging data, highlighting the differences in the zonal wind in the equatorial stratosphere between ERA5 and ERA-interim. From this part on, results using only ERA5 nudging data are presented.

Figure 8.3 shows the vertical profiles of temperature and zonal wind in these simulations. The variability of  $T$  associated with the QBO, is fairly well represented by all the nudged simulations, compared to the control simulations, even when  $T$  was not relaxed towards ERA5. This results proves that the meridional circulation imposed by the shear imposed when relaxing  $u$  is enough to force temperature variability within the model through thermal wind balance, as found in Martin et al. (2021).

The climatological zonal mean zonal wind and the variability of associated with the QBO (Fig. 8.3d-f) is much improved in the simulations with nudging, as expected, in the stratosphere. Notably, in the simulations where nudging was applied above 90 hPa, the biases lower down in the stratosphere at 150 hPa remain comparable to those of the control simulation, indicating that nudging the stratosphere does not pose a direct effect over the upper-tropospheric climatological state, in a zonal-mean sense.

The final experimental design chosen was to perform the nudging in the model levels 52-72 which roughly correspond to 90 hPa to 4 hPa, with a tapering of 4 levels, which means that full nudging was only working within levels 56-68. The nudging was done at all longitudes in the latitude band of 10°S-10°N with a latitudinal tapering of 10 degrees on both sides. Only the zonal component of the wind ( $u$ ) was relaxed, so that  $T$  and  $v$  were not relaxed. The experimental setup aims to reasonably simulate the observed variability of the zonal wind leaving the meridional component of the wind and the temperature to respond freely within the model.

Atmosphere-only and coupled ocean-atmosphere simulations were performed with this nudging setup, with corresponding control simulations in which there was no relaxation of any kind. The atmosphere-only, also referred to as AMIP, experiments were run with observed SSTs from the HadSST dataset. In all cases the nudging of the atmosphere was done only between 90 and 4 hPa and at equatorial latitudes only, whereas the surface boundary SSTs are used at all latitudes. For the nudged experiments several ensemble members were performed, three for the atmosphere-only configuration and six for the coupled ocean-atmosphere configuration.

**Table 8.1:** Experimental setup indicating the model configuration, the period, ensemble members, acronym and relaxation details.

Setup	Period	Ensemble members	Name	Nudging
Atmosphere-only	1981-2015	3	AMIP	ERA5. U-only 90 hPa
Atmosphere-only	1981-2015	1	AMIP-Control	No
Atmosphere-only	1981-2015	3	AMIP-Shifted	ERA5. U-only, 90 hPa. Relaxation shifted -1 year.
Coupled	1981-2015	6	Coupled	ERA5. U-only 90 hPa.
Coupled	1981-2015	2	Coupled Control	No.

The coupled experiments use an oceanic resolution of  $0.25^\circ$  (ORCA025) using the NEMO model. Each ensemble member was initialized from a different ocean/atmosphere initial conditions in order to decrease the role that internal variability may have on these simulations.

In addition to the nudged and control coupled and AMIP experiments, we performed another atmosphere-only experiment. In the normal AMIP Nudged experiment, the SST driving data corresponds to the zonal wind in the equatorial stratosphere that was observed in the real-world. To explore possible feedback processes between QBO winds and the SSTs, we performed an AMIP Shifted experiment, where the nudging data was shifted with a -1 year lag from the SSTs. In this experiment, e.g., the model year 1997 was run using 1997 SSTs but zonal winds in the stratosphere corresponding to 1996 of ERA5. In this way we have minimised any in-phase relationship between the QBO phase and the SSTs. An alternative approach would be to 'shuffle' the SSTs so that each year is run with randomly selected SSTs. However, since we are performing multi-year simulations this has associated issues of how to join the randomly-selected SSTs at the year-boundary, to form a coherent multi-year SST time-series. To avoid this issue we decided to simply shift the SSTs by one year so the QBO phase and SSTs were not aligned.

The following section presents the results of these experiments, first by reporting how the tropical tropopause variability is modified when nudging is applied and then by showing the surface impacts associated with the QBO in the nudged experiments, first in the atmosphere-only configuration and then in the coupled setup.

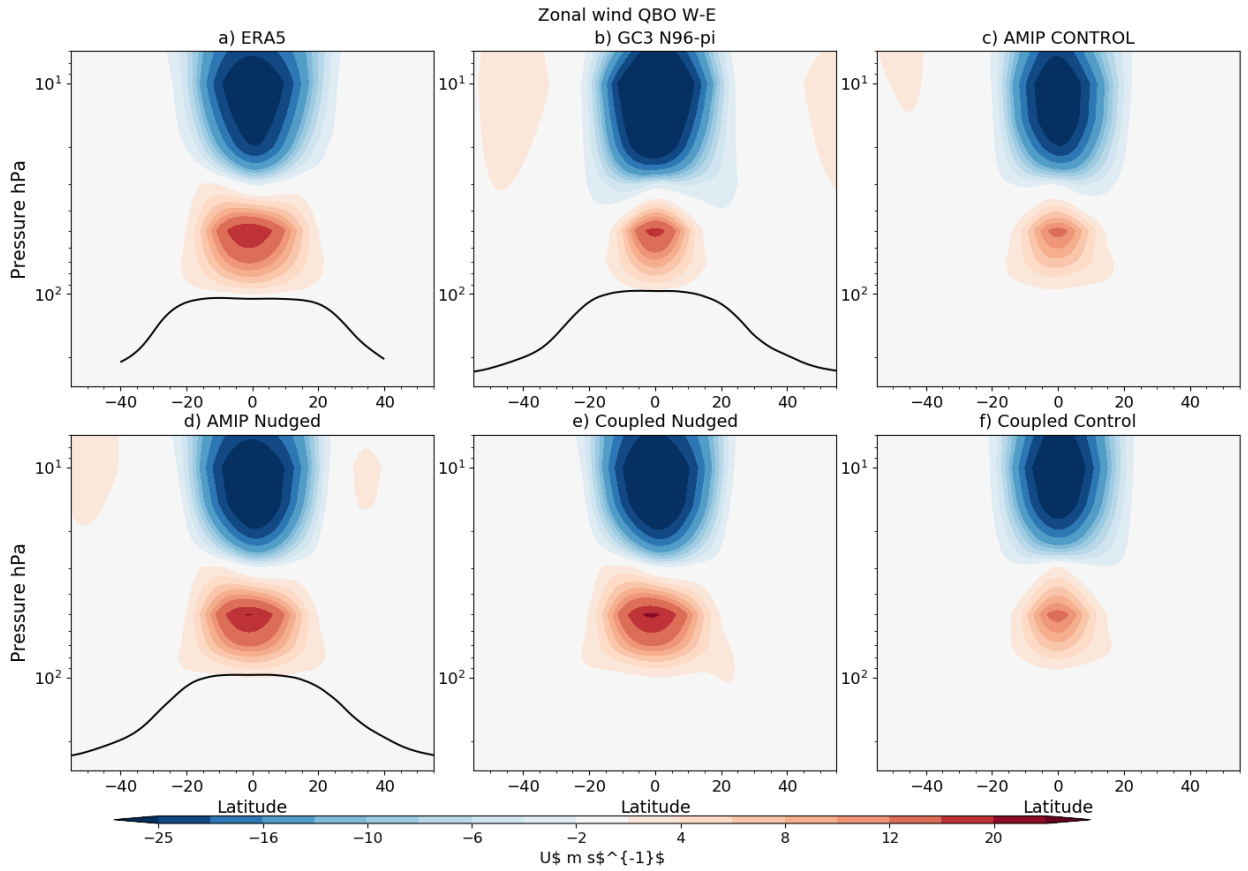


**Figure 8.4:** Latitude-height plot of the zonal-mean zonal wind differences (QBO W-E) in (a) ERA5, (b) GC3 N96-pi from CMIP6, the control simulations with no nudging in an (c) AMIP and (f) coupled configurations, and the nudged simulations in (d) AMIP and (e) coupled configurations. The black line denotes the tropopause height obtained from the model data in (b, d) and for ERA5 the tropopause height was found through the gradient threshold method. For the nudged experiments, the ensemble-mean is shown.

## 8.3 Results from nudging experiments

This section investigates the effect of nudging for the representation of the QBO, the effect of QBO in the representation of the variability in the UTLS, and surface impacts and effects on the tropical circulation associated with the QBO. The remainder of this chapter analyses the response of the tropical surface and circulation to the QBO phase in nudged and control experiments using ERA5 and the same methodologies of Chapter 7.

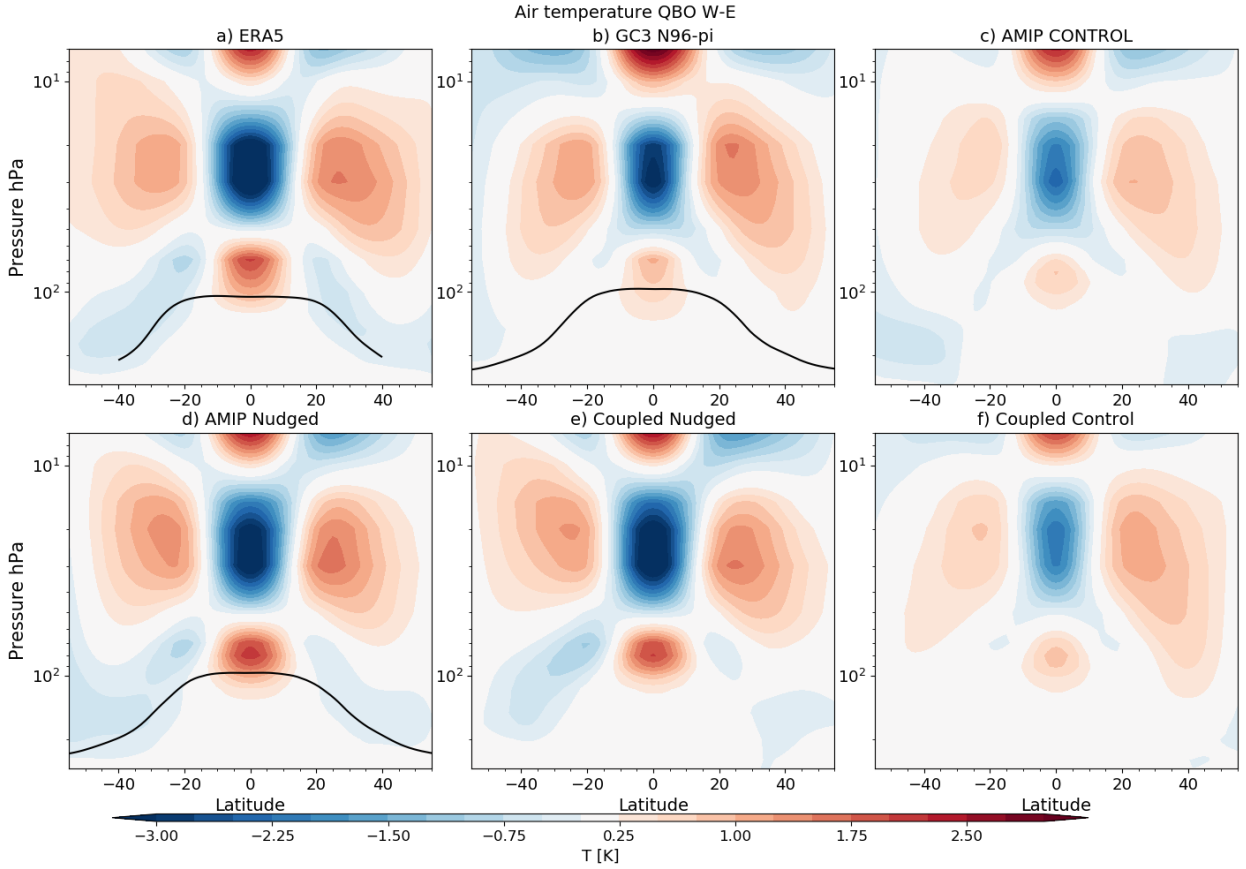


**Figure 8.5:** As in Figure 8.4 but for air temperature.

### 8.3.1 Tropical UTLS variability

Figure 8.4 shows the zonal mean difference in zonal wind associated with the QBO phase, in a latitude-height sense, in the 500-y CMIP6 GC3 N96-pi and both the AMIP and coupled 35-year (un-nudged) control simulations. The zonal wind variability in the lower stratosphere associated with the QBO is deficient in the GC3 N96-pi and control experiments, principally near the tropopause as the signal is too narrow and weaker than in the reanalysis.

The temperature is able to respond to the nudging within the model freely, Figure 8.5 reveals that nudging the zonal wind can also improve the air temperature variability in the lower stratosphere driven by the QBO shear. The positive temperature anomaly in the equatorial region around the 100 hPa at the tropopause level is much weaker in the GC3 N96-pi, AMIP Control and Coupled Control compared to the two nudged experiments and to ERA5. The Nudged experiments not only improve the temperature signal in the

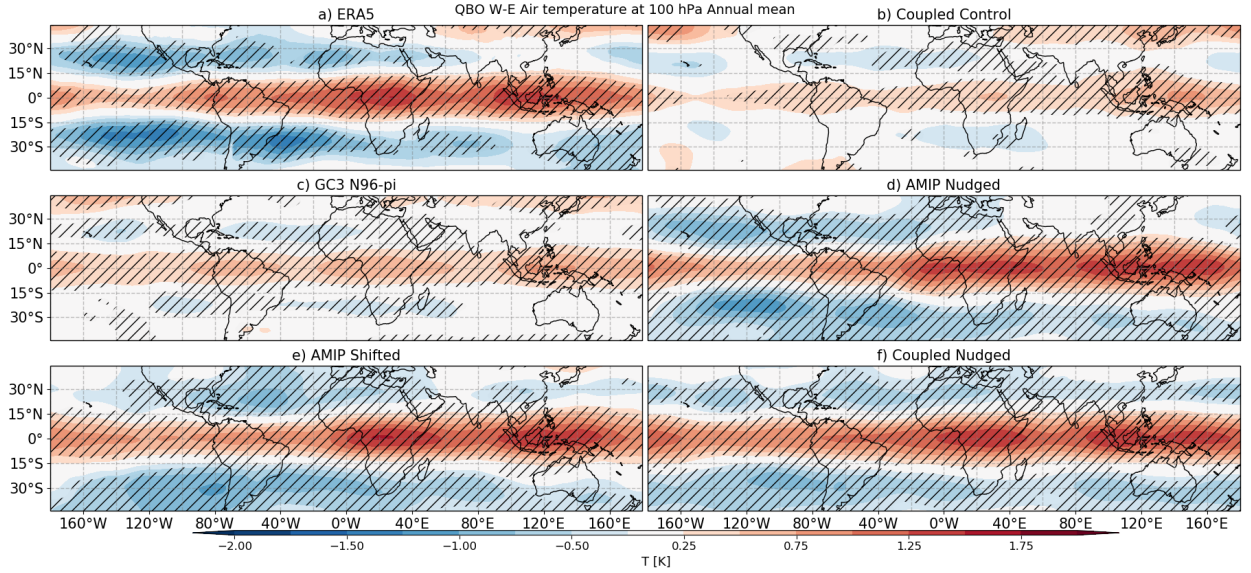


**Figure 8.6:** Air temperature QBO W-E difference at the 100 hPa level. Hatching denotes significance to the 95% confidence level.

equatorial lower stratosphere but seem to overestimate this signal around the 70 hPa level.

However, observations show a horse-shoe temperature anomaly pattern in the subtropics characterised by a negative anomaly that extends from 20-40 degrees north and south, a signal that is missing in the GC3 N96-pi, AMIP Control and Coupled Control experiments but is recovered in the Nudged experiments. This means that without nudging further away than 20 degrees north or south, the subtropical signal is obtained by improving the residual circulation associated with the QBO.

In a horizontal cross section, at the 100-hPa level, the nudging also improve the wind and temperature variability associated with the QBO (see Figure 8.6). The maximum QBO W-E differences in the zonal wind at this level are found in the Maritime continent (Tegtmeier et al., 2020b) and this pattern is also observed in ERA5 and the free running versions of the model (seen in GC3 N96-pi and Coupled Control), albeit much weaker than the observed signal (not shown).

The nudging noticeably improves the horizontal distribution and magnitude of the temperature response to the QBO at 100 hPa, as the difference between QBO phases doubles the amplitude of the un-nudged response (Figure 8.6. In addition, the temperature signal in the Nudged experiments is improved in AMIP Nudged and AMIP Shifted experiments,

indicating that these differences are not associated with the underlying SST field, rather with the QBO vertical wind shear, which has been improved by nudging. Results found in this analysis also indicate that the tropopause height and temperature exhibits more variability associated with the QBO than in the free-running model (not shown).

This section shows that the variability in UTLS temperature and zonal wind is more realistic in the nudged experiments, and that this variability is not related to the underlying SSTs but rather a result of the relaxation in the equatorial stratosphere. These results indicate that these experiments are suited to investigate tropical teleconnections associated with the QBO to test the hypothesis that the nudging experiments will exhibit a stronger surface response in the tropics to the QBO.

### 8.3.2 Atmosphere-only experiments

This section describes the results of the atmosphere-only experiments: AMIP Nudged, AMIP Control and AMIP Shifted. These simulations use the CMIP6 SST dataset used for AMIP experiments, i.e., the SSTs in these runs follow the observed seasonal and interannual variability of SSTs. The effect of nudging on the tropical circulation and precipitation is shown in the following sections.

#### The tropical circulation

The mean state of the Hadley cell in the atmosphere-only configuration is weaker than in ERA5 in the 20°S-0° region and there are also biases in the equatorial upper-level tropical and subtropical troposphere where the model shows an easterly bias (Fig. 8.7). The AMIP Nudged simulation shows positive zonal wind differences with the Control experiment in the UTLS region, i.e, improving the easterly biases of the Control experiment. However, no significant differences in the streamfunction over the tropical troposphere are observed. Similarly, no significant differences were found in the mean-state of the Hadley circulation between the Nudged and Shifted experiments (Fig. 8.7f), suggesting that the variability of the nudging data is of secondary importance relative to the SSTs and the mean state of the nudging data.

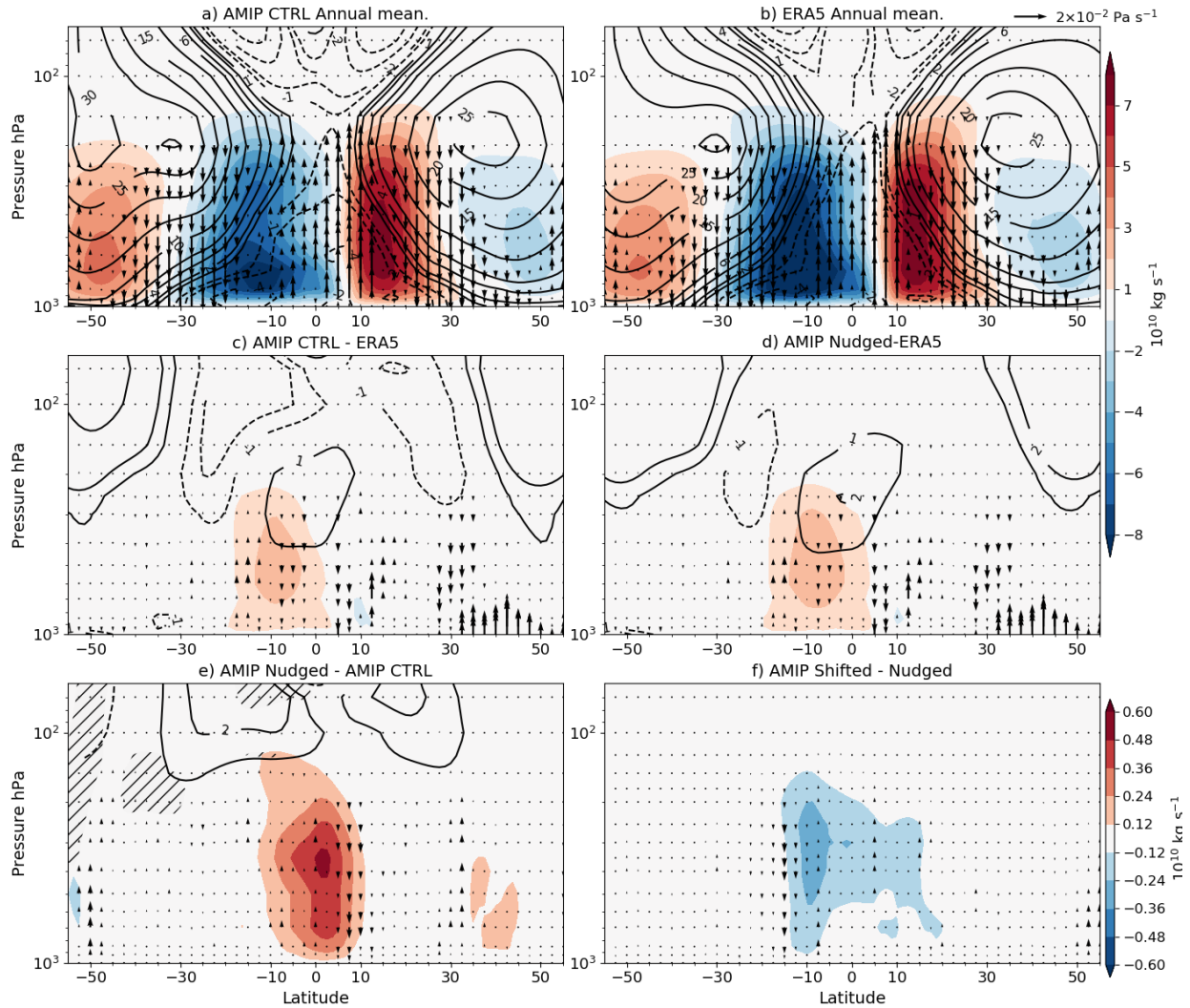


**Figure 8.7:** Hadley cell meridional mass streamfunction (shading), zonal mean zonal wind (contours in  $\text{m s}^{-1}$ ) and vertical velocity (vectors). Climatological mean in the (a) AMIP Control experiment and (b) ERA5. (c-d) show biases in the (c) Control and (d) Nudged experiments with respect to ERA5 whereas (e-f) show differences between experiments, (e) AMIP Nudged-Control and (d) AMIP Shifted-Nudged. Note that the colorbar and scale of the vectors changes are different between (a-d) and (e-f). In (e-f), significant differences (95% confidence level according to a Mann-Whitney two-sided test) in the streamfunction are highlighted with hatching .

In turn, the Walker circulation biases in the upper troposphere are notably improved in the Nudged experiment (Figure 8.8). The mean state of the Walker circulation is weaker in the AMIP Control simulation compared to ERA5, characterised by a weaker circulation in the Western Pacific and an easterly bias at upper levels. These two tropospheric biases in the Control experiment are reduced in the Nudged experiments, the relaxation is only applied above 90 hPa although significant differences in the zonal wind and zonal streamfunction

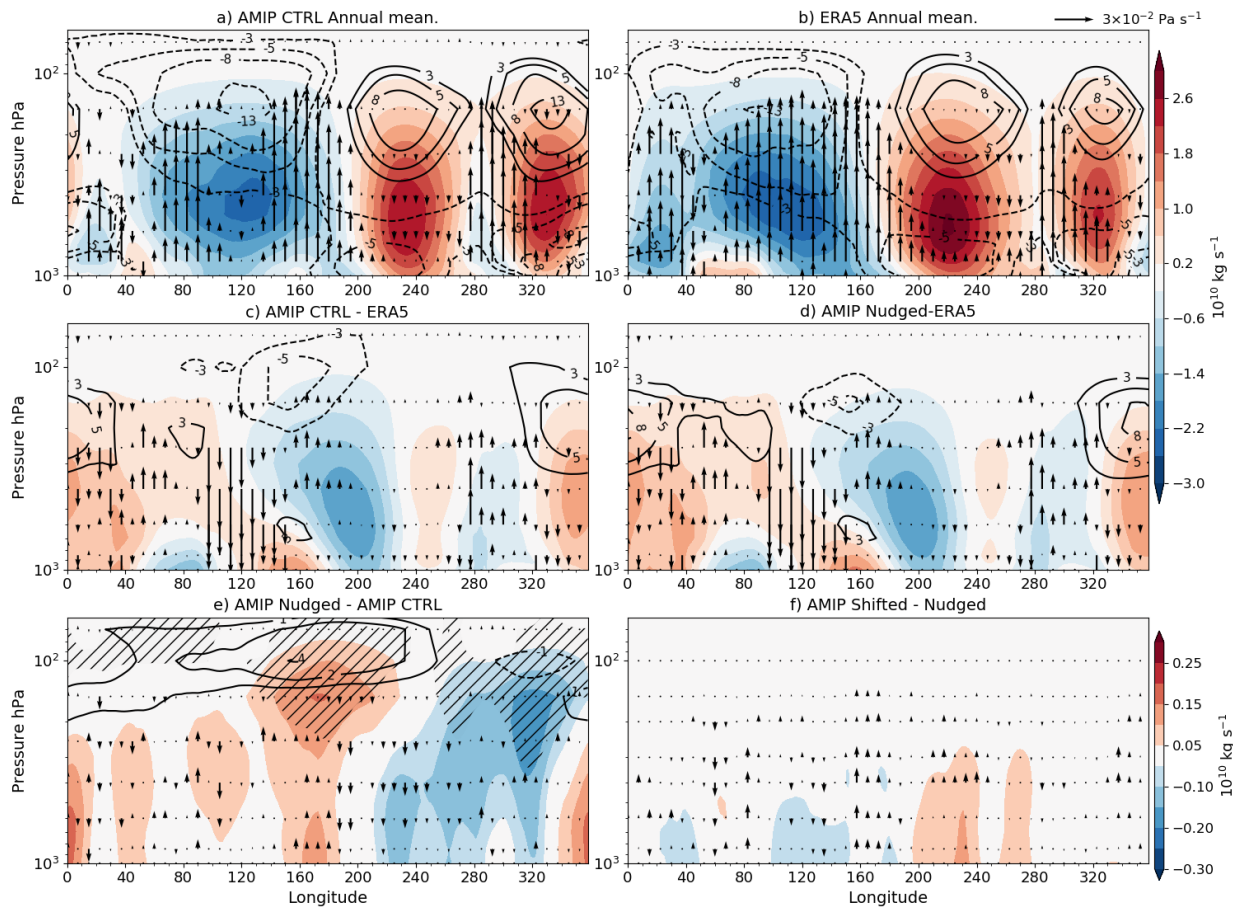


**Figure 8.8:** Zonal mass streamfunction ( $\psi$  in shading), zonal mean zonal wind (contours) and vertical velocity (vectors) averaged over the  $10^{\circ}\text{S}$ - $10^{\circ}\text{N}$ , as in Figure 8.7.

are observed at 200 hP near the dateline, over South America and over the Atlantic Ocean. However, no significant differences in the streamfunction or zonal wind in the lower troposphere are observed between the AMIP Shifted and Nudged experiments which means that the mean overturning circulation is not modified by the variability of the nudging data.

In spite of the fact that nudging reduces biases in the mean state of the Hadley and Walker circulation at upper levels, these reductions are small relative to the magnitude of the biases. Therefore, it remains unclear whether the nudging has significantly modified other aspects of tropical climate. An examination of the climatological OLR in the tropics (Figure 8.9) shows that most regions in the tropics exhibit significant and relatively large biases in AMIP Control compared to ERA5, most of which remain unchanged in the AMIP Nudged and Shifted experiments. The small and not significant differences between

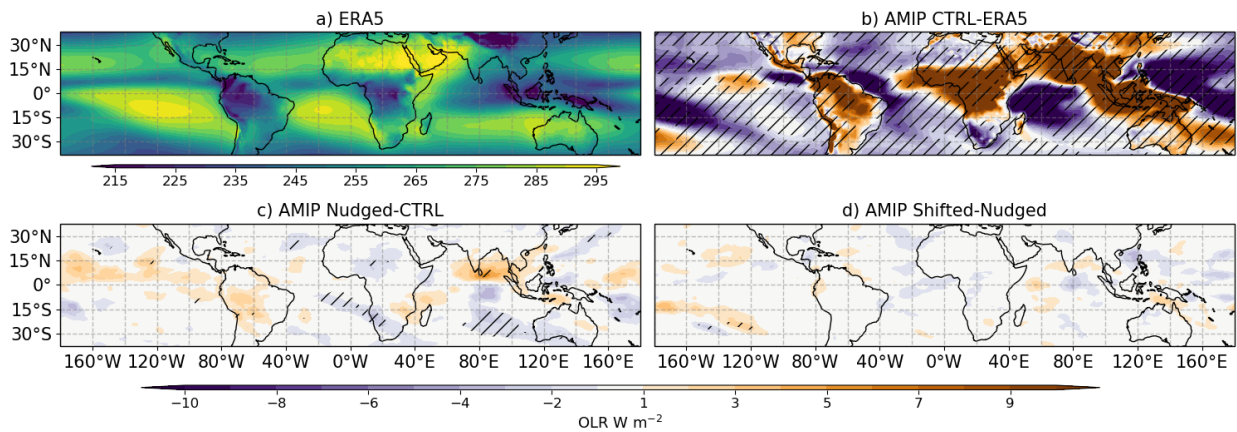


**Figure 8.9:** (a) Climatological mean OLR [ $\text{W m}^{-2}$ ] in ERA5, (b) climatological biases in the AMIP Control simulation. (c) Differences between AMIP Nudged and Control and (d) between AMIP Shifted and Nudged. Significant (95% confidence level) differences according to a Mann-Whitney U test in (c, d) are highlighted with hatching.

the Shifted and Nudged experiments suggest a small effect of the relaxation of the zonal winds over the mean state of OLR.

Similarly, Figure 8.10 shows that the zonal-mean OLR time-series averaged over the deep tropics is indistinguishable between the three AMIP experiments, and the time-series of all the experiments have the same correlation coefficient with ERA5. In other words, the tropical mean OLR remains unchanged in the nudged experiments, regardless of whether the relaxation was implemented to match the SST field or whether the nudging data was shifted from the SST time-series. Based on these results alone, it would appear that nudging has made little impact over the interannual variability of the tropical mean OLR.

### Precipitation response to the QBO

The annual-mean difference of precipitation between QBOW and E phases (Fig. 8.11) in the ensemble-mean AMIP Nudged experiment matches closely the results of GPCP, characterised by an El Niño pattern in the Pacific Ocean, a weaker Atlantic ITCZ and a gradient of precipitation in the Indian Ocean during QBOW compared to QBOE. In contrast, the free-running AMIP Control and the simulations with an out-of-phase relaxation of the winds with respect to the SST driving data (AMIP Shifted) show very different responses to the AMIP Nudged experiment and observations.

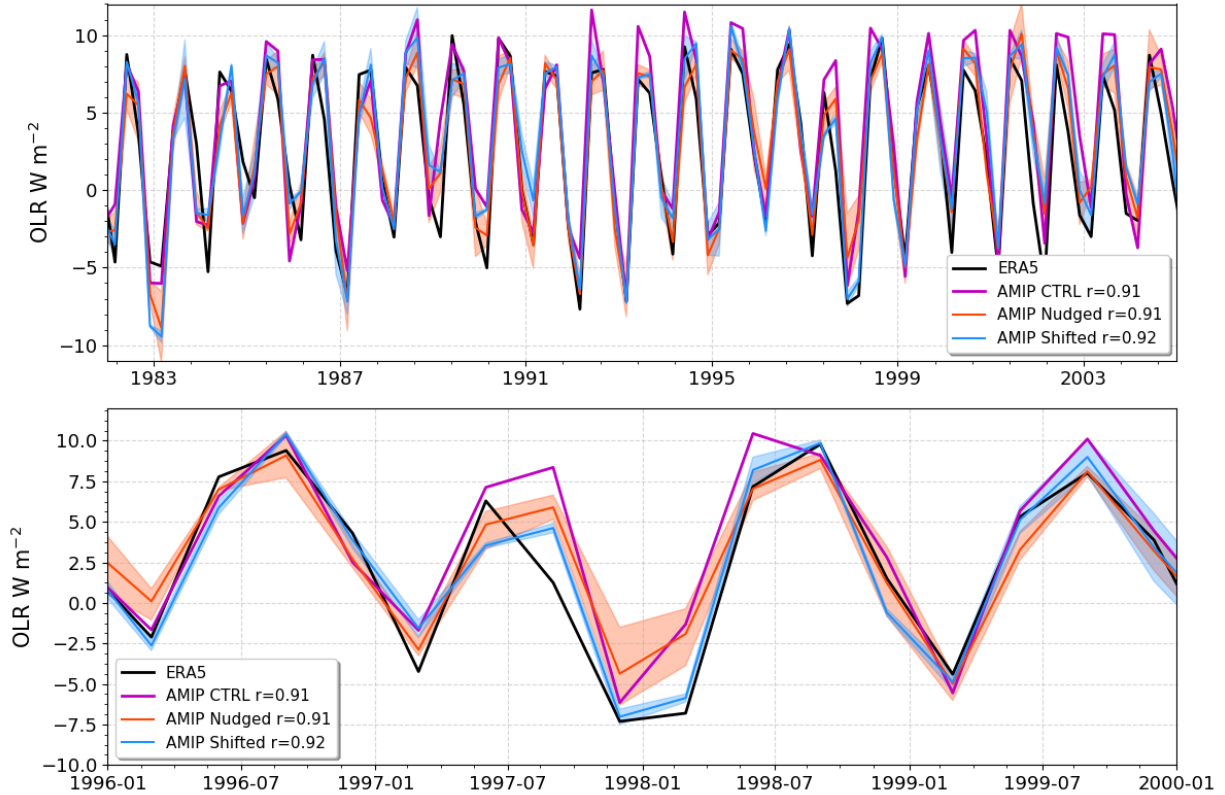


**Figure 8.10:** Time-series of zonal-mean equatorial [5°S-5°N] OLR in ERA5 and the three amip experiments for (a) 20 yrs and a (b) 5-yr period around the 1997-1998 ENSO event. For each AMIP experiment the Pearson correlation coefficient between the experiment time-series and ERA5 is shown in the legend.

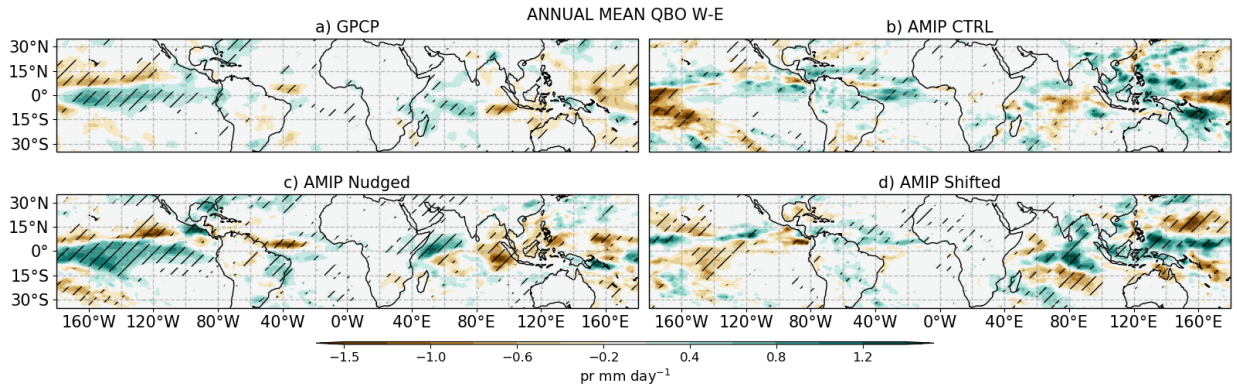


**Figure 8.11:** Annual-mean precipitation response (QBO W-E) in (a) GPCP, and atmosphere-only experiments: (b) AMIP CTRL, (c) AMIP Nudged and (d) AMIP Shifted.

A similar result is found when the composite differences only include DJF (Fig. 8.12), so that the precipitation response in the simulations where the QBO index and the SSTs match exactly as in observations (AMIP Nudged) produce a very similar response to

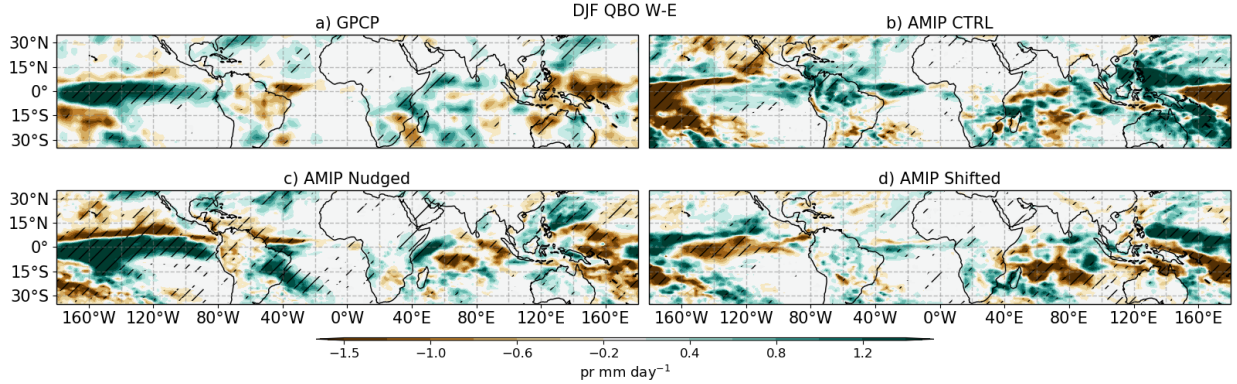


**Figure 8.12:** As in Fig. 8.11 but for the DJF season.

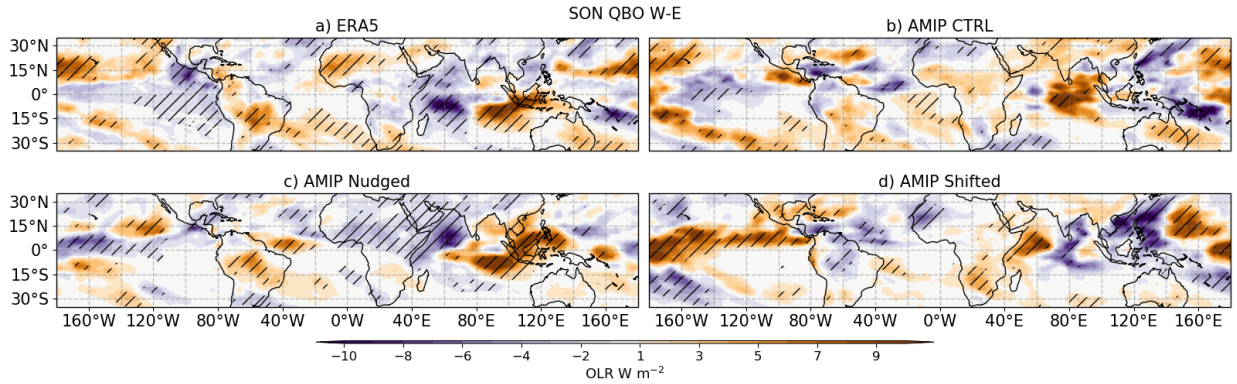


**Figure 8.13:** As in Fig. 8.11 but for OLR in the SON season.

GPCP, whereas simulations where the QBO winds do not match the same SSTs result in different responses. Results using OLR are very similar, for example, Figure 8.13 shows that a strong response is diagnosed in GPCP in the Indian Ocean which is reasonably reproduced in AMIP Nudged but AMIP CTRL and AMIP Shifted exhibit a very different response in the Indian Ocean and elsewhere.

These results suggest that the QBO winds are secondary to the effect of the SSTs for the precipitation response in these atmosphere-only experiments. The AMIP Shifted experiment has a better representation of the stratospheric variability in temperature and vertical wind shear, however, the response is entirely different to the AMIP Nudged experiments, the difference between these two experiments being the underlying SSTs. These results suggest that improving the representation of the QBO is not enough to replicate the observed response because the SST forcing dominates.

This section shows, first, that relaxing the zonal wind in the stratosphere in atmosphere-only experiments does not modify the mean state of the tropical circulation. Second, that the surface response of precipitation associated with the QBO in observations is largely associated with the underlying SSTs. The tropical mean OLR and precipitation mean state appear to be undistinguishable between Control, Nudged and Shifted experiments, whereas the composite differences between the two phases of the QBO reveal that the observed precipitation response is associated mostly with the SST anomaly pattern. However, whether the QBO has any effect over the SSTs cannot be answered in this atmosphere-only experiments, which leads to the next section which analyses the coupled nudged experiments.

### 8.3.3 Coupled experiments

This section presents the results of the coupled ocean-atmosphere experiments with (Nudged) and without (Control) relaxing the zonal wind in the tropical stratosphere. Note that all the individual experiments in this section are the same length (35 yr) and that the Coupled Nudged ensemble-mean refers to the mean results of the six ensemble members with nudging and the Control ensemble-mean to the mean of the two ensemble members. These coupled experiments differ only slightly from the setup used in the CMIP6 piControl experiments, analysed in section 7.3, with the atmospheric resolution of the nudged experiments matching the resolution of GC3 N96-pi ( $1.875^\circ \times 1.25^\circ$ ) and the oceanic resolution of these resolutions being the same as GC3 N216-pi ( $0.25^\circ$ ). The forcing is constant in both types of runs, except that in the piControl experiments, the forcing represents conditions of the year 1850 and in the nudged experiments of the year 2000. Due to these similarities, we compare the long-term CMIP6 experiments with the nudging experiments in some instances.

#### SST response

The previous section shows that in atmosphere-only experiments the SST forcing dominates over any effect of the nudging, indicating that the mechanism by which the QBO influences tropical climate involves the SSTs. In the coupled ocean-atmosphere experiments, the SSTs are able to respond and interact with any atmospheric forcing, and for that reason, this

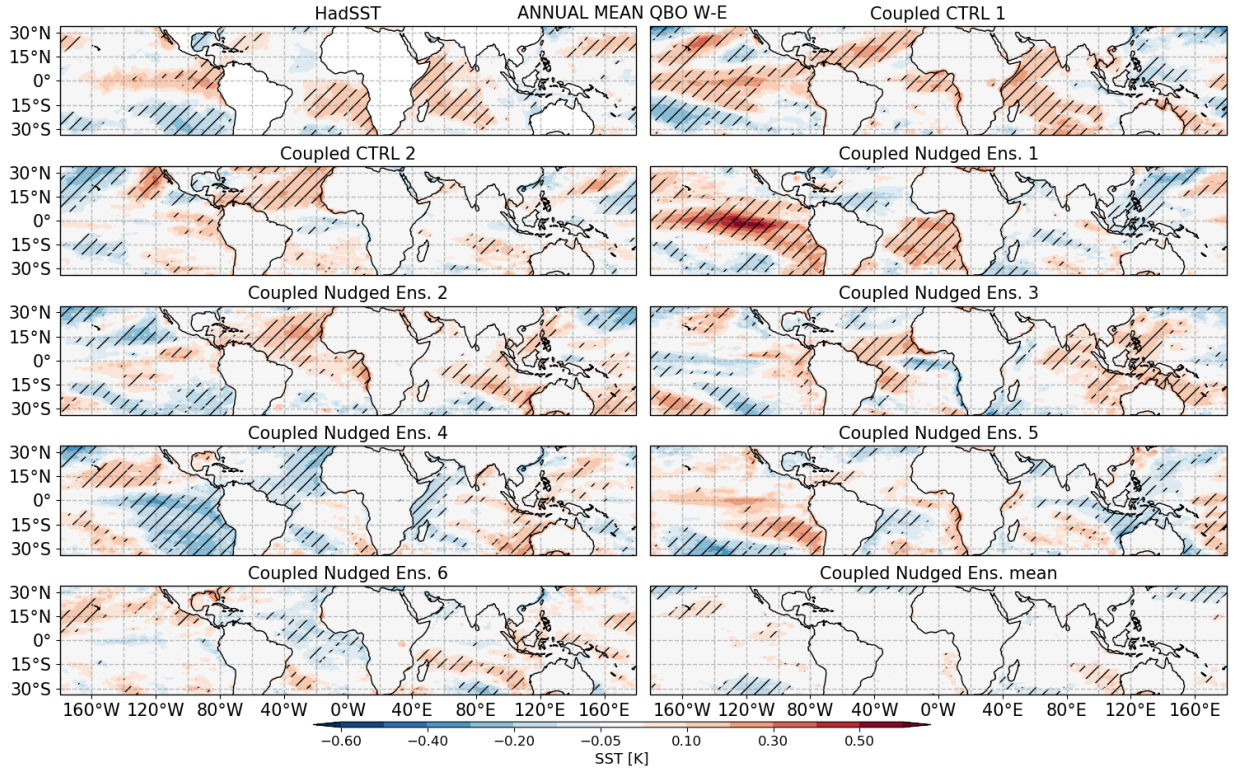


**Figure 8.14:** Annual mean SST [K] QBO W-E differences in the HadSST dataset and the Coupled Control, Coupled Nudged ensemble members and the Coupled Nudged ensemble mean. Hatching denotes significance to the 95% confidence level according to a bootstrapping with replacement test.

section first presents the annual mean and seasonal mean differences between the two phases of the QBO comparing coupled nudged and control experiments.

The annual mean QBO W-E difference in tropical SSTs in HadSST and each coupled experiment is shown in Figure 8.14. In the HadSST dataset, the differences indicate a warmer East Pacific, and equatorial Atlantic and Indian Oceans. The control experiment 1 (CTRL 1 in Fig. 8.14b) shows a very similar response in the Pacific and Indian Oceans whereas the results of the second control experiment (CTRL 2 in Fig. 8.14c) only agree with the HadSST results in the subtropical North Atlantic and in the Western Pacific. The nudged experiments, in turn, show a number of different responses, with differences being significant and positive in some regions in one ensemble and of another sign and insignificant in other ensembles.

The ensemble-mean response shows that averaging over all ensembles results in a weak mean response, with only some differences being statistically significant and different than

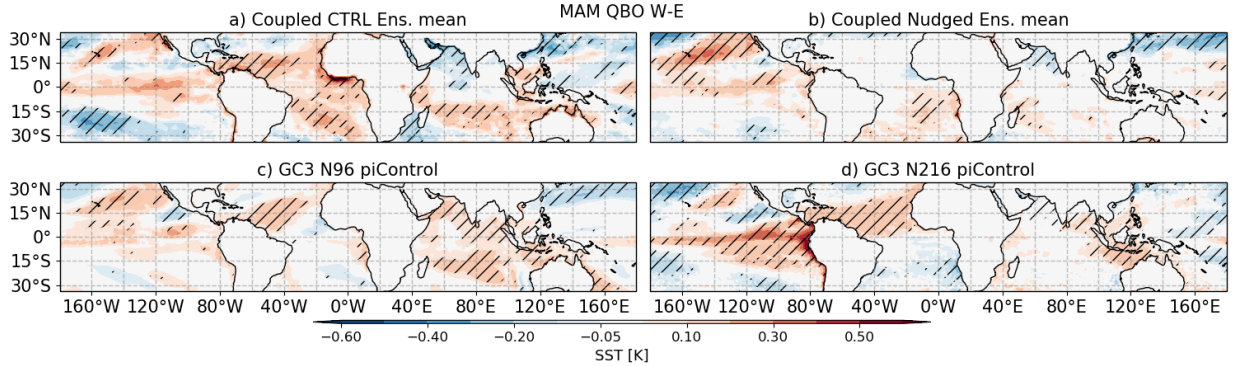


**Figure 8.15:** SST differences between QBO phases in MAM in (a) Coupled Control ensemble mean (2-member), (b) Nudged Coupled ensemble mean (6 members) and in the CMIP6 (c) GC3 N96-pi and (d) GC3 N216-pi.

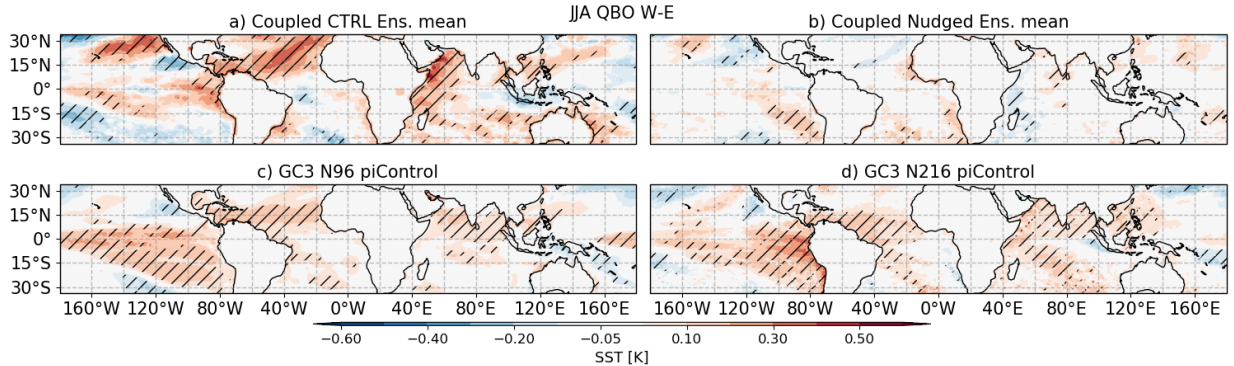


**Figure 8.16:** As in Fig. 8.15 but for JJA.

zero, for example the positive differences found over the coast of Australia and the subtropical Central Pacific. In specific seasons, such as MAM (8.15), the SST response also appears to be stronger in the tropics in the free-running Coupled Control experiments than in the nudged experiments. In MAM, a positive difference found in the Atlantic, Indian and Pacific Oceans in the CMIP6 experiments is also found in the control experiments but this response is weaker in the ensemble-mean of the nudged experiments. The nudged experiments show a relatively large difference in the eastern subtropical Pacific reaching the coast of California, in agreement with the control experiments.

The pattern of positive anomalies in the equatorial Central and Eastern Pacific, as well as in the Atlantic Ocean, appears in the control and CMIP6 experiments in most months. In boreal summer (Fig. 8.16), the patterns are particularly strong in the Coupled Control ensemble mean in the Atlantic and Indian Oceans. However, the Nudged experiments show

a very weak mean response in the tropics, with only a warm difference found in the western coast of South America. For the other seasons, SON and DJF, similar results are found (not shown) in which the ensemble mean of the control experiments agrees well with the CMIP6 experiments, whereas weaker responses are found in the nudged experiments.

These results suggest that the SST response to the phase of the QBO in the nudged experiments is not significantly larger in the experiments with nudging compared to the control or the CMIP6 experiments, especially in equatorial regions. In other words, the simulations with a stronger temperature signal associated with the QBO show the weakest response to the phase of the QBO. The lack of robust and large patterns of SST anomalies suggests that the precipitation response may also be weaker in the ensemble mean of experiments with nudging, which is the topic of the next section.

### Precipitation response

The annual mean difference between QBO phases (Fig. 8.17) in each coupled experiment reveals a strong variability of the precipitation response, suggesting an important role of long-term variability for these responses. In particular, the control experiments show two significant responses: the first control experiment shows a significant El Niño-like response over the Central and Eastern Pacific Ocean, whereas the second control experiment shows a northward shift of the Atlantic ITCZ and a wetter Caribbean Sea. Precipitation differences in the Indian Ocean and continent are also significant in both of these two coupled experiments, even though the pattern and magnitude of the difference is not a close match, both simulations suggest a wetter western Indian Ocean and continent. Note that these three responses found in the Coupled Control experiments in this setup were also observed over the longer GC3 N96 and N216-pi experiments, described previously in Chapter 7.

The nudged experiments show different precipitation responses (Fig. 8.17), with several regions showing significant responses of one sign in one ensemble member and another, also significant, response of an opposite sign in a different ensemble. These varied precipitation responses agree with similarly varied SST differences (Figure 8.14). In most ensemble members, the stronger responses are seen over the ocean rather than over land. The nudged

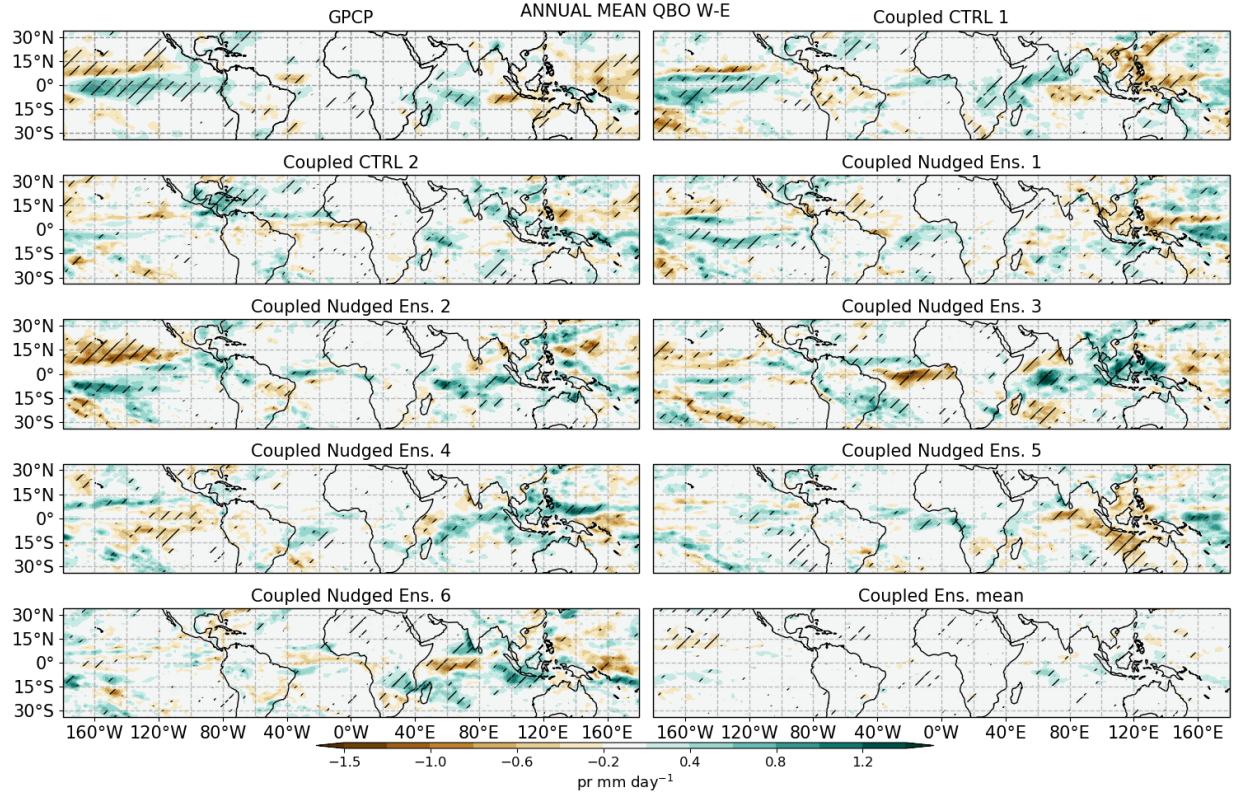


**Figure 8.17:** Annual mean precipitation QBO W-E differences in GPCP, Coupled Control, Coupled Nudged ensemble members and the Coupled Nudged ensemble mean. Hatching denotes significance to the 95% confidence level according to a bootstrapping with replacement test.

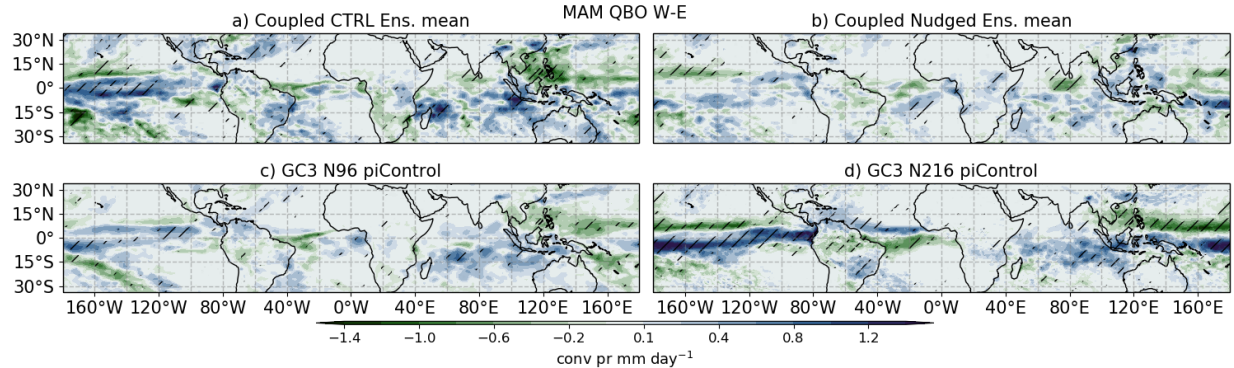


**Figure 8.18:** As in Fig. 8.15 but for convective precipitation.

ensemble mean shows regions with a significant response but the difference value in significant regions is too small to be represented by the colorbar, indicating a weak response.

The differences in a specific season are also relatively weak in the ensemble mean of the nudged experiments. For instance, in boreal spring, the differences in convective

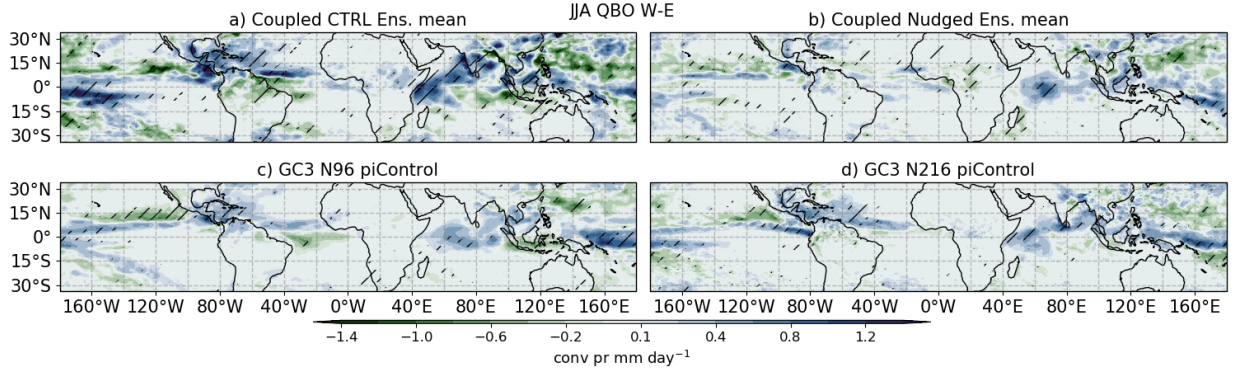


**Figure 8.19:** As in Fig. 8.18 but for JJA.

precipitation (Figure 8.18) show a wetter equatorial Pacific and a drier band at 10°N during QBOW than E in the control ensemble mean and CMIP6 experiments, whereas the nudged experiments only show the dry response. The Coupled Control ensemble mean and CMIP6 experiments agree on the sign and pattern of the response in the Western Pacific and Indian Ocean, characterized by dry anomalies in the Western Pacific ITCZ, the Philippines and the South China Sea, whereas wetter anomalies are observed in the Indian Ocean. In contrast, the composite mean results in the nudged experiments show insignificant responses in these above mentioned regions.

In other seasons, the control experiments also match the results of the CMIP6 experiments, whereas the nudged experiments show a weaker or no response. For example, in boreal summer (Fig. 8.19) the CMIP6 experiments and Coupled Control experiments show a northward shift of the Atlantic ITCZ, a wetter Caribbean Sea and Indian Oceans and a drier eastern Pacific. The nudged experiments are in reasonable agreement in the Indian Ocean, indicating wetter conditions during QBOW than E. Similarly, the effects over the Indian Ocean in SON found for the CMIP6 experiments in section 7.3, are also seen in the Coupled Control experiments, but not in the nudged experiments (not shown).

The results of the precipitation response agree with the previous results that analysed the SST differences. There is no evidence that the nudged experiments result in a stronger surface response to the phase of the QBO, even though the UTLS temperature variability associated with the QBO has been increased and improved in the nudged experiments. The

next section examines changes to the mean state and variability of the tropical circulation in the nudged experiments, in order to explain the precipitation and SST responses.

### Tropical circulation response and the IOD

In the previous section, the variability of the tropical circulation in the atmosphere-only experiments was found to be dominated by the SST forcing. However, the mean state of the upper-level branch of the Walker circulation was slightly different in the AMIP Nudged experiments compared to the Control. To understand whether similar changes to the mean state or variability of the tropical circulation are observed in the coupled experiments, Figures 8.20 and 8.21 show the impact of nudging on the mean state and variability of the Hadley and Walker circulations, respectively.

The nudging affects the mean state of zonal wind in the stratosphere (Figure 8.20) as expected but also the meridional streamfunction in the troposphere in JJA. Significant changes in the tropical UTLS streamfunction are observed in both seasons, and in DJF changes to the vertical velocity in the tropics suggest a strengthening of the Hadley cell when nudging is applied but very small changes are observed in JJA.

The difference between QBO W-E in the tropospheric state of the Hadley cell in both seasons is considerably different between Nudged and Control experiments (Figs. 8.20c-f). In DJF, the Nudged ensemble-mean shows anomalous descent over the 10°N latitude band and significantly higher values of the streamfunction at the equator extending into the lower troposphere. Similarly, the zonal wind in this season shows a positive anomaly extending as far down as 500 hPa at 20-30°N, indicative of changes to the sub-tropical jet position and strength, documented previously (e.g. Garfinkel and Hartmann, 2010).

The Nudged experiments show stronger zonal wind anomalies in the equatorial stratosphere in both seasons. However, the strengthening of the northern hemisphere subtropical jet during QBO W compared to QBO E, reported in (Garfinkel and Hartmann, 2010) is only found in the Control experiments and not in the nudged experiments. Similarly, the differences in the streamfunction and vertical velocity in the nudged experiments appear opposite to that of the Control experiments in DJF. The results for JJA are very similar; the nudging results in slightly bigger differences to the control experiments in the stratosphere

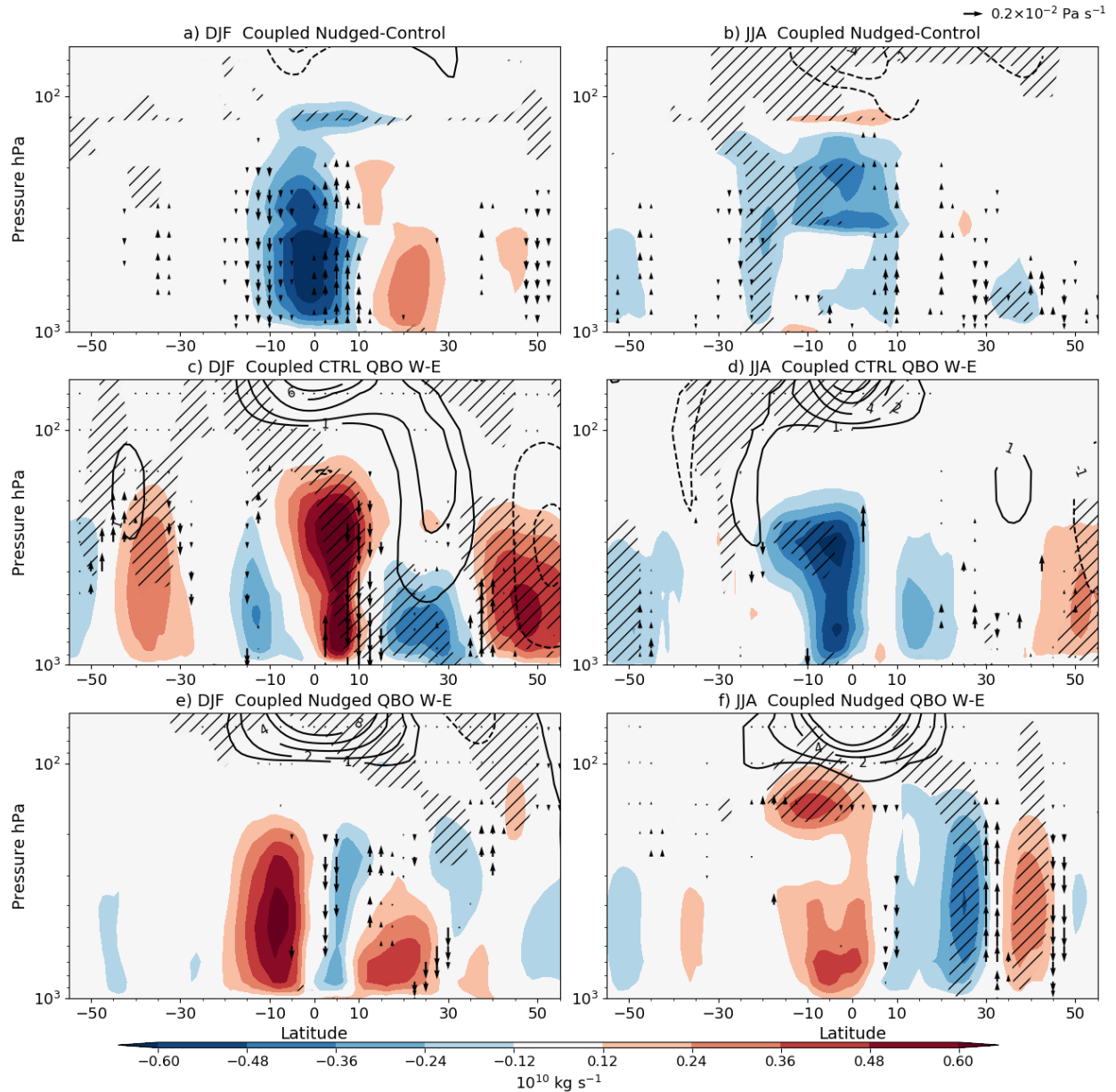


**Figure 8.20:** Hadley circulation differences in meridional mass streamfunction (shading), zonal wind (contours) and vertical velocity (vectors). (a, b) show the seasonal mean differences between Nudged and Control coupled experiments in (a) DJF and (b) JJA. (c-f) show the QBO W-E differences for the (c-d) Control and (e-f) Nudged experiments for (c,e) DJF and (d,f) JJA. In all panels, hatching denotes significant differences in the streamfunction to the 95% confidence level according to the bootstrapping method, whereas for the zonal wind and omega, only significant differences are shown.

but weaker responses in the upper-level troposphere in the subtropics. These results suggest that the process through which the QBO influences the subtropical jets is being affected by the nudging such that the response is weakened or eliminated when the nudging is applied.

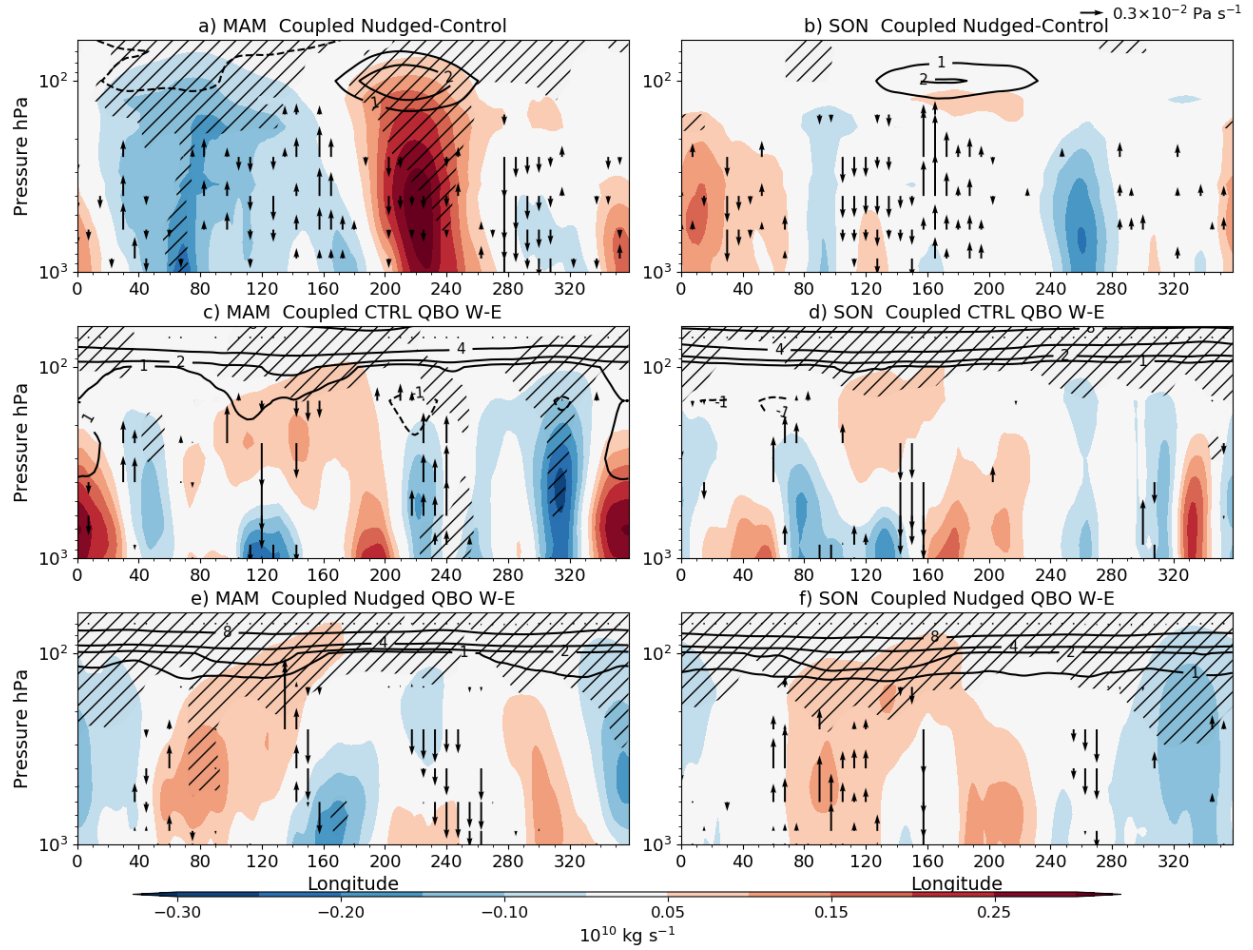


**Figure 8.21:** Walker circulation differences in zonal streamfunction (shading), zonal wind (contours) and vertical velocity (vectors). (a, b) show the seasonal mean differences between Nudged and Control coupled experiments in (a) MAM and (b) SON. (c-f) show the QBO W-E differences for the (c-d) Control ensemble-mean and (e-f) Nudged ensemble-mean for (c,e) MAM and (d,f) SON. In all panels, hatching denotes significant differences in the streamfunction to the 95% confidence level according to the bootstrapping method, whereas for the zonal wind and omega, only significant differences are shown.

The mean Walker circulation is also affected by the nudging (Fig. 8.21a-b). As in the AMIP experiments, the upper-level zonal wind and streamfunction is modified by the nudging, but in the coupled experiments significant differences are also observed in the lower troposphere over the Indian Ocean and the Eastern Pacific. In the UTLS region above the Indian and Pacific Oceans, the nudging is forcing the zonal wind towards ERA5, reducing the biases in the model in specific longitudes (see e.g. Figure 4.13). In other words, not only biases in the variability of the zonal winds in the lower stratosphere are alleviated by the nudging but also the mean state of the upper-level branch of the Walker

circulation. However, the latter may also mean that the variability of the Walker circulation is overconstrained when nudging is applied.

The response of the Walker circulation to the QBO is different in the nudged versus control experiments (Fig. 8.21c-f). In MAM, the QBO W-E differences in the control ensemble-mean suggest a weaker state of the Walker circulation or an El Niño-like pattern with anomalous ascent in the Eastern Pacific under QBO W compared to QBO E whereas the nudged simulations show the opposite. In turn, in SON, while the control experiments in the QBO W-E differences show ascending anomalies in the western Indian Ocean, the nudged experiments show ascending anomalies over the eastern Indian Ocean.

Results in Chapter 7 demonstrated that in the CMIP6 pre-industrial control experiments a statistically significant relationship is found between the IOD and ENSO, and the QBO (Fig. 7.13). Positive events of the IOD and ENSO are more commonly found during QBOW than E, and a convective precipitation index of the IOD and the SST EN3.4 index are also positive during QBOW and negative during QBOE. Figure 8.22 revisits these relationships in the coupled experiments.

The mean IOD index is positive during QBOW and negative during QBOE in the Coupled Control ensemble in boreal fall and early winter (Fig. 8.22a), in agreement with results from the CMIP6 experiments. In contrast, the mean IOD index is close to zero in the Coupled Nudged ensemble without any clear relationship between the index and the QBO phase in any month (Fig. 8.22b). These results suggest that no consistent relationship is found across the six ensemble members when nudging was applied in the simulation. However, these results may simple be due to sampling of the ocean-atmosphere state used for the nudged experiments, in other words, possibly due to decadal variability in the GC3.1 configuration.

For that reason, the CMIP6 GC3 N96-pi is used to investigate whether the results of the Nudged and Control experiments are also seen in periods of similar length in that long 500 yr simulation. While this comparison is not perfect due to differences in ocean resolution and forcing, the model setup and parametrisations, and atmospheric resolution is otherwise the same between GC3 N96-pi and these experiments. The simulation is repeatedly sampled at random for 35 yr continuous periods, and the SON IOD index is computed each time to construct a probability distribution.

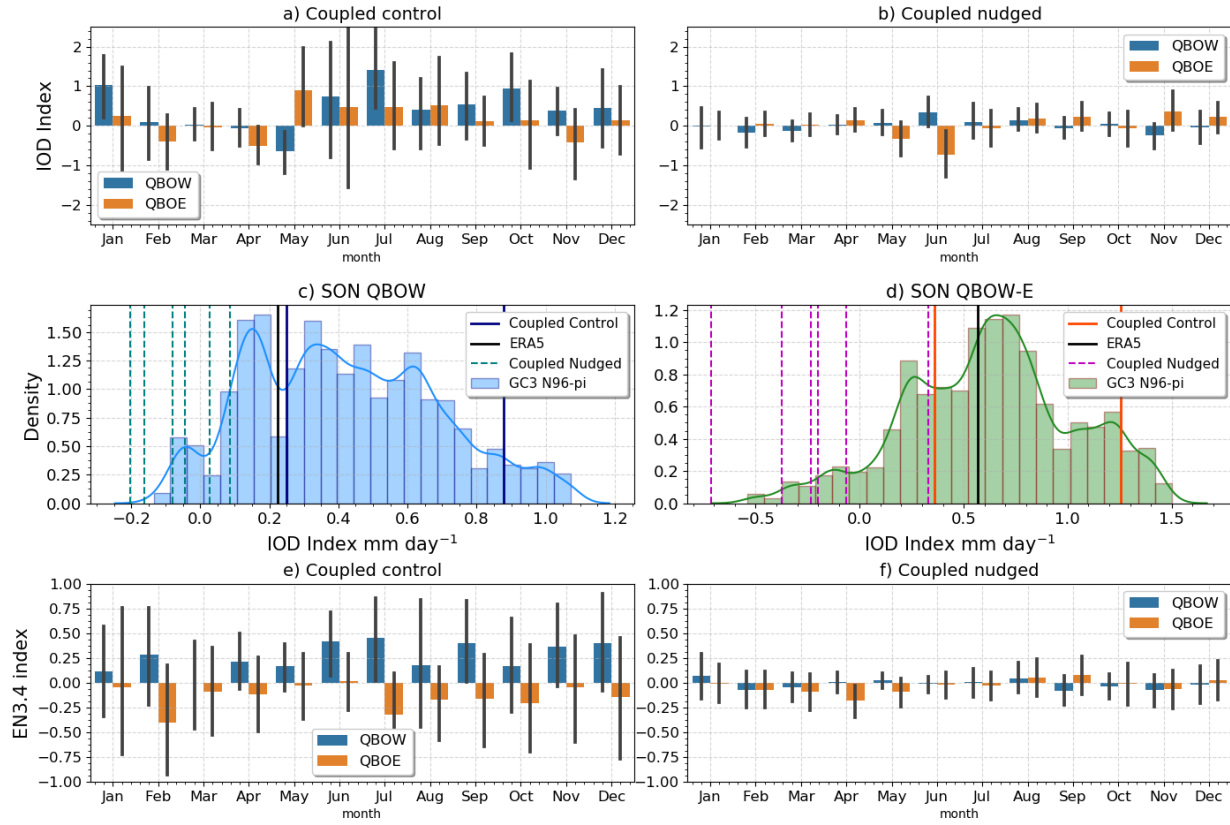


**Figure 8.22:** (a, b) Monthly-mean convective precipitation IOD index [ $\text{mm day}^{-1}$ ] in coupled (a) control and (b) nudged ensemble-means separated by QBO phase. (c, d) Probability density functions (PDFs) of the IOD convective precipitation index for (c) the mean SON during QBOW months and (d) the SON difference between QBO W-E. The PDF is obtained from the 500 yrs of the GC3 N96-pi by bootstrapping 10,000 times into 35-yr periods and obtaining the averages and differences in each subsample. The mean indices for the Coupled Control and Nudged experiments, as well as for ERA5 are also shown. (e, f) Monthly-mean EN3.4 index [K] in the ensemble mean (e) Coupled control and (f) Coupled Nudged simulations separated by QBO phase.

Figure 8.22c shows that the IOD index during QBOW in GC3 N96-pi is more frequently positive, as shown in the previous section, but in some 35-yr periods a negative mean index during QBOW can be observed in this simulation. The two Coupled Control simulations and ERA5 show a positive mean IOD index during QBOW whereas four out of the six Coupled Nudged simulations show a negative index.

Chapter 7 showed that in ERA5 and the three pre-industrial control experiments of the MOHC, positive IOD indices and events are more frequent during QBO W, and the opposite is true for QBOE. Figure 8.22d shows that the difference in the IOD index during SON between the two QBO phases is most frequently positive in GC3 N96-pi. Results from ERA5

and the two Coupled Control simulations also show a positive difference of  $0.6 \text{ mm day}^{-1}$  for the reanalysis and up to  $1.3 \text{ mm day}^{-1}$  for one of the control simulations. In contrast, the nudged experiments are found to the left of the mean of the PDF of GC3 N96-pi. These results indicate that the QBO W-E response in the IOD in the nudged experiments is weaker response and of a different sign compared to the results in ERA5, the pre-industrial control experiments of CMIP6, and the two Coupled Control experiments used in this chapter.

Finally, the ENSO index is found to be positive in the Control experiments, as in the MOHC CMIP6 experiments and in ERA5, but no robust relationship is found in the Nudged experiments. As with the CMIP6 experiments, the Coupled Control EN3.4 index is positive during QBOW and negative during QBOE throughout most of the year. However, there seems to be no relation between the QBO and the EN3.4 index in the nudged experiments. Overall, these results suggest that the relationships between the QBO and the IOD and ENSO observed in the CMIP6 or Control experiments are not found in the Nudged experiments, which show little-to-no relationship between these two indices and the QBO phase.

## 8.4 Summary and discussion

Tropical teleconnections associated with the QBO are difficult to understand in observations due to the relatively large observational uncertainty and the influence of ENSO. In models, biases in the QBO also complicate the investigation of tropical circulation and the surface response to the QBO, largely because the key aspects of the QBO that are hypothesized to be influential for stratospheric-tropospheric coupling in the tropics are poorly represented by most models. This chapter investigates the influence of the QBO over tropical climate through nudging experiments using the MOHC UM which aim to improve the representation of the QBO in the lower stratosphere while also removing any possible influence of the troposphere on the QBO.

The nudging technique results in simulations that exhibit a more realistic representation of the variability of the QBO winds and temperature in the lower stratosphere. In other words, the nudging experiments simulate a stronger response of the UTLS temperature to the QBO. However, in the atmosphere-only setup, the nudging does not modify the

variability of precipitation and OLR as the SST variability imposed dominates. Sensitivity tests with the imposed SSTs shifted by one year demonstrated that the QBO response requires the presence of the correct SSTs.

In the coupled experiments, the control simulations largely agree with the results found in the first part of the chapter using the CMIP6 versions of the model (as expected). However, in the nudged experiments, the tropical SSTs and precipitation show no consistent difference between the QBO phases across the ensemble-mean. Further evidence that analyses the circulation response and on the IOD and ENSO indices confirms that there is no indication that the nudging has made the response to the QBO stronger, or indeed closer to the observed response. In fact, the imposed nudging appears to have disrupted the mechanism that causes the QBO influence at the surface in equatorial latitudes.

One explanation for the nudged results may be that the static stability mechanism, the most cited mechanism in the literature (Collimore et al., 2003; Liess and Geller, 2012; Nie and Sobel, 2015; Gray et al., 2018; Lee and Klingaman, 2018), may not be the dominant factor that relates the QBO to the tropical surface. Specifically, in ERA5, the temperature signal becomes very small at levels lower than 125 hPa, and the 1 K difference at 100 hPa may not be large enough to modify the static stability of the whole convective profile in a significant manner.

An alternative hypothesis is that by nudging we have modified the mean state of the Walker circulation, as was demonstrated in this chapter. Therefore, the teleconnections operating through the Walker circulation simulated by the model become different in the nudged experiments, either because of the relatively minor mean-state change or because Walker circulation-QBO feedbacks have been disrupted by the relaxation. Note that the nudging was only applied to the zonal winds above 90 hPa, so while the zonal winds of the QBO and upper arm of the Walker circulation may be consistent, the meridional and vertical winds in the troposphere are unconstrained.

Another explanation could be that the relationships found in the free-running versions of the model are not due to a causal influence from the QBO downward (top-down) but rather a result of the influence of tropical convection on the phase of the QBO. Studies (e.g. Schirber, 2015; Christiansen et al., 2016) have shown that the tropical wave activity,

largely modulated by ENSO, can influence the descent rate and season of phase change of the QBO. Perhaps then, the ENSO-QBO relationship found in the CMIP6 models is lost in the nudged experiments because the forcing of ENSO cannot influence the QBO.

Future work could improve from this chapter in several ways. Firstly, instead of using a nudging scheme, which is not ideal since it does not target and improve the physical mechanisms, an improvement of the representation of tropical waves associated with deep convection would be better and simultaneously improve the representation of the QBO characteristics as well the teleconnections. One such example is seen in Serva et al. (submitted) which compares simulations with different gravity wave schemes resulting in different properties of the QBO but also precipitation responses in the tropics.

Secondly, the nudging was applied in a relatively coarse resolution configuration (N96) but the results may be different in a medium-resolution (N216) configuration due to the improvement in the tropospheric dynamics that was found in Chapter 4. Additionally, the relaxation in this chapter was done at all grid-points, due to model constraints, however, other types of nudging have been applied, for example by Martin et al. (2021), so that only the zonal mean (zonal wavenumber of zero) is nudged, allowing the wave disturbances (higher wavenumbers) to freely evolve. In this way, the wave disturbances in the lower stratosphere would be more consistent with the wave disturbances generated in the troposphere. Nudging in a zonal-mean sense using a model that can internally generate a reasonable QBO could provide more answers to some of the results in this chapter.

# 9

## Conclusions

This chapter summarises the main findings and conclusions of this thesis, discusses the limitations of this research and potential future work.

### 9.1 Summary

**Biases in the dynamics of the American monsoon:** Assessment of GCM biases in CMIP cohorts is seldom done with emphasis on biases relevant for the monsoons in the Americas. For this reason, less is known about the relationship between large and regional-scale biases for the AMS region compared to other monsoons. The first results chapter aims to provide a detailed account of the biases relevant for American monsoons in the CMIP6 MOHC simulations of UKESM1 and HadGEM3. The choice of simulations allowed to compare the effect of historical forcing, horizontal resolution, SST biases and the treatment of Earth System processes for the representation of the dynamics of the monsoon. A key bias diagnosed in Chapter 4 is the overestimation of precipitation in the boreal summer ITCZ in the East Pacific Ocean. Similarly, the position of the austral summer Atlantic ITCZ is biased southward in the coupled experiments, leading to biases in the dynamics of the South American monsoon. This bias is reduced in the atmosphere-only experiments suggesting a key role played by equatorial Atlantic SST biases for the representation of precipitation over land and in the ITCZ region. The dynamics and seasonality of the North American monsoon

and MSD regions are relatively better represented than for the South American monsoon. The Earth System processes represented by UKESM1 do not considerably improve the representation of the monsoon compared to HadGEM3. However, increasing the horizontal resolution improves a number of biases in the large-scale dynamics and monsoon rainfall. This chapter finds that the MOHC models are able to simulate a bimodal signal in the seasonal cycle of precipitation, known as the Mid-summer drought, as well as relationships between the stratospheric QBO and ENSO teleconnections in the tropics.

**A portable method to diagnose monsoon timings:** Existing methods used to separate the timings in the seasonal cycle in a monsoon are usually tailored to a dataset, which complicates comparisons of multiple datasets or simulations in which the seasonal cycle or climatological precipitation is non-stationary. A wavelet transform method is developed using the Haar wavelet aiming to diagnose onset and retreat as sharp or abrupt changes to the signal of precipitation. The results obtained using the WT method are comparable to other methodologies and the portability of the method is illustrated using observational datasets, reanalysis and climate model output. Results show that the WT method reasonably capture the mean dates of onset and retreat as well as changes in the meteorological conditions associated with the monsoons in India and North America compared to existing methodologies. Furthermore, the method can also separate the timings of a bimodal signal by finding the dates where the drier period begins and ends. The diagnosis of the timings of the MSD simulated by the MOHC simulations using this methodology show similar results to observations, indicating a good representation of the intricate seasonal cycle of precipitation in the MSD region by these models.

**A limited role for SST-cloud-radiative feedbacks in the Mid-summer drought precipitation:** Several theories exist that explain the occurrence of a bimodal signal of precipitation in Central America, southern Mexico and the Caribbean. The most cited hypothesis suggests that a feedback mechanism between the East Pacific SSTs and cloud-radiative processes is the cause for the two-peaks and trough in the seasonal cycle of precipitation. A relatively more recent study suggests that the amount of solar radiation

reaching the surface, driven by the solar declination angle crossing these latitudes twice, is the leading mechanism. Chapter 6 uses the WT method to separate the timings of the seasonal cycle and investigate more closely these two hypotheses in the CMIP6 MOHC simulations and in ERA5. No evidence is found that the East Pacific SST variability drives the precipitation, as expected by the first mechanism, or that the absorbed solar radiation is the driving mechanism, as suggested in the second hypothesis. Rather, the results suggest that absorbed solar radiation by the surface covaries with precipitation and cloudiness, and that East Pacific SSTs do not follow the predictions of the first theory. The conclusion of this analysis is that the observed interannual variability or the differences in the representation of the MSD in the simulations cannot be explained through the arguments of these two mechanisms, suggesting other factors may be more important for the seasonality of rainfall in the region.

**The role of moisture transport for precipitation in the MSD region:** The horizontal moisture transport occurring in the Caribbean is found to explain some aspects of the MSD in the CMIP6 MOHC simulations and in reanalysis. The vertically integrated moisture transport and total water content decrease considerably from the period of the first peak of rainfall to the drier MSD period, and similarly increase in late summer during the second wet period in both simulations and ERA5. The moisture transport and total water content changes are explained to a certain extent by the seasonality in the CLLJ, i.e., the low-level zonal flow in the Caribbean. The CLLJ variability skilfully explains the precipitation increases during the transition from the MSD period to the second peak period. However, the magnitude of the precipitation decrease in early summer, from the first peak to drier MSD periods is not as well explained by the CLLJ as it is by the integrated moisture transport.

**The moist static energy budget provides useful insight to the MSD problem:** The moist static energy (MSE) budget framework is a useful technique to investigate physical processes associated with tropical precipitation. The MSE budget is used in Chapter 6 to investigate how the MSE changes in the MSD region in the simulations and in the reanalysis and how the budget terms could relate to variations in precipitation. A strong relationship is found between the vertical advection term of the budget and precipitation,

indicative of the relationship between vertical velocity and precipitation in the tropics. The horizontal advection of MSE also varies notably between the wet and dry periods, however, there was little evidence to indicate a direct link between the horizontal advection term and precipitation changes. Both models and reanalysis suggest a limited role for surface fluxes in the variability of precipitation, although considerable biases in the surface energy budget of the models are apparent from this analysis. In short, the MSE budget framework may be useful for future work, albeit some improvements to the computation of the budget which are described in the following section.

**The tropical route of the QBO teleconnections in a GCM:** An investigation of the tropical route of QBO teleconnections in the MOHC models was done in the last chapter of this thesis. In the long pre-industrial control experiments of CMIP6, several responses that had previously been reported in observational works were confirmed, for example, the southward shift of the East Pacific ITCZ during QBOW compared to QBOE. The main findings of this analysis were robust shifts in the position of the Atlantic and Pacific ITCZs, as well as wetter conditions in the Caribbean Sea and Indian Oceans during QBOW compared to QBOE. Most of these impacts were found to be seasonally varying and the season of strongest influence varied from model to model. A previously unknown relationship between the QBO phase and the Indian Ocean, characterized by an IOD-like response, was found to be robust to internal variability of the simulations. This response is characterised by a zonal dipole characterised by wetter conditions in the western Indian Ocean and drier conditions in the eastern Indian Ocean are more frequently found during QBOW than during QBOE. Similarly, El Niño events are more frequent during QBOW and La Niña events during QBOE in observations and in these simulations. Finally, changes to the strength of the Walker circulation were also diagnosed to be robust; this response is characterised by a weaker overturning during QBOW than during QBOE. The results in this chapter suggest an intricate link between the ITCZs, the IOD, ENSO and the Walker circulation, and the phase of the QBO.

**QBO tropical teleconnections in a model with a nudged stratosphere:** To test the direction of causality in the relationships found in the pre-industrial control experiments, as well as to alleviate biases with the representation of the QBO within these models, a number of experiments are described in which the zonal wind in the equatorial stratosphere were relaxed towards a reanalysis. Atmosphere-only and coupled experiments were performed with and without nudging. The nudged experiments show a limited sensitivity of the tropical circulation and convective activity to the phase of the imposed QBO. Most of the relationships found in the CMIP6 experiments are also observed in the Control experiments which suggests that the nudging has damped or removed the processes that cause these impacts to occur in the simulations with an internally generated QBO. In the nudged experiments, the mean state of the Walker circulation is driven closer to observations by the nudging, alleviating biases in the upper-level branch of the circulation. Yet, the variability in the Walker circulation associated with the QBO of the nudged experiments is weaker and of a different sign than in the control experiments. In short, the nudged experiments show a stronger temperature variance in the UTLS in response to the QBO shear, yet the tropical teleconnections are not stronger than in the control experiments.

## 9.2 Limitations and future work

The investigations presented in this thesis leave a number of open questions that require future work. The main limitations of each part of the research in this thesis and a discussion on how future research could address these limitations is provided below.

**Analysis of observational and model trends in monsoon timings:** Chapter 5 shows that the WT method can be used in any observational or model data and for any monsoon so that the advantage of the method is portability. In contrast, one limitation of the method is that the WT cannot be computed without in a real-time scenario, so the method is only useful for post-hoc processing. This limitation is due to the way the WT is computed, which requires the availability of data several months past the date of monsoon onset or retreat to compute the WT. Nevertheless, due to the advantages of the method, one further

application of the method would be to diagnose observed and simulated trends in the onset and retreat dates in the global monsoon. Several regional studies exist that characterise trends in the seasonality of precipitation but due to the nature of the WT method, this diagnosis could be done across the CMIP6 chort of models, the existing reanalysis datasets and all the gridded precipitation datasets available. This research could provide a more comprehensive analysis of if and how the seasonality of the global monsoon is changing and whether these changes are also seen in CMIP6 models.

**The diagnosis of cloud-radiative effects and other quantities from reanalysis:** Chapter 6 uses ERA5 data to diagnose several quantities such as cloud-radiative effects that are known to be biased in reanalyses compared to satellite products or other observational datasets. For example, surface fluxes over land and ocean in ERA5 are also likely to depart from observations. Throughout the chapter, ERA5 data is used to compare with the CMIP6 models, yet the reanalysis does not assimilate and rather simulates some of the diagnostics used in the chapter. ERA5 data is used because the precipitation within the reanalysis is also simulated and ought to be physically consistent with the other diagnostics. In this way, ERA5 can only be used as a best-model and not as representing the observed processes associated with the MSD. Further work could use observational products to validate the results found in the chapter. In particular, a characterisation of the seasonality of CRE in observational datasets could provide insight to how cloud-radiative feedbacks vary temporally in the rainy season.

**A full moist-static energy budget:** An accurate computatiton of the MSE budget is difficult in reanalysis and model data because high temporal resolution of all the terms is required for the budget to close. This limitation is typically addressed by computing the budget terms online within a model. An experiment using the MOHC models that computes the MSE with a high frequency would better show how the budget terms vary at each grid-point with the evolution of the rainy season. Similarly, the full ERA5 data was not used to compute the budget. A daily-mean and a coarser horizontal resolution than available were used to compute all the budget terms due to time limitations, which led to

the MSE budget calculation not closing exactly. A more detailed calculation could provide a more precise quantification of how the budget variations relate to precipitation. Future work could also investigate how the shape of the vertical profile of the vertical velocity varies with the stages of the MSD in the East Pacific and over land. The shape of this profile is known to determine the vertical advection of MSE and gives relevant information of the state of the convective profile, and, therefore, evaluating temporal changes to the shape of the vertical velocity could also point to relevant processes that could affect the MSD.

**QBO teleconnections in a single model:** Chapter 7 diagnoses the response of the tropical circulation and precipitation to the phase of the QBO in the MOHC CMIP6 simulations. These simulations are all from the same modelling centre and the models are all based on the UM, i.e., these simulations use the same dynamical core and share many of their parametrisation schemes and large-scale circulation biases. The teleconnections diagnosed in that chapter could also be analysed in different models of CMIP6 and differences in the properties of the simulated QBO and surface response amongst the models could point to processes that link convection and the QBO in this cohort of models. Similarly, experiments using the same model but varying the type of convective or gravity-wave schemes could also highlight which processes are most important to represent connections in the UTLS region, while also pointing to routes for model improvement.

**Nudging the MOHC UM:** The relaxation experiments described in the second part of Chapter 7 suggest that the nudging protocol reduced the connection between the tropical stratosphere and troposphere. Several reasons could explain these results but only future work can definitively provide an answer. Firstly, several types of nudging are possible with a GCM, for example, nudging can be done through a relaxation of the zonal-mean field and not at all grid-points. This type of relaxation would allow waves simulated in the troposphere to propagate to the stratosphere whereas the nudging implemented in this thesis would constrain the wave propagation from the troposphere. Therefore, relaxation experiments in a model that (1) has a good representation of the QBO and (2) has the capability of performing a zonal-mean nudging could be better suited to diagnose the directions of causality of the

relationships between the QBO and tropical climate found in this chapter.

Secondly, another limitation of the nudging protocol in Chapter 7 is that the mean state of the Walker circulation was modified slightly by nudging the zonal wind in the stratosphere. Therefore, a nudging protocol that replicates the observed QBO variability in the circulation and temperature fields in the stratosphere without modifying the mean-state of the tropical circulation could be better suited to diagnose QBO teleconnections in the tropics.

# Bibliography

- Adams, D. K. and Comrie, A. C. (1997), 'The north American monsoon', *Bulletin of the American Meteorological Society* **78**(10), 2197–2214.
- Adams, D. K., Gutman, S. I., Holub, K. L. and Pereira, D. S. (2013), 'GNSS observations of deep convective time scales in the Amazon', *Geophysical Research Letters* **40**(11), 2818–2823.  
**URL:** <https://agupubs.onlinelibrary.wiley.com/doi/abs/10.1002/grl.50573>
- Addison, P. S. (2017), *The illustrated wavelet transform handbook: introductory theory and applications in science, engineering, medicine and finance*, CRC press.
- Adler, R. F., Huffman, G. J., Chang, A., Ferraro, R., Xie, P.-P., Janowiak, J., Rudolf, B., Schneider, U., Curtis, S., Bolvin, D., Gruber, A., Susskind, J., Arkin, P. and Nelkin, E. (2003), 'The version-2 global precipitation climatology project (GPCP) monthly precipitation analysis (1979–present)', *Journal of hydrometeorology* **4**(6), 1147–1167.
- Allan, R. P. (2011), 'Combining satellite data and models to estimate cloud radiative effect at the surface and in the atmosphere', *Meteorological Applications* **18**(3), 324–333.
- Allen, T. L. and Mapes, B. E. (2017), 'The late spring Caribbean rain-belt: climatology and dynamics', *International Journal of Climatology* **37**(15), 4981–4993.
- Amador, J. A. (2008), 'The intra-americas sea low-level jet: Overview and future research', *Annals of the New York Academy of Sciences* **1146**(1), 153–188.
- Anderson, T. G., Anchukaitis, K. J., Pons, D. and Taylor, M. (2019), 'Multiscale trends and precipitation extremes in the Central American Midsummer Drought', *Environmental Research Letters* **14**(12), 124016.
- Andrews, D. G., Holton, J. R. and Leovy, C. B. (1987), *Middle atmosphere dynamics*, Vol. 40, Academic press.
- Andrews, M. B., Knight, J. R., Scaife, A. A., Lu, Y., Wu, T., Gray, L. J. and Schenzinger, V. (2019b), 'Observed and simulated teleconnections between the stratospheric quasi-biennial oscillation and northern hemisphere winter atmospheric circulation', *Journal of Geophysical Research: Atmospheres* **124**(3), 1219–1232.
- Andrews, M., Ridley, J., Wood, R., Andrews, T., Blockley, E., Booth, B., Burke, E., Dittus, A., Florek, P., Gray, L., Haddad, S., Hardiman, S., Hermanson, L., Hodson, D., Hogan, E., Jones, G., Knight, J., Kuhlbrodt, T., Misios, S. and Sutton, R. (2020), 'Historical simulations with HadGEM3-GC3.1 for CMIP6', *Journal of Advances in Modeling Earth Systems* .
- Andrews, T., Andrews, M. B., Bodas-Salcedo, A., Jones, G. S., Kuhlbrodt, T., Manners, J.,

- Menary, M. B., Ridley, J., Ringer, M. A., Sellar, A. A., Senior, C. A. and Tang, Y. (2019a), 'Forcings, feedbacks, and climate sensitivity in HadGEM3-GC3. 1 and UKESM1', *Journal of Advances in Modeling Earth Systems* **11**(12), 4377–4394.
- Angeles, M. E., González, J. E., Ramírez-Beltrán, N. D., Tepley, C. A. and Comarazamy, D. E. (2010), 'Origins of the Caribbean rainfall bimodal behavior', *Journal of Geophysical Research: Atmospheres* **115**(D11).
- Annamalai, H. (2020), 'ENSO precipitation anomalies along the equatorial Pacific: Moist static energy framework diagnostics', *Journal of Climate* **33**(21), 9103–9127.
- Anstey, J. A. and Shepherd, T. G. (2014), 'High-latitude influence of the quasi-biennial oscillation', *Quarterly Journal of the Royal Meteorological Society* **140**(678), 1–21.
- Anstey, J. A., Simpson, I. R., Richter, J. H., Naoe, H., Taguchi, M., Serva, F., Gray, L. J., Butchart, N., Hamilton, K., Osprey, S. et al. (2021), 'Teleconnections of the Quasi-Biennial Oscillation in a multi-model ensemble of QBO-resolving models', *Quarterly Journal of the Royal Meteorological Society*.
- Arias, P. A., Fu, R. and Mo, K. C. (2012), 'Decadal Variation of Rainfall Seasonality in the North American Monsoon Region and Its Potential Causes', *Journal of Climate* **25**(12), 4258–4274.
- Arritt, R. W., Goering, D. C. and Anderson, C. J. (2000), 'The North American monsoon system in the Hadley Centre coupled ocean-atmosphere GCM', *Geophysical Research Letters* **27**(4), 565–568.
- Ashok, K. and Yamagata, T. (2009), 'The El Niño with a difference', *Nature* **461**(7263), 481–484.
- Back, L. and Bretherton, C. (2006), 'Geographic variability in the export of moist static energy and vertical motion profiles in the tropical Pacific', *Geophysical research letters* **33**(17).
- Baldwin, M., Gray, L., Dunkerton, T., Hamilton, K., Haynes, P., Randel, W., Holton, J., Alexander, M., Hirota, I., Horinouchi, T. et al. (2001), 'The quasi-biennial oscillation', *Reviews of Geophysics* **39**(2), 179–229.
- Barlow, M., Nigam, S. and Berbery, E. H. (1998), 'Evolution of the North American monsoon system', *Journal of Climate* **11**(9), 2238–2257.
- Bayr, T., Domeisen, D. I. and Wengel, C. (2019), 'The effect of the equatorial Pacific cold SST bias on simulated ENSO teleconnections to the North Pacific and California', *Climate Dynamics* **53**(7), 3771–3789.
- Bayr, T., Dommelen, D., Martin, T. and Power, S. B. (2014), 'The eastward shift of the Walker Circulation in response to global warming and its relationship to ENSO variability', *Climate dynamics* **43**(9-10), 2747–2763.
- Bechtold, P., Semane, N., Lopez, P., Chaboureau, J.-P., Beljaars, A. and Bormann, N. (2014), 'Representing equilibrium and nonequilibrium convection in large-scale models', *Journal of Atmospheric Sciences* **71**(2), 734–753.
- Becker, A., Finger, P., Meyer-Christoffer, A., Rudolf, B. and Ziese, M. (2011), 'GPCC full data reanalysis version 6.0 at 1.0: monthly land-surface precipitation from rain-gauges built on

- GTS-based and historic data', *Global Precipitation Climatology Centre (GPCC): Berlin, Germany*.
- Bellucci, A., Gualdi, S. and Navarra, A. (2010), 'The double-ITCZ syndrome in coupled general circulation models: The role of large-scale vertical circulation regimes', *Journal of Climate* **23**(5), 1127–1145.
- Biasutti, M., Voigt, A., Boos, W. R., Braconnot, P., Hargreaves, J. C., Harrison, S. P., Kang, S. M., Mapes, B. E., Scheff, J., Schumacher, C. et al. (2018), 'Global energetics and local physics as drivers of past, present and future monsoons', *Nature Geoscience* **11**(6), 392–400.
- Bischoff, T. and Schneider, T. (2016), 'The Equatorial Energy Balance, ITCZ Position, and Double-ITCZ Bifurcations', *Journal of Climate* **29**(8), 2997–3013.
- Bjerknes, J. (1969), 'Atmospheric teleconnections from the equatorial Pacific', *Mon. Wea. Rev* **97**(3), 163–172.
- Blanford, H. F. (1886), 'Rainfall of india', *Monsoon Monograph – India Meteorological Department* **3**(658).
- Bombardi, R. J. and Carvalho, L. M. (2011), 'The South Atlantic dipole and variations in the characteristics of the South American Monsoon in the WCRP-CMIP3 multi-model simulations', *Climate Dynamics* **36**(11-12), 2091–2102.
- Bombardi, R. J., Moron, V. and Goodnight, J. S. (2020), 'Detection, variability, and predictability of monsoon onset and withdrawal dates: A review', *International Journal of Climatology* **40**(2), 641–667.
- Bony, S., Dufresne, J.-L., Le Treut, H., Morcrette, J.-J. and Senior, C. (2004), 'On dynamic and thermodynamic components of cloud changes', *Climate Dynamics* **22**(2-3), 71–86.
- Boos, W. R. (2015), 'A review of recent progress on Tibet's role in the South Asian monsoon', *CLIVAR Exch* **19**(66), 23–27.
- Boos, W. R. and Korty, R. L. (2016), 'Regional energy budget control of the intertropical convergence zone and application to mid-Holocene rainfall', *Nature Geoscience* **9**(12), 892–897.
- Bordoni, S. and Schneider, T. (2008), 'Monsoons as eddy-mediated regime transitions of the tropical overturning circulation', *Nature Geoscience* **1**(8), 515–519.
- Brooks, I. M. (2003), 'Finding boundary layer top: Application of a wavelet covariance transform to lidar backscatter profiles', *Journal of Atmospheric and Oceanic Technology* **20**(8), 1092–1105.
- Bushell, A. C., Anstey, J. A., Butchart, N., Kawatani, Y., Osprey, S. M., Richter, J. H., Serva, F., Braesicke, P., Cagnazzo, C., Chen, C.-C., Chun, H.-Y., Garcia, R. R., Gray, L. J., Hamilton, K., Kerzenmacher, T., Kim, Y.-H., Lott, F., McLandress, C., Naoe, H., Scinocca, J., Smith, A. K., Stockdale, T. N., Versick, S., Watanabe, S., Yoshida, K. and Yukimoto, S. (2020), 'Evaluation of the Quasi-Biennial Oscillation in global climate models for the SPARC QBO-initiative', *Quarterly Journal of the Royal Meteorological Society* pp. 1–31.
- URL:** <https://rmets.onlinelibrary.wiley.com/doi/abs/10.1002/qj.3765>
- Bussmann, A., Elagib, N. A., Fayyad, M. and Ribbe, L. (2016), 'Sowing date determinants for

- Sahelian rainfed agriculture in the context of agricultural policies and water management', *Land Use Policy* **52**, 316 – 328.
- Byrne, M. P. and Schneider, T. (2016), 'Narrowing of the ITCZ in a warming climate: Physical mechanisms', *Geophysical Research Letters* **43**(21), 11–350.
- Byrne, M. P. and Zanna, L. (2020), 'Radiative effects of clouds and water vapor on an axisymmetric monsoon', *Journal of Climate* **33**(20), 8789–8811.
- C3S (2017), 'ERA5: Fifth generation of ECMWF atmospheric reanalyses of the global climate.', *Copernicus Climate Change Service Climate Data Store (CDS)*. date of access: 18 March 2019, <https://climate.copernicus.eu/climate-reanalysis>.
- Cai, W., McPhaden, M., Grimm, A., Rodrigues, R., Taschetto, A., Garreaud, R., Dewitte, B., Poveda, G., Ham, Y.-G., Santoso, A., Ng, B., Anderson, W., Wang, G., Geng, T., Jo, H., Marengo, J., Alves, L., Osman, M., Li, S. and Vera, C. (2020), 'Climate impacts of the El Niño–Southern Oscillation on South America', *Nature Reviews Earth & Environment* **1**(4), 215–231.
- Cai, W., Wu, L., Lengaigne, M., Li, T., McGregor, S., Kug, J.-S., Yu, J.-Y., Stuecker, M. F., Santoso, A., Li, X., Ham, Y.-G., Chikamoto, Y., Ng, B., McPhaden, M. J., Du, Y., Dommeguet, D., Jia, F., Kajtar, J. B., Keenlyside, N., Lin, X., Luo, J.-J., Martín-Rey, M., Ruprich-Robert, Y., Wang, G., Xie, S.-P., Yang, Y., Kang, S. M., Choi, J.-Y., Gan, B., Kim, G.-I., Kim, C.-E., Kim, S., Kim, J.-H. and Chang, P. (2019), 'Pan-tropical climate interactions', *Science* **363**(6430), eaav4236.
- Camargo, S. J. and Sobel, A. H. (2010), 'Revisiting the influence of the quasi-biennial oscillation on tropical cyclone activity', *Journal of Climate* **23**(21), 5810–5825.
- Caramanica, A., Mesia, L. H., Morales, C. R., Huckleberry, G., Quilter, J. et al. (2020), 'El Niño resilience farming on the north coast of Peru', *Proceedings of the National Academy of Sciences* **117**(39), 24127–24137.
- Carvalho, L. M., Jones, C. and Liebmann, B. (2004), 'The South Atlantic convergence zone: Intensity, form, persistence, and relationships with intraseasonal to interannual activity and extreme rainfall', *Journal of Climate* **17**, 88–108.
- Carvalho, L. M. V., Jones, C., Posadas, A. N. D., Quiroz, R., Bookhagen, B. and Liebmann, B. (2012), 'Precipitation characteristics of the South American Monsoon System derived from multiple datasets', *Journal of Climate* **25**(13), 4600–4620.
- Cavazos, T., Luna-Niño, R., Cerezo-Mota, R., Fuentes-Franco, R., Méndez, M., Pineda Martinez, L. F. and Valenzuela, E. (2020), 'Climatic trends and regional climate models intercomparison over the CORDEX-CAM (Central America, Caribbean, and Mexico) domain', *International Journal of Climatology* **40**(3), 1396–1420.
- Chan, J. C. (1995), 'Tropical cyclone activity in the western North Pacific in relation to the stratospheric quasi-biennial oscillation', *Monthly Weather Review* **123**(8), 2567–2571.
- Chao, W. C. and Chen, B. (2001), 'The origin of monsoons', *Journal of the Atmospheric Sciences*

- 58(22), 3497–3507.
- Chen, J., Wilson, C., Tapley, B., Yang, Z. and Niu, G. (2009), ‘2005 drought event in the Amazon River basin as measured by GRACE and estimated by climate models’, *Journal of Geophysical Research: Solid Earth* **114**(B5).
- Chevuturi, A., Turner, A. G., Woolnough, S. J., Martin, G. M. and MacLachlan, C. (2019), ‘Indian summer monsoon onset forecast skill in the UK Met Office initialized coupled seasonal forecasting system (GloSea5-GC2)’, *Climate dynamics* **52**(11), 6599–6617.
- Chou, C. and Neelin, J. D. (2004), ‘Mechanisms of global warming impacts on regional tropical precipitation’, *Journal of climate* **17**(13), 2688–2701.
- Christensen, H., Berner, J., Coleman, D. R. and Palmer, T. (2017), ‘Stochastic parameterization and El Niño–Southern Oscillation’, *Journal of Climate* **30**(1), 17–38.
- Christiansen, B., Yang, S. and Madsen, M. S. (2016), ‘Do strong warm ENSO events control the phase of the stratospheric QBO?’, *Geophysical Research Letters* **43**(19), 10–489.
- Chuvieco, E., Opazo, S., Sione, W., Valle, H. d., Anaya, J., Bella, C. D., Cruz, I., Manzo, L., López, G., Mari, N., González-Alonso, F., Morelli, F., Setzer, A., Csizsar, I., Kanpandegi, J. A., Bastarrika, A. and Libonati, R. (2008), ‘Global burned-land estimation in Latin-America using MODIS composite data’, *Ecological Applications* **18**(1), 64–79.
- Collimore, C. C., Martin, D. W., Hitchman, M. H., Huesmann, A. and Waliser, D. E. (2003), ‘On the relationship between the QBO and tropical deep convection’, *Journal of climate* **16**(15), 2552–2568.
- Cook, B. I. and Buckley, B. M. (2009), ‘Objective determination of monsoon season onset, withdrawal, and length’, *Journal of Geophysical Research: Atmospheres* **114**(D23).
- Cook, B. and Seager, R. (2013), ‘The response of the North American Monsoon to increased greenhouse gas forcing’, *Journal of Geophysical Research: Atmospheres* **118**(4), 1690–1699.
- Corrales-Suastegui, A., Fuentes-Franco, R. and Pavia, E. G. (2020), ‘The mid-summer drought over Mexico and Central America in the 21st century’, *International Journal of Climatology* **40**(3), 1703–1715.
- Curtis, S. (2002), ‘Interannual variability of the bimodal distribution of summertime rainfall over Central America and tropical storm activity in the far-eastern Pacific’, *Climate Research* **22**, 141–146.
- Curtis, S. and Gamble, D. W. (2008), ‘Regional variations of the Caribbean mid-summer drought’, *Theoretical and Applied Climatology* **94**, 25–34.
- de Sousa, K., Casanoves, F., Sellare, J., Ospina, A., Suchini, J. G., Aguilar, A. and Mercado, L. (2018), ‘How climate awareness influences farmers’ adaptation decisions in Central America?’, *Journal of Rural Studies* **64**, 11–19.
- Densmore, C. R., Sanabria, E. R. and Barrett, B. S. (2019), ‘QBO influence on MJO amplitude over the Maritime Continent: physical mechanisms and seasonality’, *Monthly Weather Review* **147**(1), 389–406.

- Derbyshire, S., Maidens, A., Milton, S., Stratton, R. and Willett, M. (2011), 'Adaptive detrainment in a convective parametrization', *Quarterly Journal of the Royal Meteorological Society* **137**(660), 1856–1871.
- Dilley, M. (1996), 'Synoptic controls on precipitation in the Valley of Oaxaca, Mexico', *International Journal of Climatology: A Journal of the Royal Meteorological Society* **16**(9), 1019–1031.
- Dimdore-Miles, O., Gray, L. and Osprey, S. (2021), 'Origins of multi-decadal variability in sudden stratospheric warmings', *Weather and Climate Dynamics* **2**(1), 205–231.
- Dinku, T., Ruiz, F., Connor, S. J. and Ceccato, P. (2010), 'Validation and intercomparison of satellite rainfall estimates over Colombia', *Journal of Applied Meteorology and Climatology* **49**(5), 1004–1014.
- Domeisen, D. I., Garfinkel, C. I. and Butler, A. H. (2019), 'The teleconnection of El Niño Southern Oscillation to the stratosphere', *Reviews of Geophysics* **57**(1), 5–47.
- Dominguez, F., Kumar, P. and Vivoni, E. R. (2008), 'Precipitation recycling variability and ecoclimatological stability—A study using NARR data. Part II: North American monsoon region', *Journal of Climate* **21**(20), 5187–5203.
- Dommelget, D., Bayr, T. and Frauen, C. (2013), 'Analysis of the non-linearity in the pattern and time evolution of El Niño Southern Oscillation', *Climate Dynamics* **40**(11–12), 2825–2847.
- Donohoe, A., Marshall, J., Ferreira, D. and Mcgee, D. (2013), 'The Relationship between ITCZ Location and Cross-Equatorial Atmospheric Heat Transport: From the Seasonal Cycle to the Last Glacial Maximum', *Journal of Climate* **26**(11), 3597–3618.
- Douglas, M. W., Maddox, R. A., Howard, K. and Reyes, S. (1993), 'The mexican monsoon', *Journal of Climate* **6**(8), 1665–1677.
- Durán-Quesada, A. M., Gimeno, L. and Amador, J. (2017), 'Role of moisture transport for Central American precipitation', *Earth System Dynamics* **8**(1), 147–161.
- Ebdon, R. (1960), 'Notes on the wind flow at 50 mb in tropical and sub-tropical regions in January 1957 and January 1958', *Quarterly Journal of the Royal Meteorological Society* **86**(370), 540–542.
- Emanuel, K. (2007), 'Quasi-equilibrium dynamics of the tropical atmosphere', *The Global Circulation of the Atmosphere* **186**, 218.
- Emanuel, K. A. et al. (1994), *Atmospheric convection*, Oxford University Press on Demand.
- Eyring, V., Bony, S., Meehl, G. A., Senior, C. A., Stevens, B., Stouffer, R. J. and Taylor, K. E. (2016), 'Overview of the Coupled Model Intercomparison Project Phase 6 (CMIP6) experimental design and organization', *Geoscientific Model Development (Online)* **9**.
- Fasullo, J. and Webster, P. (2003), 'A hydrological definition of Indian monsoon onset and withdrawal', *Journal of Climate* **16**(19), 3200–3211.
- Faulk, S., Mitchell, J. and Bordoni, S. (2017), 'Effects of rotation rate and seasonal forcing on the ITCZ extent in planetary atmospheres', *Journal of the Atmospheric Sciences* **74**(3), 665–678.

- Fereday, D., Chadwick, R., Knight, J. and Scaife, A. (2020), 'Tropical Rainfall Linked to Stronger Future ENSO-NAO Teleconnection in CMIP5 Models', *Geophysical Research Letters* **47**(22), e2020GL088664.
- Fisher, R. A. (1992), Statistical methods for research workers, in 'Breakthroughs in statistics', Springer, pp. 66–70.
- Forbes, R. M. and Ahlgrimm, M. (2014), 'On the representation of high-latitude boundary layer mixed-phase cloud in the ECMWF global model', *Monthly Weather Review* **142**(9), 3425–3445.
- Franchito, S. H., Rao, V. B., Vasques, A. C., Santo, C. M. and Conforte, J. C. (2009), 'Validation of TRMM precipitation radar monthly rainfall estimates over Brazil', *Journal of Geophysical Research: Atmospheres* **114**(D2).
- Fritsch, J. and Chappell, C. (1980), 'Numerical prediction of convectively driven mesoscale pressure systems. Part I: convective parameterization', *Journal of Atmospheric Sciences* **37**(8), 1722–1733.
- Fuentes-Franco, R., Coppola, E., Giorgi, F., Pavia, E. G., Diro, G. T. and Graef, F. (2015), 'Inter-annual variability of precipitation over Southern Mexico and Central America and its relationship to sea surface temperature from a set of future projections from CMIP5 GCMs and RegCM4 CORDEX simulations', *Climate Dynamics* **45**(1-2), 425–440.
- Fujiwara, M., Manney, G. L., Gray, L. J. and Wright, J. S. (2021), SPARC Reanalysis Intercomparison Project (S-RIP) Final Report, Technical report, World Climate Research Programme, SPARC Report No. 10. [www.sparc-climate.org/publications/sparc-reports](http://www.sparc-climate.org/publications/sparc-reports).
- Funk, C., Peterson, P., Landsfeld, M., Pedreros, D., Verdin, J., Shukla, S., Husak, G., Rowland, J., Harrison, L., Hoell, A. and Michaelsen, J. (2015), 'The climate hazards infrared precipitation with stations—a new environmental record for monitoring extremes', *Scientific data* **2**, 150066.
- Gadgil, S. (2018), 'The monsoon system: Land–sea breeze or the itcz?', *Journal of Earth System Science* **127**(1), 1.
- Gadgil, S. and Rupa Kumar, K. (2006), *The Asian monsoon — agriculture and economy*, Springer Berlin Heidelberg, Berlin, Heidelberg, pp. 651–683.
- Gamble, D. W., Parnell, D. B. and Curtis, S. (2008), 'Spatial variability of the Caribbean mid-summer drought and relation to north Atlantic high circulation', *International Journal of Climatology* **28**(3), 343–350.
- Gan, M., Kousky, V. and Ropelewski, C. (2004), 'The South America monsoon circulation and its relationship to rainfall over west-central Brazil', *Journal of climate* **17**, 47–66.
- García-Franco, J. L., Osprey, S. and Gray, L. J. (2021), 'A wavelet transform method to determine monsoon onset and retreat from precipitation time-series', *International Journal of Climatology* **41**(11), 5295–5317.
- URL:** <https://rmets.onlinelibrary.wiley.com/doi/abs/10.1002/joc.7130>
- García-Franco, J. L., Gray, L. J. and Osprey, S. (2020), 'The American monsoon system in

- HadGEM3 and UKESM1', *Weather and Climate Dynamics* **1**(2), 349–371.  
**URL:** <https://wcd.copernicus.org/articles/1/349/2020/>
- García-Martínez, I. M. and Bollasina, M. A. (2020), 'Sub-monthly evolution of the Caribbean Low-Level Jet and its relationship with regional precipitation and atmospheric circulation', *Climate Dynamics* pp. 1–18.
- Garcia, S. R. and Kayano, M. T. (2013), 'Some considerations on onset dates of the rainy season in Western-Central Brazil with antisymmetric outgoing longwave radiation relative to the equator', *International Journal of Climatology* **33**(1), 188–198.
- Garfinkel, C. I. and Hartmann, D. (2010), 'Influence of the quasi-biennial oscillation on the North Pacific and El Niño teleconnections', *Journal of Geophysical Research: Atmospheres* **115**(D20).
- Garfinkel, C. I. and Hartmann, D. L. (2011), 'The influence of the quasi-biennial oscillation on the troposphere in winter in a hierarchy of models. Part II: Perpetual winter WACCM runs', *Journal of the Atmospheric Sciences* **68**(9), 2026–2041.
- Geen, R., Bordoni, S., Battisti, D. S. and Hui, K. (2020), 'Monsoons, ITCZs and the Concept of the Global Monsoon', *Reviews of Geophysics* p. e2020RG000700.
- Geen, R., Lambert, F. H. and Vallis, G. K. (2019), 'Processes and Timescales in Onset and Withdrawal of "Aquaplanet Monsoons"', *Journal of the Atmospheric Sciences* **76**(8), 2357–2373.
- Geil, K. L., Serra, Y. L. and Zeng, X. (2013), 'Assessment of CMIP5 model simulations of the North American monsoon system', *Journal of Climate* **26**(22), 8787–8801.
- Giannini, A., Kushnir, Y. and Cane, M. A. (2000), 'Interannual variability of Caribbean rainfall, ENSO, and the Atlantic Ocean', *Journal of Climate* **13**, 297–311.
- Giannini, A., Saravanan, R. and Chang, P. (2004), 'The preconditioning role of tropical Atlantic variability in the development of the ENSO teleconnection: Implications for the prediction of Nordeste rainfall', *Climate Dynamics* **22**, 839–855.
- Gill, A. E. (1980), 'Some simple solutions for heat-induced tropical circulation', *Quarterly Journal of the Royal Meteorological Society* **106**(449), 447–462.
- Giorgetta, M. A., Bengtsson, L. and Arpe, K. (1999), 'An investigation of QBO signals in the east Asian and Indian monsoon in GCM experiments', *Climate dynamics* **15**(6), 435–450.
- Good, P., Chadwick, R., Holloway, C. E., Kennedy, J., Lowe, J. A., Roehrig, R. and Rushley, S. S. (2021), 'High sensitivity of tropical precipitation to local sea surface temperature', *Nature* **589**(7842), 408–414.
- Gray, L., Brown, M., Knight, J., Andrews, M., Lu, H., O'Reilly, C. and Anstey, J. (2020), 'Forecasting extreme stratospheric polar vortex events', *Nature communications* **11**(1), 1–9.
- Gray, L. J., Anstey, J. A., Kawatani, Y., Lu, H., Osprey, S. and Schenzinger, V. (2018), 'Surface impacts of the Quasi Biennial Oscillation', *Atmospheric Chemistry and Physics* **18**(11), 8227–8247.
- Gray, W. M. (1984), 'Atlantic seasonal hurricane frequency. Part I: El Niño and 30 mb quasi-biennial oscillation influences', *Monthly Weather Review* **112**(9), 1649–1668.

- Gray, W. M., Sheaffer, J. D. and Knaff, J. A. (1992), 'Influence of the stratospheric QBO on ENSO variability', *Journal of the Meteorological Society of Japan. Ser. II* **70**(5), 975–995.
- Grimm, A. M. (2011), 'Interannual climate variability in South America: impacts on seasonal precipitation, extreme events, and possible effects of climate change', *Stochastic Environmental Research and Risk Assessment* **25**(4), 537–554.
- Guo, Z., Zhou, T., Wang, M. and Qian, Y. (2015), 'Impact of cloud radiative heating on East Asian summer monsoon circulation', *Environmental Research Letters* **10**(7), 074014.
- Ha, K.-J., Moon, S., Timmermann, A. and Kim, D. (2020), 'Future Changes of Summer Monsoon Characteristics and Evaporative Demand Over Asia in CMIP6 Simulations', *Geophysical Research Letters* **47**(8), e2020GL087492.
- Halley, E. (1687), 'An historical account of the trade winds, and monsoons, observable in the seas between and near the tropicks, with an attempt to assign the physical cause of the said winds', *Philosophical Transactions of the Royal Society of London* **16**(183), 153–168.
- URL:** <https://royalsocietypublishing.org/doi/abs/10.1098/rstl.1686.0026>
- Hansen, F., Matthes, K. and Wahl, S. (2016), 'Tropospheric QBO–ENSO interactions and differences between the Atlantic and Pacific', *Journal of Climate* **29**(4), 1353–1368.
- Harris, I., Jones, P. D., Osborn, T. J. and Lister, D. H. (2014), 'Updated high-resolution grids of monthly climatic observations—the cru ts3. 10 dataset', *International journal of climatology* **34**(3), 623–642.
- Hartmann, D. L. (2015), *Global physical climatology*, Vol. 103, Newnes.
- Harvey, C. A., Saborio-Rodríguez, M., Martínez-Rodríguez, M. R., Viguera, B., Chain-Guadarrama, A., Vignola, R. and Alpizar, F. (2018), 'Climate change impacts and adaptation among smallholder farmers in Central America', *Agriculture & Food Security* **7**(1), 57.
- Hastenrath, S. L. (1967), 'Rainfall distribution and regime in Central America', *Archiv für Meteorologie, Geophysik und Bioklimatologie, Serie B* **15**(3), 201–241.
- Hellin, J., Cox, R. and López-Ridaura, S. (2017), 'Maize Diversity, Market Access, and Poverty Reduction in the Western Highlands of Guatemala', *Mountain Research and Development* **37**(2), 188 – 197.
- Hénin, R., Liberato, M. L., Ramos, A. M. and Gouveia, C. M. (2018), 'Assessing the use of satellite-based estimates and high-resolution precipitation datasets for the study of extreme precipitation events over the Iberian Peninsula', *Water* **10**(11), 1688.
- Herrera, E., Magaña, V. and Caetano, E. (2015), 'Air–sea interactions and dynamical processes associated with the midsummer drought', *International Journal of Climatology* **35**(7), 1569–1578.
- Hersbach, H., Bell, B., Berrisford, P., Hirahara, S., Horányi, A., Muñoz-Sabater, J., Nicolas, J., Peubey, C., Radu, R., Schepers, D., Simmons, A., Soci, C., Abdalla, S., Abellán, X., Balsamo, G., Bechtold, P., Biavati, G., Bidlot, J., Bonavita, M., De Chiara, G., Dahlgren, P., Dee, D.,

- Diamantakis, M., Dragani, R., Flemming, J., Forbes, R., Fuentes, M., Geer, A., Haimberger, L., Healy, S., Hogan, R. J., Hólm, E., Janisková, M., Keeley, S., Laloyaux, P., Lopez, P., Lupu, C., Radnoti, G., de Rosnay, P., Rozum, I., Vamborg, F., Villaume, S. and Thépaut, J.-N. (2020), 'The ERA5 global reanalysis', *Quarterly Journal of the Royal Meteorological Society* **146**(730), 1999–2049.
- Higgins, R., Yao, Y. and Wang, X. (1997), 'Influence of the North American monsoon system on the US summer precipitation regime', *Journal of Climate* **10**(10), 2600–2622.
- Hill, S. A. (2019), 'Theories for past and future monsoon rainfall changes', *Current Climate Change Reports* **5**(3), 160–171.
- Holton, J. R. and Tan, H.-C. (1980), 'The influence of the equatorial quasi-biennial oscillation on the global circulation at 50 mb', *Journal of the Atmospheric Sciences* **37**(10), 2200–2208.
- Hoskins, B., Yang, G.-Y. and Fonseca, R. (2020), 'The detailed dynamics of the June–August Hadley Cell', *Quarterly Journal of the Royal Meteorological Society* **146**(727), 557–575.
- Htway, O. and Matsumoto, J. (2011), 'Climatological onset dates of summer monsoon over Myanmar', *International Journal of Climatology* **31**(3), 382–393.
- Huffman, G. J., Adler, R. F., Bolvin, D. T. and Nelkin, E. J. (2010), The TRMM multi-satellite precipitation analysis (TMPA), in 'Satellite rainfall applications for surface hydrology', Springer, pp. 3–22.
- Huffman, G. J., Bolvin, D. T., Nelkin, E. J., Wolff, D. B., Adler, R. F., Gu, G., Hong, Y., Bowman, K. P. and Stocker, E. F. (2007), 'The TRMM Multisatellite Precipitation Analysis (TMPA): Quasi-Global, Multiyear, Combined-Sensor Precipitation Estimates at Fine Scales', *Journal of Hydrometeorology* **8**(1), 38–55.
- Inoue, K. and Back, L. E. (2015), 'Gross moist stability assessment during TOGA COARE: Various interpretations of gross moist stability', *Journal of Atmospheric Sciences* **72**(11), 4148–4166.
- Inoue, K., Biasutti, M. and Fridlind, A. M. (2021), 'Evidence that horizontal moisture advection regulates the ubiquitous amplification of rainfall variability over tropical oceans', *Journal of the Atmospheric Sciences* **78**(2), 529–547.
- Jain, M., Naeem, S., Orlove, B., Modi, V. and DeFries, R. S. (2015), 'Understanding the causes and consequences of differential decision-making in adaptation research: Adapting to a delayed monsoon onset in Gujarat, India', *Global Environmental Change* **31**, 98 – 109.
- Jakob, C. (2014), 'Going back to basics', *Nature Climate Change* **4**(12), 1042.
- Jiménez-Esteve, B. and Domeisen, D. I. V. (2020), 'Nonlinearity in the tropospheric pathway of ENSO to the North Atlantic', *Weather and Climate Dynamics* **1**(1), 225–245.
- Jobbová, E., Helmke, C. and Bevan, A. (2018), 'Ritual responses to drought: An examination of ritual expressions in Classic Maya written sources', *Human Ecology* **46**(5), 759–781.
- Johns, T. C., Durman, C. F., Banks, H. T., Roberts, M. J., McLaren, A. J., Ridley, J. K., Senior, C. A., Williams, K., Jones, A., Rickard, G. et al. (2006), 'The new Hadley Centre climate model

- (HadGEM1): Evaluation of coupled simulations', *Journal of climate* **19**(7), 1327–1353.
- Jones, C. and Carvalho, L. M. (2002), 'Active and break phases in the South American monsoon system', *Journal of Climate* **15**, 905–914.
- Jones, C. and Carvalho, L. M. (2013), 'Climate change in the South American monsoon system: present climate and CMIP5 projections', *Journal of Climate* **26**(17), 6660–6678.
- Jones, C. and Carvalho, L. M. (2018), 'The influence of the Atlantic multidecadal oscillation on the eastern Andes low-level jet and precipitation in South America', *npj Climate and Atmospheric Science* **1**(1), 1–7.
- Jorgetti, T., da Silva Dias, P. L. and de Freitas, E. D. (2014), 'The relationship between South Atlantic SST and SACZ intensity and positioning', *Climate dynamics* **42**(11-12), 3077–3086.
- Karnauskas, K. B., Seager, R., Giannini, A. and Busalacchi, A. J. (2013), 'A simple mechanism for the climatological midsummer drought along the Pacific coast of Central America', *Atmósfera* **26**, 261–281.
- Kennedy, J., Rayner, N., Smith, R., Parker, D. and Saunby, M. (2011), 'Reassessing biases and other uncertainties in sea surface temperature observations measured in situ since 1850: 2. biases and homogenization', *Journal of Geophysical Research: Atmospheres* **116**(D14).
- Kim, H., Caron, J. M., Richter, J. H. and Simpson, I. R. (2020), 'The lack of QBO-MJO Connection in CMIP6 Models', *Geophysical Research Letters* **47**(11), e2020GL087295. e2020GL087295 2020GL087295.
- Kitoh, A. and Uchiyama, T. (2006), 'Changes in onset and withdrawal of the East Asian summer rainy season by multi-model global warming experiments', *Journal of the Meteorological Society of Japan. Ser. II* **84**(2), 247–258.
- Klotzbach, P., Abhik, S., Hendon, H., Bell, M., Lucas, C., Marshall, A. and Oliver, E. (2019), 'On the emerging relationship between the stratospheric Quasi-Biennial oscillation and the Madden-Julian oscillation', *Scientific reports* **9**(1), 1–9.
- Kuhlbrodt, T., Jones, C. G., Sellar, A., Storkey, D., Blockley, E., Stringer, M., Hill, R., Graham, T., Ridley, J., Blaker, A., Calvert, D., Copsey, D., Ellis, R., Hewitt, H., Hyder, P., Ineson, S., Mulcahy, J., Siahaan, A. and Walton, J. (2018), 'The low-resolution version of HadGEM3 GC3. 1: Development and evaluation for global climate', *Journal of advances in modeling earth systems* **10**(11), 2865–2888.
- Lawrence, P. J., Feddema, J. J., Bonan, G. B., Meehl, G. A., O'Neill, B. C., Oleson, K. W., Levis, S., Lawrence, D. M., Kluzeck, E., Lindsay, K. and Thornton, P. E. (2012), 'Simulating the Biogeochemical and Biogeophysical Impacts of Transient Land Cover Change and Wood Harvest in the Community Climate System Model (CCSM4) from 1850 to 2100', *Journal of Climate* **25**(9), 3071–3095.
- Lee, J. C. K. and Klingaman, N. P. (2018), 'The effect of the quasi-biennial oscillation on the Madden–Julian oscillation in the Met Office Unified Model Global Ocean Mixed Layer configuration', *Atmospheric Science Letters* **19**(5), e816.

- Lee, J.-H., Kang, M.-J. and Chun, H.-Y. (2019), ‘Differences in the tropical convective activities at the opposite phases of the quasi-biennial oscillation’, *Asia-Pacific Journal of Atmospheric Sciences* **55**(3), 317–336.
- Li, D., Shine, K. and Gray, L. (1995), ‘The role of ozone-induced diabatic heating anomalies in the quasi-biennial oscillation’, *Quarterly Journal of the Royal Meteorological Society* **121**(524), 937–943.
- Li, G. and Xie, S.-P. (2014), ‘Tropical biases in CMIP5 multimodel ensemble: The excessive equatorial Pacific cold tongue and double ITCZ problems’, *Journal of Climate* **27**(4), 1765–1780.
- Li, T. and Hsu, P.-c. (2018), *Fundamentals of tropical climate dynamics*, Springer.
- Li, W., Fu, R. and Dickinson, R. E. (2006), ‘Rainfall and its seasonality over the Amazon in the 21st century as assessed by the coupled models for the IPCC AR4’, *Journal of Geophysical Research: Atmospheres* **111**(D2).
- Liebmann, B. and Marengo, J. (2001), ‘Interannual variability of the rainy season and rainfall in the Brazilian Amazon Basin’, *Journal of Climate* **14**(22), 4308–4318.
- Liess, S. and Geller, M. A. (2012), ‘On the relationship between qbo and distribution of tropical deep convection’, *Journal of Geophysical Research: Atmospheres* **117**(D3).
- Lim, Y., Son, S.-W., Marshall, A. G., Hendon, H. H. and Seo, K.-H. (2019), ‘Influence of the QBO on MJO prediction skill in the subseasonal-to-seasonal prediction models’, *Climate Dynamics* **53**(3), 1681–1695.
- Lorenz, E. N. (1967), *The nature and theory of the general circulation of the atmosphere*, Vol. 218, World Meteorological Organization Geneva.
- Lu, H., Hitchman, M. H., Gray, L. J., Anstey, J. A. and Osprey, S. M. (2020), ‘On the role of rossby wave breaking in the quasi-biennial modulation of the stratospheric polar vortex during boreal winter’, *Quarterly Journal of the Royal Meteorological Society* **146**(729), 1939–1959.
- Lucas-Picher, P., Christensen, J. H., Saeed, F., Kumar, P., Ashraf, S., Ahrens, B., Wiltshire, A. J., Jacob, D. and Hagemann, S. (2011), ‘Can regional climate models represent the Indian] Monsoon?’, *Journal of Hydrometeorology* **12**(5), 849–868.
- Ma, D., Sobel, A. H., Kuang, Z., Singh, M. S. and Nie, J. (2019), ‘A moist entropy budget view of the South Asian summer monsoon onset’, *Geophysical Research Letters* **46**(8), 4476–4484.
- Ma, T., Chen, W., Huangfu, J., Song, L. and Cai, Q. (2021), ‘The observed influence of the Quasi-Biennial Oscillation in the lower equatorial stratosphere on the East Asian winter monsoon during early boreal winter’, *International Journal of Climatology* .
- Machado, L., Laurent, H., Dessay, N. and Miranda, I. (2004), ‘Seasonal and diurnal variability of convection over the Amazonia: A comparison of different vegetation types and large scale forcing’, *Theoretical and Applied Climatology* **78**(1-3), 61–77.
- Magaña, V., Amador, J. A. and Medina, S. (1999), ‘The midsummer drought over Mexico and Central America’, *Journal of Climate* **12**, 1577–1588.
- Magaña, V. and Caetano, E. (2005), ‘Temporal evolution of summer convective activity over the

- Americas warm pools', *Geophysical Research Letters* **32**(2).
- Maldonado, T., Alfaro, E., Rutgersson, A. and Amador, J. A. (2017), 'The early rainy season in Central America: the role of the tropical North Atlantic SSTs', *International Journal of Climatology* **37**(9), 3731–3742.
- Malhi, Y., Aragão, L. E. O. C., Galbraith, D., Huntingford, C., Fisher, R., Zelazowski, P., Sitch, S., McSweeney, C. and Meir, P. (2009), 'Exploring the likelihood and mechanism of a climate-change-induced dieback of the Amazon rainforest', *Proceedings of the National Academy of Sciences* **106**(49), 20610–20615.
- Mapes, B. E., Liu, P. and Buenning, N. (2005), 'Indian monsoon onset and the Americas midsummer drought: Out-of-equilibrium responses to smooth seasonal forcing', *Journal of Climate* **18**(7), 1109–1115.
- Marengo, J. A., Liebmann, B., Grimm, A. M., Misra, V., Silva Dias, P. L., Cavalcanti, I. F. A., Carvalho, L. M. V., Berbery, E. H., Ambrizzi, T., Vera, C. S., Saulo, A. C., Nogues-Paegle, J., Zipser, E., Seth, A. and Alves, L. M. (2012), 'Recent developments on the South American monsoon system', *International Journal of Climatology* **32**, 1–21.
- Marengo, J. A., Liebmann, B., Kousky, V. E., Filizola, N. P. and Wainer, I. C. (2001), 'Onset and end of the rainy season in the Brazilian Amazon Basin', *Journal of Climate* **14**(5), 833–852.
- Marotzke, J., Jakob, C., Bony, S., Dirmeyer, P., O'Gorman, P., Hawkins, E., Perkins-Kirkpatrick, S., Quéré, C., Nowicki, S., Paulavets, K., Seneviratne, S., Stevens, B. and Tuma, M. (2017), 'Climate research must sharpen its view', *Nature climate change* **7**(2), 89–91.
- Martin, Z., Orbe, C., Wang, S. and Sobel, A. (2021), 'The MJO–QBO Relationship in a GCM with Stratospheric Nudging', *Journal of Climate* **34**(11), 4603–4624.
- Martin, Z., Vitart, F., Wang, S. and Sobel, A. (2020), 'The Impact of the Stratosphere on the MJO in a Forecast Model', *Journal of Geophysical Research: Atmospheres* **125**(4), e2019JD032106. e2019JD032106 2019JD032106.
- Martin, Z., Wang, S., Nie, J. and Sobel, A. (2019), 'The Impact of the QBO on MJO Convection in Cloud-Resolving Simulations', *Journal of the Atmospheric Sciences* **76**(3), 669–688.
- Martinez, C., Goddard, L., Kushnir, Y. and Ting, M. (2019), 'Seasonal climatology and dynamical mechanisms of rainfall in the caribbean', *Climate dynamics* **53**(1–2), 825–846.
- McKenna, S., Santoso, A., Gupta, A. S., Taschetto, A. S. and Cai, W. (2020), 'Indian Ocean Dipole in CMIP5 and CMIP6: characteristics, biases, and links to ENSO', *Scientific reports* **10**(1), 1–13.
- Menary, M. B., Kuhlbrodt, T., Ridley, J., Andrews, M. B., Dimdore-Miles, O. B., Deshayes, J., Eade, R., Gray, L., Ineson, S., Mignot, J., Roberts, C. D., Robson, J., Wood, R. A. and Xavier, P. (2018), 'Preindustrial control simulations with HadGEM3-GC3. 1 for CMIP6', *Journal of Advances in Modeling Earth Systems* **10**(12), 3049–3075.
- Mestas-Nuñez, A. M., Enfield, D. B. and Zhang, C. (2007), 'Water vapor fluxes over the Intra-Americas Sea: Seasonal and interannual variability and associations with rainfall', *Journal*

- of Climate **20**(9), 1910–1922.
- Misios, S., Gray, L. J., Knudsen, M. F., Karoff, C., Schmidt, H. and Haigh, J. D. (2019), ‘Slowdown of the Walker circulation at solar cycle maximum’, *Proceedings of the National Academy of Sciences* **116**(15), 7186–7191.
- Mission, T. R. M. (2011), ‘TRMM (TMPA/3B43) Rainfall Estimate L3 1 Month 0.25 Degree×0.25 Degree V7’, *Version, Greenbelt, MD, Goddard Earth Sciences Data and Information Services Center (GES DISC)*. Accessed: [12-Jan-2019].  
**URL:** [https://disc.gsfc.nasa.gov/datasets/TRMM\\_3B42\\_7/summary](https://disc.gsfc.nasa.gov/datasets/TRMM_3B42_7/summary)
- Moron, V. and Robertson, A. W. (2014), ‘Interannual variability of Indian summer monsoon rainfall onset date at local scale’, *International journal of climatology* **34**(4), 1050–1061.
- Mosíño, A. and García, E. (1966), Evaluación de la sequía intraestival en la República Mexicana, in ‘Proc. Conf. Reg. Latinoamericana Unión Geogr. Int’, Vol. 3, pp. 500–516.
- Mulcahy, J. P., Jones, C., Sellar, A., Johnson, B., Boutle, I. A., Jones, A., Andrews, T., Rumbold, S. T., Molland, J., Bellouin, N., Johnson, C. E., Williams, K. D., Grosvenor, D. P. and McCoy, D. T. (2018), ‘Improved aerosol processes and effective radiative forcing in HadGEM3 and UKESM1’, *Journal of Advances in Modeling Earth Systems* **10**(11), 2786–2805.
- Muñoz, E., Busalacchi, A. J., Nigam, S. and Ruiz-Barradas, A. (2008), ‘Winter and summer structure of the Caribbean low-level jet’, *Journal of Climate* **21**(6), 1260–1276.
- Neelin, J. D. (2007), ‘Moist dynamics of tropical convection zones in monsoons, teleconnections, and global warming’.
- Neelin, J. D., Battisti, D. S., Hirst, A. C., Jin, F.-F., Wakata, Y., Yamagata, T. and Zebiak, S. E. (1998), ‘ENSO theory’, *Journal of Geophysical Research: Oceans* **103**(C7), 14261–14290.
- Neelin, J. D. and Held, I. M. (1987), ‘Modeling tropical convergence based on the moist static energy budget’, *Monthly Weather Review* **115**(1), 3–12.
- Neelin, J. D. and Su, H. (2005), ‘Moist teleconnection mechanisms for the tropical South American and Atlantic sector’, *Journal of Climate* **18**(18), 3928–3950.
- Nie, J., Boos, W. R. and Kuang, Z. (2010), ‘Observational evaluation of a convective quasi-equilibrium view of monsoons’, *Journal of Climate* **23**(16), 4416–4428.
- Nie, J. and Sobel, A. H. (2015), ‘Responses of tropical deep convection to the QBO: Cloud-resolving simulations’, *Journal of the Atmospheric Sciences* **72**(9), 3625–3638.
- Nieto-Ferreira, R. and Rickenbach, T. M. (2011), ‘Regionality of monsoon onset in South America: a three-stage conceptual model’, *International Journal of Climatology* **31**(9), 1309–1321.
- O’Neill, B. C., Tebaldi, C., Vuuren, D. P. v., Eyring, V., Friedlingstein, P., Hurt, G., Knutti, R., Kriegler, E., Lamarque, J.-F., Lowe, J. et al. (2016), ‘The scenario model intercomparison project (ScenarioMIP) for CMIP6’, *Geoscientific Model Development* **9**(9), 3461–3482.
- Ordoñez, P., Nieto, R., Gimeno, L., Ribera, P., Gallego, D., Ochoa-Moya, C. A. and Quintanar, A. I. (2019), ‘Climatological moisture sources for the Western North American Monsoon through a lagrangian approach: their influence on precipitation intensity’, *Earth System*

- Dynamics* **10**(1), 59–72.
- Oueslati, B. and Bellon, G. (2013), ‘Convective entrainment and large-scale organization of tropical precipitation: Sensitivity of the CNRM-CM5 hierarchy of models’, *Journal of climate* **26**(9), 2931–2946.
- Oueslati, B. and Bellon, G. (2015), ‘The double ITCZ bias in CMIP5 models: Interaction between SST, large-scale circulation and precipitation’, *Climate dynamics* **44**(3-4), 585–607.
- Palmer, T. (2019), ‘Stochastic weather and climate models’, *Nature Reviews Physics* **1**(7), 463–471.
- Palmer, T. and Stevens, B. (2019), ‘The scientific challenge of understanding and estimating climate change’, *Proceedings of the National Academy of Sciences* **116**(49), 24390–24395.
- Pascale, S., Carvalho, L. M., Adams, D. K., Castro, C. L. and Cavalcanti, I. F. (2019), ‘Current and Future Variations of the Monsoons of the Americas in a Warming Climate’, *Current Climate Change Reports* pp. 1–20.
- Perdigón-Morales, J., Romero-Centeno, R., Barrett, B. S. and Ordoñez, P. (2019), ‘Intraseasonal variability of summer precipitation in Mexico: MJO influence on the midsummer drought’, *Journal of Climate* **32**(8).
- Perdigón-Morales, J., Romero-Centeno, R., Ordóñez, P. and Barrett, B. S. (2018), ‘The midsummer drought in Mexico: perspectives on duration and intensity from the CHIRPS precipitation database’, *International Journal of Climatology* **38**, 2174–2186.
- Plumb, R. A. and Bell, R. C. (1982), ‘A model of the quasi-biennial oscillation on an equatorial beta-plane’, *Quarterly Journal of the Royal Meteorological Society* **108**(456), 335–352.
- Rauscher, S. A., Giorgi, F., Diffenbaugh, N. S. and Seth, A. (2008), ‘Extension and intensification of the Meso-American mid-summer drought in the twenty-first century’, *Climate Dynamics* **31**, 551–571.
- Raymond, D. J., Sessions, S. L., Sobel, A. H. and Fuchs, Ž. (2009), ‘The mechanics of gross moist stability’, *Journal of Advances in Modeling Earth Systems* **1**(3).
- Reed, R. (1964), ‘A tentative model of the 26-month oscillation in tropical latitudes’, *Quarterly Journal of the Royal Meteorological Society* **90**(386), 441–466.
- Ribera, P., Peña-Ortiz, C., García-Herrera, R., Gallego, D., Gimeno, L. and Hernández, E. (2004), ‘Detection of the secondary meridional circulation associated with the quasi-biennial oscillation’, *Journal of Geophysical Research: Atmospheres* **109**(D18).
- Richter, J. H., Anstey, J. A., Butchart, N., Kawatani, Y., Meehl, G. A., Osprey, S. and Simpson, I. R. (2020), ‘Progress in simulating the Quasi-Biennial Oscillation in CMIP models’, *Journal of Geophysical Research: Atmospheres* **125**(8), e2019JD032362. e2019JD032362 10.1029/2019JD032362.
- Ridley, J., Menary, M., Kuhlbrodt, T., Andrews, M. and Andrews, T. (2018), ‘MOHC HadGEM3-GC31-LL model output prepared for CMIP6 CMIP piControl’.
- URL:** <https://doi.org/10.22033/ESGF/CMIP6.6294>
- Ridley, J., Menary, M., Kuhlbrodt, T., Andrews, M. and Andrews, T. (2019a), ‘Mohc

- hadgem3-gc31-ll model output prepared for cmip6 cmip amip'.  
**URL:** <https://doi.org/10.22033/ESGF/CMIP6.5853>
- Ridley, J., Menary, M., Kuhlbrodt, T., Andrews, M. and Andrews, T. (2019b), 'MOHC HadGEM3-GC31-LL model output prepared for CMIP6 CMIP historical'.  
**URL:** <https://doi.org/10.22033/ESGF/CMIP6.6109>
- Ridley, J., Menary, M., Kuhlbrodt, T., Andrews, M. and Andrews, T. (2019c), 'MOHC HadGEM3-GC31-MM model output prepared for CMIP6 CMIP piControl'.  
**URL:** <https://doi.org/10.22033/ESGF/CMIP6.6297>
- Rodrigues, R. R., Haarsma, R. J., Campos, E. J. and Ambrizzi, T. (2011), 'The impacts of inter-El Niño variability on the tropical Atlantic and northeast Brazil climate', *Journal of Climate* **24**(13), 3402–3422.
- Ropelewski, C. F. and Halpert, M. S. (1986), 'North american precipitation and temperature patterns associated with the el niño/southern oscillation (enso)', *Monthly Weather Review* **114**(12), 2352–2362.
- Ropelewski, C. F. and Halpert, M. S. (1987), 'Global and regional scale precipitation patterns associated with the El Niño/Southern Oscillation', *Monthly weather review* **115**(8), 1606–1626.
- Ryu, J.-H. and Hayhoe, K. (2014), 'Understanding the sources of Caribbean precipitation biases in CMIP3 and CMIP5 simulations', *Climate dynamics* **42**(11-12), 3233–3252.
- Sahana, A. S., Ghosh, S., Ganguly, A. and Murtugudde, R. (2015), 'Shift in Indian summer monsoon onset during 1976/1977', *Environmental Research Letters* **10**(5), 054006.
- Saji, N., Goswami, B. N., Vinayachandran, P. and Yamagata, T. (1999), 'A dipole mode in the tropical Indian Ocean', *Nature* **401**(6751), 360–363.
- Schenzinger, V., Osprey, S., Gray, L. and Butchart, N. (2017), 'Defining metrics of the Quasi-Biennial oscillation in global climate models', *Geoscientific Model Development* **10**(6).
- Schirber, S. (2015), 'Influence of ENSO on the QBO: Results from an ensemble of idealized simulations', *Journal of Geophysical Research: Atmospheres* **120**(3), 1109–1122.
- Schneider, T., Bischoff, T. and Haug, G. H. (2014), 'Migrations and dynamics of the Intertropical Convergence Zone', *Nature* **513**(7516), 45.
- Sellar, A. A., Jones, C. G., Mulcahy, J., Tang, Y., Yool, A., Wiltshire, A., O'Connor, F. M., Stringer, M., Hill, R., Palmieri, J., Woodward, S., de Mora, L., Kuhlbrodt, T., Rumbold, S., Kelley, D. I., Ellis, R., Johnson, C. E., Walton, J., Abraham, N. L., Andrews, M. B., Andrews, T., Archibald, A. T., Berthou, S., Burke, E., Blockley, E., Carslaw, K., Dalvi, M., Edwards, J., Folberth, G. A., Gedney, N., Griffiths, P. T., Harper, A. B., Hendry, M. A., Hewitt, A. J., Johnson, B., Jones, A., Jones, C. D., Keeble, J., Liddicoat, S., Morgenstern, O., Parker, R. J., Predoi, V., Robertson, E., Siahaan, A., Smith, R. S., Swaminathan, R., Woodhouse, M. T., Zeng, G. and Zerroukat, M. (2019), 'UKESM1: Description and evaluation of the UK Earth System Model', *Journal of Advances in Modeling Earth Systems* **11**(12), 4513–4558.
- Serva, F., Anstey, J. A., Bushell, A. C., Butchart, N., Cagnazzo, C., Gray, L., Kawatani, Y.,

- Osprey, S. M., Richter, J. H. and Simpson, I. R. (submitted), ‘The impact of the QBO near the tropical tropopause layer in QBOi models: present-day simulations’, *Quarterly Journal of the Royal Meteorological Society*.
- Shepherd, T. G. (2014), ‘Atmospheric circulation as a source of uncertainty in climate change projections’, *Nature Geoscience* **7**(10), 703–708.
- Small, R. J. O., De Szoeke, S. P. and Xie, S.-P. (2007), ‘The Central American midsummer drought: Regional aspects and large-scale forcing’, *Journal of Climate* **20**(19), 4853–4873.
- Smyth, J. E., Hill, S. A. and Ming, Y. (2018), ‘Simulated responses of the West African Monsoon and zonal-mean tropical precipitation to early holocene orbital forcing’, *Geophysical Research Letters* **45**(21), 12–049.
- Smyth, J. E. and Ming, Y. (2020), ‘Characterizing drying in the South American monsoon onset season with the moist static energy budget’, *Journal of Climate* **33**(22), 9735–9748.
- Sobel, A. H., Nilsson, J. and Polvani, L. M. (2001), ‘The weak temperature gradient approximation and balanced tropical moisture waves’, *Journal of the atmospheric sciences* **58**(23), 3650–3665.
- Son, S.-W., Lim, Y., Yoo, C., Hendon, H. H. and Kim, J. (2017), ‘Stratospheric control of the Madden–Julian oscillation’, *Journal of Climate* **30**(6), 1909–1922.
- Stensrud, D. J., Gall, R. L. and Nordquist, M. K. (1997), ‘Surges over the Gulf of California during the Mexican monsoon’, *Monthly Weather Review* **125**(4), 417–437.
- Storkey, D., Blaker, A. T., Mathiot, P., Megann, A., Aksenov, Y., Blockley, E. W., Calvert, D., Graham, T., Hewitt, H. T., Hyder, P. et al. (2018), ‘UK Global Ocean GO6 and GO7: A traceable hierarchy of model resolutions’, *Geoscientific Model Development* **11**(8), 3187–3213.
- Straffon, A., Zavala-Hidalgo, J. and Estrada, F. (2019), ‘Preconditioning of the precipitation interannual variability in southern Mexico and Central America by oceanic and atmospheric anomalies’, *International Journal of Climatology*.
- Sulca, J., Takahashi, K., Espinoza, J.-C., Vuille, M. and Lavado-Casimiro, W. (2018), ‘Impacts of different ENSO flavors and tropical Pacific convection variability (ITCZ, SPCZ) on austral summer rainfall in South America, with a focus on Peru’, *International Journal of Climatology* **38**(1), 420–435.
- Sultan, B., Baron, C., Dingkuhn, M., Sarr, B. and Janicot, S. (2005), ‘Agricultural impacts of large-scale variability of the west african monsoon’, *Agricultural and Forest Meteorology* **128**(1), 93 – 110.
- Takahashi, K. (2004), ‘The atmospheric circulation associated with extreme rainfall events in Piura, Peru, during the 1997–1998 and 2002 El Niño events’.
- Tang, Y., Rumbold, S., Ellis, R., Kelley, D., Mulcahy, J., Sellar, A., Walton, J. and Jones, C. (2019a), ‘MOHC UKESM1.0-LL model output prepared for CMIP6 CMIP historical’.  
URL: <https://doi.org/10.22033/ESGF/CMIP6.6113>
- Tang, Y., Rumbold, S., Ellis, R., Kelley, D., Mulcahy, J., Sellar, A., Walton, J. and Jones, C. (2019b), ‘MOHC UKESM1.0-LL model output prepared for CMIP6 CMIP piControl’.

- URL:** <https://doi.org/10.22033/ESGF/CMIP6.6298>
- Tedeschi, R. G., Grimm, A. M. and Cavalcanti, I. F. (2015), 'Influence of Central and East ENSO on extreme events of precipitation in South America during austral spring and summer', *International Journal of Climatology* **35**(8), 2045–2064.
- Tegtmeier, S., Anstey, J., Davis, S., Dragani, R., Harada, Y., Ivanciu, I., Pilch Kedzierski, R., Krüger, K., Legras, B., Long, C., Wang, J. S., Wargan, K. and Wright, J. S. (2020a), 'Temperature and tropopause characteristics from reanalyses data in the tropical tropopause layer', *Atmospheric Chemistry and Physics* **20**(2), 753–770.
- Tegtmeier, S., Anstey, J., Davis, S., Ivanciu, I., Jia, Y., McPhee, D. and Pilch Kedzierski, R. (2020b), 'Zonal Asymmetry of the QBO Temperature Signal in the Tropical Tropopause Region', *Geophysical Research Letters* **47**(24), e2020GL089533. e2020GL089533 2020GL089533.
- Thompson, D. W., Baldwin, M. P. and Solomon, S. (2005), 'Stratosphere–troposphere coupling in the southern hemisphere', *Journal of Atmospheric Sciences* **62**(3), 708–715.
- Trejo, F. J. P., Barbosa, H. A., Peñaloza-Murillo, M. A., Moreno, M. A. and Farías, A. (2016), 'Intercomparison of improved satellite rainfall estimation with CHIRPS gridded product and rain gauge data over Venezuela', *Atmósfera* **29**(4), 323–342.
- Trenberth, K. E. (1997), 'The definition of el nino', *Bulletin of the American Meteorological Society* **78**(12), 2771–2778.
- Trenberth, K. E., Branstator, G. W., Karoly, D., Kumar, A., Lau, N.-C. and Ropelewski, C. (1998), 'Progress during TOGA in understanding and modeling global teleconnections associated with tropical sea surface temperatures', *Journal of Geophysical Research: Oceans* **103**(C7), 14291–14324.
- Troup, A. (1965), 'The ‘southern oscillation’', *Quarterly Journal of the Royal Meteorological Society* **91**(390), 490–506.
- Turner, A. G. and Annamalai, H. (2012), 'Climate change and the South Asian summer monsoon', *Nature Climate Change* **2**(8), 587–595.
- Turrent, C. and Cavazos, T. (2009), 'Role of the land-sea thermal contrast in the interannual modulation of the North American Monsoon', *Geophysical Research Letters* **36**(2).
- Vera, C., Higgins, W., Amador, J., Ambrizzi, T., Garreaud, R., Gochis, D., Gutzler, D., Lettenmaier, D., Marengo, J., Mechoso, C. R., Nogues-Paegle, J., Dias, P. L. S. and Zhang, C. (2006), 'Toward a unified view of the American monsoon systems', *Journal of Climate* **19**(20), 4977–5000.
- Walker, G. T. (1924), 'Correlations in seasonal variations of weather. I. A further study of world weather', *Mem. Indian Meteorol. Dep.* **24**, 275–332.
- Walker, G. T. (1932), 'World weather v memories r.', *Meteor. Soc.* **4**, 53–84.
- Walters, D., Boutle, I., Brooks, M., Melvin, T., Stratton, R., Vosper, S., Wells, H., Williams, K., Wood, N., Allen, T., Bushell, A., Copsey, D., Earnshaw, P., Edwards, J., Gross, M., Hardiman, S., Harris, C., Heming, J., Klingaman, N., Levine, R., Manners, J., Martin, G., Milton, S.,

- Mittermaier, M., Morcrette, C., Riddick, T., Roberts, M., Sanchez, C., Selwood, P., Stirling, A., Smith, C., Suri, D., Tennant, W., Vidale, P. L., Wilkinson, J., Willett, M., Woolnough, S. and Xavier, P. (2019), 'The Met Office Unified Model global atmosphere 7.0/7.1 and JULES global land 7.0 configurations', *Geoscientific Model Development* **12**(5), 1909–1963.
- Wang, B., Biasutti, M., Byrne, M. P., Castro, C., Chang, C.-P., Cook, K., Fu, R., Grimm, A. M., Ha, K.-J., Hendon, H. et al. (2021), 'Monsoons climate change assessment', *Bulletin of the American Meteorological Society* **102**(1), E1–E19.
- Wang, B. and Ding, Q. (2008), 'Global monsoon: Dominant mode of annual variation in the tropics', *Dynamics of Atmospheres and Oceans* **44**(3-4), 165–183.
- Wang, C. and Picaut, J. (2004), 'Understanding ENSO physics—A review', *Earth's Climate: The Ocean–Atmosphere Interaction, Geophys. Monogr.* **147**, 21–48.
- Wang, P. X., Wang, B., Cheng, H., Fasullo, J., Guo, Z., Kiefer, T. and Liu, Z. (2017), 'The global monsoon across time scales: Mechanisms and outstanding issues', *Earth-Science Reviews* **174**, 84–121.
- Wang, S., Tippett, M. K., Sobel, A. H., Martin, Z. and Vitart, F. (2019), 'Impact of the QBO on prediction and predictability of the MJO convection', *J. Geophys. Res. Atmos.*.
- Wang, X. and Wang, C. (2014), 'Different impacts of various El Niño events on the Indian Ocean Dipole', *Climate dynamics* **42**(3-4), 991–1005.
- Webb, M. J., Andrews, T., Bodas-Salcedo, A., Bony, S., Bretherton, C. S., Chadwick, R., Chepfer, H., Douville, H., Good, P., Kay, J. E. et al. (2017), 'The cloud feedback model intercomparison project (CFMIP) contribution to CMIP6', *Geoscientific Model Development* **10**(1), 359–384.
- Webster, P. J. (2020), *Dynamics of the Tropical Atmosphere and Oceans*, John Wiley & Sons.
- Webster, P. J. and Yang, S. (1992), 'Monsoon and Enso: Selectively Interactive Systems', *Quarterly Journal of the Royal Meteorological Society* **118**(507), 877–926.
- Whitcher, B., Guttorp, P. and Percival, D. B. (2000), 'Wavelet analysis of covariance with application to atmospheric time series', *Journal of Geophysical Research: Atmospheres* **105**(D11), 14941–14962.
- Wilks, D. S. (2011), *Statistical methods in the atmospheric sciences*, Vol. 100, Academic press.
- Williams, K. D., Copsey, D., Blockley, E. W., Bodas-Salcedo, A., Calvert, D., Comer, R., Davis, P., Graham, T., Hewitt, H. T., Hill, R., Hyder, P., Ineson, S., Johns, T. C., Keen, A. B., Lee, R. W., Megann, A., Milton, S. F., Rae, J. G. L., Roberts, M. J., Scaife, A. A., Schiemann, R., Storkey, D., Thorpe, L., Watterson, I. G., Walters, D. N., West, A., Wood, R. A., Woollings, T. and Xavier, P. K. (2018), 'The Met Office global coupled model 3.0 and 3.1 (GC3. 0 and GC3. 1) configurations', *Journal of Advances in Modeling Earth Systems* **10**(2), 357–380.
- Wing, A. A., Camargo, S. J., Sobel, A. H., Kim, D., Moon, Y., Murakami, H., Reed, K. A., Vecchi, G. A., Wehner, M. F., Zarzycki, C. et al. (2019), 'Moist static energy budget analysis of tropical cyclone intensification in high-resolution climate models', *Journal of Climate* **32**(18), 6071–6095.
- Xie, P. and Arkin, P. A. (1997), 'Global precipitation: A 17-year monthly analysis based on gauge

- observations, satellite estimates, and numerical model outputs', *Bulletin of the American Meteorological Society* **78**, 2539–2558.
- Xie, P., Arkin, P. A. and Janowiak, J. E. (2007), *CMAP: The CPC Merged Analysis of Precipitation*, Springer Netherlands, Dordrecht, pp. 319–328.
- Yang, B., Zhang, Y., Qian, Y., Song, F., Leung, L. R., Wu, P., Guo, Z., Lu, Y. and Huang, A. (2019), 'Better monsoon precipitation in coupled climate models due to bias compensation', *NPJ Climate and Atmospheric Science* **2**(1), 1–8.
- Yin, L., Fu, R., Shevliakova, E. and Dickinson, R. E. (2013), 'How well can CMIP5 simulate precipitation and its controlling processes over tropical South America?', *Climate Dynamics* **41**(11–12), 3127–3143.
- Yoon, J.-H. and Zeng, N. (2010), 'An Atlantic influence on Amazon rainfall', *Climate dynamics* **34**(2), 249–264.
- Yu, B. and Zwiers, F. W. (2010), 'Changes in equatorial atmospheric zonal circulations in recent decades', *Geophysical Research Letters* **37**(5).
- Zermeño-Díaz, D. M. (2019), 'The spatial pattern of midsummer drought as a possible mechanistic response to lower-tropospheric easterlies over the intra-americas seas', *Journal of Climate* **32**(24), 8687–8700.
- Zhai, J. and Boos, W. (2015), 'Regime transitions of cross-equatorial Hadley circulations with zonally asymmetric thermal forcings', *Journal of the Atmospheric Sciences* **72**(10), 3800–3818.
- Zhao, Z., Holbrook, N. J., Oliver, E. C., Ballesteros, D. and Vargas-Hernandez, J. M. (2020), 'Characteristic atmospheric states during mid-summer droughts over Central America and Mexico', *Climate Dynamics* pp. 1–21.
- Zhao, Z. and Zhang, X. (2021), 'Evaluation of methods to detect and quantify the bimodal precipitation over Central America and Mexico', *International Journal of Climatology* **41**, E897–E911.
- Zhou, T., Turner, A. G., Kinter, J. L., Wang, B., Qian, Y., Chen, X., Wu, B., Liu, B., Zou, L. and Bian, H. (2016), 'GMMIP (v1. 0) contribution to CMIP6: global monsoons model inter-comparison project', *Geoscientific Model Development* **9**, 3589–3604.
- Zou, L. and Zhou, T. (2015), 'Asian summer monsoon onset in simulations and CMIP5 projections using four Chinese climate models', *Advances in Atmospheric Sciences* **32**(6), 794–806.